Theoretische Physik

Localized States in Dissipative Systems with Inhomogeneities

Inaugural-Dissertation
zur Erlangung des Doktorgrades
der Naturwissenschaften im Fachbereich Physik
der Mathematisch-Naturwissenschaftlichen Fakultät
der Westfälischen Wilhelms-Universität Münster

vorgelegt von
Felix Tabbert
aus Frankfurt

2019

institut für
theoretische physik

Abstract

In this thesis we investigate the formation and dynamics of localized structures in the vicinity of spatial inhomogeneities. We describe the drastic effects on these structures stemming from the inclusion of even small inhomogeneities. Since these inhomogeneities are inevitable in most experimental setups, we argue that they should be explicitly considered in theoretical modeling approaches.

We therefore introduce the concept of localized structures (LSs) or dissipative solitons in chapter 1, which can be understood as an extension of the concept of classical solitons to the case of dissipative systems with energy gain and loss. We then explain the formation of LSs in the paradigmatic Brusselator model which is one of the first models describing pattern formation in dissipative systems. By deploying numerical path continuation techniques we are able to obtain the bifurcation structure of LSs and effectively determine their region of stability.

We then focus on the formation of LSs in the context of nonlinear optics. After giving a brief overview of the state of research in this field we provide experimental evidence of the formation of LSs in the transverse plane of the cavity of a vertical cavity surface emitting laser (VCSEL) which is optically pumped. The influence of small inhomogeneities, e.g., in the optically injected field has been experimentally reported and becomes particularly obvious when considering time-delayed optical feedback. First experimental results on this matter exhibit an oscillatory motion of LSs around fixed spots. Theoretical investigations based on translationally symmetric mean-field models however suggest that time-delayed feedback should induce a free drift of LSs. We propose to resolve this discrepancy by including small spatial inhomogeneities in the theoretical modeling of these systems, since these inhomogeneities are unavoidable in experimental setups.

We concentrate our analysis on two well known theoretical models which we derive in chapter 2. The Swift-Hohenberg equation (SHE) is one of the most studied systems in various fields of pattern formation. In nonlinear optics it describes the emergence of patterns in the transverse plane of an optically pumped cavity at the onset of optical bistability. The Lugiato-Lefever equation (LLE) is one of the first models specifically describing pattern formation in nonlinear optics. It is often interpreted as an extended dissipative version of the nonlinear Schrödinger equation with additional terms describing optical injection, losses and detuning. Within the field of nonlinear optics, the LLE is one of the most versatile models because it can describe both transversal and longitudinal (or temporal) pattern formation.

In chapter 3 we focus on the SHE and start with a description of the bifurcation structure of the LSs in this system. We describe the limitations of the SHE without spatial inhomogeneities focusing on the discrepancies between theory and experiment when considering time-delayed optical feedback. We then propose to introduce a small amplitude inhomogeneous injection and demonstrate how breaking the translational symmetry of the system resolves these discrepancies. The interplay of an attracting inhomogeneity and destabilizing time-delay leads to an oscillatory LS. We describe the transition from a stable to oscillating to depinning LS in the framework of two different semi-analytical approaches demonstrating that the behavior of a LS in the

vicinity of an inhomogeneity can be modeled by describing the LS as an overdamped particle in a potential well. We provide an explicit expression for the induced potential and a quantitative comparison between the full system and the reduced potential well model.

Finally, chapter 4 focuses on the LLE. We start with a discussion of the classical LLE without time-delayed feedback or spatial inhomogeneities and provide a description of the bifurcation structure explaining the emergence of periodic patterns and LSs in different parameter regimes. Next, we include an inhomogeneity in the injection and discuss its effects. In this chapter, we focus on the influence of the inhomogeneity on the bifurcation structure and stability regimes. Finally, we introduce time-delayed feedback, pointing out the main similarities and differences to the SHE. We close with a brief discussion of the effects of spatially inhomogeneous detuning, which can occur, e.g., due to inaccuracies in the cavity width. This section only provides preliminary results and has to be seen as an outlook, proposing further investigations on this subject.

Both the SHE and the LLE are of paradigmatic simplicity and are suitable to describe a variety of different applications in the field of pattern formation. The inclusion of spatial inhomogeneities has similar, yet drastic effects on the stability and dynamics of LSs in both models. Small spatial inhomogeneities are however hardly considered in theoretical descriptions. The main goal of this thesis therefore is to demonstrate, that the inclusion of possible inhomogeneities is necessary to gain a more realistic description of real experimental setups.

Kurzzusammenfassung

In dieser Dissertation werden lokalisierte Strukturen (LS) und ihre Dynamik in räumlich oder zeitlich inhomogenen dissipativen Systemen untersucht. Hierbei werden die weitreichenden Auswirkungen beschrieben, die Inhomogenitäten auf LS und ihre Stabilität haben. Da solche Inhomogenitäten in den meisten experimentellen Anordnungen unvermeidbar sind, wird in dieser Dissertation dafür plädiert, diese in theoretischen Modellierungsansätzen explizit zu berücksichtigen.

Hierzu wird zunächst eine Definition von LS eingeführt, welche auch häufig als dissipative Solitonen bezeichnet werden. In der in Kapitel 1 vorgestellten Definition wird daher insbesondere eine Abgrenzung zu klassischen Solitonen vorgenommen. Die hier untersuchten LS können als Erweiterung des Solitonenkonzepts auf dissipative Systeme aufgefasst werden. Unter einem dissipativen System wird hierbei ein System verstanden, das sowohl Energieverlusten als auch einer externen Energiezufuhr ausgesetzt ist. Als erstes Beispiel wird die Entstehung von LS im Brüsselatormodell untersucht, welches eines der ersten und weit verbreitetsten Modelle zur Beschreibung von Strukturbildung in dissipativen Systemen darstellt. Mit Hilfe numerischer Pfadkontinuierung wird die Bifurkationsstruktur und der Stabilitätsbereich von LS bestimmt.

Nach dieser Einführung werden LS in den Fokus gerückt, die in nichtlinearen optischen Systemen auftreten. Zu diesem Thema erfolgt zunächst eine kurze Zusammenfassung der bisherigen theoretischen und experimentellen Forschungsergebnisse. Anschließend wird die experimentelle Erzeugung von LS in einem oberflächenemittierenden Laser beschrieben. Durch Variation der optischen Pumpleistung lassen sich einzelne LS erzeugen und vernichten. Hierbei wird insbesondere der Einfluss beschrieben, den kleine Inhomogenitäten auf die Position der LS haben. Bei Versuchen, LS durch zeitverzögerte optische Rückkopplung zu manipulieren, treten die Auswirkungen von Inhomogenitäten besonders deutlich zu Tage. Die zeitverzögerte Rückkopplung destabilisiert LS und erzeugt im Experiment eine Oszillation von LS um bestimmte Positionen. Im Gegensatz dazu sagen theoretische Untersuchungen basierend auf translationsinvarianten Modellen einen Drift der LS verursacht durch Rückkopplung voraus. Im weiteren Verlauf der Arbeit wird daher u.a. gezeigt, dass diese Diskrepanz durch die explizite theoretische Berücksichtigung räumlicher Inhomogenitäten ausgeräumt werden kann.

Hierfür werden zwei mathematische Modelle betrachtet, deren Herleitungen zunächst in Kapitel 2 präsentiert werden. Die Swift-Hohenberg Gleichung (SHE) zählt zu den am meisten untersuchten strukturbildenden Gleichungen. In der nichtlinearen Optik findet sie Verwendung zur Beschreibung von Strukturbildung in der transversalen Ebene eines durch injiziertes Licht optisch gepumpten Resonators an der Schwelle zur optischen Bistabilität. Als zweites Modell wird die Lugiato-Lefever Gleichung (LLE) untersucht, die eines der ersten und vielseitigsten Modelle zur Beschreibung von Strukturbildung in der nichtlinearen Optik darstellt. Die LLE wird häufig als eine verallgemeinerte dissipative Variante der nichtlinearen Schrödinger Gleichung beschrieben, in welcher Verluste innerhalb des Resonators, ein optischer Pumpprozess und eine Verstimmung (detuning) berücksichtigt werden. Die Vielseitigkeit der LLE liegt u.a. darin begründet, dass sie sowohl Strukturbildung in transversaler Richtung als auch longitudinale (oder zeitliche) Strukturbildung beschreibt.

In Kapitel 3 wird die SHE untersucht und zunächst eine Analyse der Bifurkationsstruktur von LS vorgestellt. Es folgt eine Beschreibung der durch zeitverzögerte Rückkopplung in der klassischen translationsinvarianten SHE entstehenden Dynamik von LS, wobei erneut die Unterschiede zu experimentellen Resultaten hervorgehoben werden. Anschließend wird eine kleinamplitudige inhomogene Injektion eingeführt, die die Translationssymmetrie des Systems explizit bricht. Die Berücksichtigung dieses Zusatzterms führt zu einer realistischeren Dynamik von LS in der Umgebung der Inhomogenität. Die konkurrierenden Effekte einer attraktiv wirkenden Inhomogenität und einer destabilisierenden zeitverzögerten Rückkopplung führen zu LS, die um die Inhomogenität oszillieren. Im Folgenden wird der Übergang von einer stabilen LS zu einer oszillierenden LS und von der oszillierenden zu einer frei driftenden LS im Rahmen zweier semi-analytischer Ansätze beschrieben, wobei u.a. gezeigt wird, dass eine LS in der Umgebung der Inhomogenität durch ein überdämpftes Teilchen in einem Potential approximiert werden kann. In diesem Zusammenhang wird ein expliziter Ausdruck für das durch die Inhomogenität verursachte Potential hergeleitet und anschließend ein quantitativer Vergleich des reduzierten Potentialmodells mit dem ursprünglichen Modell der SHE mit zeitverzögerter Rückkopplung durchgeführt.

Im letzten Kapitel 4 wird die LLE untersucht, wobei mit der klassischen translationsinvarianten LLE ohne Inhomogenitäten oder zeitverzögerte Rückkopplung begonnen wird. Hier wird die Bifurkationsstruktur von periodischen Lösungen und von LS in verschiedenen Parameterbereichen abhängig von der optischen Pumpleistung und der Verstimmung untersucht. Anschließend wird erneut eine Inhomogenität im optischen Pumpvorgang eingeführt. Bei der Untersuchung der Auswirkung von Inhomogenitäten liegt der Fokus in diesem Kapitel auf Veränderungen der Bifurkationsstruktur und der Stabilitätsbereiche. Im letzten Abschnitt des Kapitels wird erneut eine zeitverzögerte Rückkopplung eingeführt und es werden Unterschiede und Ähnlichkeiten zur Dynamik in der SHE aufgezeigt. Das Kapitel endet mit einer kurzen Diskussion von inhomogener Verstimmung, welche u.a. durch Ungenauigkeiten in der Breite des Resonators entstehen kann. Es werden jedoch nur einige erste Ergebnisse zu dieser Thematik vorgestellt, die weiter vertieft werden sollten.

Sowohl die SHE als auch die LLE zählen zu den weit verbreitetsten strukturbildenden Modellen und können aufgrund ihrer paradigmatischen Einfachheit eine Vielzahl unterschiedlicher Phänomene beschreiben. Die Berücksichtigung von Inhomogenitäten hat in beiden Modellen ähnliche und durchaus drastische Auswirkungen auf die Stabilität und Dynamik von LS. Kleine räumliche Inhomogenitäten in experimentellen Aufbauten sind in der Regel nicht vollständig zu vermeiden, werden in theoretischen Modellen jedoch häufig vernachlässigt. Das Hauptziel dieser Dissertation ist daher aufzuzeigen, dass die Berücksichtigung von Inhomogenitäten für eine realistischere theoretische Beschreibung von experimentellen Ergebnissen notwendig ist.

Contents

Introduction

The self-organized formation of patterns is an everyday phenomenon which can be observed in a variety of different fields spanning from biology, where such patterns can be found on the skin or fur of animals [KA95, KS09, MMF$^+$17] or in vegetation [vHMSZ01, TLV08], to chemistry [PL68] and of course to physics, where prominent examples are the formation of clouds [BB99] or periodic patterns in the sand of dunes and deserts [AA10]. The process of pattern formation in these systems can be denoted as self-organized, because the emergence of patterns is not forced externally but results from a complex interplay between the constituents of the system. The length and time scales of the arising macroscopic patterns are typically much larger than those of the constituents and are also not determined externally [CH93].

Despite its omnipresence, pattern formation has only started to draw the attention of theoretical physicists in the last century [CH93], although irregular patterns in turbulent flows in particular, have fascinated scientists for much longer [Eck05]. A pioneering step towards the understanding of spatio-temporal pattern formation was Alan Turing's work on "The Chemical Basis of Morphogenesis" [Tur90], in which he presents a mechanism for pattern formation consisting of an interplay between nonlinear effects and diffusion. Initially, Turing's work on this matter did not receive much attention. This changed when Prigogine and Lefever picked up Turing's ideas. They proposed a simple model of two partial differential equations which describes the emergence of patterns in a chemical system [PL68] and is now known as the Brusselator model [PnPG01]. The Brusselator model exhibits periodic stripe patterns or hexagonal patterns, which are often referred to as Turing patterns. These patterns emerge due to an instability of a homogeneous solution with respect to perturbations of a finite wavelength.

The emergence of Turing patterns is a good example of the above described principle of self-organization, since the unstable finite wave-length leading to periodic patterns is determined by system parameters and is not defined by external factors such as, e.g., the geometry of the domain or a periodic forcing. Nevertheless, pattern formation relies on external energy supply, i.e., patterns can not emerge in thermal equilibrium which would contradict the second law of thermodynamics [Pri78]. Prigogine therefore developed the theory of dissipative structures where he underlined the importance of nonequilibrium conditions for the formation of macroscopic structures [PL73].

Since then, the theoretical and experimental investigation of pattern formation in dissipative systems has been an active field of research [CH93]. A class of patterns which has been studied extensively aside from Turing patterns are localized structures (LSs), which can be found in a variety of different systems ranging from plant ecology [TLV08, TCP18] to nonlinear optics [BTB$^+$02]. A localized structure basically consists of an isolated peak surrounded by a uniform state. Following this simple definition, these structures have similarities to solitons, which in the strict mathematical sense are defined as exact solutions of integrable conservative systems, such as the Korteweg–de Vries equation or the nonlinear Schrödinger equation [AA08]. Localized structures in dissipative systems, i.e., in systems that are not conservative and typically can not be solved analytically, therefore are sometimes referred to as dissipative solitons [BP95]. However, a variety of different terms for these structures exists, depending on the context they

appear in. Despite the obvious similarities between LSs and classical solitons, some important differences arise from the dissipative nature of the systems exhibiting LSs. Akhmediev et al. therefore developed a concept of dissipative solitons as an extension of the classical soliton concept [AA08].

We present this concept in chapter 1, however we refer to these structures as localized structures or localized states (LSs) to avoid confusion with classical solitons. In contrast to classical solitons, the theoretical investigation of LSs mainly relies on numerical approaches such as direct numerical time simulations or numerical path continuation. We apply both methods with a focus on continuation techniques. These techniques are used to obtain steady state solutions of a PDE-system while varying one or more parameters of the system, the so-called continuation parameters. As a first example of a dissipative system exhibiting LSs as solutions, we discuss the paradigmatic Brusselator model. By employing numerical path continuation we are able to determine the bifurcation structure of these solutions which has not been reported yet. We then focus on the field of nonlinear optics. This extremely rich field sums up all optical phenomena, which are based on non-neglectable nonlinear effects [LPB15]. These effects typically become relevant at high intensities of light, which is why the field of research has gained significance with the invention and mass production of lasers. Nonlinear optics provide a variety of possibilities to intentionally implement and exploit desired nonlinear effects in an experimental setup. One of the simplest examples of an optical nonlinearity stems from the optical Kerr effect, which describes the nonlinear dependency of the refractive index of a given medium on the intensity of the electrical field in the medium [LPB15]. The Kerr effect occurs in any medium, however, the nonlinear contributions only become relevant for large enough intensities and only in certain media, which are referred to as Kerr media. Due to the variety of different nonlinear effects, nonlinear optical setups are particularly suited for the experimental observation of pattern formation as we shall explain in chapter 1.

Self-organization in nonlinear optical systems was first described by Hermann Haken [Hak70], who developed a complete semi-classical laser theory based on the ideas of self-organization far from equilibrium. The concept of dissipative pattern formation was first theoretically extended to the field of nonlinear optics by the work of Lugiato and Lefever [LL87]. They proposed a simplified paradigmatic model (the so-called Lugiato-Lefever model) which describes pattern formation in the slowly varying amplitude of an electrical field in the transverse plane of a cavity filled with a Kerr medium. The crucial role of diffusion in the works of Turing and Prigogine is in this case replaced by diffraction which provides a similar spatial interaction.

The Lugiato-Lefever equation (LLE) is one of the most studied models in nonlinear optics due to its paradigmatic simplicity and its versatile applicability. Besides describing the formation of Turing patterns in the transverse plane of a cavity, it was shown that the model also exhibits LSs [LPGK18]. Furthermore, the LLE does not only describe pattern formation in the transverse plane of a cavity, but a mathematically identical equation can be used to describe the formation of temporal (or longitudinal) patterns in a ring cavity [HTW92]. This interpretation of the LLE gained new significance, when it was shown that it is suitable to describe the generation of frequency combs in Kerr microresonators [CRSE13].

Experimentally, both temporal [DSA$^+$07] and transversal [BTB$^+$02] LSs have been realized in a variety of different setups. We provide a short review of the state of research on this matter in chapter 1 before discussing the experimental generation of LSs in the transverse plane of the cavity of a broad area vertical cavity surface emitting laser (VCSEL) in more detail.

The mean field models used to theoretically investigate the formation of LSs in nonlinear optics typically posses a continuous translational symmetry [LPB15]. Nevertheless, experimen-

tal results suggest that small spatial inhomogeneities play a crucial role in the formation of LSs [BTB$^+$02]. Furthermore, first attempts of controlling LSs experimentally by implementing time-delayed optical feedback show drastic discrepancies compared to theoretical predictions based on models with translational symmetry.

Analytical and numerical investigations of these models suggest that time-delayed feedback induces a drift of LSs [TVPT09, GF13]. First experimental results, however, show that a destabilization of a LS by time-delayed feedback leads to an oscillation of the LS around a fixed position [Ave18]. In the course of this thesis, we show that the inclusion of spatial inhomogeneities into theoretical models can resolve this discrepancy. Therefore, the description of spatial inhomogeneities and their effect on the formation and dynamics of LSs is the main focus of this thesis.

After discussing the formation of LSs in general and in nonlinear optics in particular in chapter 1, we then focus on two well-known models, namely the Swift-Hohenberg equation (SHE) and the Lugiato-Lefever equation (LLE). In chapter 2 we present the derivations of both models. In the context of nonlinear optics, the SHE describes pattern formation in the transverse plane of an optically pumped cavity at the onset of optical bistability [MT04]. As stated above, the LLE is valid in different interpretations [LPGK18]: On the one hand, the LLE describes pattern formation in the transverse plane of an optically pumped cavity. On the other hand, it can be used to describe the formation of longitudinal or temporal patterns in a ring resonator filled with a Kerr medium.

In the following chapters 3 and 4 we present the main results of this thesis. In chapter 3 we concentrate on the SHE. We present the bifurcation structure responsible for the emergence of stable LSs and also explain the origin of asymmetric so-called rodlike solutions which have, so far, only been observed in direct numerical time simulations [BC15]. These solutions are stretched in one direction leading to LSs which are not radially symmetric.

Next, we briefly summarize previous results concerning the destabilization of LSs by time-delayed feedback and show that the predominant drift of LSs is independent of the specific properties of the SHE but occurs in every model with a continuous translational symmetry and time-delayed feedback. Since this behavior is not observed in experiments, we then propose the inclusion of a small amplitude inhomogeneous injection in the SHE and show, that the resulting dynamics are more realistic. The competing effects of an attracting inhomogeneity and destabilizing time-delayed feedback lead to a LS oscillating in position around the inhomogeneity. Only for larger values of the inhomogeneity, the LS depins and starts to drift. We continue with a more systematic analysis of the induced dynamics proposing two different approaches: First, we derive an order parameter equation for the onset of oscillations identifying the transition from resting to oscillating LSs as a delay-induced Hopf bifurcation. Then, we close the analysis of the SHE with the introduction of a potential well model, where we treat the LS in the vicinity of the inhomogeneity as an overdamped particle in a potential well. We provide an analytical expression for the induced potential and show that the proposed model captures the induced dynamics both qualitatively and quantitatively.

The analysis of the LLE is presented in chapter 4. We start with the classical LLE and discuss its solution structure and the emergence of LSs. To this aim, we deploy numerical continuation techniques varying the two main parameters of the LLE, namely the amplitude of the injected field E_i and the detuning θ between the resonant frequency of the cavity and the frequency of the injected field. The formation of periodic patterns and LS in the region of low detuning ($\theta < 2$) has been investigated previously whereas the emergence of these structures in the region of large detuning $\theta > 2$ was only recently discussed [PRGGK18a]. We present

the bifurcation structure of LSs and show that a systematic differentiation between solutions consisting of several LSs and periodic solutions is not possible in this regime.

We then introduce inhomogeneous injection to the LLE and discuss its effects in the different regimes of detuning. Especially for low values of the detuning ($\theta < 2$), the inhomogeneity has drastic effects on the stability of LSs. These effects of small inhomogeneities on LSs can be desirable for experimental realizations, since it is possible to enlarge the region of stability of LSs and avoid a multistability between a single peak LS and other solutions.

The influence of inhomogeneous injection in regions of larger detuning is far more intricate. A given inhomogeneity can act either attracting or repelling on LSs depending on other parameters of the system. We explain this behavior based on recent results from Hendry et al. [HCW$^+$18] who investigated Gaussian injection in the LLE. We identify the bifurcations responsible for the transition from attracting to repelling inhomogeneities and apply the potential well model derived in chapter 3. Then, we close with a systematic description of the whole parameter space of the LLE and demonstrate the changes induced by an inhomogeneity. To this aim we deploy numerical continuation techniques with additional constraints, which enable us to follow fold and bifurcation points in parameter space.

In the final section of chapter 4, we introduce time-delayed feedback to the LLE and discuss the occurring delay-induced instabilities. Due to several eigenmodes which are close to instability in the LLE without delay, the resulting dynamics is more complex than in the SHE. However, the induced dynamics with and without inhomogeneities show similarities to the SHE, suggesting that the effects of inhomogeneities presented in this thesis can be translated to other mean-field models. We close with a brief discussion of spatially inhomogeneous detuning, which can occur naturally due to small inaccuracies of, e.g., the cavity width [BTB$^+$02]. We demonstrate that these inhomogeneities have a more complex impact on the dynamics of LSs which might serve as a criterion to distinguish different types of inhomogeneities encountered in experiments.

Both the SHE and the LLE are among the most studied equations in pattern formation. The LLE serves as a versatile model describing different scenarios in nonlinear optics and is particularly relevant in the field of optical frequency comb generation where it serves as a quantitatively accurate model. Optical frequency combs consist of a large number of equidistant peaks in the frequency domain and are therefore commonly used for high precision measurements of frequencies. The SHE has been studied in a variety of different applications ranging from hydrodynamics to plant ecology [LBCL09] and nonlinear optics. In this thesis we are able to demonstrate that the inclusion of even small spatial inhomogeneities in both models has similar but drastic effects on the solution structure. Our findings suggest that the consideration of inhomogeneities results in substantial differences to the idealized perfectly homogeneous models. Therefore it is worthwhile to extend the study of inhomogeneities and to consider them in theoretical modeling approaches in order to gain a more realistic description of pattern forming systems.

1 Localized states in dissipative systems

In this chapter we introduce the main subject of this thesis, i.e., localized solutions or localized states (LSs) in dissipative systems. Therefore, we first define LSs and differentiate them from classical solitons. We then provide a first theoretical example of LSs in the paradigmatic Brusselator model describing pattern formation in a chemical system. Employing numerical parameter continuation we identify the bifurcations leading to the formation of LSs and determine their region of stability. The bifurcation structure of LSs in the Brusselator has not been studied before, making this section the only part of this chapter where we present novel results.

In the remaining part of the chapter we focus on localized solutions appearing in the context of nonlinear optics and briefly outline the most important theoretical and experimental results responsible for the growing research interest in these structures. We then focus on a specific experimental setup used in the laboratories of the K. Panajotov group where we were able to generate LSs in the transverse plane of an optically and electrically pumped cavity. These results were one of the key reasons to include small spatial inhomogeneities into the theoretical models which we discuss in this thesis.

1.1 Formation of localized states

A localized state or localized solution in the broadest sense can be phenomenologically described as a temporal profile or a spatial profile in one or more dimensions of a given quantity q, which consists of a amplitude peak surrounded by a uniform background. The term "localized state" applies to both theoretical and experimental observations while the term "localized solution" refers more specifically to a solution of a mathematical model, usually a system of partial differential equations (PDEs)or time-delayed PDEs. In the following we use both terms synonymously and after introducing the concept in this section, only refer to them as LS(s).

In some systems, two or more of these peaks can form bound states which also qualify as a localized solution as long as they do not fill the complete domain under consideration. In the case where the peak profile is inverted, the solution is often referred to as a dark LS.

Judging from the rough definition above, similarities to classical solitons, e.g., solutions of the nonlinear Schrödinger equation, are evident. Depending on the context of their appearance LSs are called dissipative solitons [AA08] or are simply referred to as solitons which, however, is imprecise. In nonlinear optics they are often called cavity solitons [BTB+02] or Kerr solitons when occurring in a Kerr medium [KGLG18, CSE+18]. In the following we point out some similarities and differences between classical solitons and LSs to gain a more precise definition of both.

The first phenomenological description of a soliton-like structure date back at least to the 19th century when John Scott Russell described a single large amplitude wave propagating with preserved shape in a water channel [Waz09]. The first mathematical description was achieved by Zabusky and Kruskal [ZK65] analyzing the Korteweg-de Vries equation which describes e.g.,

waves in shallow water. By solving the Korteweg-de Vries equation numerically they find single peak solutions which they name solitons. These solitons drifted with a velocity proportional to their amplitude while remaining constant in shape.

Fundamental for the mathematical definition of a soliton is the work of Gardner et al. [GGKM67], who solved the Korteweg-de Vries equation analytically introducing the inverse scattering transform. This approach is applicable to a number of systems exhibiting soliton-like solutions which leads to the mathematically definition of a soliton. A soliton in this strict sense is defined as the exact solution of a system which can be solved by the inverse scattering method [AA08]. These systems are described by one or more autonomous partial differential equations (PDEs). The time-evolution of the order parameter q is then given by:

$$\partial_t q(x,t) = F\left[q(x,t), \partial_x q(x,t)...\left(\partial_x\right)^n q(x,t)\right], \tag{1.1}$$

where the function F on the right-hand side depends on q and its derivatives with respect to the spatial coordinate x. We restrict ourselves to the example of a single order parameter in one spatial dimension, however a system under consideration may be described by a set of order parameters resulting in coupled PDEs. The extension of the example to more than one spatial dimension is also straightforward.

The best known examples for equations with classical solitons as solutions besides the Korteweg-de Vries equation are the nonlinear Schrödinger equation and the Sine-Gordon equation. In both cases the soliton solution can be determined analytically by means of the inverse scattering technique.

The emergence of a soliton can be ascribed to two competing effects resulting in the stable shape of a solitary solution. On the one hand, group-velocity dispersion, i.e., the fact that components of different frequency travel with different velocities through a medium, broadens a peaked solution. This effect has to be counterbalanced by a nonlinearity which steepens the peak. Only if these two effects are balanced, a stable soliton can exist. That is, the formation of a soliton can be considered as a process of self-organization in the sense that the shape of the soliton is not explicitly set by an external forcing but evolves from the complex interplay between dispersion and nonlinearity. Nevertheless, the height of a resulting soliton is typically not fixed but depends on the initial condition. Furthermore, solitons exist in solution families [AA08], i.e., initializing the system with an initial condition of larger amplitude (or larger energy) results in a soliton of larger amplitude. The existence of solution families of classical solitons is closely related to the properties of the system they appear in.

Classical solitons exist in integrable systems, which are always conservative. A direct consequence of energy conservation is the fact that the phase space volume of the system is not contracted in time [Str01] which excludes the possibility of fixed points or attractors. The impossibility of fixed points in a conservative system can be explained rather intuitively: Since two initial conditions with slightly different energies will maintain these different energies, they can never converge into the same solution, i.e., be pulled into the same attractor. In systems exhibiting classical solitons, two slightly different initial conditions can only result in two slightly different solitons of the same soliton family.

However, most realistic physical systems exhibit energy losses or are supplied with some source of energy. In the following we sum up both energy losses and energy supply with the term "dissipation" although it is often only understood as loss of energy.

Since dissipation in this broader sense occurs in almost any physical system, it is helpful to develop a more generalized concept of soliton-like solutions in dissipative systems. Akhmediev

et al. proposed such a concept in [AA08], which besides the classical soliton concept includes two more constituents, namely the theory of nonlinear dynamics and Prigogines concepts of the self-organized emergence of dissipative structures [PL73].

The formation of stable patterned solutions far from equilibrium is a phenomenon which has been first theoretically described by Alan Turing [Tur90] and gained scientific interest with the pioneering work of Ilya Prigogine et al. [PL68], who propose the Brusselator model as a first spatially extended chemical system exhibiting pattern formation far from equilibrium. A suitable mathematical framework for the analysis of these patterns was found by extending the theory of nonlinear dynamical systems and bifurcation theory to spatially extended systems. In this context the emergence of periodic Turing patterns in a Turing instability can be identified as a pitchfork bifurcation of the homogeneous solution.

Analogously, stationary soliton-like solutions in dissipative systems can be classified as a fixed point of an infinite dimensional dynamical system. Hence, an oscillating soliton-like solution is represented by a periodic orbit in phase space. In the following, we denote soliton-like solutions in dissipative systems as localized solutions or localized structures (LSs) to avoid any confusion with classical solitons.

The intuitive explanation for the formation of solitons as the result of a balance between broadening dispersion and amplifying nonlinearity alone fails in the case of LSs. Since energy is not preserved, a balance between gain and loss of energy has to be reached additionally, to maintain a stable LS. Akhmediev et al. [AA08] therefore propose to interpret a LS (dissipative soliton in their work) as the result of a double-balance between dispersion (or any other form of spatial interaction) and nonlinearity on the one hand, as well as gain and loss of energy on the other hand. Since energy is not conserved in dissipative systems, different initial conditions with differing energies may end up in the same stable solution since they can in principle loose excessive energy or gain lacking energy from an external pumping process. Stable LSs therefore typically do not occur as solution families, but as isolated attractors in phase space [AA08]. This, however, does not exclude the possibility of more than one stationary LS in a system. Hence, the solution structure of a dissipative PDE system has to be analyzed, e.g., by a bifurcation analysis.

Before we take a closer look at the bifurcation structure of LSs in the Brusselator model as a first example, we can summarize a few properties which apply to stable LSs in general. Due to the distinct structure of a LS consisting of a single peak while the rest of the arbitrarily large domain is occupied by a uniform state, this uniform state itself has to be stable. Hence, a homogeneous and stable solution apart from the LS has to exist. Any system exhibiting stable LSs is therefore at least bistable in the parameter regime where LSs are stable. Depending on the initial conditions, the system will relax into one of the two stable solutions or, in the case where the initial condition does not lie within the basin of attraction of any of the two attractors, exhibit an entirely different dynamics. This necessary condition of a stable homogeneous solution holds for any system with a translational symmetry, however we shall see in chapter 4 that exceptions to this rule have to be taken into account when dealing with spatially inhomogeneous systems, as in these cases the existence of a homogeneous solution is prevented by the inhomogeneities.

Furthermore, LSs typically arise in the vicinity of a Turing bifurcation. More specifically they often bifurcate [BK07] close to or at the Turing point as unstable small amplitude solutions before gaining stability in a fold. In these cases they exist as stable solutions in a parameter regime where both the homogeneous and at least one periodic solution is stable. A hand-waving argument for this coexistence can be found in [Gom03], where a single LS is interpreted as the

remaining single peak of an otherwise domain filling periodic hexagonal pattern, surrounded by the uniform state. Therefore, a promising region in parameter space to encounter stable LSs is close to a subcritical Turing bifurcation. Only in the subcritical case of a Turing bifurcation the periodic and the homogeneous solution can coexist stably [BK07]. Systems with a conservation law pose an exception to this general rule of thumb as was first shown by Matthew and Cox [MC00]. In these systems, e.g., the overall quantity of the order parameter q is conserved and LSs can form when the Turing bifurcation is supercritical. In this case the LSs exist in parameter regions where no periodic solution exist. An example can be found in [TAR⁺13]. Although these systems are dissipative and should not be confused with conservative systems, we do not discuss them any further in this thesis since they do not apply to optical systems. After this general discussion of properties and nomenclature of solitons and resembling solutions, we will now focus on an exemplary system and discuss the formation of LSs in more detail.

1.1.1 Localized solutions in the Brusselator model

In this section we discuss the emergence of LSs in the spatially extended Brusselator model. This discussion is fruitful for two reasons. The Brusselator model is one of the paradigmatic and most studied pattern forming dissipative systems and therefore serves as a good example. Furthermore, the LSs in the Brusselator model were discovered only recently. With the following description of their bifurcation structure (which has been published already in [KTT⁺18]) we are able to provide new insights into the solution structure of this well established model.

The Brusselator model was first proposed as an idealized model for pattern formation in a chemical system by Prigogine and Lefever in 1968 [PL68]. It models the simple scheme of reactions:

$$\overline{A} \to \overline{X}, \tag{1.2}$$

$$2\overline{X} + \overline{Y} \to 3\overline{X}, \tag{1.3}$$

$$\overline{B} + \overline{X} \to \overline{Y} + \overline{C}, \tag{1.4}$$

$$\overline{X} \to \overline{E}, \tag{1.5}$$

with the reactants $(\overline{A}, \overline{B}, \overline{C}, \overline{E}, \overline{X}, \overline{Y})$. The concentrations of the reactants $(A, B, C, E \in \mathbb{R}^+)$ are kept constant by continuously supplying the system with missing molecules or taking exceeding molecules out of the system. This assumption yields the dissipative nature of the system, however, it also represents a strong idealization. Nevertheless, proposing a more realistic model for chemical reactions exceeds the scope of this thesis.

The Brusselator model provides evolution equations for the concentrations of the reactants $X, Y \in \mathbb{R}^+$, which are also referred to as activator (X) and inhibitor (Y) in two spatial dimensions (x, y) considering also the diffusion of the components. The non-dimensional version of the Brusselator model reads:

$$\frac{\partial X}{\partial t} = \frac{\partial X^2}{\partial x^2} + \frac{\partial X^2}{\partial y^2} + A - (B+1)X + X^2 Y,$$

$$\frac{\partial Y}{\partial t} = D\left(\frac{\partial Y^2}{\partial x^2} + \frac{\partial Y^2}{\partial y^2}\right) + BX - X^2 Y, \tag{1.6}$$

where D represents the ratio of the diffusion constants of Y and X, respectively. Typically, in pattern forming systems, one component diffuses much faster than the other, i.e., $D \gg 1$

(in the following $D = 150$). The constant concentrations A and B are the control parameters of the model (1.6), which determine the stationary and dynamical solutions of the system. Typical solutions which have been studied extensively for the Brusselator model include a spatially homogeneous solution $(X_s, Y_s) = (A, B/A)$, periodic solutions in time or in space or the combination of both, resulting in traveling or spiraling waves [KTT$^+$18].

A Turing instability of the spatially homogeneous solution occurs at $B = (1 + A/\sqrt{D})^2$, $D^{-1} < 1$ which leads to a finite band of unstable wavelengths resulting in spatially periodic patterns. Depending on the stability regime, both stripe solutions and hexagonal structures exist [PnPG01]. For values of $B > 1 + A^2$ an Andronov-Hopf instability occurs [KTT$^+$18], leading to temporal oscillations. Since we are interested in the study of stable LSs, we will remain in the parameter region $B < 1 + A^2$.

Going beyond the results of a linear stability analysis of the homogeneous solution one can either apply a weakly nonlinear analysis [PnPG01] or solve Eq. (1.6) for a given set of parameters by direct numerical time simulations. For a more systematic analysis of the solution structure we employ numerical continuation techniques provided by the Matlab package *pde2path* [UWR14]. Numerical parameter continuation in two spatial dimensions is a novel technique in theoretical chemistry or pattern formation in general, so far only few recent works have addressed this issue in, e.g., the modeling of thin films [EWGT16, EGU$^+$18] and laser dynamics [GJ17, SJG18]. The main idea of numerical parameter continuation is to explore the parameter space of a given system with an effective numerical scheme. Starting from a known stationary solution for a fixed set of parameters, one slightly alters a control parameter in each step and approximates the new solution using Newton's method. This procedure leads to a step by step exploration of the parameter space. To follow a given solution branch around a fold (or saddle-node bifurcation), one has to apply the pseudo-arclength or Keller method [Kel79] in which both the control parameter and the solution branch are approximated functions of the arclength. By introducing additional constraints which are fulfilled at saddle-node, pitchfork or Andronov-Hopf bifurcations, as well as an additional free parameter we are also able to follow bifurcation points in a parameter space spanned by two parameters. For a more detailed description of numerical continuation techniques, we refer the reader to [Wil16, ET17].

In the Brusselator model we use a LS obtained by direct numerical simulations as a starting solution and then follow this solution in parameter space when varying the control parameter B. As a solution measure we use the L_1-norm of the activator which we define as:

$$L_{1X} = \int |X - \overline{X}| \mathrm{d}x\mathrm{d}y, \tag{1.7}$$

where $\overline{X}$ denotes the mean activator concentration in the domain, i.e., a homogeneous solution is represented by $L_{1X} = 0$. For the sake of numerical accuracy and efficiency, we use a mesh refinement, i.e., a more dense spatial discretization where necessary and a more sparse discretization where possible. Since we are interested in radially symmetric solutions, we consider only a quarter of the domain with Neumann boundary conditions and then unfold the symmetric solutions afterwards.

A first bifurcation diagram is depicted in Fig. 1.1. The black line corresponds to the homogeneous solution branch, which becomes unstable in a Turing point at $B \approx 1.1$. At this point a periodic rhombic solution (red line) branches off. The branch of LS (blue line) bifurcates from the periodic branch close to the Turing point. According to recent work on this subject [BBKM08], this is due to a finite size effect, i.e., on an infinite domain both branches would bifurcate exactly in the Turing point. The LS branch bifurcates in a supercritical pitchfork
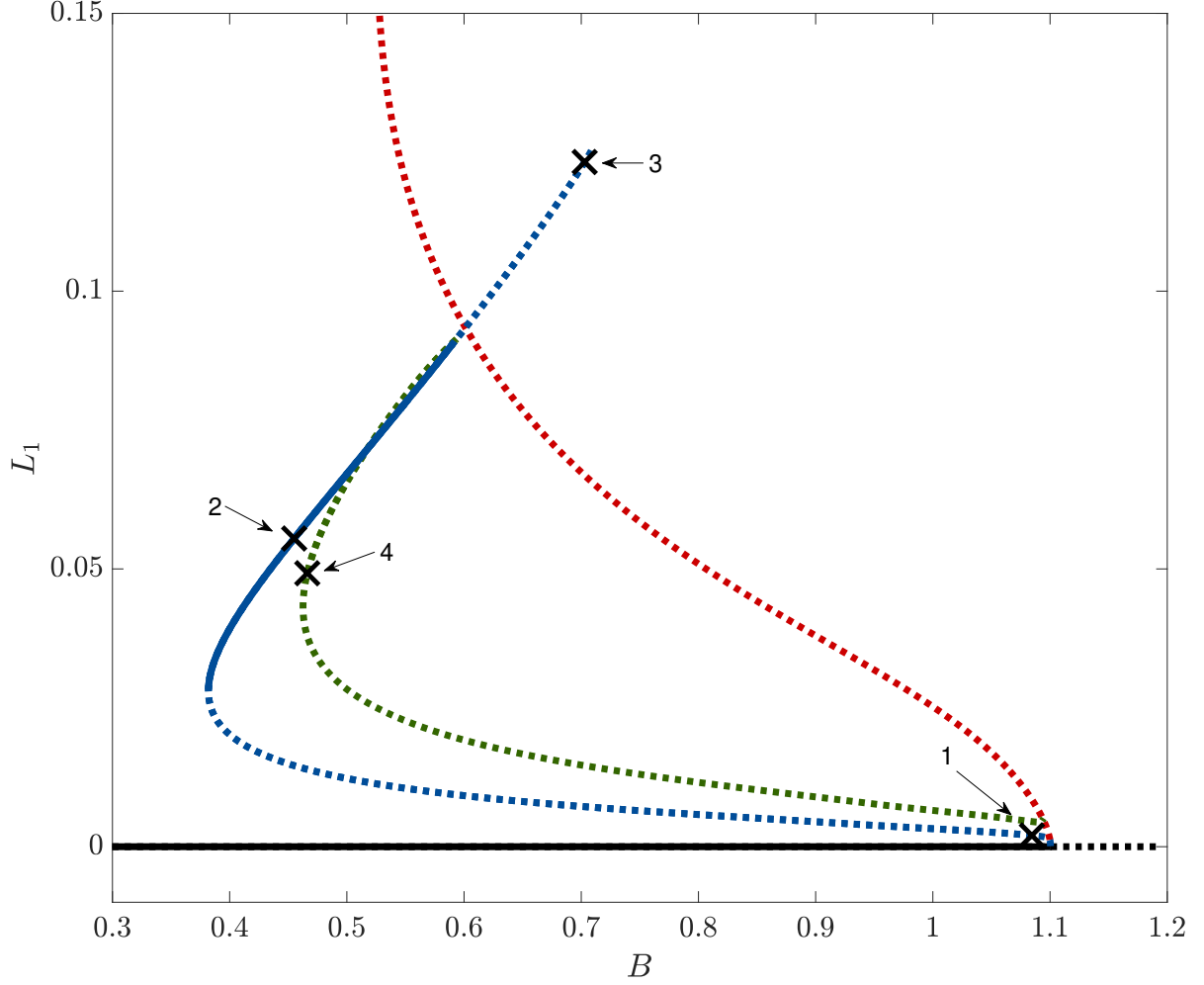
Figure 1.1: Bifurcation diagram for a single localized solution of the two-dimensional Brusselator model (1.6) obtained by numerical continuation. Depicted is the L_1-norm with respect to the mean field of the first variable X for different solutions. The continuation parameter is B. Fixed parameters are the domain size $L_x = L_y = 80$, $D = 150$, $A = 0.6$. Solid (dashed) lines mark branches of stable (unstable) solutions. The black line corresponds to the homogeneous solution branch. At the Turing point, periodic solutions (dashed red line) bifurcate from the homogeneous solution. The dashed red line represents the periodic rhombic solution which bifurcates subcritically. Shortly after, the single localized solution (dashed blue line) bifurcates from the unstable periodic rhombic solution in a supercritical pitchfork bifurcation. The localized solution becomes stable in a fold (solid blue line) and then again unstable in a subcritical pitchfork bifurcation, in which a ringlike (dashed blue line) and a self-replicated solution (dashed green line) branch off. Solution profiles for the positions marked with a cross (1-4) can be found in Fig. 1.2.
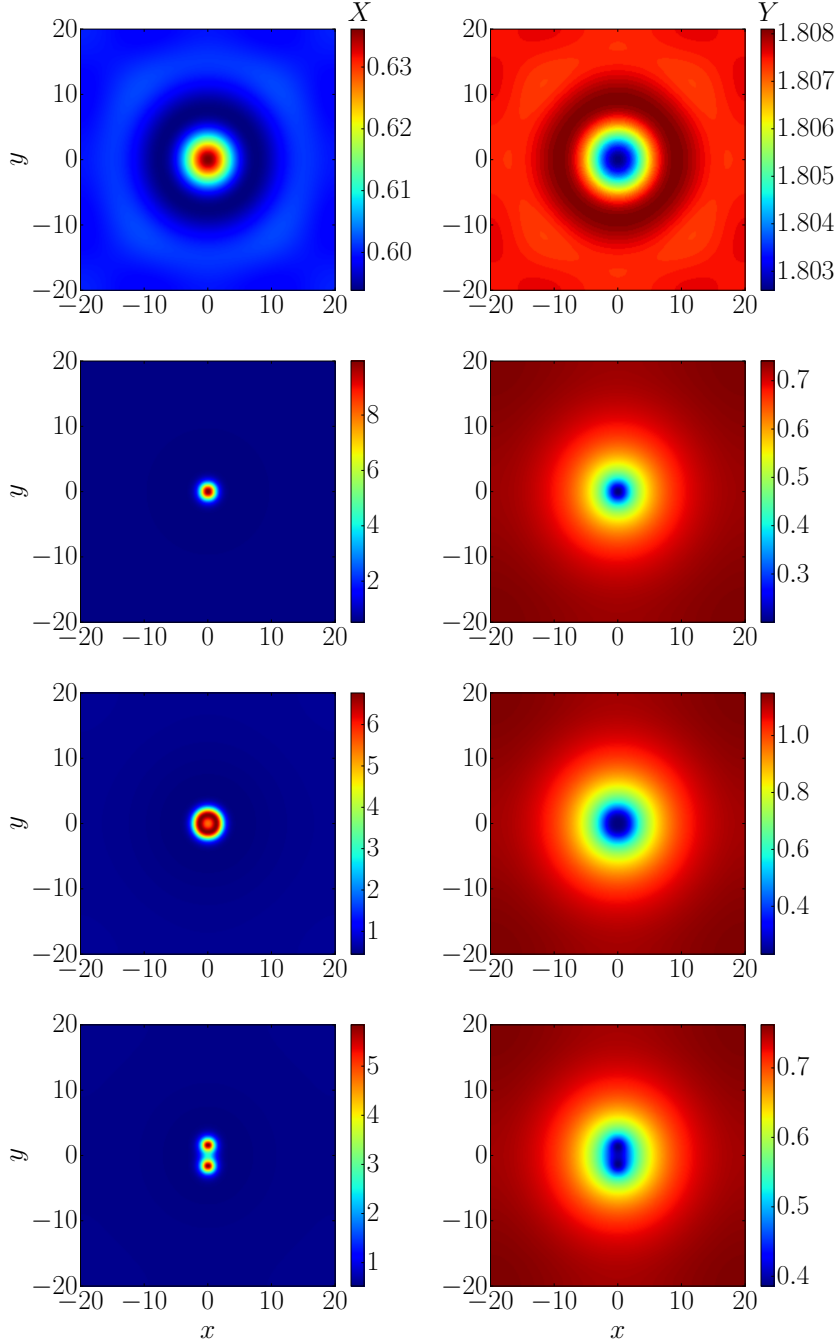
Figure 1.2: Profiles of the single localized solution in the Brusselator model (1.6) at the marked positions in Fig. 1.1. The concentration of the activator X (inhibitor Y) is depicted in the left (right) column.
First row: Unstable low-amplitude solution at position (1) in Fig. 1.1.
Second row: Stable localized solution at position (2) in Fig. 1.1.
Third row: Ringlike solution at position (3) in Fig. 1.1.
Fourth row: Self-replicated solution at position (4) in Fig. 1.1.

bifurcation from the already unstable periodic branch, i.e., the branch is unstable at first. The low amplitude unstable LS is depicted in the top row of Fig. 1.2. The solution then gains stability in a fold after increasing in amplitude (Fig. 1.2, second row). This behavior is typical for LSs, as they are not stable for small amplitudes. Stable LSs can therefore not be obtained by a weakly nonlinear analysis of the homogeneous solution. Atypically for LS, the solution again looses stability in a subcritical pitchfork bifurcation which limits the region of stability. Following the LS branch (blue) further, more bifurcations occur, leading to more unstable eigenvalues of the LS. We therefore stop to trace the LS branch at $B \approx 0.71$.

Following the branch emerging from the subcritical pitchfork bifurcation, we observe a localized solution with a broken radial symmetry (green line in Fig. 1.1, bottom solution in Fig. 1.2). This solution consists of two well separated peaks in the activator concentration X. Taking a closer look at the concentration of the inhibitor Y, the two peaks are more blurred, resulting in an oval shaped LS. In general, the activator concentration X provides much sharper peaks, whereas the inhibitor concentration shows more blurry patterns with smaller amplitude. This difference appears due to the faster diffusivity of the inhibitor represented by $D = 150$. The solution branch of this self-replicated LSs then decreases in amplitude and goes towards the periodic solution again. However, it remains to be investigated, if the branch connects again to the periodic branch.

Focusing again on stable LSs we were able to identify the bifurcation responsible for the emergence of LS and determine the region of stability of single LS. The stability of LSs is limited by a fold at $B \approx 0.4$ and a subcritical pitchfork bifurcation which we refer to as a selfreplicating bifurcation at $B \approx 0.6$. This region of stability is in good agreement with direct numerical time simulations [KTT$^+$18].

Another stable localized solution in the Brusselator model consists of two LSs separated by half the domain size, which form a bound state (Fig. 1.4, second row). The interaction between the two peaks becomes apparent, when considering the inhibitor concentration. Although the two peaks seem well separated in the slower diffusing activator, they clearly overlap and therefore interact with each other in the inhibitor concentration. The bifurcation structure of this solution is depicted in Fig. 1.3. Again, the solution starts as a small amplitude solution (light blue dashed line) and then grows in amplitude. However it gains stability in a fold followed by a subcritical pitchfork bifurcation. In this bifurcation the two-peak solution stabilizes and an asymmetric solution bifurcates creating a solution where one of the peaks decreases along the branch (orange line in Fig. 1.3, fourth row in Fig. 1.4). It seems reasonable that this branch connects to the unstable single LS branch at some point. However, we are not yet able to follow both branches long enough to find a connection. Going back to the stable solution consisting of two peaks (light blue line), the solution also looses stability in a self-replicating bifurcation, where a self-replicated solution (light green line in Fig. 1.3, fifth row in Fig. 1.4) branches off.

Both bifurcation diagrams of Fig. 1.1 and Fig. 1.3 are combined in Fig. 1.5 for better comparison. To summarize, we find that LSs emerge as unstable low amplitude solutions from the periodic branch and then gain stability in a fold. This behavior is typical and can be found in a variety of systems which exhibit LSs. How the solution branch evolves after gaining stability differs from system to system. In the above example we are able to identify a self-replicating bifurcation in the form of a subcritical pitchfork bifurcation. In the following chapters we discuss two more examples of LS, their emergence and their disappearance, namely in the Swift-Hohenberg equation in chapter 3 and in the Lugiato-Lefever equation in chapter 4.
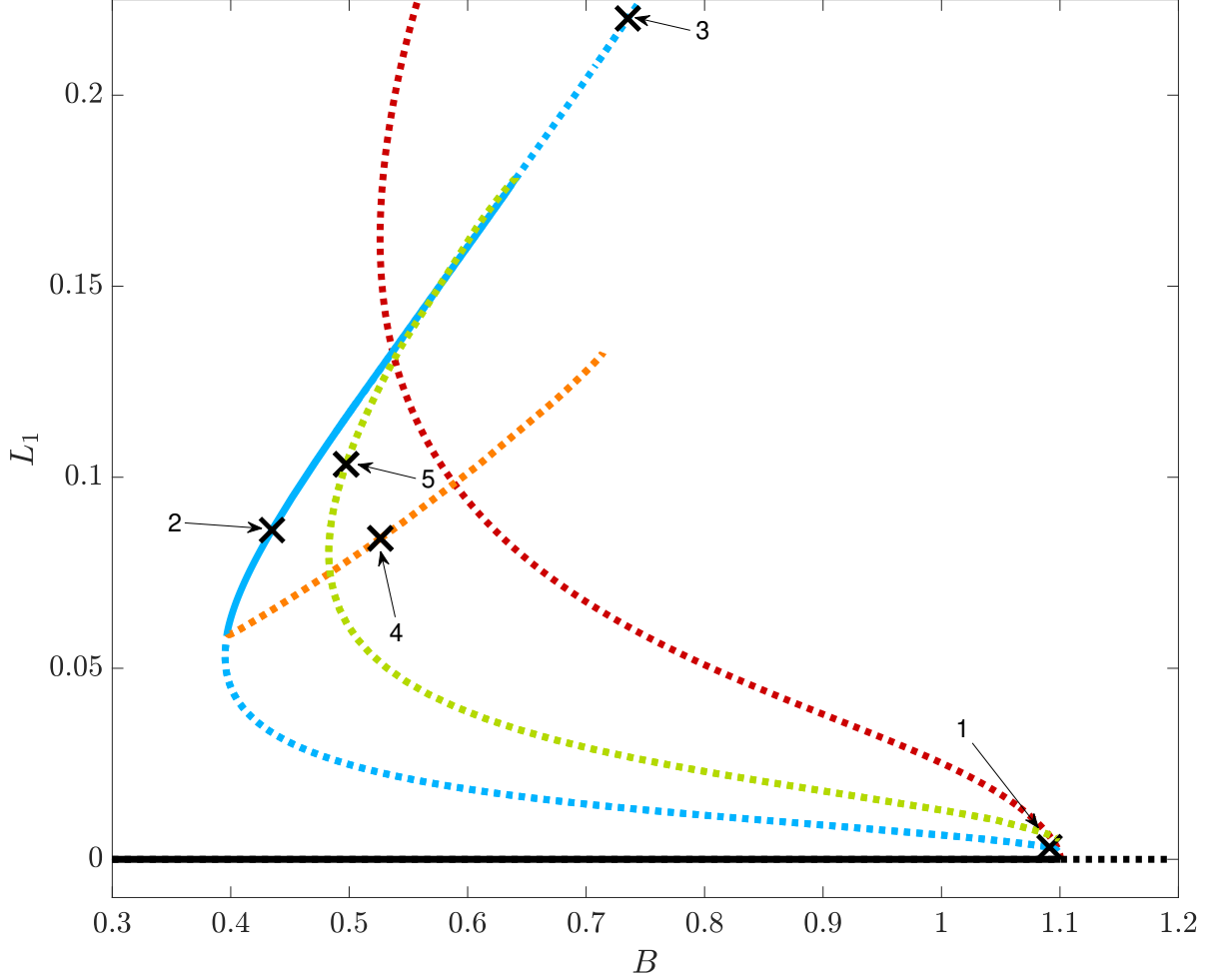
Figure 1.3: Bifurcation diagram for bound localized solutions in the two-dimensional Brus-
selator model (1.6) obtained in the same way as the results depicted in Fig. 1.1.
Shortly after the Turing point, the bound localized solution branch (dashed blue
line) bifurcates from the periodic solution (dashed red line) in a supercritical
pitchfork bifurcation. The localized solution becomes stable in a saddle-node
bifurcation (solid blue line), where also an unstable solution branches off (orange
dashed line), with one of the structures decreasing in amplitude. The stable
solution then again becomes unstable in a subcritical pitchfork bifurcation, in
which a ringlike (dashed blue line) and a self-replicated solution (dashed green
line) branch off. Solution profiles for the positions marked with a cross (1-5) can
be found in Fig. 1.4.
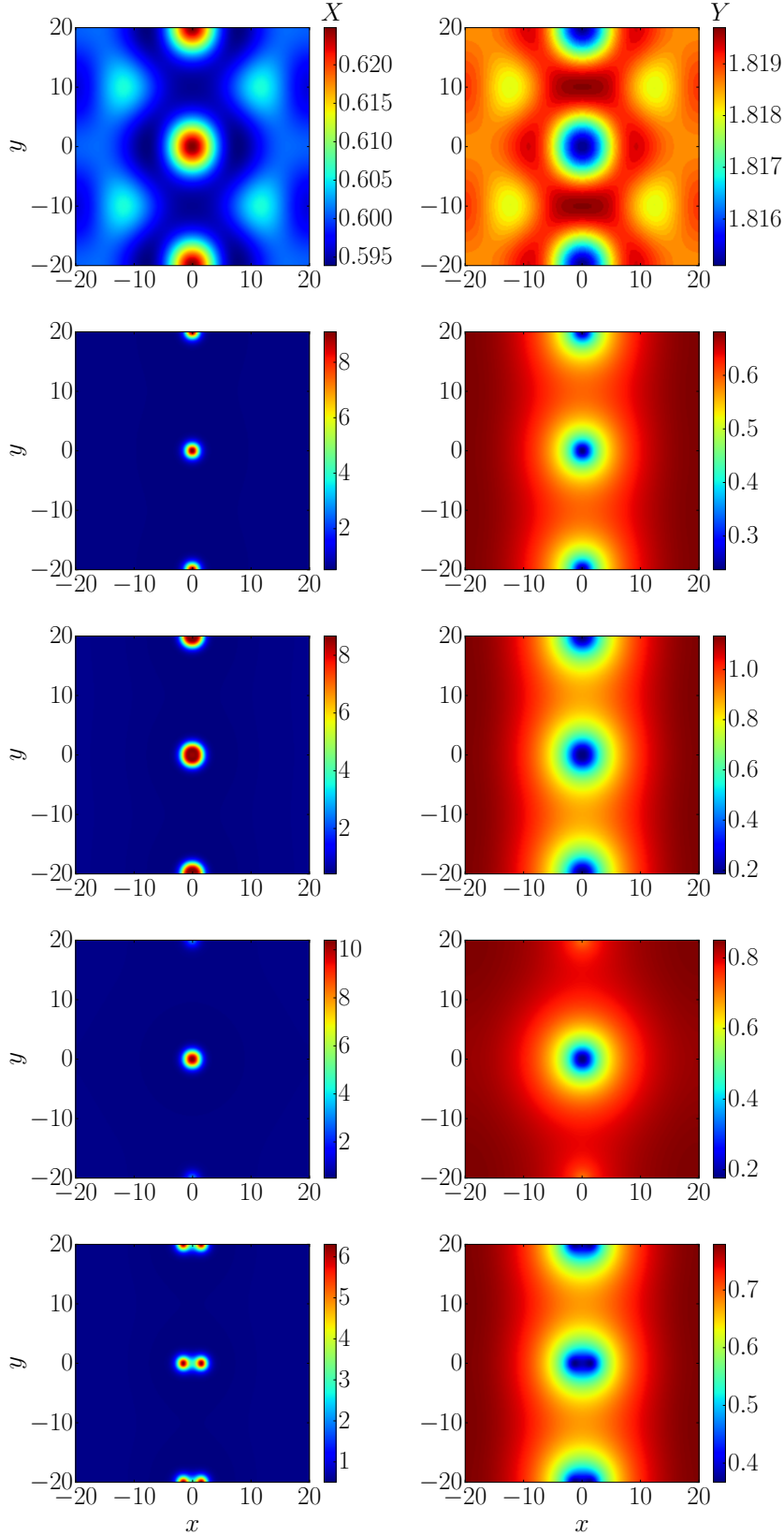
Figure 1.4: Profiles of the bound localized solution in the Brusselator model (1.6). The concentration of the activator X (inhibitor Y) is depicted in the left (right) column.
First row: Unstable low-amplitude solution at position (1) in Fig. 1.3.
Second row: Stable localized solution at position (2) in Fig. 1.3.
Third row: Ringlike solution at position (3) in Fig. 1.3.
Fourth row: Unstable localized bound solution with one of the peaks decreasing in amplitude at position (4) in Fig. 1.3.
Fifth row: Self-replicated solution at position (5) in Fig. 1.3.
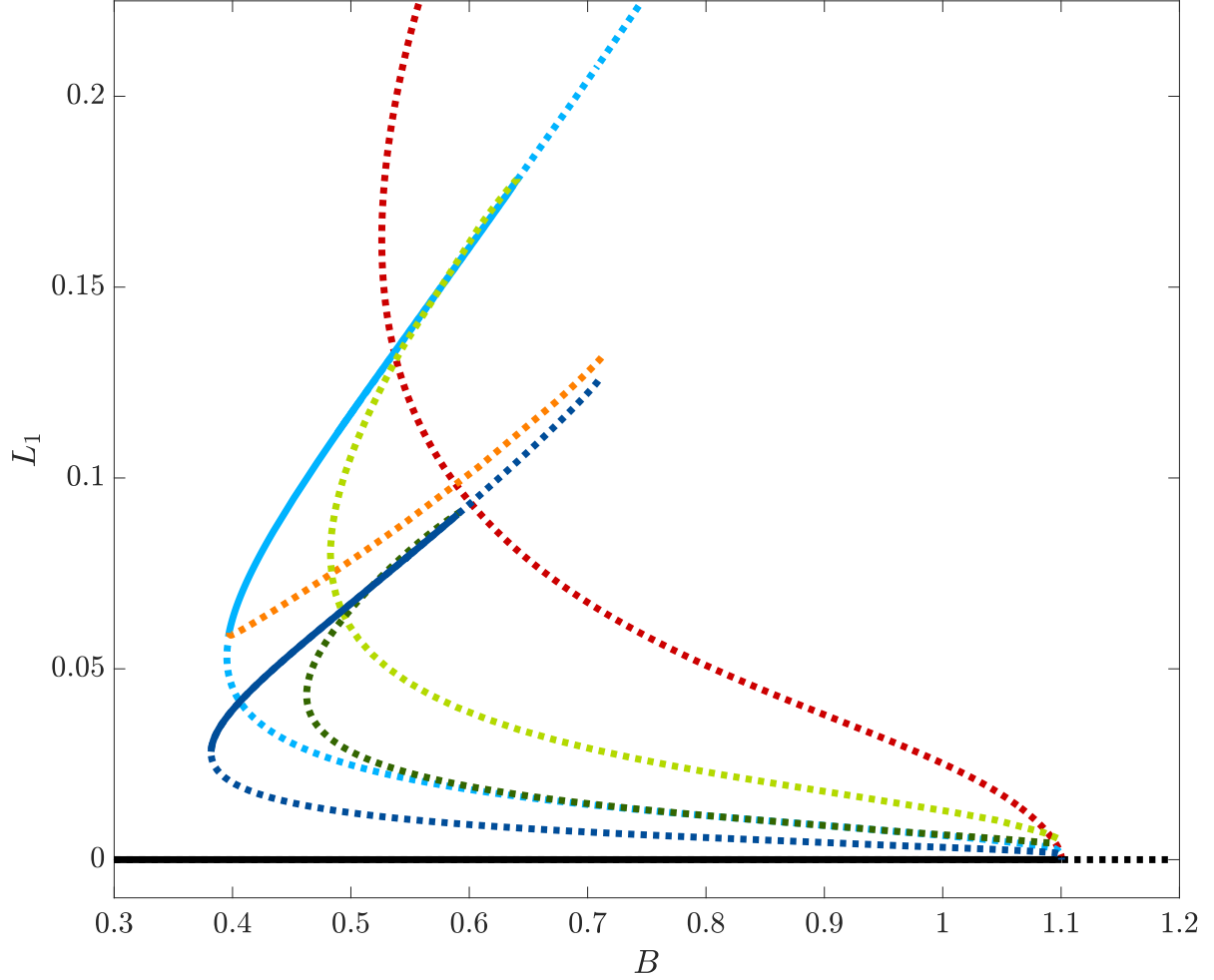
Figure 1.5: Bifurcation diagram for localized solutions in the two-dimensional Brusselator model (1.6). Here, the two localized solution branches (dark and light blue lines) depicted in Fig. 1.1 and Fig. 1.3 are compared. The shape and the stability characteristics of both branches are very similar. The existence of other stable localized solutions is probable, but most of them will depend on the domain size alike the localized solution consisting of two spots (upper blue line). Furthermore, a green dashed solution branch exhibits qualitatively the same bifurcation scenario as the single localized spot solution does.

1.2 Localized states in nonlinear optics

After discussing the formation of LSs in a general framework and providing the paradigmatic Brusselator reaction-diffusion system as an example of a system forming LSs, we now focus on the field of nonlinear optics.

Nonlinear optical setups are especially suited to provide the conditions necessary for pattern formation in dissipative systems in general and for the formation of LSs in particular as we shall discuss briefly in the following. Nonlinear effects often have to be taken into account in optics and can be experimentally implemented in a number of ways, e.g., by using a saturable absorber [BTV92, STP+17], by operating a laser in the vicinity of the lasing threshold [TGKW00, BTB+02] or by simply filling an optically driven cavity or fiber with a material exhibiting a strong optical Kerr effect [OTL11, OTC+14].

The spatial interaction necessary for the creation of LS is typically realized by diffraction of light and/or carrier diffusion. However, a special focus in the field of pattern formation in nonlinear optics lies on the formation of patterns in the temporal domain, in which this "spatial" interaction is obtained by, e.g., group velocity dispersion [LPB15]. These models typically possess a fast time and a slow time opposed to space and time, respectively [HTW92, LPB15, LPGK18]. Due to the mathematical analogy between transverse and temporal pattern formation we summarize the derivatives with respect to spatial or fast time coordinates as "spatial effects", keeping in mind that when treating, e.g., the Lugiato-Lefever model of nonlinear optics [LL87], two different interpretations of these effects are valid. We shall show during the derivation in chapter 2, that the Lugiato-Lefever equation (LLE) models both spatial and temporal pattern formation.

The last necessary condition for the formation of LSs, namely the dissipative nature of the systems under consideration is most evidently realized in any real optical setup, where losses due to e.g., imperfect reflectivity of cavity mirrors [AFO09] or most obviously due to the necessity of experimental detection have to be accounted for and compensated by a source of energy if one wants to observe pattern formation on the comparatively long time-scales of e.g., minutes. The external source of energy typically is provided by, e.g., an injected field from a suitable source (optical pump) or by electrically pumping a system [LPB15].

The motivation to focus on pattern formation in the context of nonlinear optics in this thesis is twofold: From the point of view of an applied physicist, pattern forming optical systems provide a number of promising applications which we only briefly discuss in this thesis. Examples of already existing and possible future applications of LSs in nonlinear optics are the generation of frequency combs using the frequency spectrum of dissipative temporal Kerr solitons [LPGK18] and the implementation of spatial LSs in optical cavities as, e.g., optical bits in information processing [BLP+97, BTB+02].

From the point of view of a theoretician interested in the field of pattern formation, nonlinear optics provide several advantages which render the experimental implementation of theoretical models easier feasible than in other fields of application. Compared to other relevant research areas such as pattern formation in plant ecology [TSP+14], experimental realizations in nonlinear optics benefit from the much smaller intrinsic time- and length-scales allowing experiments under controlled laboratory conditions. In, e.g., pattern formation processes in the transverse plane of a VCSEL (vertical cavity surface emitting laser) which we discuss in more detail in the following, the intrinsic time scale is given by the carrier lifetime in the cavity which is in the order of nanoseconds whereas the diameter of such devices ranges from 40-120 μm [Ave17]. Furthermore, the controlled change of parameters is comparatively easy to obtain in nonlinear

optical experiments, since main parameters such as input currents, the intensity of optical pumping or the detuning between the frequency of an injected field and the resonant frequency of a cavity can be altered [Ave17].

More specifically to this thesis the field of nonlinear optics suggests itself since our previous results [Tab14, TSTG17] focused on the effect of time-delayed feedback control on pattern forming systems, which we also discuss in chapters 3 and 4. Although the implementation of time-delayed feedback loops is in general complicated, it is feasible in nonlinear optics by considering an external cavity [PCT+07, vTL95]. In such a scenario, a small amount of the intracavity field escapes the cavity in which pattern formation is observed. The light is reflected in the external cavity and then reintroduced into the original cavity. Again, due to the fast intrinsic time-scales of the pattern forming system, the roundtrip time in the external cavity constitutes an unneglectable delay-time even for typical lengths of external cavities ranging from 30-100 cm. Nonlinear optics therefore provide a good opportunity to experimentally observe delay-induced dynamics, which have been studied theoretically for spatially extended systems [TSS13, TVPT09, GF13, TSTG17].

In the following we briefly summarize the historical development of the study of LSs in nonlinear optics before exemplarily showing some experimental observations of LSs obtained in a setup in the K. Panajotov lab at the Vrije Universiteit Brussel. This section however does not comprise a complete review of pattern formation in nonlinear optics. We refer the reader to, e.g., the textbooks of Paul Mandel [Man05] or Luigi Lugiato [LPB15] for a comprehensive introduction to the field of nonlinear optics and to reviews regarding nonlinear optics in general [ABR99], pattern formation in the transverse plane of a cavity [MT04], the Lugiato-Lefever model [LPGK18] and dissipative cavity solitons [AFO09] for more detailed discussions of recent research on the topic.

The nonlinear Schrödinger equation (NSE) provides a good starting point for the historical overview of LSs in nonlinear optics since it is one of the oldest and most extensively studied models in this field. The NSE describes the time evolution of the envelope E of an electrical field in a Kerr medium. The time evolution is governed by diffraction and a nonlinearity due to the Kerr effect and reads [AFO09]:

$$i\frac{\partial}{\partial t}E + \frac{\partial^2}{\partial x^2}E + |E|^2 E = 0, \tag{1.8}$$

where the sign of the nonlinear term indicates that we consider a self-focusing nonlinearity. We assume an appropriate choice of rescaled dimensionless variables x and t.

The NSE originally describes the propagation of light in an infinitely long Kerr medium in the longitudinal direction z, where the derivative with respect to time in Eq. (1.8) is replaced by the derivative with respect to the longitudinal direction z. For Eq. (1.8) we already assumed that the infinitely large medium is replaced by a cavity confining the light to the Kerr medium with reflectors perpendicular to the z-direction. In this case, one can replace the derivative with respect to z by a derivative with respect to t [AFO09].

Equation (1.8) is integrable and exhibits classical solitons as solutions, which were first analytically described in 1972 by Shabat et al. [SZ72]. Bright solitons are stable in one spatial dimension in the self-focusing case and can be explicitly written as:

$$E(x,t) = E_0 \text{sech}\left(\frac{x}{\sqrt{2}}\right) \exp\left(\frac{iE_0^2 t}{2}\right), \tag{1.9}$$

where E_0 denotes the amplitude of the soliton which is determined by the initial condition. Due to the conservation of energy in Eq. (1.8), solitons of different height exist depending on the initial condition.

An alternative formulation of the NSE possess dark soliton solutions (i.e., gaps in an otherwise homogeneous electrical field amplitude) in the self-defocusing regime. Furthermore, temporal solitons can be described in the case where we consider the evolution of a field along a fiber, where the roles of x and t are reversed, i.e., group velocity dispersion takes over the role of spatial interaction previously ascribed to diffraction.

Nonetheless, the NSE as defined in Eq. (1.8) does not consider dissipative effects, which we again define in the broader sense of both losses and energy gain by, e.g., optical pumping. Energy losses, however, are inevitable and therefore have to be considered. The assumption of perfect reflectivity of the reflectors confining the electrical field in the cavity on the one hand is not realistic [AFO09] and on the other hand is not even desirable since in a typical cavity setup one needs to implement an optical output from the cavity for the sake of experimental detection or applications.

To obtain a more realistic version of the NSE in dissipative systems, we can formulate a dissipative extension of the NSE incorporating the basic effects of losses, an optical injection compensating these losses and cavity detuning, which accounts for the difference between the frequency of the injected beam and the resonant frequency of the cavity. Ackemann et al. [AFO09] therefore propose:

$$\mathrm{i}\frac{\partial}{\partial t}E + \frac{\partial^2}{\partial x^2}E + |E|^2 E = \mathrm{i}\epsilon\left(-E - \mathrm{i}\theta E + E_i\right), \tag{1.10}$$

where the terms on the right-hand side represent a correction to the NSE in the form of losses, cavity detuning characterized by the detuning parameter θ and a driving injected field which is considered to be a plane wave of amplitude E_i.

The correction terms on the right-hand side of Eq. (1.10) are small as long as ϵ is small. Setting $\epsilon = 1$, e.g., by rescaling the time to the decay time of the cavity and rescaling x accordingly, one obtains the Lugiato-Lefever equation (LLE) (4.1). This heuristic motivation of the LLE emphasizes the close connection between LLE and NSE which is why the LLE is sometimes referred to as a driven, damped and detuned nonlinear Schrödinger equation [Gom03]. Nevertheless, the original paper proposing the LLE by Luigi Lugiato and René Lefever [LL87] did not rely on the heuristic extension of the NSE but stated that the LLE can be derived from the Maxwell-Bloch equations. The derivation is carried out in [LO88] and we present it in chapter 2.

The aim of Lugiato and Lefever when proposing the LLE in 1987 [LL87], was to formulate a simple paradigmatic model that allows to introduce the new concepts of the formation of dissipative structures formulated by Prigogine to the field of nonlinear optics [LPGK18]. By choosing a simple cubic Kerr nonlinearity combined only with defraction, dissipation and detuning the authors hoped to propose a model of similar paradigmatic simplicity as the Brusselator model [PL68]. The short original paper on the LLE only describes the proposed model and comprises a linear stability analysis as well as a weakly nonlinear analysis showing that the model undergoes a Turing instability, which occurs either in a sub- or supercritical pitchfork bifurcation depending on the choice of parameters. This instability gives rise to stationary periodic solutions in the transverse plane of a cavity. Given the limited possibilities of numerical simulations at that time, the proof of pattern forming instabilities constitutes a breakthrough in nonlinear optics.

Since then, the LLE has been studied intensively [LPGK18] which provided new insights such as the formation of LSs [PRGM+14a]. The work of Haeltermann et al. brought new attention to the LLE, since they formulated a mathematically identical formulation of the LLE which describes the emergence of temporal patterns in a ring cavity [HTW92]. We present the derivation in chapter 2. Localized solutions of this temporal version of the LLE are referred to as temporal Kerr solitons. The investigation of these structures gained new significance only recently, when Del'Haye et al. demonstrated that Kerr microresonators can be utilized for the generation of optical frequency combs [DSA+07]. Optical frequency combs consist of a large number of equidistant spectral lines in the frequency domain and can be used to precisely measure frequencies [KHD11].

The connection to the LLE was established shortly after the work of Del'Haye et al., when several groups demonstrated that the LLE is the appropriate model to describe the comb generation in microresonators [MSL+11, CRSE13, CM13, GBCC14]. More precisely it was shown that the frequency spectrum of temporal LSs constitutes an optical frequency comb [LPGK18].

Although the LLE represents one of the first attempts to model pattern formation in nonlinear optics and is still used due to its applicability to optical frequency comb generation, it is by far not the only system exhibiting LSs. The emergence of LSs has been reported in a variety of different systems both in theory and experiment.

Broad area VCSELs are especially suited for the experimental realization of spatial LSs in the transverse plane of a cavity since they provide a large aspect ratio which allows to neglect the evolution of the field in the longitudinal direction. Furthermore, the large transverse plane of broad area VCSELs allows to study the dynamics of LSs without interacting with the boundaries of the system.

The formation of LSs in VCSELs was first theoretically described using mean field models for the evolution of the slowly varying electrical field amplitude [BLP+97, MPL97, STB+98]. The first experimental observation of LSs in a broad area resonator was achieved in 2000 by Tarenko et al. [TGKW00]. In this work, the resonator is used in a passive configuration, i.e., only driven by an injected beam in an area of about 60 μm. The detection of various pattern forming processes including LSs was performed within microseconds to avoid thermal effects.

The first detection of LSs in a VCSEL on longer macroscopic time-scales of several minutes was reported by Barland et al. [BTB+02]. In their pioneering work they used an elaborate experimental setup consisting of a VCSEL electrically pumped below the lasing threshold and an edge emitting laser as an optical pump. The output from this laser is split into two beams before injection: A holding beam which is broadened to (approximately) homogeneously drive the entire active area of the VCSEL (150 μm in diameter) and a smaller focused writing beam which only drives a small area of the VCSEL ($\sim$ 10-15 μm in diameter). The phase of the writing beam can be changed with respect to the phase of the holding beam and the writing beam can be blocked independently from the holding beam. For a more detailed description of the experimental setup and especially the detection branches we refer the reader to the original paper [BTB+02] and the following work [HBF+04].

Employing the writing beam in phase with the holding beam in a region where the VCSEL was close to but below a modulational instability, they create a peak of high intensity surrounded by a low intensity background field. After blocking the writing beam, this structure remains stable thus suggesting that it is indeed a stable LS. Utilizing the writing beam with a phase difference of π with respect to the holding beam, it is possible to erase the previously created LS. The authors mention that, depending on the initial position of the writing beam, a short

movement of the LS towards a more favorable position can be observed after releasing the LS from the writing beam. The authors ascribe this effect to the influence of small inhomogeneities in the optical pumping stemming from the holding beam and to the detuning gradient in the VCSEL. However they do not include these inhomogeneities in the theoretical mean field model they compare their experimental results with. The inclusion of these inhomogeneities into mean field models of nonlinear optics is the main focus of this thesis.

Authors from the same group experimentally proof the existence of LSs in a similar setup in which the VCSEL is electrically pumped above threshold [HPC$^+$06]. They also demonstrate that a LS appears spontaneously when increasing the injection power and then remains stable when decreasing the injection power again, i.e., it exhibits hysteresis. Further recent developments include the detection of LSs without a holding beam in a VCSEL with a saturable absorber [EGB$^+$10], where the authors again describe the hysteresis behavior of LSs with respect to varying input power, concluding that LS can be created spontaneously without using a writing beam. Other setups in which LSs have been created include a VCSEL subjected to optical feedback instead of a holding beam proposed in [TAFJ08] or a configuration in which two VCSELs face each other [BHE$^+$08]. First experimental evidences of homoclinic snaking of LSs were reported in [FCS07, BHE$^+$08]. Homoclinic snaking is a phenomenon mostly discussed in theoretical physics: It describes a sequence of consecutive bifurcations resulting in the addition of peaks to a LS, i.e., the solution goes from 1 peak to 3,5,7... $2n + 1$ peaks until the domain is filled or from 2 to 4,6,8...$2n$ peaks. We will discuss this phenomenon in detail in the context of the LLE in chapter 4.

1.2.1 Experimental evidence of localized states

In this section we present experimental observations of LSs in a VCSEL cavity obtained by the author during a research stay in the K. Panajotov lab at the Vrije Universiteit Brussel. The experimental work was carried out under instruction of E. Averlant who also assembled the experimental setup. A thorough description of the experimental setup can be found in [Ave17], results obtained in the experimental setup were published in [ATT$^+$14, VPG$^+$14, TAV$^+$15, Ave17]. The setup is schematically depicted in Fig. 1.6. We observe the formation of patterns in the transverse plane of an InGaAs quantum well VCSEL with a diameter of 80 μm. The VCSEL is bottom-emitting and electrically pumped close to the lasing threshold. The choice of a bottom-emitting device is due to the more homogeneous distribution of the pumping current in the active region.

The injection branch of the setup (depicted in box (i) in Fig. 1.6) consists of a diode laser with an external cavity in the Littrow configuration which allows wave-length tuning between 910-985nm. An optical isolator (OI in 1.6) prevents undesired feedback to the laser. A lambda half plate ($\lambda/2$ in 1.6) and a variable optical density filter (VODF) are used to alter the polarization direction and the intensity of the injected beam. Four mirrors are used to control the direction of the beam and ensure that it is injected into the VCSEL. Directly before the injection, a small portion of the injected light is separated by a beam splitter and is sent into a photodiode (PD$_1$) to measure the input power.

The detection branch of the setup (depicted in box (iii) in Fig. 1.6) consists of a photodiode (PD$_2$) to measure the output intensity, an optical spectrum analyzer (OSA) to measure the frequency spectrum of the output signal and a CCD camera to obtain spatially resolved images of the near-field output of the VCSEL. The output beam is split up by beam splitters before each portion of the beam enters one of the detection devices.
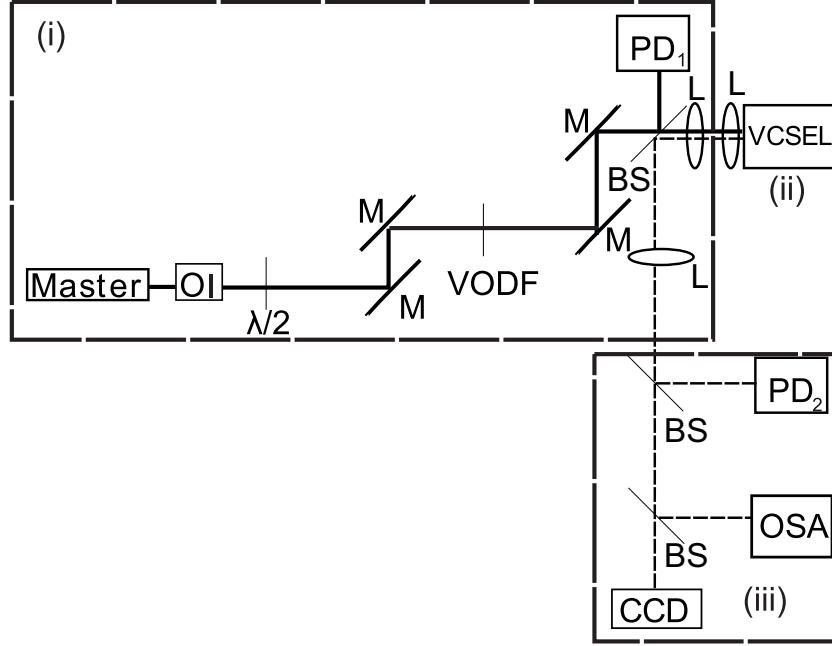
Figure 1.6: Schematic setup for the generation of LSs in the transverse plane of a VCSEL used in the Panajotov lab. The setup can be divided into the injection branch (i), the actual VCSEL (ii) and the detection branch (iii). The injection branch consists of a tunable master laser, an optical isolator (OI) a half wave plate ($\lambda/2$), four mirrors (M) a variable optical density filter (VODF), a beamsplitter (BS) and a photodiode (PD_1). The solid line represents the injected beam going from the master laser to the VCSEL. The detection branch consists of beam splitters (BS), a photodiode to measure the optical output power (PD_2), an optical spectrum analyzer (OSA) and a CCD camera. The dashed line represents the output beam going from the VCSEL to the devices of the detection beam. Several lenses are used to collimate the light where necessary. The figure is reprinted with permission from [Ave17].

For the experiment, the master laser is operated at a wave-length which should be slightly larger than the wave-length of the free running VCSEL. The VCSEL is electrically pumped close to the lasing threshold. We then increase the intensity of the injected beam until a localized peak of high intensity occurs (see Fig. 1.7, bottom left). When decreasing the injected intensity again, the LS remains stable for values of the injection, where it did not appear while increasing the injection. Hence, a hysteresis effect can be observed which is also depicted in the top panel of Fig. 1.7. There, the output power depending on the input power is depicted, showing the bistability between a localized structure and an approximately homogeneous near-field (see Fig. 1.7, bottom right).

During different runs of this experiment, the LSs occur at various positions within the cavity. However, when going through the hysteresis loop in Fig. 1.7, the structure always appears at the same position suggesting that this position is particularly favorable for the creation of LS. When taking a closer look at the background intensity (see Fig. 1.7, bottom right), an inhomogeneity of the intracavity field at the position where the LS occurs can be observed. In Fig. 1.7, the sensitivity of the CCD camera was very high in order to detect small inhomogeneities in the background field. Therefore the peak of the LS can not be resolved but is burned out. The LS peak is more than an order of magnitude larger than the inhomogeneities in the background although the difference in height does not appear that large in Fig. 1.7.

A similar hysteresis curve was described in [ATT+14, Ave17], when altering the current which pumps the VCSEL electrically. In recent experiments the destabilization of LSs by time-delayed optical feedback provided by an external cavity is studied (the results are not published yet). The LS is destabilized and starts to move in a wiggling motion on the spot. Although the destabilization of LS has been studied widely [TSS13, TVPT09, GF13, TSTG17], these experimental observations differ from theoretical predictions. We discuss this discrepancy between experimental and theoretical results in chapter 3 and show how the inclusion of small inhomogeneities in theoretical models resolves this problem.

Overall, both the results presented in this section as well as the previous work of other groups such as [BTB+02] suggest that small inhomogeneities in an experimental setup have a drastic influence on the creation, existence and stability of LSs in optical cavities. We therefore want to include small inhomogeneities in mean-field models, which typically posses a continuous symmetry of translation. Since this is early work on the topic we confine our analysis to two very commonly used models in nonlinear optics, namely the Swift-Hohenberg equation and the Lugiato-Lefever equation. In the next chapter we derive both equations before discussing each system separately in the following chapters.
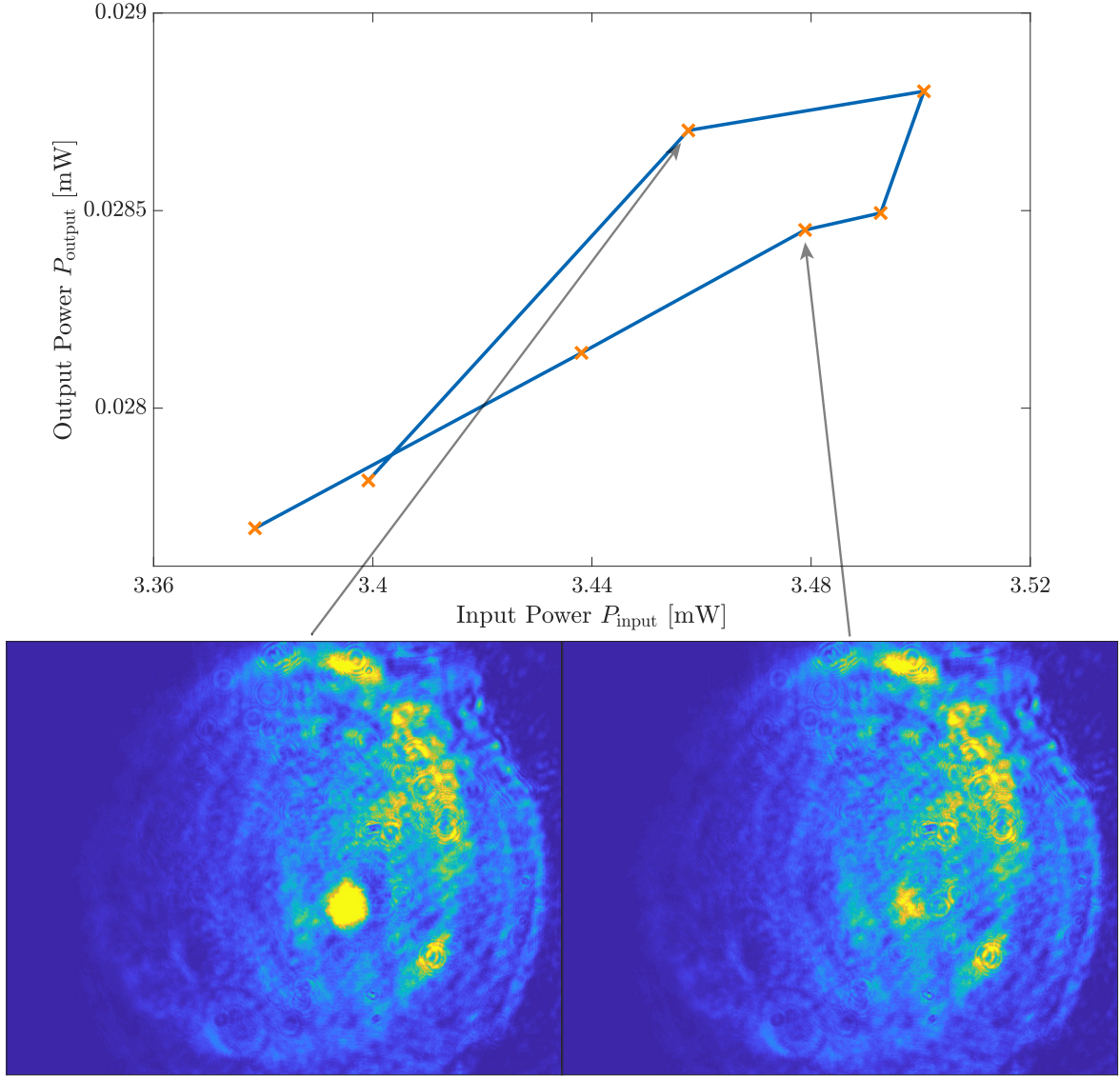
Figure 1.7: Observation of a single LS in a VCSEL using the setup depicted in Fig. 1.6. Top panel: Output power P_{output} for different values of the input power P_{input} marked by crosses. The blue line indicates the sequence in which the measurements were acquired which accentuates the hysteresis effect. Starting from the point at the far left (input power $P_{\text{input}} \approx 3.38$ mW) we slowly increase the input power. No formation of a LS is observed until we reach the far values of the input power $P_{\text{input}} \gtrsim 3.49$ mW where the system jumps to a state consisting of a single LS on the higher branch. Reducing the input power again, the LS remains stable until it vanishes between an input power of $P_{\text{input}} = 3.44$ and $P_{\text{input}} = 3.4$ mW. Bottom panels: Near-field profile at the marked positions showing a stable LS (left) and an approximately homogeneous profile (right). The sensitivity of the CCD camera was chosen to detect small inhomogeneities in the background. Therefore, the large amplitude of the LS can not be resolved, the structure appears burned out and the difference in amplitude between the LS and the inhomogeneities in the background seems smaller than it actually is. The input power was detected at the photodiode PD_1 and the output power at the photodiode PD_2.

2 Theoretical Background

In this chapter we derive the optical pattern forming equations we are going to analyze in the next chapters, namely the Lugiato-Lefever equation [LL87] and a modified Swift-Hohenberg equation [SH77]. We are going to start the derivation with the Maxwell-Bloch equations for an optically driven cavity exhibiting pattern formation in the transverse plane. Adiabatic elimination of the population inversion and the polarization combined with the assumption of large atomic detuning yields the Lugiato-Lefever equation. This derivation can also be found in e.g., [LPB15].

We then derive the optical Swift-Hohenberg equation, which describes the same setup as above, only at the onset of optical bistability. We therefore apply a series expansion of all the necessary quantities in the vicinity of the critical point associated with the onset of optical bistability. This derivation is sketched in [Man05].

We close with a derivation of the temporal Lugiato-Lefever equation following [HTW92]. The temporal Lugiato-Lefever equation in this context describes a fiber ring cavity filled with a Kerr medium.

2.1 The Maxwell-Bloch equations

As a starting point for our investigations we use the Maxwell-Bloch equations that describe the macroscopic time evolution of the electrical field envelope E, the polarization P and the population inversion D in an optically pumped cavity filled with a two-level medium. The Maxwell-Bloch equations read [LPB15]:

$$\frac{\partial}{\partial t}E(x,y,t) = -\kappa\left[(1+\mathrm{i}\theta)E(x,y,t) - E_i(x,y) + 2CP(x,y,t) - \mathrm{i}a\nabla_\perp^2 E(x,y,t)\right], \quad (2.1)$$

$$\frac{\partial}{\partial t}P(x,y,t) = \gamma_\perp\left[E(x,y,t)D(x,y,t) - (1+\mathrm{i}\Theta)P(x,y,t)\right], \quad (2.2)$$

$$\frac{\partial}{\partial t}D(x,y,t) = -\gamma_\parallel\left[\frac{\overline{E}(x,y,t)P(x,y,t)}{2} + \frac{E(x,y,t)\overline{P}(x,y,t)}{2} + D(x,y,t) - 1\right], \quad (2.3)$$

Equations (2.1)-(2.3) describe the time-evolution of the state variables in the transverse plane of a cavity, i.e., in two spatial dimensions (x,y). The dependence on the longitudinal coordinate z is canceled out by applying a paraxial, a low transmission and a single-longitudinal-mode approximation. For a detailed derivation we refer the reader to [LPB15].

The cavity is driven by an external injected field of amplitude $E_i(x,y)$. The injected field typically is assumed to be a plane wave (i.e. $E_i = \mathrm{const.}$), however in the scope of this thesis we will explicitly discuss the effects of an inhomogeneous injection $E_i(x,y)$. The phase of the injected field is fixed to zero, i.e., we assume E_i to be real-valued. The atomic detuning, i.e. the difference between the atomic two-level transition frequency ω_a and the frequency of the injected field ω_0 is accounted for as $\Theta = \frac{\omega_a - \omega_0}{\gamma_\perp}$, the cavity detuning denoting the difference between the resonant frequency of the cavity ω_c and the frequency of the injected field ω_0 is

introduced accordingly as $\theta = \frac{\omega_c - \omega_0}{\kappa}$. The parameter C is called the bistability parameter and accounts for transition rates between the two states. Spatial effects are included by adding a diffraction term, where $\nabla_\perp$ denotes the derivative in the transverse directions (x, y) and a is a measure for the diffractive length. The parameters κ, $\gamma_\perp$ and $\gamma_\parallel$ define the time scales on which the time evolution of the different variables takes place and $\overline{E}$, $\overline{P}$ refer to the complex conjugates of the electrical field and the polarization respectively.

2.1.1 Adiabatic Elimination

In the following we are going to simplify Eqs. (2.1)-(2.3) further by adiabaticly eliminating the polarization P and the population inversion D resulting in one closed equation that describes the time evolution of the electrical field envelope E.

The concept of adiabatic elimination was first brought up by Hermann Haken [Hak83] and applies to dynamical systems with two or more variables, where the typical time-scale of at least one variable is much shorter than the time-scale of the other variables. In this case it is justified to neglect the independent temporal evolution of said variable and to assume that this variable adjusts instantaneously (on the slow time-scale of the other variables) to a change of the systems state. The state of the fast variable is therefore at all times given by the steady state solution of the underlying dynamical system. The (fast) dynamics towards this state are neglected.

In the present case of Eqs. (2.1)-(2.3) one can adiabaticly eliminate P and D if both $\gamma_\perp, \gamma_\parallel \gg \kappa$. Laser cavities which justify this approximation are referred to as "class A" lasers. In this case both the population inversion D and the polarization P undergo a much faster dynamics than the electrical field envelope E and it is therefore reasonable to assume:

$$\frac{\partial}{\partial t} P = \frac{\partial}{\partial t} D \approx 0. \tag{2.4}$$

This approximation allows us to explicitly calculate D and P in dependance of E. Inserting Eq. (2.4) into Eq. (2.2) yields:

$$P(x, y, t) = \frac{E(x, y, t) D(x, y, t)}{1 + \mathrm{i}\Theta}. \tag{2.5}$$

By introducing Eqs. (2.4) and (2.5) into Eq. (2.3), one obtains:

$$D(x, y, t) = \frac{1 + \Theta^2}{1 + \Theta^2 + |E(x, y, t)|^2}. \tag{2.6}$$

Inserting the expression (2.6) into Eq. (2.5) yields:

$$P(x, y, t) = E(x, y, t) \frac{1 - \mathrm{i}\Theta}{1 + \Theta^2 + |E(x, y, t)|^2}. \tag{2.7}$$

Replacing the expressions (2.6) for D and (2.7) for P in Eq. (2.1), one obtains a single closed equation determining the time evolution of $E(x, y, t)$:

$$\frac{\partial}{\partial t} E = -\kappa \left[(1 + \mathrm{i}\theta) E - E_i + 2CE \frac{1 - \mathrm{i}\Theta}{1 + \Theta^2 + |E|^2} - \mathrm{i}a\nabla_\perp^2 E \right], \tag{2.8}$$

where the dependence on (x, y, t) has been dropped for the sake of clarity and simplicity.

Eq. (2.8) exhibits optical bistability, which can be due to absorptive or dispersive effects [LO88]. The purely absorptive case $\Theta = 0$ in which the frequency of the injected field coincides with the frequency of the two-level transition will only be mentioned briefly. In this case Eq. (2.8) reduces to:

$$\frac{\partial}{\partial t}E = -\kappa \left[(1 + \mathrm{i}\theta)E - E_i + \frac{2CE}{1 + |E|^2} - \mathrm{i}a\nabla_\perp^2 E \right]. \tag{2.9}$$

2.2 Limit of large atomic detuning

In contrast to Eq. (2.9) we will now investigate the limit of large atomic detuning $|\Theta| \gg 1$, also refered to as the limit of pure dispersion. In this case it is reasonable to expand and approximate the nonlinear expression of Eq. (2.8) as:

$$\frac{1}{1 + \Theta^2 + |E|^2} \approx \frac{1}{\Theta^2} \left(1 - \frac{1 + |E|^2}{\Theta^2} \right). \tag{2.10}$$

Inserting Eq. (2.10) into Eq. (2.8) and neglecting terms of $\mathcal{O}(\frac{1}{\Theta^4})$ yields:

$$\frac{\partial}{\partial t}E = -\kappa \left[(1 + 2C\epsilon)\, E + \mathrm{i} \left(\theta - 2C\Theta\epsilon + 2C\Theta\epsilon^2 \right) E - E_i + \mathrm{i}2\epsilon^2 C\Theta|E|^2 E - \mathrm{i}a\nabla_\perp^2 E \right], \tag{2.11}$$

where we introduced the parameter of smallness:

$$\epsilon = \frac{1}{\Theta^2}. \tag{2.12}$$

This equation already has the mathematical form of the Lugiato-Lefever equation as it was proposed in 1987 by Luigi Lugiato and René Lefever as a simple pattern forming model in nonlinear optics [LL87].

For the sake of simplicity it is convenient to rescale the variable E and introduce new effective parameters denoted by a bar as follows:

$$E = \sqrt{\frac{1 + 2C\epsilon}{-2C\Theta\epsilon^2}}\ \overline{E}, \tag{2.13}$$

$$E_i = \sqrt{\frac{(1 + 2C\epsilon)^3}{-2C\Theta\epsilon^2}}\ \overline{E_i}, \tag{2.14}$$

$$\theta = (1 + 2C\epsilon)\,\overline{\theta} + 2C\Theta\epsilon - 2C\Theta\epsilon^2, \tag{2.15}$$

$$\kappa = \frac{\overline{\kappa}}{1 + 2C\epsilon}, \tag{2.16}$$

$$a = (1 + 2C\epsilon)\overline{a}. \tag{2.17}$$

With this choice of rescaling we restrict ourself to the case of negative atomic detuning $\Theta < 0$, because we assume a real-valued injection $\overline{E}_i$. This simplifications leads to:

$$\frac{1}{\overline{\kappa}}\frac{\partial}{\partial t}\overline{E} = -(1 + \mathrm{i}\overline{\theta})\overline{E} + \overline{E_i} + \mathrm{i}|\overline{E}|^2\overline{E} + \mathrm{i}\overline{a}\nabla_\perp^2 \overline{E}. \tag{2.18}$$

Rescaling $\overline{t} = \overline{\kappa}t$ as well as $\overline{x} = \frac{x}{\sqrt{a}}$ and $\overline{y} = \frac{y}{\sqrt{a}}$ and immediately dropping all the bars finally yields the minimal Lugiato-Lefever equation in the form it will be discussed in the following:

$$\frac{\partial}{\partial t}E = -(1 + \mathrm{i}\theta)E + E_i + \mathrm{i}|E|^2 E + \mathrm{i}\nabla_\perp^2 E. \tag{2.19}$$

2.3 The onset of optical bistability

In this section we will focus specifically on the onset of optical bistability following an analysis that can be found in [Man05]. Optical bistability sets in when two different stable homogeneous solutions exist for a given set of parameters [LPB15]. This definition stems from investigations of systems which are not spatially extended, i.e., systems of ordinary differential equations (ODEs). In spatially extended systems, these homogeneous solutions also exist, however they can be unstable with respect to perturbations of finite wave-length, i.e., both homogeneous solutions ar not necessarily stable considering spatial effects as we shall se in chapter 4. Nevertheless, we refer to this region as bistable following a convention in this field of research.

If we only consider homogeneous stationary solutions E_s of Eqs. (2.1)-(2.3) and look at the function $|E_s|^2(|E_i|^2)$ which yields the intra-cavity intensity $|E_s|^2$ as a function of the input intensity $|E_i|^2$, this function exhibits an infinite slope at the onset of optical bistability (Fig 2.1). The critical point associated with the onset of optical bistability can therefore be determined by the conditions:

$$\frac{\partial}{\partial |E_s|}|E_i|^2 = 0, \qquad \text{and} \qquad \frac{\partial^2}{\partial |E_s|^2}|E_i|^2 = 0. \tag{2.20}$$

Assuming a homogeneous stationary solution E_s and using Eq. (2.8), one can determine:

$$|E_i|^2 = |E_s|^2 \left[(1 + \theta^2) + 4C \frac{1 - \theta\Theta}{1 + \Theta^2 + |E_s|^2} + 4C^2 \frac{1 + \Theta^2}{(1 + \Theta^2 + |E_s|^2)^2} \right]. \tag{2.21}$$

Figure 2.1 shows the function $|E_s|^2(|E_i|^2)$ for different values of C below and above the onset of optical bistability. In the following we are going to determine the onset of optical bistability and analyze the dynamics of Eqs. (2.1)-(2.3) in the vicinity of this point. For the sake of simplicity of the following analysis we consider the case of antisymmetric detuning, i.e. $\theta = -\Theta$. Applying the conditions given by Eq. (2.20), one can calculate the position of the critical point, where optical bistability sets in. Furthermore using Eqs. (2.1)-(2.3), one can also calculate the homogeneous steady state solution at this point. Solving this set of in total five equations yields:

$$C_{\text{crit.}} = 4(1 + \Theta^2), \tag{2.22}$$

$$E_{i\text{crit.}} = 3\sqrt{3}(1 + \Theta^2) \tag{2.23}$$

for the parameters characterizing the position of the critical point and:

$$E_{s\text{crit.}} = \sqrt{3}(1 + i\Theta), \tag{2.24}$$

$$P_{\text{crit.}} = \frac{\sqrt{3}}{4}, \tag{2.25}$$

$$D_{\text{crit.}} = \frac{1}{4} \tag{2.26}$$

for the steady state solution at the critical point. The atomic detuning Θ remains a free parameter due to the fact that the critical point is only defined by two conditions i.e. by two parameters.
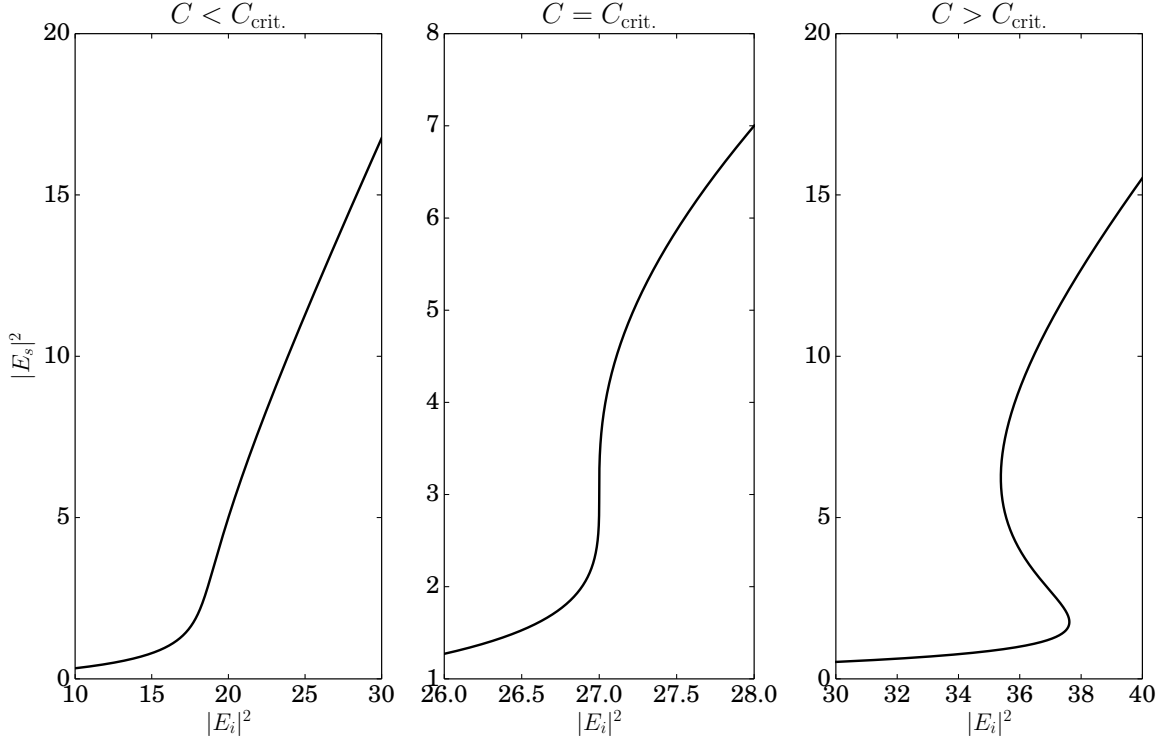
Figure 2.1: Intensity of the homogeneous stationary intracavity field $|E_s|^2$ in dependence of the injected field intensity $|E_i|^2$ in the completely absorptive scenario $\theta = \Theta = 0$ for three different values of C. On the left, the monostable case where C is below its critical value $C = 3.0 < C_{\text{crit.}}$ is depicted. In the middle, the onset of bistability is depicted with C at its critical value $C = 4.0 = C_{\text{crit.}}$, showing the critical point characterized by an infinite slope at $|E_i|^2 = 27.0$. On the right, the bistable case for $C = 5.0 > C_{\text{crit.}}$ is shown. All curves were obtained by evaluating Eq. (2.21).

2.3.1 Limit of small atomic detuning close to the critical point

We now restrict ourselves to dynamics close to the critical point. We therefore choose $C = C_{\text{crit.}} + \alpha \epsilon^2$, where ϵ is a parameter of smallness, and $\alpha = \pm 1$ indicates whether the system is below or above the critical value of C. We also consider small detuning $\Theta = \epsilon \Theta_1$ and rescale time and space as follows:

$$\tau = \epsilon^2 t, \qquad\qquad (\tilde{x}, \tilde{y}) = \sqrt{\epsilon}(x, y). \qquad\qquad (2.27)$$

We also expand the input field E_i in ϵ around its critical value:

$$E_i = E_{i\text{crit.}} + \epsilon E_{i,1} + \mathcal{O}(\epsilon^2), \qquad\qquad (2.28)$$

and proceed in the same manner with the three variables $X = (E, P, D)$:

$$X(t, x, y,) = X_{\text{crit.}} + \epsilon X_1(\tau, \tilde{x}, \tilde{y}) + \mathcal{O}(\epsilon^2), \qquad\qquad (2.29)$$

where $X_{\text{crit.}}$ is the stationary solution at the critical point. Because we consider deviations from the critical parameters $E_{i\text{crit.}}$ and $C_{\text{crit.}}$, the solution $X_{\text{crit.}}$ does not represent a stationary solution of the full system under consideration. On the contrary $X_{\text{crit.}}$ might not be stationary but X might become a stationary solution when considering the higher order terms in ϵ. One can now insert the expressions for C, E_i, E, P and D into Eqs. (2.1)-(2.3) and, after cancelling out every term that contributes to the stationary solution at the critical point, sort the remaining terms by their order in ϵ.

Order ϵ:

To this order the remaining terms are:

$$0 = -E_1 - 8P_1 + E_{i,1}, \qquad\qquad (2.30)$$
$$0 = -P_1 + E_1 D_{\text{crit.}} + E_{\text{crit.}} D_1, \qquad\qquad (2.31)$$
$$0 = -D_1 - \frac{1}{2}\left(\overline{E}_1 P_{\text{crit.}} + E_1 \overline{P}_{\text{crit.}} + \overline{E}_{\text{crit.}} P_1 + E_{\text{crit.}} \overline{P}_1\right). \qquad\qquad (2.32)$$

Inserting the solution $X_{\text{crit.}}$ at the critical point given by Eqs. (2.24)-(2.26) in the above equations yields:

$$0 = -E_1 - 8P_1 + E_{i,1}, \qquad\qquad (2.33)$$

$$0 = -P_1 + \frac{E_1}{4} + \sqrt{3} D_1, \qquad\qquad (2.34)$$

$$0 = D_1 + \frac{\sqrt{3}}{4} E_1 + \sqrt{3} P_1, \qquad\qquad (2.35)$$

where we assumed E_1 and P_1 to be real. This set of equations is solved by:

$$P_1 = -\frac{E_1}{8}, \qquad D_1 = -\sqrt{3}\frac{E_1}{8}, \qquad E_{i,1} = 0, \qquad\qquad (2.36)$$

where E_1 is a real function that remains to be determined. The overall aim of this section is to consider the higher order terms in ϵ and hence derive a closed evolution equation for E_1.

Order ϵ^2:

Collecting all the terms of $\mathcal{O}(\epsilon)$ and inserting all the expressions for $X_{\text{crit.}}$ and X_1 yields:

$$E_2 = \mathrm{i}\Theta_1 E_1 - 8P_2 - 2\alpha\frac{\sqrt{3}}{4} + E_{i,2} + \mathrm{i}a\tilde{\nabla}^2 E_1, \tag{2.37}$$

$$P_2 = \mathrm{i}\Theta_1\frac{E_1}{8} + \sqrt{3}D_2 - \mathrm{i}3\Theta_1\frac{E_1}{8} + \frac{1}{4}E_2 - \frac{\sqrt{3}}{8}E_1^2, \tag{2.38}$$

$$D_2 = -\frac{1}{2}\left(\sqrt{3}(P_2 + \overline{P}_2) + \frac{\sqrt{3}}{4}(E_2 + \overline{E}_2) - \frac{E_1^2}{4}\right). \tag{2.39}$$

By comparing the constant contributions to Eq. (2.37), one can directly set:

$$E_{i,2} = \alpha\frac{\sqrt{3}}{2}. \tag{2.40}$$

Now introdrucing the real valued new variable

$$B_2 = 4(P_2 + \overline{P}_2) + (E_2 + \overline{E}_2), \tag{2.41}$$

one can rewrite Eq. (2.39) as follows:

$$D_2 = \frac{1}{8}\left(-\sqrt{3}B_2 + E_1^2\right). \tag{2.42}$$

Replacing the expression (2.42) in Eq. (2.38), one obtains:

$$P_2 = -\frac{1}{4}(\Theta_1 E_1 + E_2) - \frac{3}{8}B_2. \tag{2.43}$$

Inserting Eqs. (2.40) and (2.43) into Eq. (2.37) yields:

$$E_2 = \mathrm{i}\Theta_1 E_1 + B_2 + \mathrm{i}\frac{1}{3}a\tilde{\nabla}^2 E_1. \tag{2.44}$$

Reinserting this expression into Eq. (2.43) one obtains an expression for P_2. For the sake of clarity all the results from the analysis in $\mathcal{O}(\epsilon)$ are summarized:

$$E_{i,2} = \alpha\frac{\sqrt{3}}{2}, \tag{2.45}$$

$$E_2 = \mathrm{i}\Theta_1 E_1 + B_2 + \mathrm{i}\frac{1}{3}a\tilde{\nabla}^2 E_1, \tag{2.46}$$

$$P_2 = -\frac{1}{8}B_2 + \mathrm{i}\frac{1}{12}a\tilde{\nabla}^2 E_1, \tag{2.47}$$

$$D_2 = \frac{1}{8}\left(-\sqrt{3}B_2 + E_1^2\right). \tag{2.48}$$

Order ϵ^3:

Collecting all the third order terms and replacing the expressions (2.24) for $X_{\text{const.}}$ leads to:

$$\frac{1}{\kappa}\frac{\partial}{\partial\tau}E_1 = -E_3 + \mathrm{i}\Theta_1 E_2 - 8P_3 - 8\Theta_1^2 P_1 - 2\alpha P_1 + E_{i,3} + \mathrm{i}a\tilde{\nabla}^2 E_2, \tag{2.49}$$

$$\frac{1}{\gamma_\perp}\frac{\partial}{\partial\tau}P_1 = -P_3 - \mathrm{i}\Theta_1 P_2 + \sqrt{3}(D_3 + \mathrm{i}\Theta_1 D_2) + E_1 D_2 + E_2 D_1 + \frac{1}{4}E_3, \tag{2.50}$$

$$\frac{1}{\gamma_\parallel}\frac{\partial}{\partial\tau}D_1 = -D_3 - \frac{1}{2}\left[\sqrt{3}(P_3 + \overline{P}_3) + \mathrm{i}\sqrt{3}\Theta_1(\overline{P}_2 - P_2)\right.$$

$$\left. + E_1(P_2 + \overline{P}_2) + P_1(E_2 + \overline{E}_2) + \frac{\sqrt{3}}{4}(E_3 + \overline{E}_3)\right]. \tag{2.51}$$

Combining Eq.(2.51) and (2.36) yields:

$$D_3 = \frac{1}{\gamma_\parallel}\frac{\sqrt{3}}{8}\frac{\partial}{\partial\tau}E_1 - \frac{1}{2}\left[\sqrt{3}(P_3 + \overline{P}_3) + \mathrm{i}\sqrt{3}\Theta_1(\overline{P}_2 - P_2)\right.$$

$$\left. + E_1(P_2 + \overline{P}_2) + P_1(E_2 + \overline{E}_2) + \frac{\sqrt{3}}{4}(E_3 + \overline{E}_3)\right]. \tag{2.52}$$

Substituting D_3 in Eq. (2.50):

$$P_3 = \frac{1}{8}\left(\frac{1}{\gamma_\perp} + \frac{3}{\gamma_\parallel}\right)\frac{\partial}{\partial\tau}E_1 - \mathrm{i}\Theta_1 P_2 + \mathrm{i}\sqrt{3}\Theta_1 D_2 - \frac{3}{2}\left[P_3 + \overline{P}_3 + \mathrm{i}\Theta_1(\overline{P}_2 - P_2)\right]$$

$$- \frac{\sqrt{3}}{2}\left[E_1(P_2 + \overline{P}_2) + (E_2 + \overline{E}_2)P_1\right] - \frac{3}{8}(E_3 + \overline{E}_3) + \frac{1}{4}E_3 + E_2 D_1 + E_1 D_2. \tag{2.53}$$

Since we are interested in deriving a closed equation for the time evolution of E_1, which is real, it is convenient to consider only the real parts of Eq (2.53), which is:

$$\Re(P_3) = \frac{1}{4}\left[\frac{1}{8}\left(\frac{1}{\gamma_\perp} + \frac{3}{\gamma_\parallel}\right)\frac{\partial}{\partial\tau}E_1 - 2\Theta_1\Im(P_2) - \sqrt{3}E_1\Re(P_2)\right.$$

$$\left. - \sqrt{3}\Re(E_2)P_1 - \frac{1}{2}\Re(E_3) + \Re(E_2)D_1 + E_1 D_2\right]. \tag{2.54}$$

We now consider the real part of Eq. (2.49):

$$\frac{1}{\kappa}\frac{\partial}{\partial\tau}E_1 = -\Re(E_3) - \Theta_1\Im(E_2) - 8\Re(P_3) - (8\Theta_1^2 + 2\alpha)P_1 + E_{i,3} - a\tilde{\nabla}^2\Im(E_2). \tag{2.55}$$

To obtain a closed equation we finally insert all the previously obtained expressions for E_2 (Eq. (2.46)), P_1 (Eq. (2.36)) and $\Re(P_3)$ (Eq. (2.54)) into the above equation:

$$\left(\frac{4}{\kappa} + \frac{1}{\gamma_\perp} + \frac{3}{\gamma_\parallel}\right)\frac{\partial}{\partial\tau}E_1 = 4E_{i3} + \alpha E_1 - E_1^3 - 4\Theta_1 a\tilde{\nabla}^2 E_1 - \frac{4}{3}a^2\tilde{\nabla}^4 E_1. \tag{2.56}$$

The above result represents the desired closed equation for the evolution of the first order correction E_1. With the Laplace operator $\tilde{\nabla}^2$, the biharmonic operator $\tilde{\nabla}^4$ and the cubic nonlinearity one can already see that Eq.(2.56) takes the form of a Swift-Hohenberg equation.

Rescaling $q = \epsilon E_1$ and reintroducing the original variables x and t and the parameter $\Theta = \epsilon \Theta_1$ yields:

$$\beta_0 \frac{\partial}{\partial t} = 4\epsilon^3 E_{i3} + \alpha \epsilon^2 q - q^3 - 4\Theta a \nabla^2 q - \frac{4}{3} a^2 \nabla^4 q, \tag{2.57}$$

where:

$$\beta_0 = \left(\frac{4}{\kappa} + \frac{1}{\gamma_\perp} + \frac{3}{\gamma_\parallel} \right). \tag{2.58}$$

However, since it is more convenient to work with variables and parameters in the order of $\mathcal{O}(1)$, we are going to use the Swift-Hohenberg equation in the form it was introduced in e.g. [GF13, TSTG17]:

$$\frac{\partial}{\partial t} q = Y_0 + Cq - q^3 - a_1 \nabla^2 q - a_2 \nabla^4 q, \tag{2.59}$$

Which can be obtained from Eq.(2.56) by appropriately rescaling t. The injected field now is $Y_0 = 4E_{i3}$, the detuning determines $a_1 = 4\Theta$, the diffractive length a is set to unity by rescaling x and y, hence $a_2 = \frac{4}{3}$. The parameter defining whether the system is below or above the onset of bistability is $\alpha = C$ and will be fixed to $C = 1.0$, i.e., we consider the bistable regime in the following.

Equation 2.59 can be transformed into the classical Swift-Hohenberg equation. Choosing:

$$q = \psi - \frac{\delta}{3}, \tag{2.60}$$

$$Y = \frac{\delta}{3} \left(\epsilon - k_c^4 + \frac{2}{9} \delta^2 \right), \tag{2.61}$$

$$C = \epsilon - k_c^4 + \frac{1}{3} \delta^2, \tag{2.62}$$

$$a_1 = 2, \tag{2.63}$$

$$a_2 = 1, \tag{2.64}$$

$$\tag{2.65}$$

yields:

$$\frac{\partial}{\partial t} \psi = \left[\epsilon - \left(k_c^2 + \nabla^2 \right) \right] \psi + \delta \psi^2 - \psi^3. \tag{2.66}$$

This is the classical Swift-Hohenberg equation as it was first proposed by Jack B. Swift und Pierre C. Hohenberg in 1977 [SH77] with an additional quadratic nonlinearity which breaks the $\psi \to -\psi$ symmetry. In Eq. (2.59), this symmetry-breaking effect which is necessary for the formation of hexagonal and localized patterns [KG16] is achieved by the constant contribution of the injected field Y.

2.4 Derivation of the temporal Lugiato-Lefever equation

In section 2.1 and 2.2 we derived the classical Lugiato-Lefever equation (LLE) starting from the Maxwell-Bloch equations (2.1-2.3). The LLE was originally proposed [LL87] to provide a

paradigmatic model for pattern formation in the transverse plane of a driven nonlinear cavity. However, as shown by Haeltermann et al. [HTW92], the LLE can also be derived in a different context modeling temporal pattern formation in a ring cavity. This temporal interpretation of the LLE only recently brought the LLE back into focus, when Del'Haye et al. [DSA+07] demonstrated that microresonators with a Kerr nonlinearity are suitable for the generation of frequency combs. The theoretically link to the temporal LLE, more specifically to localized solutions (also called Kerr solitons) was established in [CM13, CRSE13]. Here, it was shown that the LLE provides an effective a precise model for Kerr microresonators and that localized solutions of the LLE correspond to broad Kerr combs in the frequency domain.

Due to its high impact on recent scientific developments, we now derive the temporal version of the LLE. Two other derivations starting from the Maxwell-Bloch equations can be found in [CBG+17], however we are going to closely follow the original derivation by Haeltermann et al. [HTW92] due to its simplicity. This derivation also emphasizes the close relation between the LLE and the nonlinear Schrödinger equation, which is why the LLE is also referred to as driven, damped and detuned nonlinear Schrödinger equation [CBG+17].

We assume a fiber ring cavity, driven by an external electrical field E_i which is coupled into the ring cavity by a beam splitter with the reflection and transmission coefficients R and T. The longitudinal variable z measures the distance to the beam splitter inside the ring cavity of length L, i.e. $0 \leq z \leq L$. The electrical field envelope E_{n+1} inside the cavity at the beginning of the $(n + 1)$th roundtrip is given by the following map:

$$E_{n+1}(z = 0, \xi) = T E_i(\xi) + R \exp\left(-\mathrm{i}\theta\right) E_n(z = L, \xi). \tag{2.67}$$

The above equation simply reflects that the electrical field envelope at the beginning of a roundtrip is composed of the transmitted portion of the injected field E_i and the reflected portion of the intracavity field at the end of the last roundtrip. The variable ξ in this context is the physical time in a reference frame traveling with the group velocity of light [THM98]. θ is the cavity detuning, i.e. the phase shift aquired during one roundtrip.

To calculate the time-evolution of the intracavity field the only missing component is $E_n(z = L, \xi)$, i.e. one needs to know how the intracavity field evolves during one roundtrip from $z = 0$ to $z = L$. The evolution in the z direction in case of a Kerr nonlinearity is governed by the nonlinear Schrödinger equation:

$$\partial_z E_n = -\mathrm{i}\frac{k_0}{2}\partial_{\xi\xi}^2 E_n + \mathrm{i}\gamma|E_n|^2 E_n, \tag{2.68}$$

where k_0 is the group velocity dispersion and γ is proportional to the first correction term of the refractive index due to the Kerr effect.

In principle, the combination of Eq. (2.67) and Eq. (2.68) provides a full mathematical description of the Kerr fiber loop, since the evolution of the field inside the cavity is modeled by the nonlinear Schrödinger equation and the driving field, losses and detuning are accounted for in the discrete map. One could in principle start with an initially injected field, calculate its evolution during the first roundtrip by integrating Eq. (2.68) and calculate the transitions after one roundtrip by evaluating Eq. (2.67). However, such an approach is highly unpractical in terms of computation time since, e.g. for the generation of Kerr combs high Q cavities are used, where the time-evolution of the intracavity field evolves over millions of roundtrips [CRSE13], which renders the above approach highly inefficient.

It is therefore necessary to combine Eqs. (2.67) and (2.68) to one equation by introducing a slow time t, which describes the time-evolution over many roundtrips. Assuming the number

n of roundtrips is larger, one can introduce t as follows:

$$E(t = nt_R, \xi) = E_n(z = 0, \xi), \tag{2.69}$$

where t_R is the round trip time of the cavity. In the quasi-continuous limit of many roundtrips, it is also straightforward to introduce the derivative with respect to the slow time t as:

$$\partial_t E(t = nt_R, \xi) = \frac{E_{n+1}(z = 0, \xi) - E_n(z = 0, \xi)}{t_R} \tag{2.70}$$

Assuming that the dispersion length of the intracavity field is much larger than the cavity length L we can average over Eq. (2.68) instead of integrating it, i.e.:

$$E_n(z = L, \xi) = E_n(z = 0, \xi) - \mathrm{i}L\frac{k_0}{2}\partial_{\xi\xi}^2 E_n(z = 0, \xi) + \mathrm{i}\gamma L|E_n(z = 0, \xi)|^2 E_n(z = 0, \xi). \tag{2.71}$$

Due to the high finesse of the cavity it is reasonable to approximate $R = 1 - \frac{T^2}{2}$, which is obtained by a Taylor expansion of $R = \sqrt{1 - T^2}$ to quadratic order. Furthermore, the cavity has to be pumped externally close to resonance, i.e. both the linear and nonlinear phase-shift has to be small, i.e. $\theta \ll 1$ and $\gamma L|E|^2 \ll 1$. Equation (2.67) now reads:

$$E_{n+1}(z = 0, \xi) = TE_i(\xi) + \left(1 - \frac{T^2}{2} - \mathrm{i}\theta\right) E_n(z = L, \xi). \tag{2.72}$$

Inserting Eq. (2.71) into Eq. (2.72) yields:

$$E_{n+1} = TE_i(\xi) + \left(1 - \frac{T^2}{2} - \mathrm{i}\theta\right) E_n - \mathrm{i}L\frac{k_0}{2}\partial_{\xi\xi}^2 E_n + \mathrm{i}\gamma L|E_n|^2 E_n$$
$$- \left(\frac{T^2}{2} + \mathrm{i}\theta\right)\left(-\mathrm{i}L\frac{k_0}{2}\partial_{\xi\xi}^2 E_n + \mathrm{i}\gamma L|E_n|^2 E_n\right), \tag{2.73}$$

where we introduced the shorter notion $E_n(z = 0, \xi) = E_n$, which is now unambiguous, since we eliminated $E_n(z = L, \xi)$ in the last step. The gray colored terms in the last row can be considered neglectable compared to the first row due to the assumptions of a high finesse cavity. Now applying the definition of the derivative with respect to the slow time t yields the desired equation:

$$t_R\partial_t E(t, \xi) = TE_i(\xi) - \frac{T^2}{2}E(t, \xi) - \mathrm{i}\theta E(t, \xi) + \mathrm{i}\gamma L|E(t, \xi)|^2 E(t, \xi) - \mathrm{i}L\frac{k_0}{2}\partial_{\xi\xi}^2 E(t, \xi). \tag{2.74}$$

By rescaling t, ξ and E and redefining θ, γ and E_i, we obtain the nondimensional form of the LLE:

$$\partial_t E(t, \xi) = E_i + \left[-(1 + \mathrm{i}\theta) + \mathrm{i}\gamma|E|^2 + \mathrm{i}\partial_{\xi\xi}^2\right] E(t, \xi). \tag{2.75}$$

Depending on the sign of the nonlinearity γ, the LLE is called the self-focussing LLE ($\gamma > 0$) or defocusing LLE ($\gamma < 0$) [LL87]. In the following we are going to restrict our analysis to the self focusing case by setting $\gamma = 1$, which is the more relevant case when considering pattern formation.

3 Analysis of the inhomogeneous Swift-Hohenberg equation

In this chapter we are going to analyze the Swift-Hohenberg equation (SHE) as it was derived in chapter 2 with and without additional spatial inhomogeneities. The Swift-Hohenberg equation was first proposed in the context of fluid dynamics [SH77] and has been used and modified to model different pattern forming systems ranging from plant ecology [LBCL09] and chemical systems [HDB96] to the field of nonlinear optics [TVT⁺10, GF13, TSTG17]. In its original form it describes the time-evolution of a single order parameter and only possesses a cubic nonlinearity. It serves as a paradigmatic model for pattern formation exhibiting a finite wavelength instability also denoted as Turing instability and, depending on the choice of parameters, stable stripe solutions.

One of the most important modifications of the SHE is the addition of a quadratic nonlinearity which breaks the parity symmetry of the system, thus allowing the formation of hexagonal patterns and localized solutions [CH93]. The SHE possesses a Lyapunov functional [CH93], i.e., any initial state will evolve towards one of the minima of the functional and no long-term dynamics can be observed. Other modifications of the SHE include a conserved SHE, which is used, e.g., to model pattern formation in liquid crystals [ML13, OGT18]. Further nonvariational extensions of the SHE are also applied in various fields of pattern formation [KT07].

Since the SHE is one of the most studied equations in pattern formation, we focus our analysis on a few issues, which have not been addressed in detail yet, namely the localized solutions (LS) in the vicinity of inhomogeneities and under the influence of time-delayed feedback. We therefore restrict the discussion of previous work concerning the SHE to the results necessary for our analysis.

We begin with the optical SHE as it was derived in chapter 2, which is equivalent to the SHE with quadratic and cubic nonlinearity [KG16]. We discuss the bifurcation structure of the SHE and the emergence of LS. A special focus in this section lies on the emergence of solutions with broken radial symmetry. The existence of such solutions in the SHE was already reported [BC15], however the bifurcation structure of these solutions was unknown so far. We briefly discuss the bifurcations responsible for the emergence of these structures, although in the remainder of this chapter we solely address radially symmetric LSs.

We proceed with the introduction of time-delayed feedback which served as a main motivation for the consideration of spatial inhomogeneities. Time-delayed feedback breaks the variational structure of the SHE, resulting in the possibility of long-term dynamics. Delay-induced dynamics have been thoroughly studied in the SHE [TVPT09, TVT⁺10, GF13, KG16]. Theoretically a drift of otherwise stable LSs is the predominant dynamics, when the delay-parameters surpass the threshold of instability. The occurrence of drifting LSs is not confined to the SHE but has been reported with the same threshold in other pattern forming systems [STP⁺17, Gur14]. We briefly discuss this phenomenon and show why the predominant occurrence of drifting structures is a consequence of the continuous translational symmetry of the system under

consideration. Since experimental realizations of LSs in optically driven cavities do not exhibit a free drift of LSs, but rather display a pinned movement on the spot, we propose to break the translational symmetry in the following.

Considering, e.g., the case of slightly inhomogeneous injection breaks the translational symmetry of the systems and leads to more realistic delay-induced dynamics as we show in section 3.2.2. The competing effects of an attracting inhomogeneity and destabilizing time-delayed feedback lead to oscillations of the LSs. Only for increased feedback parameters, the LSs can depin from the inhomogeneity and drift freely. At this point, it does not matter whether the inhomogeneities are introduced into the system intentionally or if they occur naturally due to small inaccuracies in the experimental setup. Even small inhomogeneities compared to the overall value of injection change the dynamics of the system qualitatively.

We then proceed with the analysis of the transitions from stable LSs to oscillating LSs by deriving an order parameter equation showing that the onset of the oscillations can be described as a delay-induced Andronov-Hopf bifurcation. In the last section of this chapter we go one step further by describing both transitions from resting to oscillating LSs and from oscillating to depinning LSs in the framework of a semi-analytical approach. More specifically, we approximate the motion of the LSs in the vicinity of the inhomogeneity as an overdamped particle in a potential well. We provide an expression to estimate the potential induced by the inhomogeneity and show that the model both qualitatively and quantitatively reproduces the oscillatory and depinning dynamics obtained by direct numerical time simulations of the full system.

3.1 The Swift-Hohenberg equation with homogeneous injection

We start our analysis with the optical SHE derived in chapter 2, i.e., with homogeneous injection and without time-delayed feedback. The SHE reads:

$$\partial_t q(\mathbf{x}, t) = \left(-a_1 \Delta - a_2 \Delta^2 + C\right) q(\mathbf{x}, t) + Y_0 - q(\mathbf{x}, t)^3, \tag{3.1}$$

where q denotes the deviation of the electrical field amplitude from its critical value at the onset of optical bistability. The deviation of the amplitude of the injected field from its critical value for now is constant Y_0 accounting for homogeneous plain wave injection. For the sake of simplicity we denote Y_0 in the following as the injected field, keeping in mind that it is actually the deviation of the injected field amplitude from its value at the onset of optical bistability. All other parameters remain fixed in the following chapter. The detuning is accounted for in $a_1 = 2.0$. The derivation of the SHE yielded fixed values of $a_2 = \frac{4}{3}$ and $C = 1.0$, meaning that we are investigating the region of bistability. The spatial coordinate is $\mathbf{x} = (x, y)$ in two spatial dimensions and reduces to $\mathbf{x} = x$ when we consider the SHE in one spatial dimension for the sake of simplicity.

The injection Y_0 breaks the parity symmetry $q \to -q$ of the system, which is crucial for the formation of hexagonal patterns and LSs. As shown in chapter 2, Eq. (3.1) is equivalent to the more common classical version of the SHE with an additional quadratic nonlinearity, which has the same symmetry breaking effect.

3.1.1 Bifurcation structure of localized solutions in 2D

We now discuss the emergence of LSs in Eq. (3.1), by deploying numerical parameter continuation using the Matlab package *pde2path* [UWR14]. The bifurcation structure of the classical SHE with quadratic and cubic nonlinearity has been already discussed in detail, e.g., in [BK06]. In particular, varying the coefficient of the linear term, LSs follow a homoclinic snaking bifurcation structure. A branch consisting of an even number of peaks and a branch consisting of an odd number of peaks gain additional peaks in a sequence of folds until they connect to periodic solutions. In the following we present a different bifurcation structure since we vary the parameter Y_0, i.e., the amplitude of the injected beam.

The aim is to follow different stationary solutions of Eq. (3.1) in parameter space changing the continuation parameter and thus constructing a bifurcation diagram using a suitable norm as a solution measure to distinguish different solutions.

Figure 3.1 depicts the bifurcation diagram for single LS. We use Y_0 as a continuation parameter and as in chapter 1 use the L_1-norm as a measure:

$$L_1 = \int |q(x,y) - \overline{q}| \mathrm{d}x \mathrm{d}y, \tag{3.2}$$

where $\overline{q}$ is the order parameter averaged over the domain size. The continuation is performed on half the domain size and (where possible) on a quarter of the domain size exploiting the symmetries of the solutions under consideration and thus gaining computational efficiency.

The single LS branch (red line in Fig. 3.1) bifurcates from the periodic branch (dark green) close to the Turing bifurcation point where the homogeneous solution (light green) looses stability. As in the case of the Brusselator this can be considered a finite size effect [BBKM08]. However, the result is that the small amplitude LS bifurcates in a supercritical pitchfork bifurcation in contrast to a subcritical pitchfork directly from the homogeneous solution. The LS gains stability in a fold and remains stable until it looses stability in a second bifurcation. In this subcritical pitchfork bifurcation, another branch bifurcates (blue line) consisting of LSs which are stretched in one longitudinal direction (solutions at the marked positions are depicted in Fig. 3.3).

This branch gains stability in a fold, yielding stable LS that are not rotationally symmetric. In fact, the stability of such solutions has been reported in [BC15] where they were named rodlike solutions, yet their bifurcational origin was so far unknown. Following the rodlike solution branch (blue line) further, these solutions follow a snaking behavior, i.e., they loose and regain stability in a sequence of consecutive folds. However, the parameter region in which this snaking occurs is very narrow. The stretched rodlike solutions grow larger until at some point they interfere with the boundaries and can therefore not be tracked further. It is therefore not possible yet to determine whether on an infinite domain they would connect to a periodic branch at some point or not.

Following the branch of the classical LSs (red line) further, a secondary bifurcation occurs, in which the solution becomes more unstable. Similar to the rodlike solutions, another solution branch bifurcates (orange line), consisting of triangular LSs as depicted in Fig. 3.4. In contrast to the rodlike structures, this branch does not gain stability. Stable triangular solutions were also detected close to this branch, however they could not be connected to any other solution branch and are therefore not depicted in Fig. 3.1. Following the branch of radial LSs (red line), they start to grow in size (Fig. 3.2) until they become ring-like, exhibiting a small dent at the center. Along the branch it becomes increasingly difficult to track the solutions in parameter
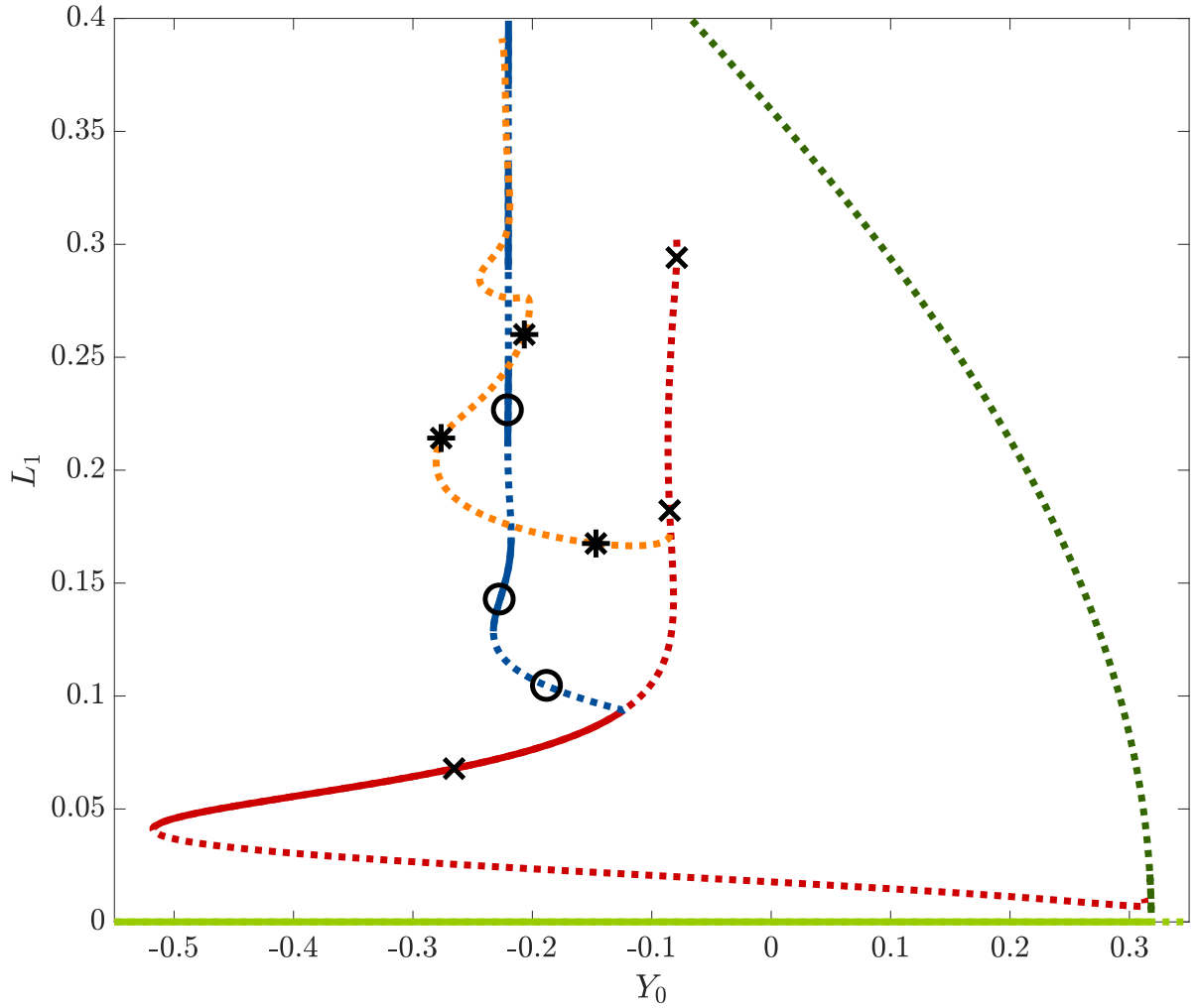
Figure 3.1: Bifurcation diagram of LSs obtained by numerical continuation of the SHE (3.1). Unstable (stable) solutions are marked by dotted (solid) lines. The homogeneous solution (light green) becomes unstable at the Turing point, where a periodic solution bifurcates subcritically. Close to the Turing point, a radially symmetric LS (red line) branches off from the periodic solution in a supercritical pitchfork bifurcation. The LS gains stability in a fold and then becomes unstable in a subcritical pitchfork bifurcation, where a solution with broken radial symmetry bifurcates (blue branch). This solution gains and looses stability snaking in a narrow parameter regime. The solutions along this branch are LSs which are elongated in one spatial direction. Following the radially symmetric branch, another solution with broken radial symmetry bifurcates (orange line), corresponding to triangular solutions. The radially symmetric LSs grow in size until they develop a dent at the center. Solution profiles at the marked positions can be found in Fig. 3.2 (crosses), Fig. 3.3 (circles) and Fig. 3.4 (asterisks). Remaining parameters are $a_1 = 2.0$, $a_2 = \frac{4}{3}$, $C = 1.0$.
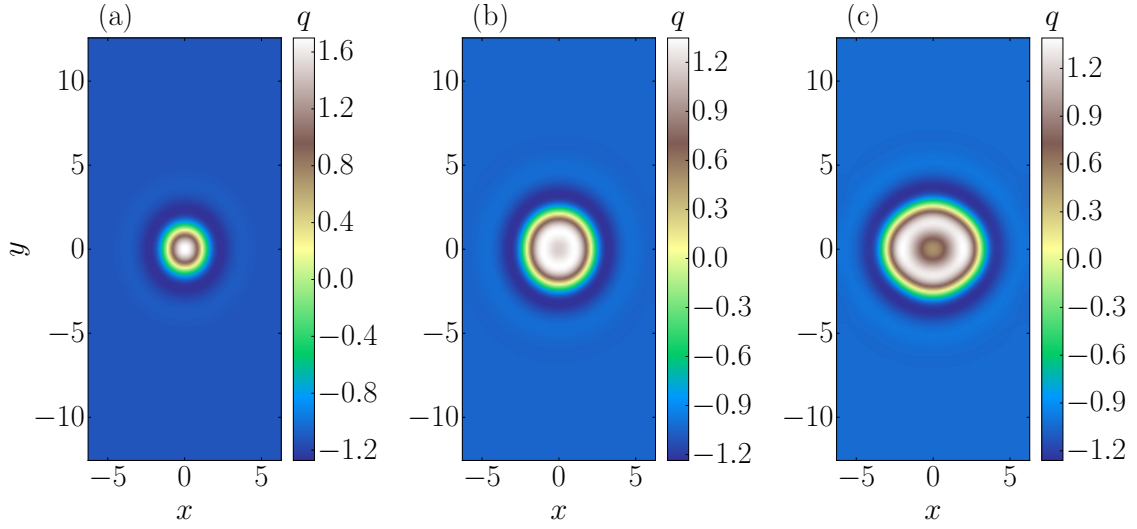
Figure 3.2: Solution profiles of radially symmetric solutions $q_0(x, y)$ of Eq. (3.1) for different Y_0 at the positions marked by crosses in Fig. 3.1. Solution (a) is stable, whereas (b) and (c) depict unstable LSs.
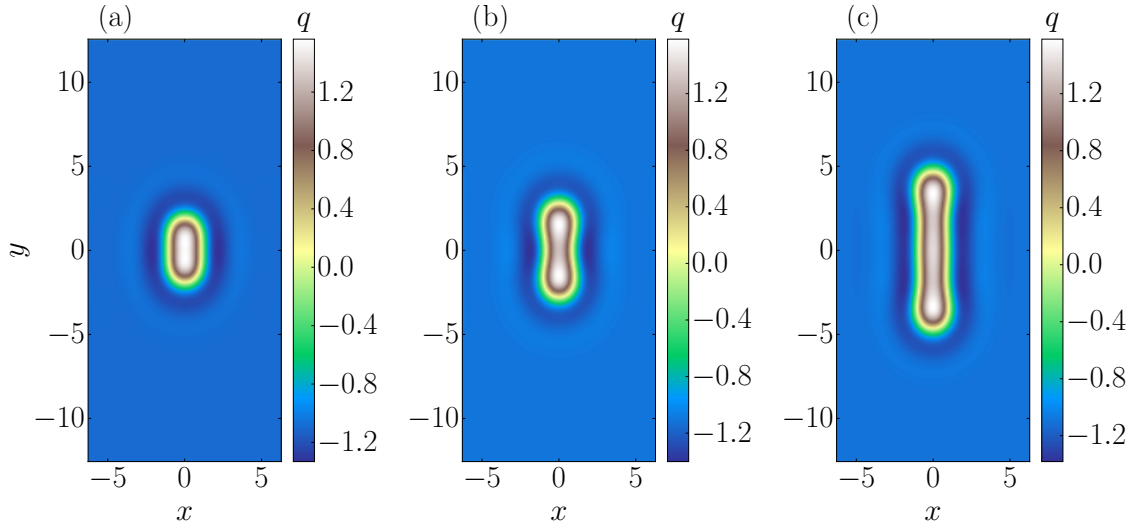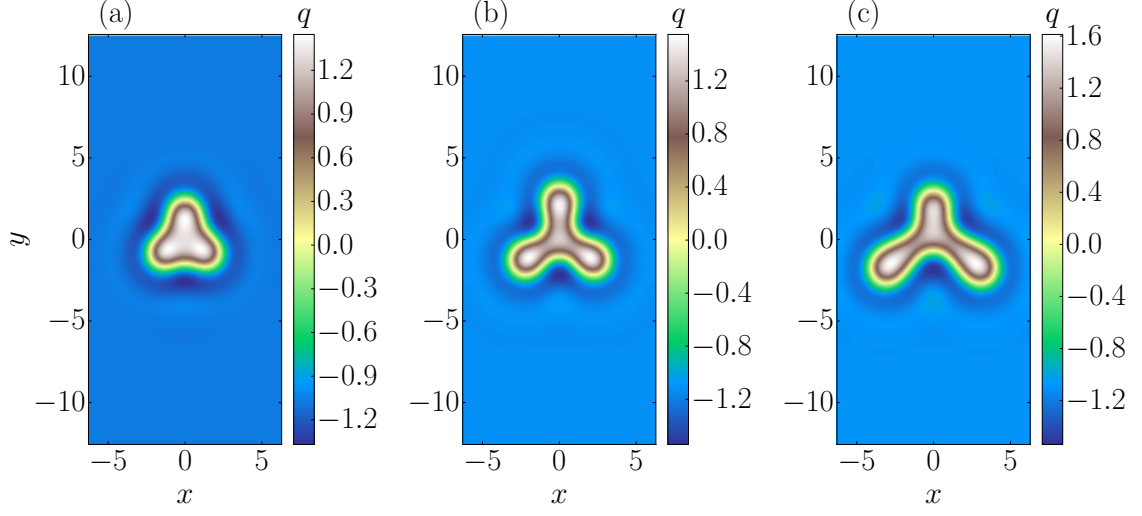

Figure 3.3: Solution profiles of rodlike solutions $q_0(x, y)$ of Eq. (3.1) for different Y_0 at the positions marked by circles in Fig. 3.1, going from the symmetry-breaking bifurcation to higher L_1-norms (from left to right). Solution (a) is unstable and can be found close to the bifurcation point. Solution (b) is a stable rodlike solution which gained stability in a fold. Solution (c) is also stable and corresponds to the solution on the next branch of the snaking diagram, i.e., after two more folds.

41

Figure 3.4: Solution profiles of triangular solutions $q_0(x, y)$ of Eq. (3.1) for different Y_0 at the positions marked by asterisks in Fig. 3.1. Solution (a) can be found close to the bifurcation point, whereas (b) and (c) depict solutions further along the branch. All solutions are unstable.

space since the solution starts to interact with the boundaries, which is why we decided to stop the continuation. This seems justified considering that these solutions are highly unstable. A second branch consisting of two bound LSs exhibits a similar bifurcation structure. The branches are however not connected and these solutions are out of the scope of this thesis.

Numerical continuation however proofed very useful to detect the emergence of LSs and determine their region of stability. Furthermore, we were able to explain the emergence of rodlike solutions in a symmetry breaking pitchfork bifurcation. However, in the following we focus on the properties of radial LSs, which we simply refer to as LSs. We therefore consider the regime of stable radial LS by fixing $Y_0 = -0.4$. We now proceed with the introduction of time-delayed feedback and discuss how it affects the stability of LSs.

3.1.2 Delay-induced dynamics of LSs

After examining the emergence and stability of different localized solutions in the SHE, we now discuss the destabilization of the radially symmetric localized structure (which we will refer to as LS) by time-delayed feedback and analyze the induced dynamics.

Time-delayed feedback in a driven nonlinear cavity can be implemented by adding an external cavity to the experimental setup, where a small proportion of the intra-cavity field leaves the cavity, is reflected by an external reflector and is then reintroduced into the cavity. The delay-strength α in this scenario is proportional to the reflectivity of the reflector and can therefore easily be altered experimentally. Assuming a small delay-strength, one can model the time-delay mathematically by employing the Rosanov-Lang-Kobayashi approximation [Roz75, LK80], where only a single roundtrip in the external cavity is taken into account. In this approximation, the system can be modeled by a single delay-time τ, which is proportional to the length of the

external cavity.

Introducing a time-delayed feedback term to Eq. (3.1) yields:

$$\partial_t q(\mathbf{x}, t) = \left(-a_1 \Delta - a_2 \Delta^2 + C\right) q(\mathbf{x}, t) + Y_0 - q(\mathbf{x}, t)^3 + \alpha \left(q(\mathbf{x}, t) - q(\mathbf{x}, t - \tau)\right), \qquad (3.3)$$

where α is the delay-strength and τ the delay-time. The time-delayed feedback term in Eq. (3.3) has the form of a so-called Pyragas control [Pyr92], where the time-delayed feedback term is proportional to the difference between the present state of the system $q(\mathbf{x}, t)$ and the delayed state of the system $q(\mathbf{x}, t - \tau)$. This assumption is again an approximation taking advantage of the assumption of weak delay strength α. From a mathematically point of view, Pyragas control has several advantages which we discuss in the following. Equation (3.3) has been extensively studied in the context of nonlinear optics [TML94, TVPT09, TVT$^+$10, GF13, Tab14, TSTG17], which is why we briefly discuss results, which are relevant in the context of this work.

To analyze the dynamics induced by time-delayed feedback, it is useful to start with a linear stability analysis of stationary solutions of Eq. (3.3). Due the special form of Pyragas control, stationary solutions $q_0(x, y)$ without time-delay ($\alpha = 0$) are also stationary solutions of the full delayed system, since the delay term vanishes, if the system remains in the stationary solution for a time τ. The LSs discussed in the previous section are therefore stationary solutions of the delayed system, however, time-delayed feedback can change the stability properties of the LSs.

Before performing the linear stability analysis of a localized solution, one can gain first insights into the eigenvalue spectrum of the linearized system by symmetry arguments following Goldstone's theorem of particle physics [GSW62]. The full argument can be found in [Fri93, Tab14]. Assuming periodic boundaries, Eq. (3.1) and (3.3) are continuously symmetric under translation since no terms explicitly depend on the spatial coordinates (x, y). This symmetry is spontaneously broken by a localized solution $q_0(x, y)$. Therefore for every spatial direction an eigenmode $\varphi(x, y)$ with an eigenvalue $\mu = 0$ must exist, that corresponds to an infinitesimal shift of the LS. In two dimensions, these eigenmodes are:

$$\varphi_x(x, y) = \frac{\partial}{\partial x} q_0(x, y) \qquad \text{and} \qquad \varphi_y(x, y) = \frac{\partial}{\partial y} q_0(x, y). \qquad (3.4)$$

A short derivation can be found in [Fri93, Tab14] but one can also quickly recognize the validity of Eq. (3.4) because a translationally invariant system should be neutrally stable against infinitesimal shifts of a given solution (hence, $\mu = 0$), i.e., a small shift of the LS should neither be suppressed nor amplified. An infinitesimally small shift ϵ of the solution $q_0(x, y)$ in the x-direction is achieved by adding the Goldstone mode $\varphi_x(x, y)$, since:

$$q_0(x + \epsilon, y) = q_0(x, y) + \epsilon \frac{\partial}{\partial x} q_0(x, y), \qquad (3.5)$$

for infinitesimal ϵ. Besides these two Goldstone modes, a single LS $q_0(x, y)$ possesses further discrete eigenvalues with corresponding localized eigenfunctions, which have to be obtained by linearizing the system around the LS . One can than, e.g., discretize the linearized system in space using finite differences and diagonalize the resulting sparse matrix numerically. This procedure yields a spectrum of five discrete eigenvalues close to zero and a well-separated continuous spectrum of eigenvalues. All eigenvalues are $\mu \leq 0$, since the solution is stable.

The discrete eigenvalues close to zero correspond to localized eigenfunctions, some of which are depicted in Fig. 3.5 along with the LS (top left). The two Goldstone modes of translation

have the eigenvalue $\mu = 0$ as discussed above. One of the Goldstone modes is depicted in Fig. 3.5 (top right). The other Goldstone mode resembles the depicted mode but is rotated by $\frac{\pi}{2}$.

Further localized eigenfunctions with corresponding eigenvalues are one radially symmetric eigenfunction that would induce a change in size of the LS if it were to become unstable ($\mu = -0.46$, bottom left of Fig. 3.5) and two eigenmodes that would induce a deformation of the LS ($\mu = -0.84$, one is depicted in the bottom right of Fig. 3.5), i.e., the LS would elongate in one direction while contracting in the perpendicular direction. For the sake of simplicity we refer to the first mode as growth mode and to the latter as deformation modes.
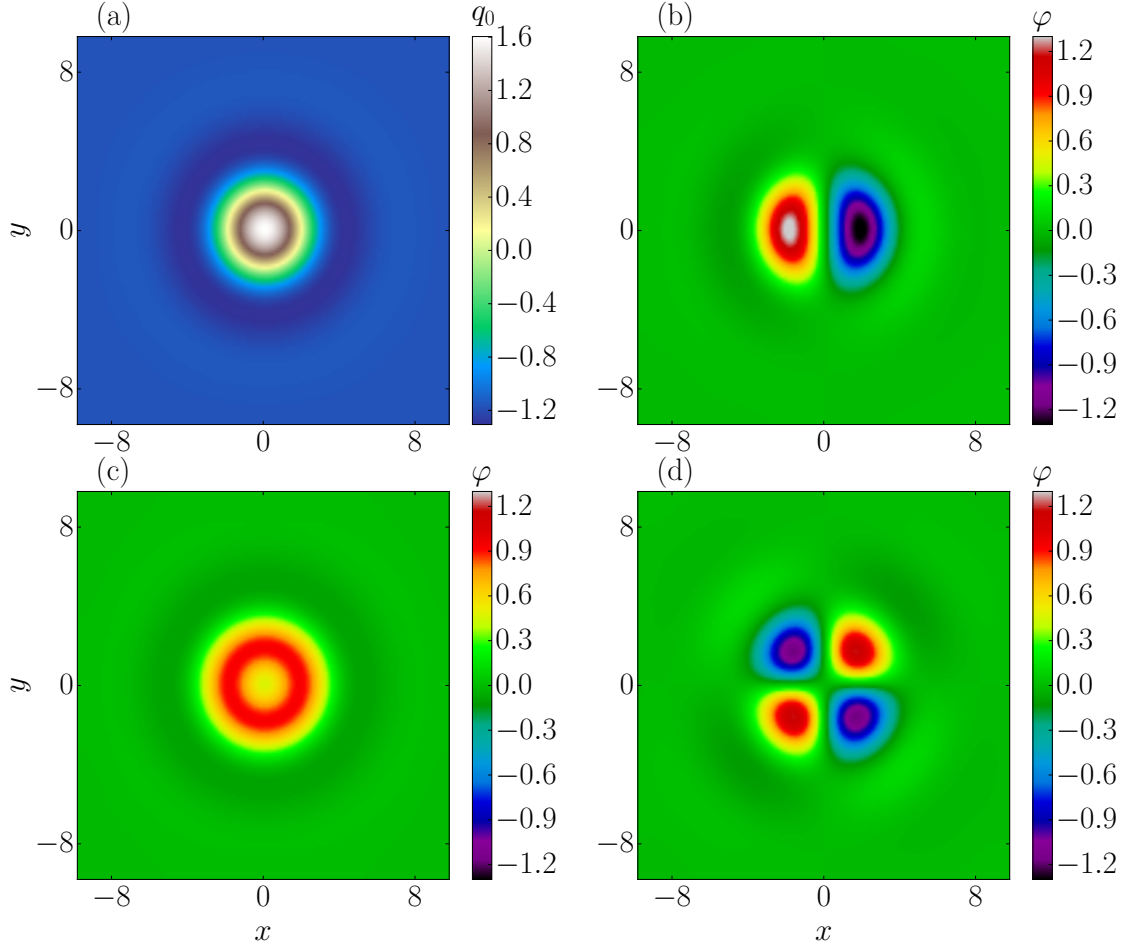
Figure 3.5: (a) Stable localized solution $q_0(\mathbf{x})$ obtained by 2D numerical time simulations of Eq. (3.1) as well as three localized eigenfunctions $\varphi_k(\mathbf{x})$ as solutions of the linear eigenvalue problem: (b) translational Goldstone mode ($\mu = 0$), (c) growth mode ($\mu = -0.46$), (d) deformation mode ($\mu = -0.84$). Other parameters are: $L_x = L_y = 19.6$, $a_1 = 2.0$, $a_2 = \frac{4}{3}$, $Y_0 = -0.4$, $C = 1.0$. An altered version of this figure was published in [TSTG17] and was used in [Tab14].

Proceeding now with the linear stability analysis in the presence of time-delayed feedback,

one can again take advantage of the Pyragas control term. Under the influence of Pyragas control, the spatial shape of the eigenfunctions remains the same since the spatially scalar time-delayed feedback term commutes with the linearized operator of the system. One therefore only has to calculate the new resulting eigenvalues λ for the different eigenfunctions [GF13]. Calculating the time-evolution of a given eigenfunction φ_k corresponding to an undelayed eigenvalue μ_k in the delayed linearized system, one obtains the following implicit equation [GF13, Gur13, TSTG17]:

$$\lambda_k = \mu_k + \alpha \left(1 - e^{-\lambda_k \tau} \right), \tag{3.6}$$

which connects the eigenvalue μ_k of the undelayed system with the eigenvalue λ_k of the delayed system. Equation (3.6) can only be solved in terms of the Lambert W function [CGH$^+$96], which is defined as the multi-valued inverse of $z \to ze^z$. Inserting this definition yields:

$$\lambda_{k,m} = \mu_k + \alpha + \frac{1}{\tau} W_m \left[-\alpha\tau \cdot e^{-\tau(\mu_k + \alpha)} \right], \qquad m \in \mathbb{Z}, \tag{3.7}$$

where W_m is the m-th branch of the Lambert W function. The addition of time-delayed feedback yields an infinite amount of eigenvalues $\lambda_{k,m}$ for each eigenvalue μ_k of the system without delay, which is understandable since the delayed feedback term adds infinite dimensions to the phase space of the system. In the limit of vanishing delay (i.e., $\alpha \to 0$ or $\tau \to 0$), the eigenvalues behave as follows [Tab14]:

$$\lim_{\alpha,\tau \to 0} \lambda_{k,m} = \begin{cases} \mu_k & \text{for } m = 0 \\ -\infty & \text{for } m \neq 0 \end{cases} \tag{3.8}$$

It is worthwhile to treat the eigenvalue problem of the neutral Goldstone modes separately, since in the special case of $\mu_k = 0$, Eq. (3.6) reduces to

$$\lambda = \alpha \left(1 - e^{-\lambda_k \tau} \right), \tag{3.9}$$

which leads to a trivial solution

$$\lambda_{\mathrm{I}} = 0, \tag{3.10}$$

which is evident since the addition of time-delayed feedback does not break the translational symmetry, i.e., the neutrally stable Goldstone modes still exist. Additionally, one can obtain a second approximated eigenvalue assuming $|\lambda| \ll 1$ by performing a Taylor expansion up to second order, which yields:

$$\lambda_{\mathrm{II}} = -\frac{2}{\tau} \frac{(1 - \alpha\tau)}{\alpha\tau}. \tag{3.11}$$

This eigenvalue λ_{II} becomes positive for values of $\alpha\tau > 1$, which results in an unstable translational eigenmode that induces a drift of the LS. Indeed, LS drifting with constant velocity as well as the analytical threshold of $\alpha\tau > 1$ have been reported, e.g., in [TVPT09]. In [GF13] the bifurcation responsible for the onset of drift was identified as a pitchfork bifurcation of the velocity. A drifting LS in one spatial dimension obtained in direct numerical simulations

is shown in Fig. 3.6. The simulations are performed using a semi-implicit timestep. The spatial derivatives are calculated in Fourier space using a pseudo-spectral method with periodic boundary conditions. Choosing the same parameters as in Fig. 3.6 in two spatial dimensions would result in a drift of the LS in an arbitrary direction. Examples of dynamics in two spatial dimensions and a detailed description of the numerical methods can be found in [Tab14].

Further increasing the feedback strength α or the delay time τ leads to the destabilization of other eigenmodes leading to more complex dynamics (see, e.g., [GF13, Tab14]). However in any system with a continuous translational symmetry that only possesses real-valued eigenvalues μ_k without delay, a drift bifurcation is the first bifurcation to occur at $\alpha\tau = 1$. Even in systems without a variational structure (i.e., $\mu \in \mathbb{C}$), the analytical expression for the onset of drift is identical, however there can exist complex eigenvalues, which get destabilized before the drift-inducing modes [Gur13].
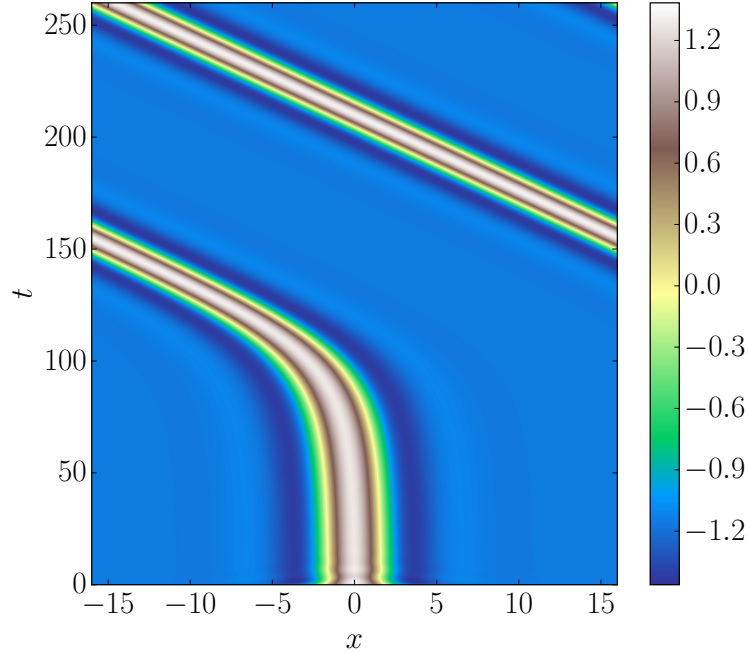
Figure 3.6: Direct numerical simulation of Eq. (3.3) in one spatial dimension depicted in a space-time plot. The simulation shows a LS with an unstable translational eigenfunction which induces a drift. After accelerating, the LS drifts with a constant velocity. When reaching the boundaries of the domain of size $L = 32$, the LS is reintroduced into the domain on the opposite side due to periodic boundary conditions. Parameters are: $\alpha = 0.525$, $\tau = 2.0$, $Y = -0.4$, $C = 1.0$, $a_1 = 2.0$, $a_2 = \frac{4}{3}$. A similar figure based on the same simulation was used in [Tab14].

In the following section we discuss how this behavior changes, when the translational symmetry is explicitly broken by small inhomogeneities in the injected field Y. We demonstrate, that the inclusion of small inhomogeneities in the theoretical model leads to more complex and most importantly to more realistic induced dynamics.

3.2 The Swift-Hohenberg equation with inhomogeneous injection

The delayed Swift-Hohenberg equation (DSHE) as presented in the previous section has been extensively studied in the context of pattern formation in nonlinear optics [TML94, TVPT09, TVT⁺10, GF13, Tab14, TSTG17] but is by far not the only mean-field model which has been discussed in the context of pattern formation in nonlinear optics[PT10, PVG⁺13, PT14]. The observation of a drift instability leading to moving LSs as depicted in Fig. 3.6 is however not limited to the case of Eq. (3.3) but, as argued in the previous section is a general feature that will occur in any PDE-model with a continuous translational symmetry that allows the formation of LSs. Even the calculation of the onset of instability at $\alpha\tau = 1$ does not depend on any properties which are specific to the DSHE, but applies to any system with translational symmetry and Pyragas control. For other types of delayed feedback control the onset of a drift bifurcation is shifted, but still has been reported theoretically [PT10]. In spite of the thorough theoretical description of delay-induced drift, such a behavior of cavity solitons or LSs has not been reported experimentally yet. Experiments conducted by E. Averlant in the K. Panajotov lab at the Vrije Universiteit Brussel with time-delayed feedback do show feedback induced dynamics of LSs, however, the structures do not drift freely but instead show a wiggling or trembling motion on the spot [PT]. This fundamental discrepancy between theoretical and experimental results provided the major motivation for the scope of this work. In the following we introduce a small spatial inhomogeneity to Eq. (3.3), which explicitly breaks the translational symmetry of the system and therefore prevents the mechanism presented above, which is responsible for the onset of drift. We discuss and quantify the effects of the inhomogeneity on LSs and show that the inclusion of the inhomogeneity into the model results in more realistic delay-induced dynamics.

We start our analysis of spatially inhomogeneous systems with the DSHE as presented in Eq. (3.3) with an additional Gaussian injection. The DSHE now reads:

$$\partial_t q(\mathbf{x}, t) = \left(-a_1 \Delta - a_2 \Delta^2 + C \right) q(\mathbf{x}, t) + Y - q(\mathbf{x}, t)^3 + \alpha \left(q(\mathbf{x}, t) - q(\mathbf{x}, t - \tau) \right), \qquad (3.12)$$

with

$$Y = Y_0 + A\exp\left(-\frac{\mathbf{x}^2}{B} \right), \qquad (3.13)$$

where Y represents the injected field which consists of a homogeneous portion Y_0 which corresponds to a plane wave driving the cavity and an additional Gaussian portion defined by the amplitude A and the width $\sqrt{B}$. Throughout the following analysis we leave the width of the Gaussian fixed to $\sqrt{B} = 2$, which is of comparable size as the width of the LS. Altering the width of the Gaussian does not affect the solution structure of Eq. (3.12) qualitatively as long as B is chosen to be within a reasonable range (e.g., comparable to the typical lengthscales of the system given by the wavelength or the width of a LS). We will typically consider the case of small amplitudes A, in which the inhomogeneous injection can either be coincidental due to small inhomogeneities in the otherwise plane wave driving field or it can be implemented artificially, e.g., by using an additional injected beam as in [BTB⁺02]. We decided to analyze the effects of small inhomogeneities in the framework of the SHE, although its applicability to nonlinear optics is limited to the onset of bistability. Nonetheless the SHE provides the advantage of being one of the and most studied equations in pattern formation [CH93], which

allows us to completely focus on the additional effects of the inhomogeneity. Furthermore, the onset of a drift instability in the case of homogeneous injection is paradigmatic and not limited to the case of the SHE, which suggests that our results can be translated to more realistic descriptions of experimental setups.

3.2.1 Linear stability analysis in the presence of inhomogeneities

Starting the investigation of LSs in Eq. (3.12) with direct numerical simulations without time-delay ($\alpha = 0$), the resulting inhomogeneity acts attracting on LSs in its vicinity for positive values of A. Placing a LS close to the center of the inhomogeneity results in a fast drift of the LS towards the center of the inhomogeneity where the solution stabilizes. In contrast, at larger distances to the center of the inhomogeneity, LSs are repelled by the inhomogeneity, which we discuss further in section 3.2.4. The homogeneous solution also is affected by the inhomogeneity as described in [PRGMC13]. In the vicinity of the inhomogeneity, the solution is slightly altered leading to a small dent or bump depending on the sign of A, in the otherwise homogeneous solution. We refer to this solution as quasi-homogeneous, since the local deviation from the homogeneous solution is solely an effect of the locally altered injection.
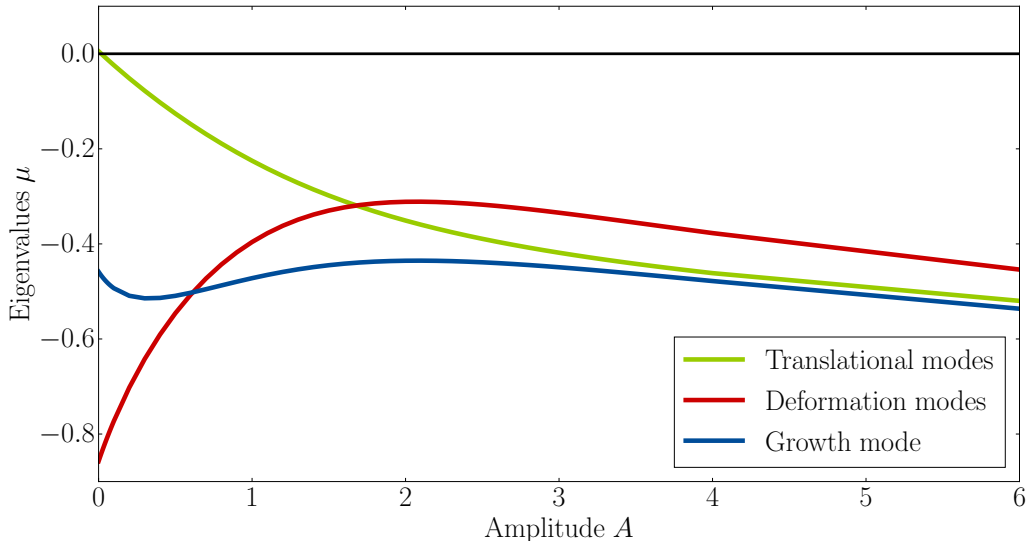

Figure 3.7: Eigenvalues μ of Eq. (3.12) without time-delay ($\alpha = 0$) corresponding to the two drift-inducing modes (green line), the growth-inducing mode (blue line) and the two deformation-inducing modes (red line) for different amplitudes A of the inhomogeneity Y. Remaining parameters are $a_1 = 2.0$, $a_2 = \frac{4}{3}$, $Y_0 = -0.4$, $C = 1.0$. The same figure was used in [Tab14] and was published in [TSTG17].

For now, we perform a linear stability analysis of a single LS resting on the center of an attracting inhomogeneity ($A > 0$). Although the resulting eigenvalues and eigenfunctions change with respect to the homogeneous undelayed case depicted in Fig. 3.5, one can still clearly identify two translational modes, a growth mode and two deformation modes. The resulting eigenvalues depending on the amplitude of the inhomogeneity A are depicted in Fig. 3.7.

The eigenvalue of the translational mode (green line) is drastically lowered with increasing A, which reflects the symmetry breaking effect we aimed for, when introducing the inhomogeneity. Due to the broken translational symmetry for $A \neq 0$, no neutrally stable Goldstone mode exists, the zero eigenvalue from the case $A = 0$ is lowered. This result is rather intuitive and not surprising, since we already described the attracting effect of the inhomogeneity on LSs. The eigenvalue $\mu < 0$ of the translational mode only represents the fact that the LSs is not neutrally stable against translations but any small perturbation in the form of a translation will be suppressed by the attracting inhomogeneity.

Concerning the other discrete eigenvalues of the system, the eigenvalue of the growth mode (blue line) is not strongly affected by the inhomogeneity. In contrast, the eigenvalue of the deformation modes (green line) initially increases, i.e., it becomes less stable compared to the case of homogeneous injection. For large values of $A \approx 2$, the eigenvalue of the deformation modes even represents the highest eigenvalue of the system.

Except for the pinning effect of the inhomogeneity which becomes visible when placing an LS close but not directly on the center of the inhomogeneity, none of the changes of eigenvalues depicted in Fig. 3.5 become apparent in direct numerical simulations. This changes in the presence of destabilizing time-delayed feedback. Time-delayed feedback generates an infinite number of eigenvalues $\lambda_{k,m}$ with $m \in \mathbb{Z}$ for every eigenvalue of the undelayed system. The resulting eigenvalues for given delay parameters α and τ can be calculated using Eq. (3.7). Since we study the destabilization of LSs by time-delayed feedback, only the highest resulting eigenvalue generated by the main branch W_0 of the Lambert W function is relevant. The real parts of these eigenvalues are depicted in Figs. 3.8 and 3.9, showing different scenarios for the destabilization of pinned LSs.

The fact that the eigenvalue of the translational mode is $\mu \neq 0$ poses the most drastic difference to the case of delay-induced dynamics in the homogeneous case. As described in section 3.1.2, Eq. (3.7) typically yields complex eigenvalues $\lambda_{k,m}$. Only in the particular case of $\mu = 0$, the two largest eigenvalues of the delayed system are real-valued. We therefore have to expect complex-valued eigenvalues of the translational modes, which would allow oscillatory dynamics.

The real part of the eigenvalue of the translational mode for $\alpha = 1.1$, $\tau = 1.0$ is depicted in Fig. 3.8 (green line). The eigenvalue is positive for small to moderate values of A and exhibits a sharp kink at the far left of Fig. 3.8. This kink is not an artifact, but a result of the Lambert W function. At this position the eigenvalue of the translational mode goes from real-valued for $A \ll 1$ to complex-valued. In the case depicted in Fig. 3.8, only the eigenvalue of the translational mode is unstable for certain values of A. The eigenvalues of the deformation mode, although close to instability, remain stable.

A different scenario with a larger delay-time $\tau = 5.7$ and a reduced delay-strength is depicted in Fig. 3.9. The eigenvalue of the translational mode is comparable to Fig. 3.8, the eigenvalue of the deformation modes however becomes unstable and for large values A even is the only unstable eigenvalue. Both parameter regimes are just examples for the destabilization by time-delayed feedback, yet other parameter values could be used. In fact, for a given delay time τ one only needs to choose the delay strength sufficiently large to destabilize at least one eigenvalue. However, the analytically calculated stability threshold $\alpha\tau = 1$ (see section 3.1.2) for the translational modes does not hold in the presence of inhomogeneities. The destabilization of the translational modes now requires delay parameters $\alpha\tau > 1$, depending on the amplitude of the inhomogeneity.
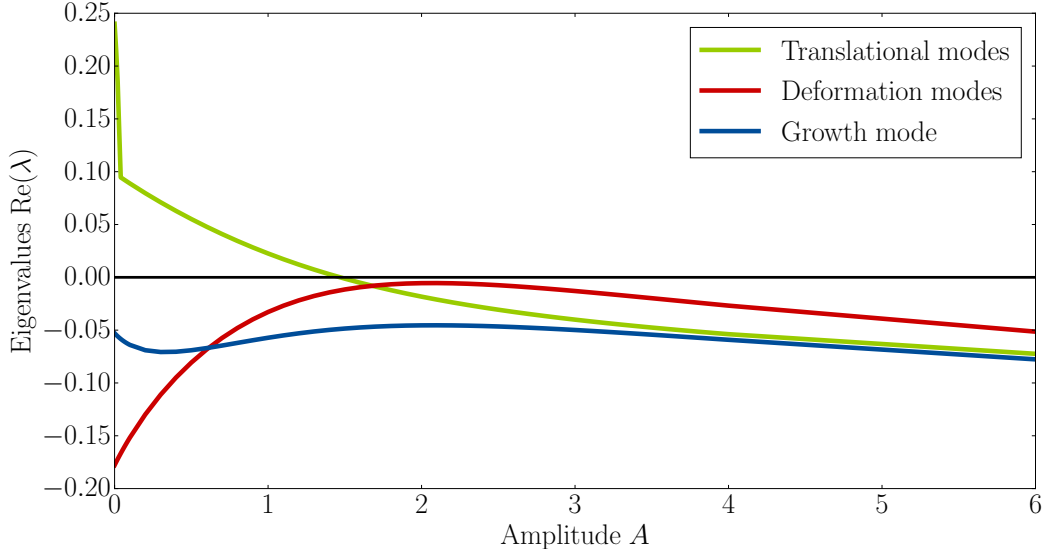
Figure 3.8: Real parts of the eigenvalues $\lambda_{k,0}$ of Eq. (3.12) after linearization in the presence of delay for $\alpha = 1.1$, $\tau = 1$ corresponding to the drift-inducing modes (green line), the growth-inducing mode (blue line) and the deformation-inducing modes (red line) for different amplitudes A of the inhomogeneity Y. For a wide range of different amplitudes A, the translational eigenfunctions are unstable whereas the other localized eigenfunctions are stable. Remaining parameters are $a_1 = 2.0$, $a_2 = \frac{4}{3}$, $Y_0 = -0.4$, $C = 1.0$, $B = 4.0$. The same figure was published in [TSTG17].

3.2.2 Delay-induced oscillations and depinning in the presence of inhomogeneities

In the previous section it was shown that it is possible to destabilize stationary LSs pinned by an inhomogeneity deploying time-delayed feedback. However, solely from a linear stability analysis it is not possible to predict the long term dynamical behavior of the destabilized solution, although the shape of the destabilized eigenmodes might allow a first guess.

We therefore use direct numerical simulations in the parameter regimes which appear to be promising in the linear stability analysis. In the scenario depicted in Fig. 3.9, where the deformation mode is unstable, direct numerical simulations in two spatial dimensions have shown the emergence of a rotating spiral [Tab14, TSTG17]. We are not going to discuss these dynamics further but focus on the regime of small inhomogeneities, where only the translational modes are unstable.

In the following, we fix $\tau = 1.0$ and vary only the delay strength α. However, the dynamics observed can also be induced with a fixed α by choosing τ sufficiently large.

Figure 3.10 depicts the results of two direct numerical simulations in one spatial dimension, for $\tau = 1.0$, and a delay-strength $\alpha > \alpha_{\mathrm{crit1}}$, i.e., sufficiently large to destabilize the eigenvalue of the translational mode. In the top panel, one can clearly recognize the influence of the complex unstable eigenvalue, which does not result in a free drift of the LS, but instead leads to an LS oscillating in position. At the onset of instability, the frequency of the oscillation coincides with the imaginary part of the unstable eigenvalue as can be seen in Fig. 3.11.
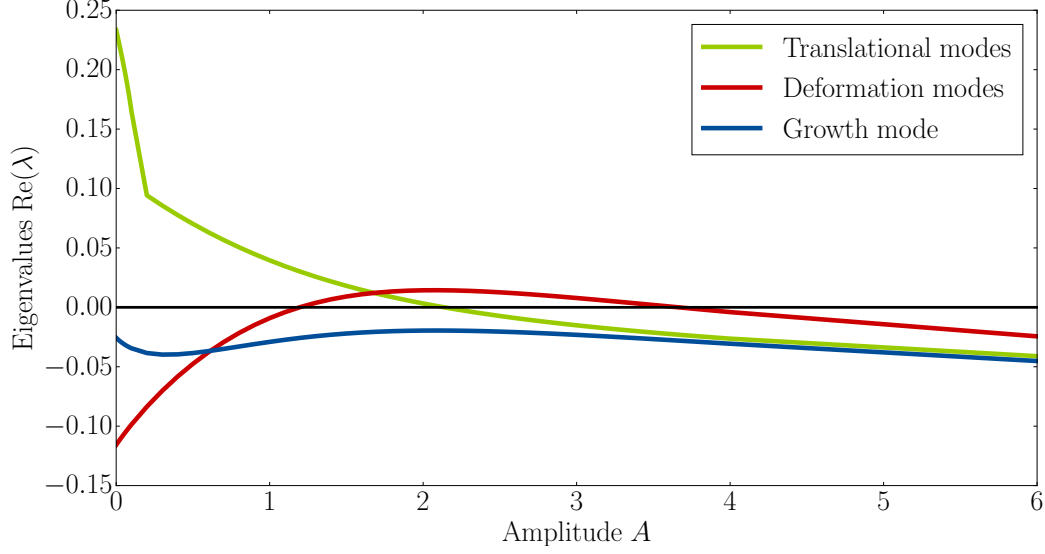
Figure 3.9: Real parts of the eigenvalues $\lambda_{k,0}$ of Eq. (3.12) after linearization in the presence
of delay for $\alpha = 0.31$, $\tau = 5.7$ corresponding to the drift-inducing modes (green
line), the growth-inducing mode (blue line) and the deformation-inducing modes
(red line) for different amplitudes A of the inhomogeneity Y. Depending on the
choice of the amplitude A, either an instability of the translational eigenfunctions,
both the translational and deformation modes, or only the deformation modes is
induced. Other parameters are $a_1 = 2.0$, $a_2 = \frac{4}{3}$, $Y_0 = -0.4$, $C = 1.0$, $B = 4.0$.
The same figure was published in [TSTG17].

The oscillation of the LS can be interpreted as the interplay of destabilizing time delay
and pinning inhomogeneity. The unstable translational mode competes with the attracting
inhomogeneity resulting in the observed oscillation. Above the threshold of instability $\alpha > \alpha_{\text{crit1}}$,
increasing the delay strength α leads to a growing amplitude of the oscillation. However, the
growth of the amplitude is limited, as at a certain value α_{crit2} the amplitude is large enough for
the LS to depin from the inhomogeneity and to start to drift freely. Depending on how large
the delay-parameters are, the LS either depins directly or oscillates around the inhomogeneity
a few times before depinning, as depicted in the bottom panel of Fig. 3.10.

The induced dynamics do not change qualitatively in two spatial dimensions [Tab14, TSTG17].
In this case, the LS starts to oscillate in two spatial directions, which results in a wiggling
motion around the inhomogeneity, since the two oscillations do not have a fixed phase dif-
ference. The depinning in two spatial dimensions results in a drift with constant velocity
in an arbitrary direction. We confine ourselves to the analysis of the one-dimensional case,
since one-dimensional simulations require less computational effort, thus allowing a far better
systematical comparison of direct numerical results and the semi-analytical approaches we are
going to discuss in the following sections. Examples of direct numerical simulations in two
dimensions can be found in [Tab14, TSTG17].

The transition from resting to oscillating LS at α_{crit1} can be understood and accurately
described in the framework of a linear stability analysis of the stationary solution. Yet to
further analyze the depinning process, i.e., the transformation from an oscillating to a drifting
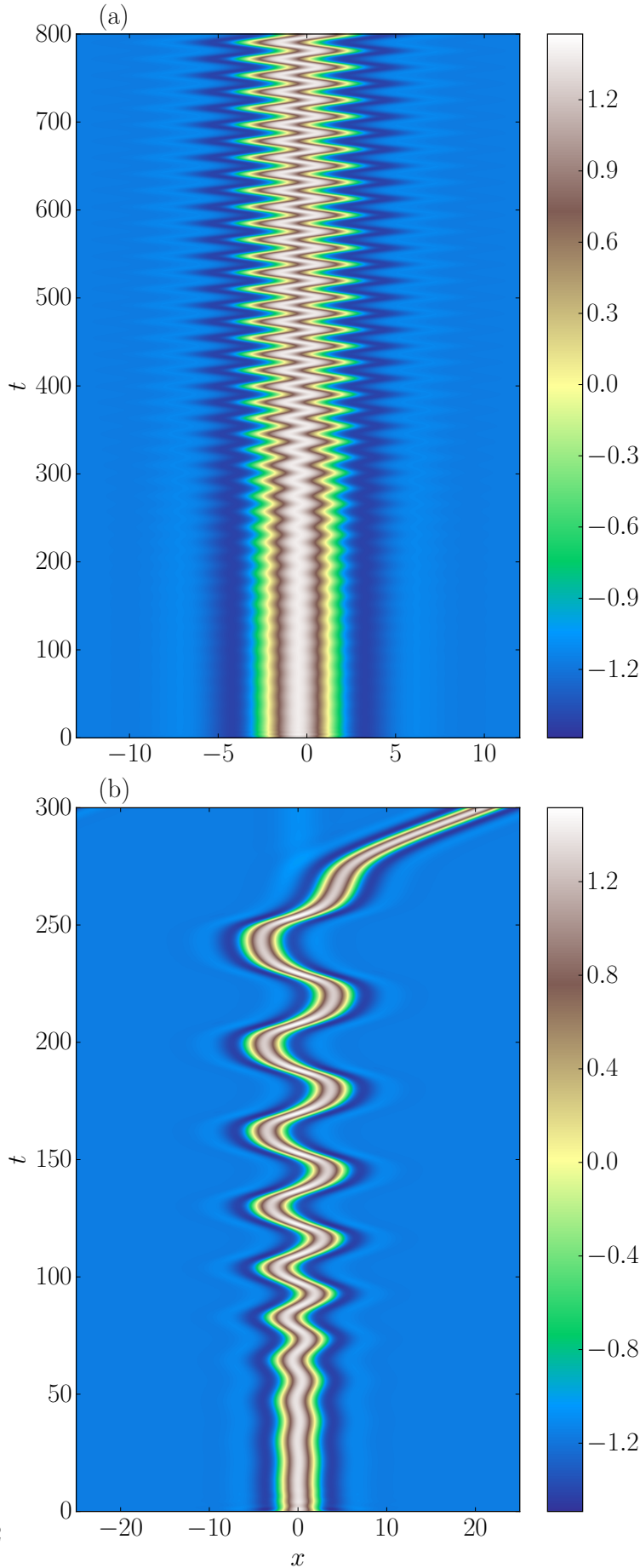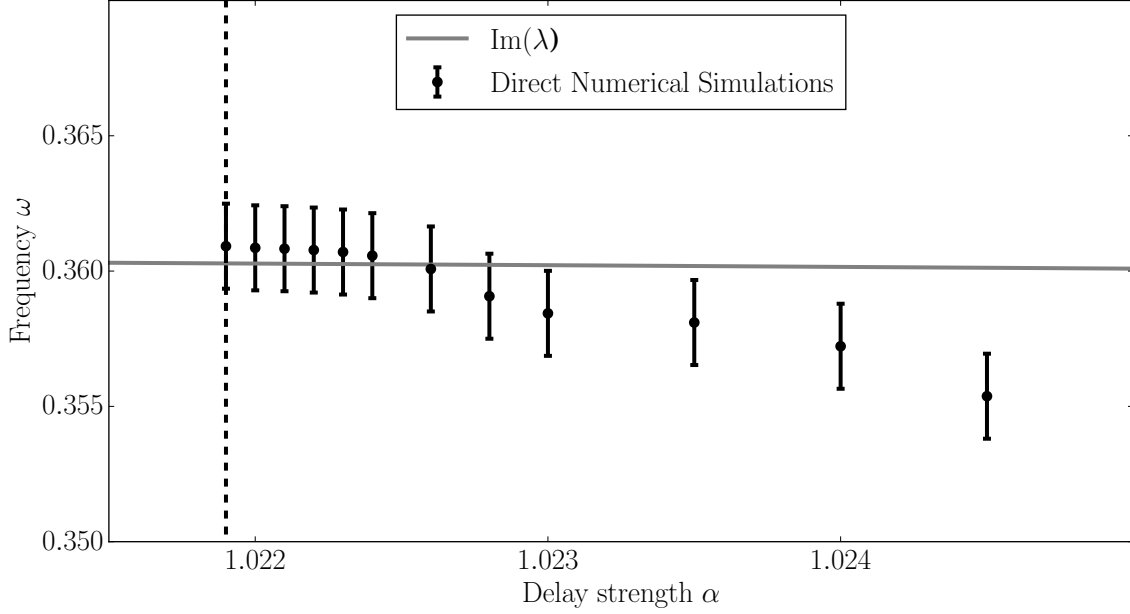
Figure 3.10: Direct numerical simulations in one dimension with a fixed delay-time $\tau = 1$.

Top panel: A localized solution oscillates around the inhomogeneity for $\alpha = 1.035$. Bottom panel: A localized structure depins from the inhomogeneity and starts to drift freely for $\alpha = 1.073$. The amplitude of the inhomogeneity is fixed to $A = 0.2$. Remaining parameters are: $a_1 = 2.0$, $a_2 = \frac{4}{3}$, $Y_0 = -0.4$, $C = 1.0$, $B = 4.0$. The same figure was published in [TSTG17].

Figure 3.11: Frequency ω of the oscillations of the localized structure around the inhomogene-
ity obtained from direct numerical simulations in one dimension for $\tau = 1.0$ and
varying values of α. The dashed line marks the onset of instability, while the
gray solid line depicts the imaginary part of the eigenvalue corresponding to the
unstable translational mode. The frequency of the oscillations coincides with
the imaginary part of the unstable eigenmode in the vicinity of the bifurcation
point but deviates from the eigenvalue when α is increased. The error bars of
the frequencies are given by $\Delta\omega = \frac{2\pi}{\Delta t}$, where Δt is the sampling time of the
simulation. Remaining parameters are $a_1 = 2.0$, $a_2 = \frac{4}{3}$, $Y_0 = -0.4$, $C = 1.0$.
The same figure was published in [TSTG17].

LS at α_{crit2}, the linear stability analysis does not suffice. To this aim, a numerical parameter
continuation using DDE-BIFTOOL [ELR02] was presented in [TSTG17] (see Fig. 3.12), using
the delay strength α as a continuation parameter and the period time T of the oscillatory
solution as a solution measure.

Following the time-periodic orbit and calculating the Floquet multipliers μ_F, the periodic
solution is stable (Fig. 3.12, black line, $\mu_F < 1$) until it collides with an unstable periodic
orbit (red dotted line, $\mu_F > 1$) and vanishes at α_{crit2} in a saddle node bifurcation of a periodic
orbit. This critical value α_{crit2} marking the onset of the depinning motion coincides with the
value obtained from direct numerical simulations. Although these results from the numerical
continuation of a PDE system are promising, one has to acknowledge, that DDE-BIFTOOL
was originally designed to treat systems of delayed ODEs and already reaches its limits when
treating a single order parameter PDE in one spatial dimension on a relatively small domain of
$L = 32$. The spatial discretization for Fig. 3.12 was performed manually using finite differences
with a discretization of $N = 64$. To analyze larger domains, two-dimensional systems or more
complex PDE systems with more than one order parameter, one has to deploy other semi-
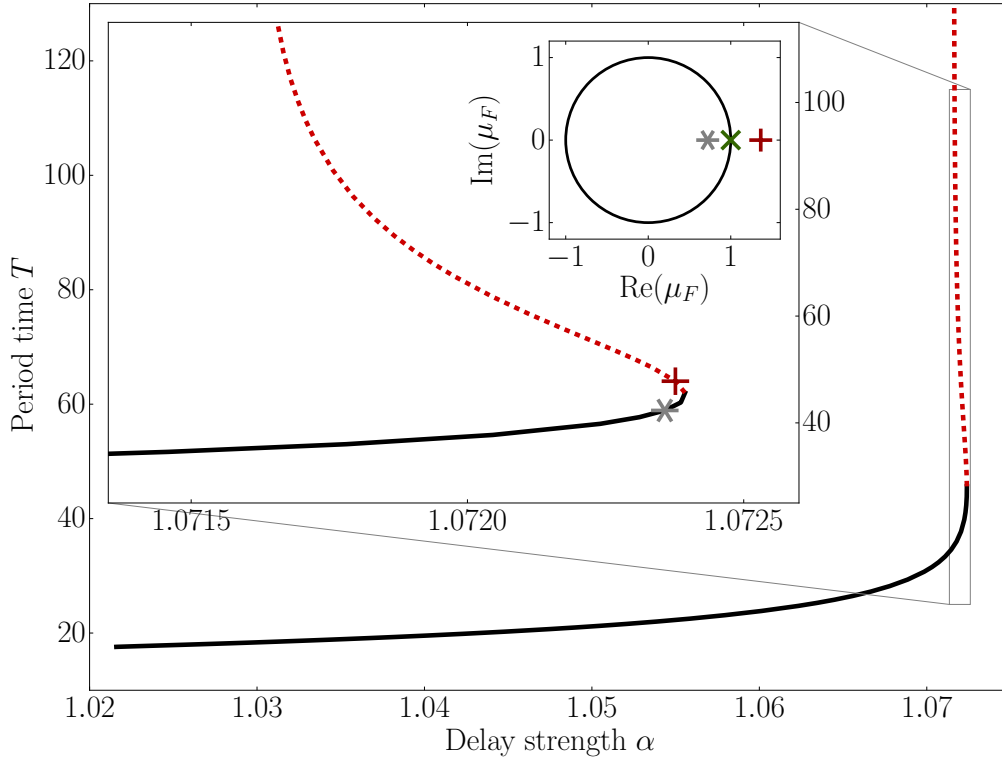analytic methods to simplify the system under consideration. Two possible approaches are

Figure 3.12: Period time T of the oscillatory solution depending on the delay strength α obtained by numerical continuation using DDE-BIFTOOL. The zoomed in version shows the parameter region in the vicinity of the bifurcation point α_{crit2}, where the saddle-node bifurcation of limit cycles sets in. The small box at the top shows the Floquet multipliers μ_F of the stable (black solid line, $*$) and the unstable (red dotted line, $+$) periodic branch at the marked positions. Other parameters are $\tau = 1.0$, $a_1 = 2.0$, $a_2 = \frac{4}{3}$, $Y_0 = -0.4$, $C = 1.0$. The figure was already published in [TSTG17]. The numerical continuation was performed as part of a cooperation by the second author Christian Schelte.

going to be presented in the next sections.

3.2.3 Derivation of an order parameter equation for the onset of instability

In this section we present the derivation of on order parameter equation describing the transition from resting LSs to oscillating LSs at α_{crit1}. For the sake of simplicity, we restrict the analysis to a one-dimensional system. However the approach (and the one presented in the next section) can be easily generalized to more than one dimension and may also be applied to other inhomogeneous systems.

As a first approach we use an Ansatz similar to [Gur14], that describes the solution of the

system as the stationary solution $q_0(\mathbf{x})$ with an additional oscillation in the spatial form of the translational eigenmode $\varphi(\mathbf{x})$:

$$q(\mathbf{x}, t) = q_0(\mathbf{x}) + \tilde{q}(\mathbf{x}, t) = q_0(\mathbf{x}) + \xi(t)\varphi(\mathbf{x})\mathrm{e}^{\mathrm{i}\omega t} + \overline{\xi}(t)\varphi(\mathbf{x})\mathrm{e}^{-\mathrm{i}\omega t} + \xi_0(\mathbf{x}, t), \qquad (3.14)$$

where $\xi(t)$ is a complex valued order parameter, $\overline{\xi}(t)$ is its complex conjugate, $\omega = \mathrm{Im}(\lambda_0)$ is the frequency of the oscillation given by the imaginary part of the eigenvalue λ_0 of the translational mode with delay and $\xi_0(\mathbf{x}, t)$ accounts for further contributions of stable eigenmodes.

Inserting the Ansatz (3.14) into equation (3.12) and collecting only the terms of $\mathcal{O}\left(\mathrm{e}^{\mathrm{i}\omega t}\right)$ leads to:

$$\dot{\xi}\varphi + \mathrm{i}\omega\xi\varphi = \xi\mathfrak{L}'\varphi + \xi\mathfrak{L}''\xi_0\varphi + \frac{1}{2}|\xi|^2\xi\mathfrak{L}'''\varphi\varphi\varphi + \alpha\left(\xi(t) - \xi(t-\tau)e^{-\mathrm{i}\omega\tau}\right)\varphi, \qquad (3.15)$$

where $\mathfrak{L}^{(n)}$ denotes the nth Fréchet derivative of the nonlinear right hand side of equation (3.12) without the delayed terms.

To estimate $\xi_0(\mathbf{x}, t)$, we collect only the non-oscillating terms:

$$\dot{\xi}_0 = \mathfrak{L}'\xi_0 + |\xi|^2\mathfrak{L}''\varphi\varphi, \qquad (3.16)$$

where time-delayed feedback has been neglected following [Gur14]. Assuming that $\xi_0(t)$ changes rapidly in time compared to the order parameter $\xi(t)$, one can adiabatically eliminate the time evolution of ξ_0, which leads to:

$$\mathfrak{L}'X_0 = -\mathfrak{L}''\varphi\varphi, \qquad (3.17)$$

where $\xi_0 = X_0|\xi|^2$ has been introduced. X_0 can be calculated by numerically inverting $\mathfrak{L}'$, i.e., by solving equation (3.17). Inserting the solution for ξ_0 and projecting onto $\langle\varphi|$ finally yields the order parameter equation:

$$\dot{\xi} = (\mu - \mathrm{i}\omega)\xi + b|\xi|^2\xi + \alpha\left(\xi(t) - \xi(t-\tau)e^{-\mathrm{i}\omega\tau}\right), \qquad (3.18)$$

where μ is the eigenvalue of $\mathfrak{L}'$ corresponding to the eigenfunction φ and

$$b = \frac{\langle\varphi|\mathfrak{L}''X_0\varphi\rangle}{\langle\varphi|\varphi\rangle} + \frac{1}{2}\frac{\langle\varphi|\mathfrak{L}'''\varphi\varphi\varphi\rangle}{\langle\varphi|\varphi\rangle}. \qquad (3.19)$$

The notation $\langle.|.\rangle$ stands for the scalar product defined by integration over the full domain. Without time-delay, equation (3.18) takes the normal form of an Andronov-Hopf bifurcation. Since $b < 0$, the bifurcation is supercritical. Without time-delay, the system is below the bifurcation point due to $\mu < 0$. Therefore, without the delay as well as for sufficiently small choices of α, the stable solution of equation (3.18) is $\xi = 0$ corresponding to a stable solution $q(\mathbf{x}, t) = q_0(\mathbf{x})$. For larger values of α the complex order parameter ξ starts to oscillate between its real and imaginary part with a constant amplitude $|\xi|$. One can calculate the resulting maximum shift, i.e., the amplitude $R_{\max}$ of the oscillation of the localized structure, by evaluating the Ansatz given by Eq. (3.14):

$$q(\mathbf{x}, t) = q_0(\mathbf{x}) + |\xi|\varphi(\mathbf{x}) + X_0|\xi|^2. \qquad (3.20)$$

The shift of the maximum of $q(\mathbf{x}, t)$ compared to the maximum of $q_0(\mathbf{x})$ yields the amplitude of the oscillations $R_{\max}$.

Solving equation (3.18) numerically with a classical Runge-Kutta method for different values of α, one can compare the maximum shift resulting from equation (3.20) with the amplitude of the oscillations in the full model (3.12) obtained by direct numerical simulations. As can be seen in Fig. 3.13, the order parameter model bifurcates at α_{crit1}, i.e., the approximations made for the derivation of the order parameter equation seem to be justified in the direct vicinity of the bifurcation point. However, for larger values of α, the model quickly looses its validity and a significant difference between the direct numerical simulations and the order parameter model can be observed. In the next section we are going to present a different approach which captures both the onset of oscillations as well as the depinning behavior of the LSs while also being quantitatively more accurate.
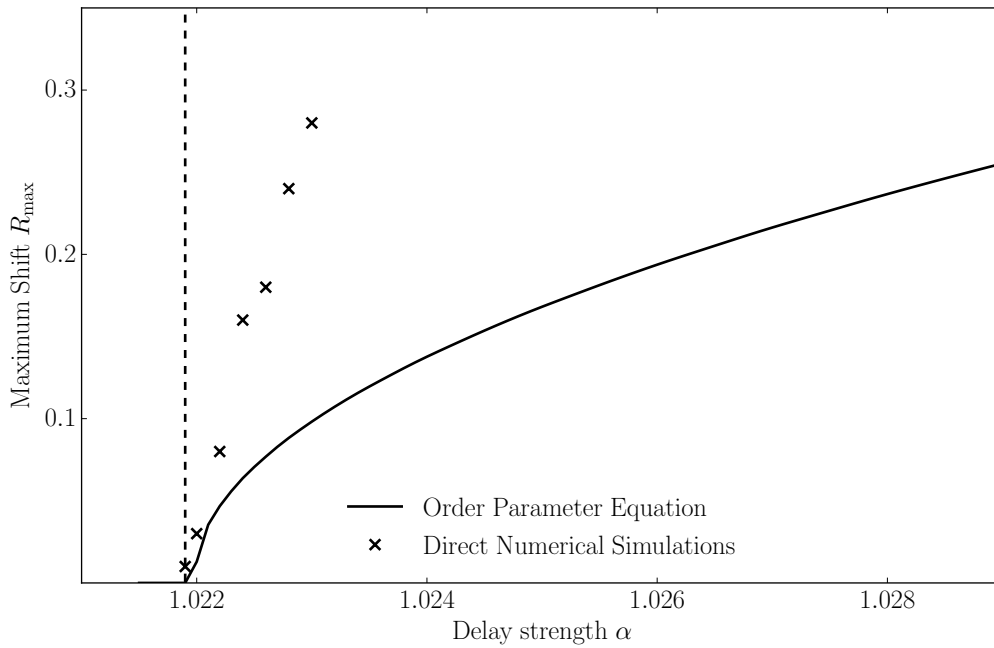
Figure 3.13: Maximum amplitude of the oscillations R_{max} in dependence of the delay strength α obtained by direct numerical simulations (crosses) of the full model (3.12) and by the order parameter model (3.18) (black solid line). The dashed line marks the first Hopf bifurcation point $\alpha_{\mathrm{crit}} = 1.0219$ found both in the direct numerical simulations and in the order parameter model. However, Eq. 3.13 is only valid in the direct vicinity of α_{crit} and looses its validity for increasing delay strengths. Remaining parameters are $\tau = 1.0$, $a_1 = 2.0$, $a_2 = \frac{4}{3}$, $Y_0 = -0.4$, $C = 1.0$. The figure was already published in [TSTG17].

3.2.4 Modeling oscillating and depinning LSs as particles in a potential well

The main idea of the second approach is to describe the oscillations occurring after the bifurcation at α_{crit1} as the overdamped dynamics of a particle in a potential well generated by the inhomogeneity, where the time-delayed feedback acts as a driving force. We therefore decompose the right hand side of Eq. (3.12) into an inhomogeneous part $\mathbf{N}_{\mathrm{inh}}$ containing the

inhomogeneity, a delay part containing the time-delayed terms and a homogeneous part $\mathbf{N}_{\text{hom}}$ containing all other terms, i.e.:

$$\partial_t q(\mathbf{x}, t) = \mathbf{N}_{\text{hom}}[q] + \mathbf{N}_{\text{inh}}[\mathbf{x}] + \alpha(q(\mathbf{x}, t) - q(\mathbf{x}, t - \tau)). \tag{3.21}$$

We assume the solution $q(\mathbf{x}, t)$ to be constant in shape, i.e., we neglect shape deformations due to the oscillation:

$$q(\mathbf{x}, t) = q_0(\mathbf{x} - R(t)) = q_{0\text{h}}(\mathbf{x} - R(t)) + w(\mathbf{x} - R(t)), \tag{3.22}$$

where q_0 is the stationary solution of the inhomogeneous system, $q_{0\text{h}}$ is the stationary solution of the homogeneous system, w is the difference between the LS with and without inhomogeneity and $R(t)$ is the position of the center of the LS relative to the center of the inhomogeneity. The goal is, to derive an ordinary differential equation that describes the time evolution of $R(t)$.

Inserting the Ansatz 3.22 into equation (3.23) yields:

$$-\dot{R}(t)\partial_x q_0(\mathbf{x} - R(t)) = \mathbf{N}_{\text{hom}}[q_0(\mathbf{x} - R(t))] + \mathbf{N}_{\text{inh}}[\mathbf{x}] + \alpha\left(q_0(\mathbf{x} - R(t)) - q_0(\mathbf{x} - R(t - \tau))\right), \tag{3.23}$$

Expanding $\mathbf{N}_{\text{hom}}[q_0(\mathbf{x} - R(t))]$ around $q_{0\text{h}}(\mathbf{x} - R(t))$ results in:

$$\mathbf{N}_{\text{hom}}[q_0] = \mathbf{N}_{\text{hom}}[q_{0\text{h}}] + \mathfrak{L}'[q_{0\text{h}}]w + \frac{1}{2}\mathfrak{L}''[q_{0\text{h}}]ww + \frac{1}{6}\mathfrak{L}'''[q_{0\text{h}}]www. \tag{3.24}$$

Looking at equation (3.24) one can easily verify, that $\langle \varphi_G(\mathbf{x} - R(t)) | \mathbf{N}_{\text{hom}}[q_0(\mathbf{x} - R(t))] \rangle = 0$, where φ_G is the translational mode of the homogeneous system, i.e., a Goldstone mode. The contributions of $\mathbf{N}_{\text{hom}}[q_{0\text{h}}]$ vanish, because $q_{0\text{h}}$ is a stationary solution of the homogeneous system. The linear term in w vanishes, because $\mathfrak{L}'$ is a self-adjoint operator and the eigenvalue corresponding to φ_G is $\mu = 0$. The quadratic and cubic terms vanish, because even and odd functions are multiplied and integrated over the full domain.

Projecting $\langle \varphi_G(\mathbf{x} - R(t)) |$ onto Eq. (3.23) therefore leads to:

$$\dot{R}(t) = \frac{-1}{\langle \varphi_G(\mathbf{x}) | \partial_x q_0(\mathbf{x}) \rangle} \left(\langle \varphi_G(\mathbf{x}) | \mathbf{N}_{\text{inh}}[\mathbf{x} + R(t)] \rangle - \alpha \langle \varphi_G(\mathbf{x}) | q_0\left(\mathbf{x} + R(t) - R(t - \tau)\right) \rangle \right). \tag{3.25}$$

The first term on the right hand side of Eq. (3.25) yields a function $F(R)$ that can be interpreted as the attracting force of the inhomogeneity acting on the localized structure. Figure 3.14 depicts the potential well $V(R)$ of the inhomogeneity, which is defined by: $-\partial_R V(R) = F(R)$.

Without time-delayed feedback, the potential $V(R)$ can also be used to estimate the basin of attraction of the inhomogeneity. Placing a LS in the direct vicinity of the inhomogeneity leads to the structure being pulled to the minimum of the potential at $R = 0$. A solution at the center of the inhomogeneity ($R = 0$) is stationary, since all integrals necessary for the calculation of $F(R)$ vanish for $R = 0$. However, the potential also has two maxima in the periphery of the inhomogeneity, i.e., for larger values of R, the potential also acts repelling on the LSs. These results are in good agreement with the behavior of localized structures observed in direct numerical simulations, which we briefly discussed in section 3.2.1.

With time-delayed feedback ($\alpha \neq 0$), the stable solution $R = 0$ is destabilized for large enough values of α leading to an oscillation in the potential well, where the time-delayed feedback acts as a driving force. Solving Eq. (3.25) with a classical Runge-Kutta method yields
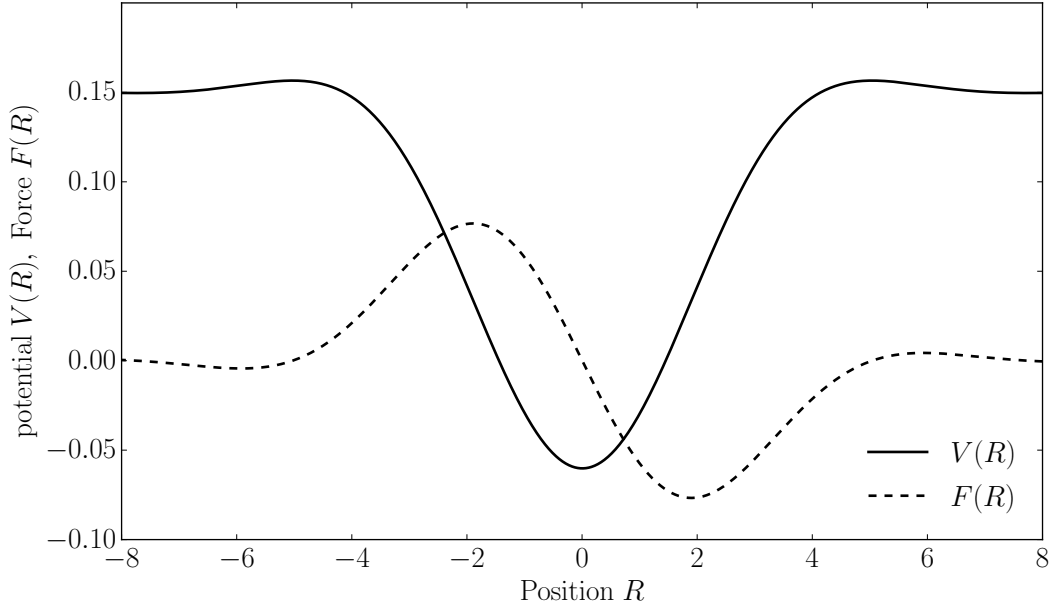
Figure 3.14: Potential well $V(R)$ and attracting force $F(R)$ of an inhomogeneity Y calculated numerically for $A = 0.2$, $B = 4.0$. Remaining parameters are $\tau = 1.0$, $a_1 = 2.0$, $a_2 = \frac{4}{3}$, $Y_0 = -0.4$, $C = 1.0$. The figure was already published in [TSTG17].

oscillatory dynamics of $R(t)$ which are depicted in Fig. 3.15. With increasing delay-strength α the oscillations grow in amplitude until they escape the potential well, which is in qualitative accordance with the results obtained in direct numerical simulations of the full model (3.12) described in section 3.2.2.

For a quantitative assessment of the potential well model we consider the maximum amplitude of these oscillations, which we shall denote as $R_{\max}$ since this value corresponds to the shift obtained by the first approach. Figure 3.16 contains a comparison between $R_{\max}$ from the potential well model and the results obtained from direct numerical simulations of the full system (3.12). As can be seen, the first bifurcation in the potential well model occurs at α_{crit1}, i.e., at the value expected from linear stability analysis. The predictions from the potential well model are accurate throughout most of the parameter regime, where oscillations occur. Only close to the secondary instability at α_{crit2}, where the LS depins from the inhomogeneity, notable differences between the potential well model and the direct numerical results can be observed. These differences can be attributed to the deformation of the LS which is neglected in the potential well approach. The approach still reproduces the depinning, i.e., the escape of the overdamped particle from the potential well due to a large driving force induced by time-delayed feedback. However, this secondary instability occurs at a value of $\alpha = 1.079$, which is slightly larger than the expected value $\alpha_{\mathrm{crit2}} = 1.072$.

The potential well model qualitatively describes the behavior of the localized structure in the complete parameter regime, including the first and the secondary instability. It is also quantitatively accurate for most values of α that are not too close to the secondary instability at α_{crit2}. The order parameter equation presented in section 3.2.3 only reproduces the behavior of the system in a small vicinity of the bifurcation point at α_{crit1} and is less accurate throughout

the rest of the parameter regime. However, due to the form of equation (3.18), it provides a better understanding of the occurring Andronov-Hopf instability. In contrast, the potential well model proofed to be a very useful approach, enabling us to reduce the full delayed PDE model to a more intuitive and numerically less expensive model which is however still quantitatively accurate throughout most of the parameter regime exhibiting oscillations. Furthermore, the potential well approach appears to be a suitable way to treat small inhomogeneities in general, which is why we also apply it in the following chapter.
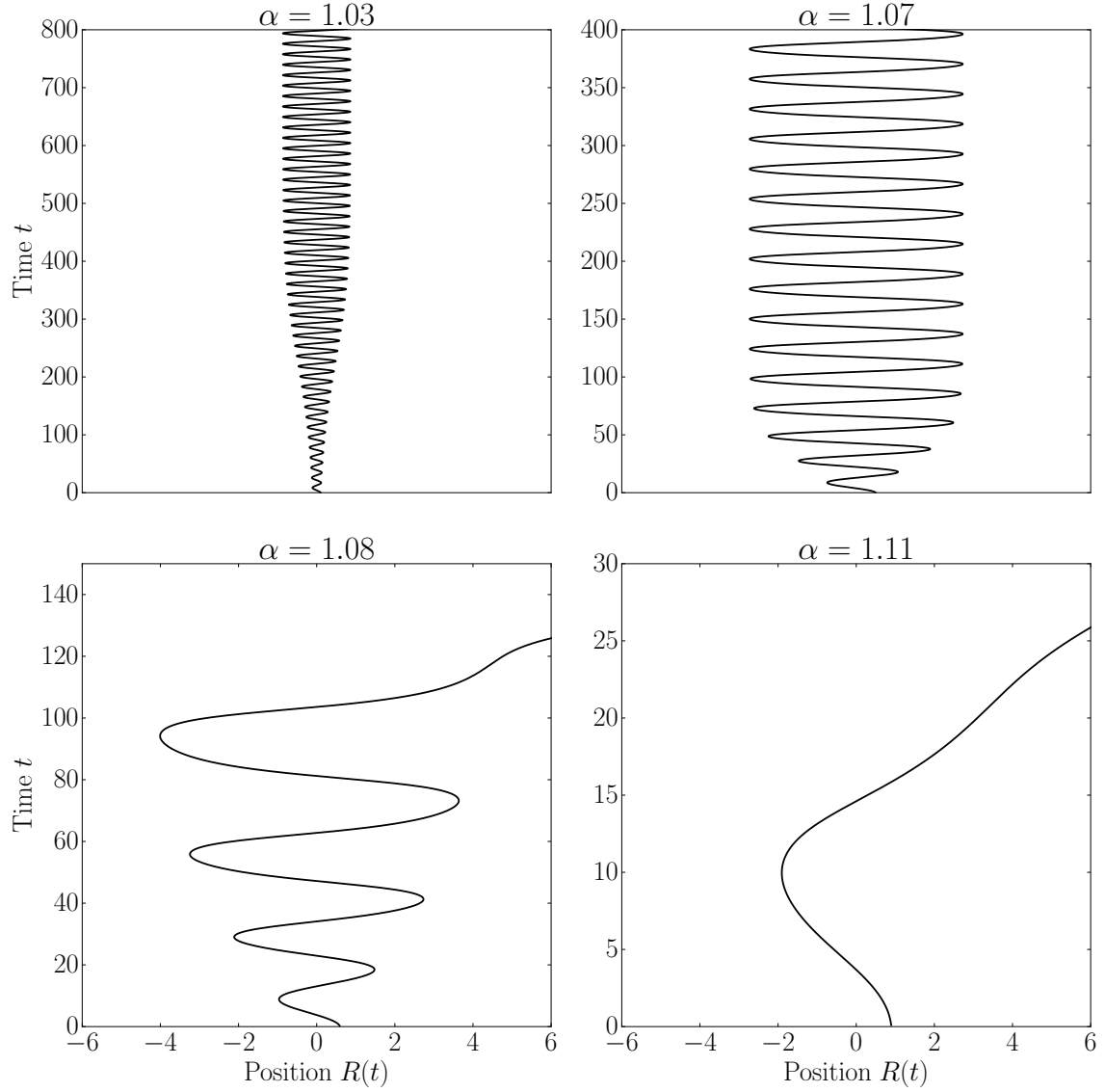
Figure 3.15: Time evolution of the position R of the LS obtained by numerically solving Eq. 3.25 for increasing values of α. Choosing the delay strength just above the critical value $\alpha_{crit1} = 1.0219$ induces an oscillation of the position of small amplitude (top left panel, $\alpha = 1.03$). With increasing delay strength the maximum amplitude of the oscillations increases and the maximum amplitude is reached faster (top right panel, $\alpha = 1.07$). When further increasing the delay strength the amplitude of the oscillations grows large enough for the LS to escape the potential well (bottom left panel, $\alpha = 1.08$. Even larger values of α accelerate the depinning process (bottom right panel, $\alpha = 1.11$). The potential well approach qualitatively captures the dynamics obtained in simulations of the full model (3.12) described in section 3.2.2. A quantitative comparison between the full and the reduced model is shown in Fig. 3.16. The results are obtained for an inhomogeneity of $A = 0.2$, $B = 4.0$ and the delay-time is $\tau = 1.0$ in all simulations.
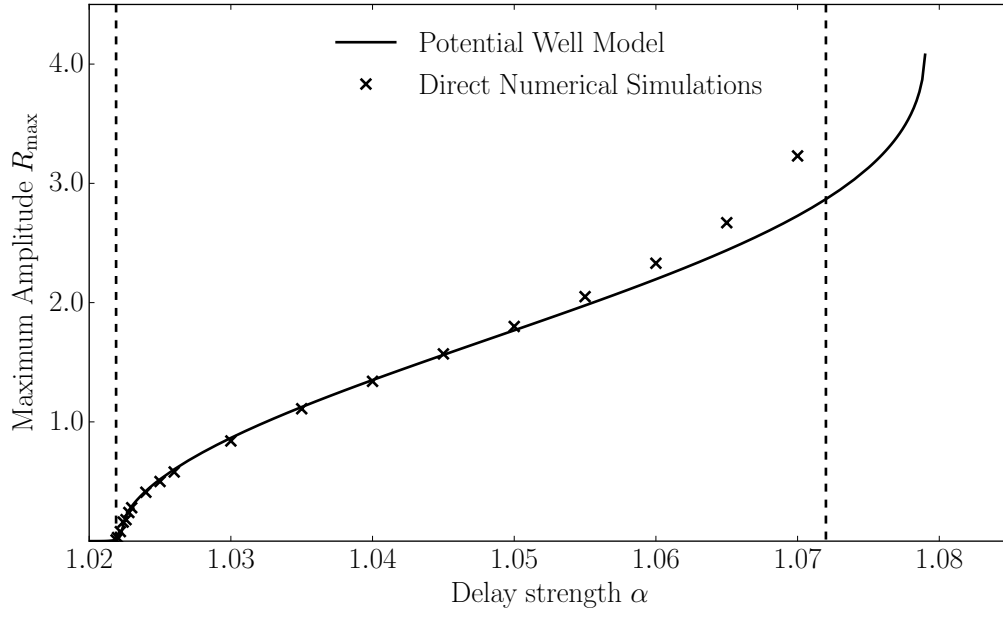
Figure 3.16: Maximum amplitude of the oscillations R_{max} in dependence of the delay strength α obtained by direct numerical simulations (crosses) and by the potential well model (black line). The dotted lines mark the two bifurcation points in the direct numerical simulations. The first bifurcation leading to an oscillation of the structure appears at the same value $\alpha_{crit1} = 1.0219$ in the direct numerical simulations and in the potential well model, respectively. The depinning instability occurs in the potential well model at $\alpha > \alpha_{crit2}$, i.e., for a larger delay strength than in the direct numerical simulations. Remaining parameters are $A = 0.2$, $B = 4.0$, $\tau = 1.0$, $a_1 = 2.0$, $a_2 = \frac{4}{3}$, $Y_0 = -0.4$, $C = 1.0$. The figure was already published in [TSTG17].

4 Analysis of the inhomogeneous Lugiato-Lefever Equation

In this chapter, we analyze the Lugiato-Lefever equation (LLE) with and without inhomogeneous injection. A special focus again lies on the formation of localized solutions (LSs). Although the LLE was proposed in 1987 [LL87] and has been intensively studied since, the formation of LSs has sparked new interest only recently, when it was shown that the frequency spectrum of a LS in the temporal LLE serves as a frequency comb [CRSE13]. The direct link between frequency Kerr combs (KCs) and LS will be briefly discussed in Sec. 4.1.3 and can be seen as additional motivation to investigate the formation of LSs.

In the following, we start with an analysis of the homogeneous, periodic and localized stationary solutions in the classical LLE with homogeneous injection, where we mostly summarize previous results but also add some new results concerning the formation of periodic patterns and especially the formation of LSs in regions of high detuning.

We then proceed with the introduction of an inhomogeneous injection. The LLE under the influence of inhomogeneous injection has been studied, e.g., by Hendry et al. [HCW$^+$18], where an injected beam in the form of a Gaussian was assumed, showing that LSs in this setup are not necessarily drawn towards minima or maxima of the injection but instead to certain ideal values of injection. We implement these findings in our studies of the LLE. In contrast to [HCW$^+$18], we do not assume completely Gaussian injection but as in chapter 3 a homogeneous injection with an added Gaussian inhomogeneity of smaller amplitude, which serves as a first simplified model for small inhomogeneities occurring involuntarily in the system. However, as we demonstrate in section 4.2, these small inhomogeneities can provide certain benefits for the creation of LSs, which suggests that the intentional implementation of small inhomogeneities can proof useful for applications.

The analysis of inhomogeneities in the LLE is first performed in two different parameter regimes defined by different values of the detuning, namely the regime of homoclinic snaking and the regime of foliated snaking. While the influence of inhomogeneous injection in the first regime is straight forward, the effects of an inhomogeneity in the latter regime are far more complex. We analyze these effects in terms of bifurcation theory, showing that a given inhomogeneity can act attracting or repelling on LSs depending on other system parameters. Furthermore we apply the potential well model first described in chapter 3 and close this section with a comparison of the full region of stability of LSs with and without inhomogeneities.

In the final section of this chapter we investigate time-delayed feedback starting with the classical LLE without inhomogeneities. We discuss the destabilization of stable LSs and analyze the eigenfunctions responsible for the onset of dynamics. The stabilization of unstable LSs by time-delayed feedback will be briefly discussed too, showing that it is possible to stabilize unstable complex eigenvalues depending on the choice of delay parameters. We then proceed with the study of the competing effects of inhomogeneities and destabilizing time-delay emphasizing similarities and differences to the Swift-Hohenberg equation discussed in the previous chapter. Finally we present some preliminary results on inhomogeneities in the

detuning in the presence of time-delayed feedback, showing that the induced dynamics are much more complex including intermittent behavior where an LSs goes from oscillations to free drift and back to oscillations erratically. However, this section only serves as a motivation for further investigations.

4.1 The Classical Lugiato-Lefever model

The classical LLE as proposed by Luigi Lugiato and René Lefever in 1987 [LL87] describes the evolution of the envelope $E(\xi, t)$ of an electrical field. The resulting PDE reads:

$$\frac{\partial E(\xi, t)}{\partial t} = E_i + \left[-(1 + i\theta) + i|E(\xi, t)|^2 + i\frac{\partial^2}{\partial \xi^2} \right] E(\xi, t). \tag{4.1}$$

As suggested in Chapter 2, where Eq. (4.1) has been derived in two different ways, the LLE allows different interpretations: Originally it was intended as a paradigmatic simplified model for pattern formation in the transverse plane of an optically pumped cavity filled with a nonlinear optical medium. The nonlinearity can either stem from a two-level system pumped in the off-resonant case of large atomic detuning (cf. chapter 2.2), where nonlinear effects are mostly due to the optical Kerr effect [LPB15], or the nonlinearity can stem from a non-excitable medium that purely exhibits a strong optical Kerr-effect leading to a cubic nonlinearity. The LLE in this interpretation can be seen as a dissipative version of the nonlinear Schrödinger equation with additional detuning [LPGK18]. In this case, the longitudinal direction in the cavity is neglected, the variable ξ represents the spatial coordinate (in 1d) or a set of two spatial coordinates (in 2d) in the transverse plane of the cavity. In this case, the second derivative in ξ represents the diffraction inside the cavity. The time is represented by t.

In a different scenario Haeltermann et al. derived a longitudinal or temporal version of the LLE [HTW92] as described in Chapter 2. Starting point of the derivation in this case is the nonlinear Schrödinger equation. By considering a ring-fiber it is possible to neglect all transversal effects in the material, i.e., realizing a truly one-dimensional dynamic. The authors furthermore restrict the derivation to the case of a high finesse cavity. In this case the dissipative effects (i.e., loss and input) in a single round-trip are comparably small and the evolution of the electrical field-amplitude develops over many round-trips. This allows to go from a discrete number of round-trips to a quasi-continuous slow-time t. Whereas t represents the slow time variable, ξ is in this case a fast time variable. This fast time describes the evolution of the shape of the pattern in the cavity ring, whilst t describes the temporal evolution over many round-trips In this interpretation, the second derivative in ξ no longer represents diffraction but the group velocity dispersion [LPGK18].

Both the transversal and the temporal (or longitudinal) form of the LLE have mathematically the same form. We will therefore not restrict ourselves to one specific case in the following. For the sake of clarity we will refer to t as time and to ξ as the spatial coordinate, bearing in mind, that it can also take the form of a fast time.

In both cases, the parameters are the amplitude of the injected field E_i and the detuning θ. In the original LLE that has been thoroughly studied for many years, both parameters are assumed to be independent of ξ, i.e., constant in space or the fast time respectively. In the following we summarize a few properties of the classical LLE that are of importance for this work. Subsequently, we discuss the emergence of LSs in the classical LLE before we proceed with the consideration of inhomogeneous injection, inhomogeneous detuning and time-delayed feedback.

4.1.1 Homogeneous Solutions of the Lugiato-Lefever Equation

Without inhomogeneities, the LLE possesses homogeneous stationary solutions E_{hs}, which can be easily calculated by setting the spatial and temporal derivatives in Eq. (4.1) to zero. This yields the implicit expression:

$$|E_{\mathrm{i}}|^2 = |E_{hs}|^2 \left(1 + (\theta - |E_{hs}|^2)^2\right), \tag{4.2}$$

The implicit expression given in Eq. (4.2), can be split up in two expressions for the real and the imaginary part of the solution, respectively:

$$\mathrm{Re}(E_{hs}) = \frac{E_i}{1 + (|E_{hs}|^2 - \theta)^2}, \tag{4.3}$$

$$\mathrm{Im}(E_{hs}) = \frac{E_i(|E_{hs}|^2 - \theta)}{1 + (|E_{hs}|^2 - \theta)^2}. \tag{4.4}$$

Furthermore, Eq. (4.2) shows that for $\theta < \sqrt{3}$ the system is monostable, i.e., only one homogeneous stationary solution exists. For $\theta > \sqrt{3}$, three solutions exist if the input power is chosen accordingly. The transition from a single solution to three possible solutions is sometimes referred to as a Cusp bifurcation due to the cusp-like shape of the response curve [PRGGK18a]. Neglecting spatial modulations (i.e., analyzing the ODE-system resulting from Eq. (4.1) and neglecting the spatial derivatives), two of these states are stable, which is why this coexistence is often referred to as optical bistability (see section 2.3 for details). Figure 4.1 shows the absolute value of the homogeneous solution $|E_{hs}|$ depending on the input field E_i for different values of the detuning θ, demonstrating the transition from a monostable to a bistable regime.

Taking into account the possibility of spatial modulations by analyzing the full Eq. (4.1) including the spatial derivatives, a linear stability analysis [LL87] shows that the homogeneous stationary solution undergoes a modulational (or Turing) instability. In particular, at $|E_{hs}| = 1$, an eigenmode with the critical wavelength $k_c = \sqrt{2 - \theta}$ becomes unstable. Therefore, the modulational instability can only occur for values of $\theta < 2$. For $\theta \geq 2$, the homogeneous solution still looses stability in a fold (or saddle-node bifurcation). Figure 4.2 again shows the homogeneous stationary solutions of Eq. (4.1), however this time considering spatial modulations. The monostable and the critical curve show the loss of stability in the modulational instability. The curve that was bistable in Fig. 4.1 looses stability in the fold. However it does not regain stability due to secondary spatial instabilities. This sequence of additional instabilities leads to chaotic behavior for large values of E_i [PRGM$^+$14a].

Although in the expanded system we are interested in, a bistability between two homogeneous states does not exist (cf. Fig. 4.2), we refer to the regime of $\theta > \sqrt{3}$ as the optically bistable regime or the regime of optical bistability following a very common convention in the field of nonlinear optics. It has to be noted though, that this denomination technically is only correct for non-extended ODE-systems.

To further analyze the modulational instability, a weakly nonlinear analysis also provided in the original paper proposing the LLE [LL87], shows that this bifurcation is supercritical for $\theta < \frac{41}{30}$ and subcritical for $\theta > \frac{41}{30} = 1.3\overline{6}$. Since in non-conserved systems LSs can only occur in a region where a stable homogeneous solution coexists with stable patterned solutions we will restrict ourselves to the latter subcritical case. It is worth noting, that the distinction between a super- and subcritical bifurcation does not coincide with the above-mentioned differentiation between the mono- and bistable regime, i.e., localized solutions can exist in both regimes.
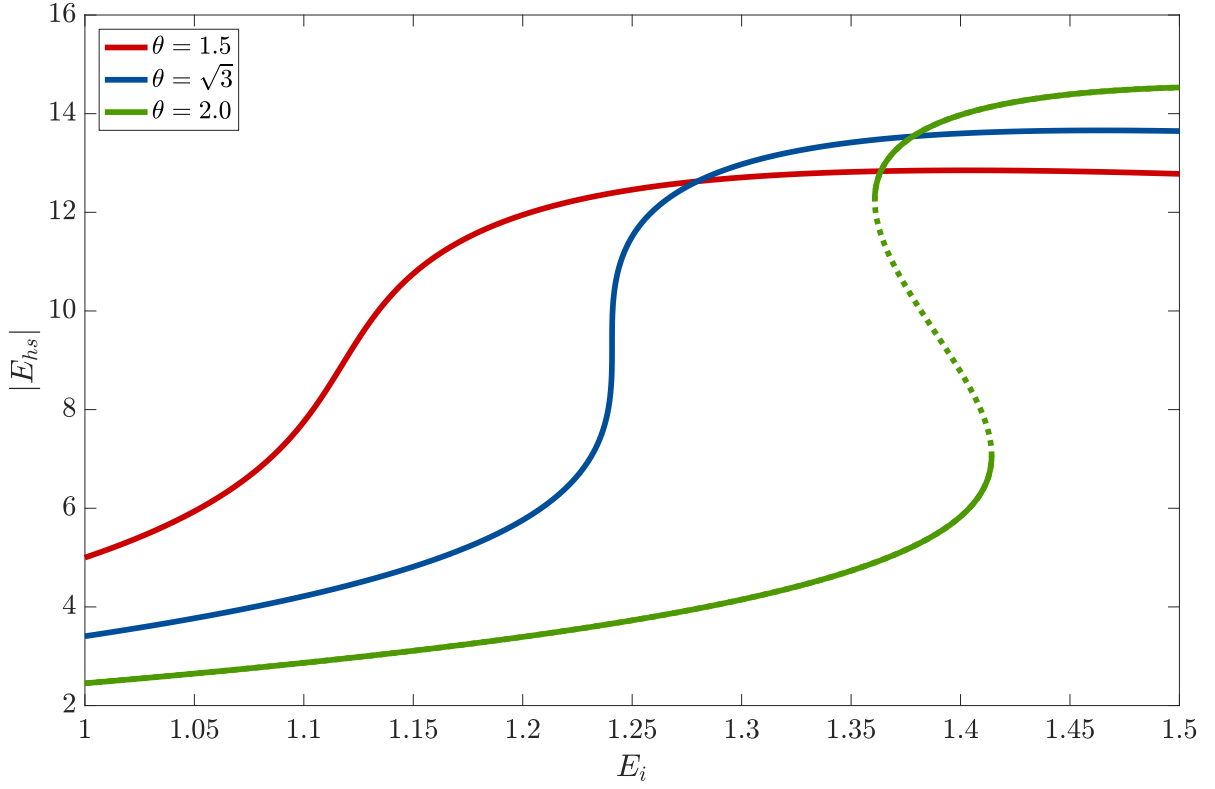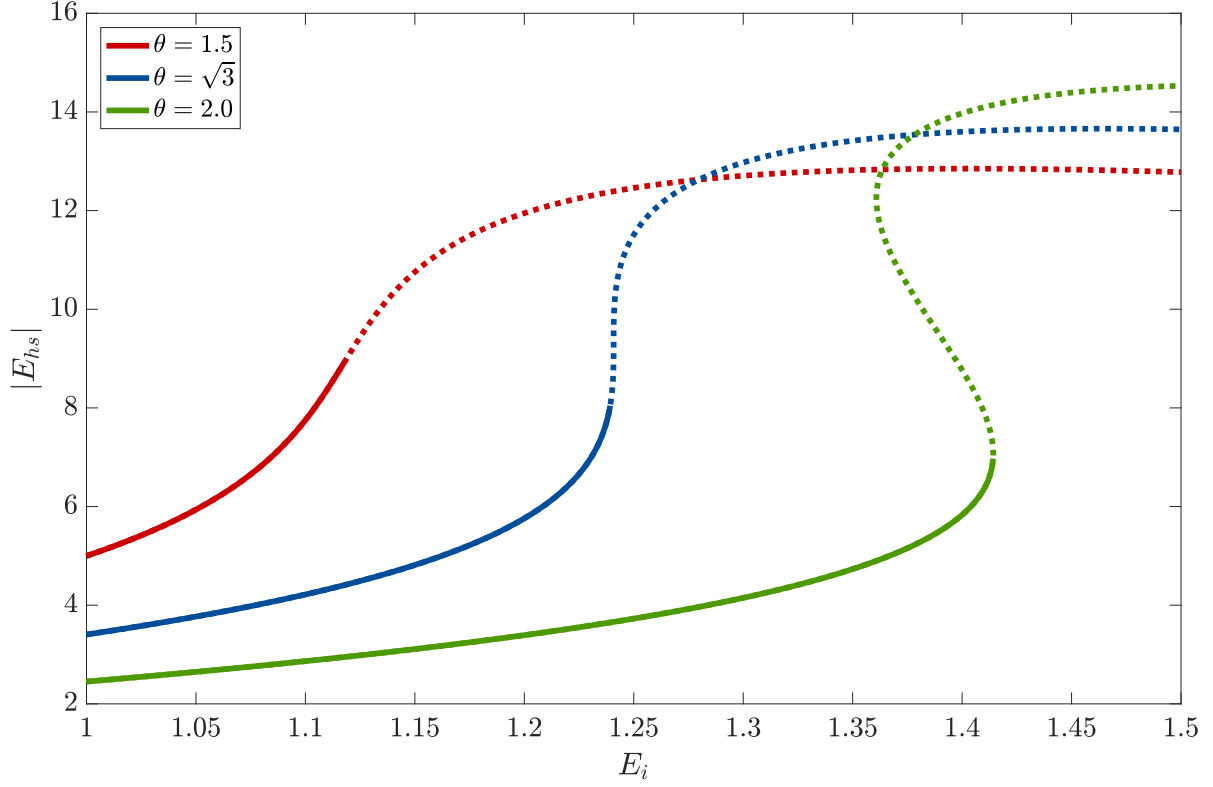
Figure 4.1: Intensity of the homogeneous stationary field $|E_{hs}|$ in dependence of the injected field intensity E_i for three different values of the detuning θ. All curves are obtained by numerical continuation of Eq. (4.1) without considering spatial effects, i.e., neglecting the diffractive term. Dotted lines represent unstable solutions, whereas solid lines depict stable solutions. The transition from a monostable ($\theta = 1.5$, red line) to a bistable regime ($\theta = 2.0$, green line) in a cusp bifurcation is clearly visible. For $\theta = 2.0$ there exists a region of parameters where three different stationary solutions exist, with the middle one being unstable. The blue line depicts the response curve at the critical value of $\theta = \sqrt{3}$, i.e., the border between the monostable and the bistable regime.

Figure 4.2: Intensity of the homogeneous stationary field $|E_{hs}|$ in dependence of the injected field intensity E_i. All values are the same as in Fig. 4.1, except now spatial modulations are considered, showing that the monostable (red) and critical curve (blue) loose stability in a modulational instability. The bistable curve (green) looses stability at the same point as in Fig. 4.1, however does not regain stability due to secondary spatial instabilities.

4.1.2 Periodic Solutions of the Lugiato-Lefever Equation

A Turing instability first described by Alan Turing [Tur90] is one of the paradigmatic mechanisms responsible for the formation of periodic patterns in reaction-diffusion systems. In optics, a Turing instability is often referred to as a modulational instability. After a Turing instability, the periodic patterns with the critical wave number k_c either are directly stable in the case of a supercritical bifurcation or they gain stability in a subsequent fold in the case of a subcritical bifurcation. Especially the latter scenario provides conditions suitable for the formation of localized structures since in this case a stable periodic and a stable homogeneous solution coexist [AA08].

The formation of stable periodic patterns in a Turing or modulational instability has been thoroughly discussed [PRGGK18b], especially in the monostable regime of $\theta < \sqrt{3}$. Our findings suggest that one can distinguish four different parameter regimes depending on θ with stable periodic solutions, however, the mechanisms leading to these solutions are more intricate in the bistable regime of $\theta > \sqrt{3}$.

In the following, we describe each of the four different regimes briefly and show how stable periodic patterns emerge.

$\boldsymbol{\theta < \frac{41}{30}}$

In this region, the emergence of stable periodic patterns is straight forward. In the above described Turing bifurcation, the homogeneous solution becomes unstable with respect to perturbations with the critical wave-number $k_c = \sqrt{2 - \theta}$. A pattern with said wavelength emerges in this supercritical bifurcation and directly is linearly stable. It is worth noting that due to a finite size effect, not all wave-numbers k can be realized in the system. Assuming periodic boundary conditions in a system with the domain-length L only wave-numbers $k_n = \frac{2\pi}{L}n$, with $n \in \mathbb{Z}$ are possible. In the case, where k_c is not one of the allowed wave-numbers k_n, one of the two allowed neighboring wave-numbers is the first to become unstable. The effect of discretized wave-numbers however is not confined to this parameter regime of the LLE but has to be taken into account in the following as well.

$\boldsymbol{\frac{41}{30} < \theta < \sqrt{3}}$

This parameter regime is of larger interest for the scope of this work, since in contrast to the before mentioned regime it allows the formation of localized solutions. Figure 4.3 shows for $\theta = 1.7$ how a finite band of wave numbers around $k_c = 0.5477$ becomes unstable with increasing E_i. Considering a finite domain size of $L = 100$, only discretized values of $k = n\Delta k$ can be realized in the system. Hence, the first mode to become unstable is $k = 9\Delta k$, followed by the neighboring modes $k = 8\Delta k$ and $k = 10\Delta k$. As described above, the bifurcation in which the homogeneous solution looses stability towards perturbations with these k-values is subcritical in this parameter regime, i.e., after undergoing the bifurcation, both the homogeneous and the periodic solutions are unstable. Figure 4.4 depicts the onset of instability for $\theta = 1.7$, showing that the solution corresponding to $k = 9\Delta k$ gains stability in a fold leading to a stable periodic solution, whereas the solution corresponding to $k = 8\Delta k$ remains unstable.
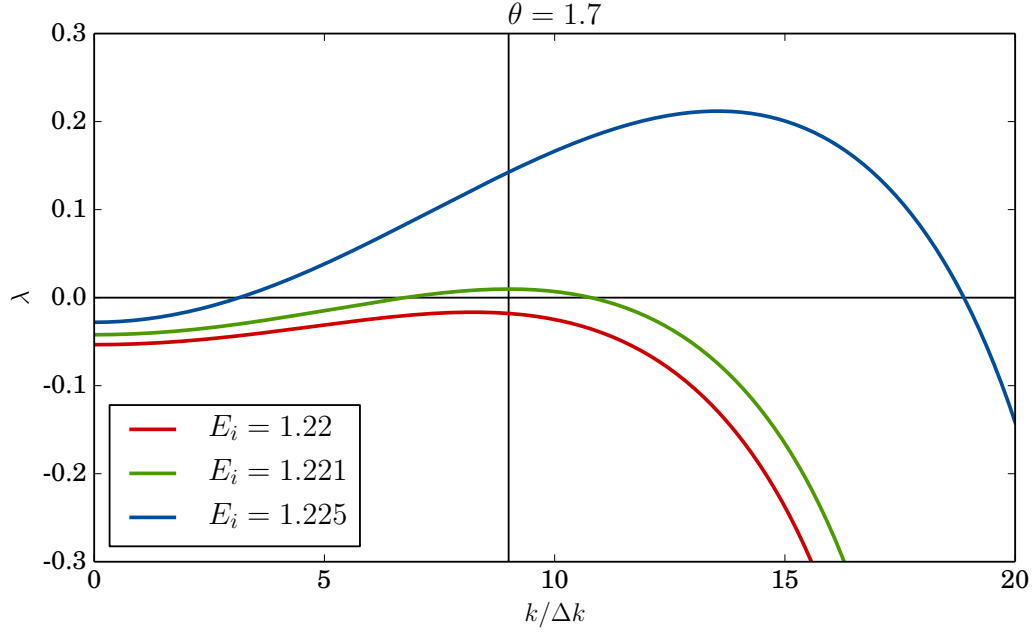
Figure 4.3: Dispersion relation of the linearized LLE (4.1) showing the results of a linear stability analysis of the homogeneous solution for $\theta = 1.7$ and different values of E_i. The Eigenvalues λ depending on the wave-number k of a spatially periodic perturbation are depicted, showing the typical dispersion relation of a Turing bifurcation. The x-axis is depicted in units of Δk, since only integer values of the x-axis can be realized in a finite system. For $E_i = 1.22$ (red line), the homogeneous solution is stable, i.e., all eigenvalues are negative. With increasing injection, a finite band of eigenvalues around $k = 9\Delta k$ (marked by vertical line) becomes unstable ($E_i = 1.221$, green line), whereas spatially homogeneous perturbations ($k = 0$) are still damped. Further increasing the injection to $E_i = 1.225$ (blue line) leads to a growth of the unstable band of eigenvalues. Domain parameters are $L = 100$ and $\Delta k = \frac{2\pi}{L} \approx 0.063$.

Surprisingly in this parameter regime, also the branch with $k = 10\Delta k$ gains stability, same goes for all branches with $k > k_c$. The branch corresponding to $k = 10\Delta k$ possesses five unstable eigenvalues directly after bifurcating the homogeneous solution, of which only one gets stabilized in the fold depicted in Fig. 4.4. The other four unstable eigenvalues stabilize in two bifurcations, close to the original Turing bifurcation and require further investigation.
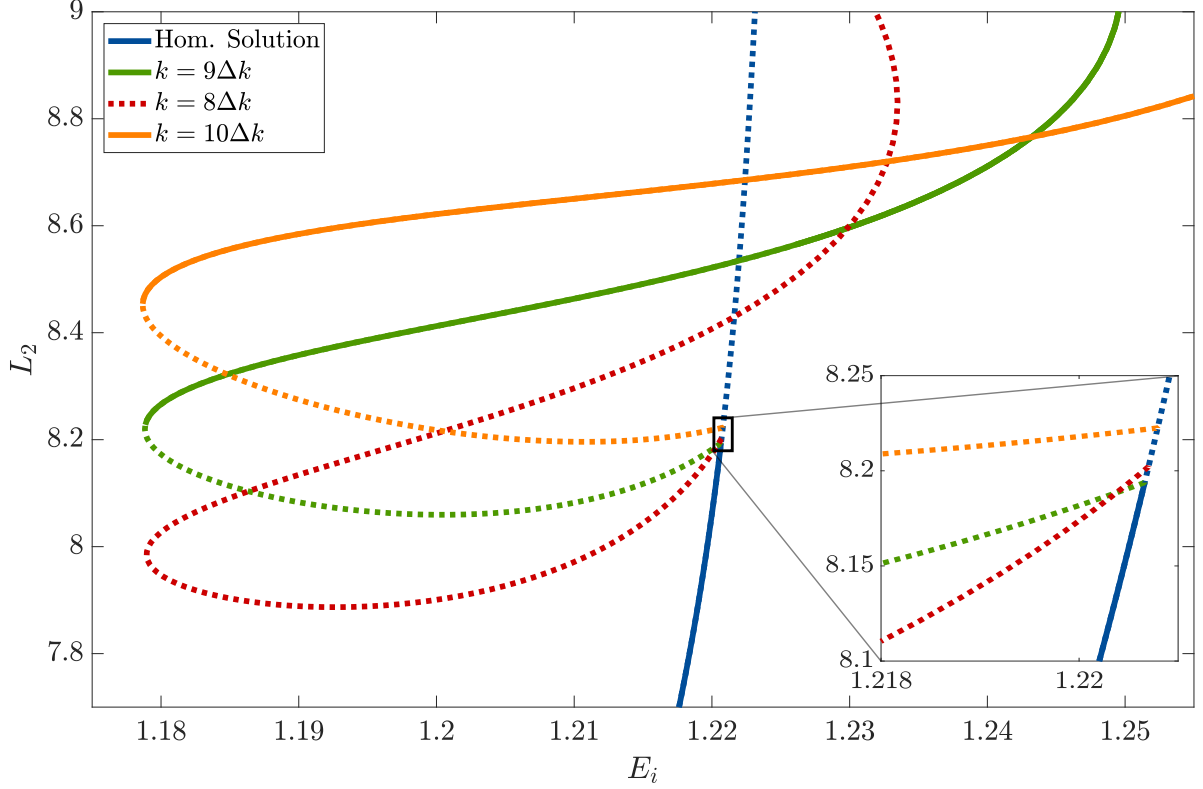

Figure 4.4: Bifurcation diagram showing the destabilization of the homogeneous solution (blue line) by subsequent Turing bifurcations for $\theta = 1.7$. The curves are obtained by numerical continuation of Eq. (4.1) with E_i as the main continuation parameter and the norm $L_2 = \int d\xi |\text{Re}(E)|^2$ as a solution measure. With increasing E_i, the first k-value to branch off is $k = 9\Delta k$ (green line), followed by $k = 8\Delta k$ (red line), $k = 10\Delta k$ (orange line) and further surrounding values of k (not depicted). The first branch $k = 9\Delta k$ gains stability in a fold, whereas all branches with $k < 9\Delta k$ do not gain stability. The branches with $k > 9\Delta k$ also gain stability although they initially posses more than one unstable eigenvalue. The bifurcations responsible for the stabilization of the additional unstable eigenvalues occurs close to the homogeneous branch, however it remains to be examined which solutions branch off at these bifurcations. The inset depicts a zoomed in version around the primary bifurcation point. Parameters are $L = 100$ and $\Delta k = \frac{2\pi}{L} \approx 0.063$.

$$\sqrt{3} < \theta < 2$$

In this rather narrow regime at the onset of optical bistability (i.e., the homogeneous solution curve is s-shaped, see Fig. 4.1 and 4.2), the Turing bifurcation still exists, however $k_c = \sqrt{2-\theta}$ becomes increasingly small until it vanishes for values of $\theta > 2$. Figure 4.5 depicts the destabilization of the homogeneous solution for $\theta = 1.9$, showing that the Turing bifurcation sets in very close to the fold with $k_c = 5\Delta k$. In contrast to the previously discussed cases it is however not this branch that gains stability and yields a stable periodic solution. Since the first Turing bifurcation is so close to the fold, other k-values branch off from the already unstable homogeneous solution after the fold (see inset of Fig. 4.5). This results in a fundamentally different dispersion relation (cf. Fig. 4.6), as now the eigenvalue corresponding to $k = 0$ is positive. Figure 4.5 shows that it is actually a branch corresponding to $k = 9\Delta k$ that first gains stability. Again, there are several bifurcations along the branch leading to the stabilization of said solution. Surprisingly, our results suggest, that in this parameter regime all the modes fulfilling $k > k_c(\theta = \sqrt{3}) \approx 0.52$ become stable. At this point a weakly nonlinear analysis seems promising to better understand this wavelength-selection.

$2 < \theta$

For $\theta > 2$, the Turing bifurcation vanishes, since no real k_c exists anymore. The lower branch of the homogeneous solution stays stable until it looses stability in a fold (cf. Fig. 4.2). Stable periodic solutions still exist and have been reported, however it was unclear so far, how they emerge [PRGM^{+}14a].

To analyze the emergence of the periodic and localized solutions one has to take a closer look at the unstable homogeneous solution connecting the upper and the lower homogeneous branch. Considering that this solution is unstable towards the other two homogeneous solutions, it is trivial that this solution is unstable towards homogeneous perturbations (i.e., perturbations with $k = 0$). Moving from the fold where the solution emerges along the branch towards lower values of E_i, further bifurcations exist, where one by one, growing values of k become unstable in supercritical pitchfork bifurcations. Figure 4.7 shows how with decreasing E_i more and more k-values become unstable starting with $k = \Delta k$.

Following the first branch corresponding to $k = \Delta k$ (red line in Fig. 4.8), the solution quickly develops from a sinusoidal solution with one peak (inset on the right), to a sharp single peak solution (middle inset) and then gains stability. The same behavior occurs for multiple peak solutions with $k = n\Delta k$ (see e.g., $k = 9\Delta k$, green line). The peaks position at a maximum possible distance. As will be discussed in the next section, localized solutions in this parameter regime do not form bound states but align at the maximum possible distance, i.e., one can not clearly differentiate solutions of multiple localized solutions from periodic solutions.

4.1.3 Localized Solutions of the Lugiato-Lefever Equation

After discussing both homogeneous and periodic solutions of the LLE we now focus on LSs. The investigation of LSs has sparked new interest recently, since a direct link between LSs of the temporal LLE and Kerr frequency combs (KCs) has been established [KHD11, FML^{+}11, CM13]. It was shown that the frequency spectrum of a temporal LS created, e.g., in a microresonator consists of a sequence of equidistant peaks spanning over a broad frequency band. An example of a LS together with the corresponding KC can be found in Fig. 4.9.
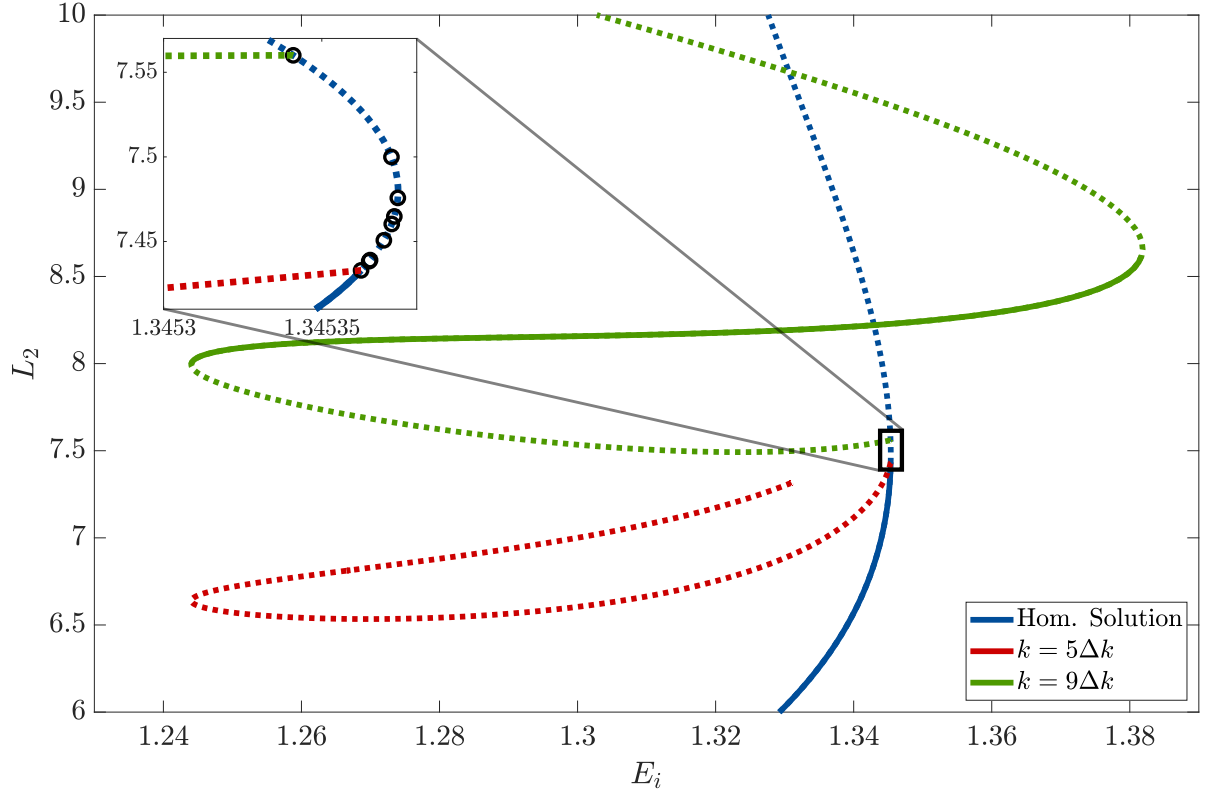
Figure 4.5: Bifurcation diagram showing the destabilization of the homogeneous solution (blue line) for $\theta = 1.9$. The curves are obtained by numerical continuation of Eq. (4.1) with E_i as the main continuation parameter and the L_2-norm as a solution measure. The first k-value to branch off before the fold associated with optical bistability is $k = 5\Delta k$ (red line). However this solution does not gain stability. The first branch to gain stability corresponds to $k = 9\Delta k$ (green line) and branches off after the fold in the ninth bifurcation. This branch is highly unstable after branching off in a supercritical pitchfork bifurcation having 17 unstable eigenvalues due to the previous bifurcations. However it looses all but one unstable eigenvalue in a sequence of bifurcations that are yet to be examined before finally stabilizing in a fold. The inset depicts a zoomed in version marking the bifurcation points where periodic solutions branch off. Parameters are $L = 100$ and $\Delta k = \frac{2\pi}{L} \approx 0.063$.
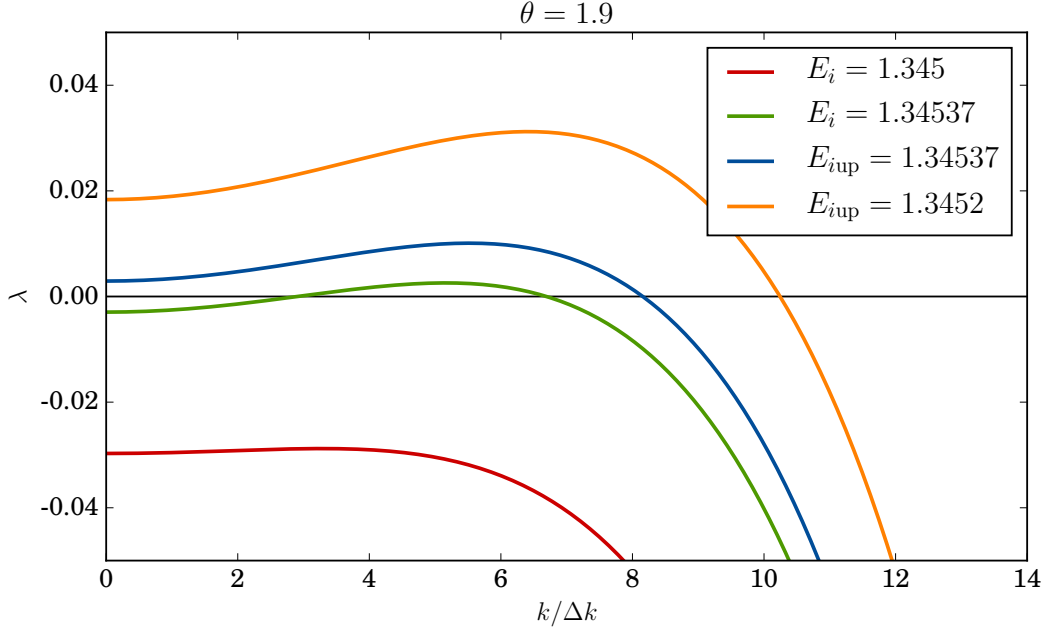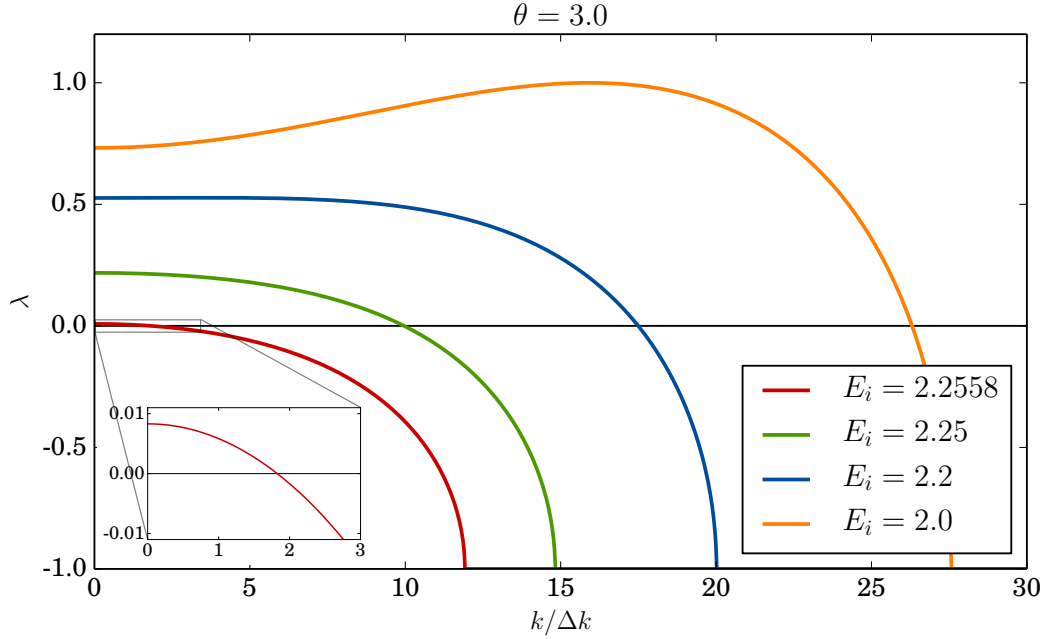
Figure 4.6: Dispersion relation showing the results of a linear stability analysis of the homogeneous solution for $\theta = 1.9$ and different values of E_i along the fold shown in Fig. 4.5. The Eigenvalues λ depending on the wave-number k of a spatially periodic perturbation are depicted. The x-axis is depicted in units of Δk, since only integer values of the x-axis can be realized in a finite system. For $E_i = 1.345$ (red line), the lower homogeneous solution is stable, i.e., all eigenvalues are negative. With increasing injection, the solution undergoes a Turing bifurcation ($E_i = 1.34537$, green line). Following the solution branch depicted in Fig. 4.5 the solution then becomes unstable towards homogeneous perturbations ($k = 0$) in a fold (see also Fig. 4.2). A linear stability analysis of this middle branch of the bistability curve at $E_{i\mathrm{up}} = 1.34537$ yields the blue curve showing an unstable band of eigenvalues going from $k = 0$ to a finite value. Further increasing the injection to $E_{i\mathrm{up}} = 1.3452$ leads to a growth of this parameter region. Parameters are $L = 100$ and $\Delta k = \frac{2\pi}{L} \approx 0.063$.

Figure 4.7: Dispersion relation showing the results of a linear stability analysis of the homogeneous solution for $\theta = 3.0$ and different values of E_i. The Eigenvalues λ depending on the wave-number k of a spatially periodic perturbation are depicted. The x-axis is depicted in units of Δk, since only integer values of the x-axis can be realized in a finite system. The homogeneous solution is stable up to the first fold associated with optical bistability. All curves shown in this figure provide results for the already unstable middle branch of the optical bistability curve (see Fig. 4.2). Since the homogeneous solution is already unstable the eigenmode with $k = 0$ always possesses a positive eigenvalue. Shortly after the fold ($E_i = 2.2558$, red line), the next eigenmode corresponding to $k = \Delta k$ becomes unstable (see inset). Following the homogeneous solution branch and decreasing E_i, further eigenmodes with $k = n\Delta k$, $(n = 1, 2, 3...)$ become unstable. Parameters are $L = 100$ and $\Delta k = \frac{2\pi}{L} \approx 0.063$.
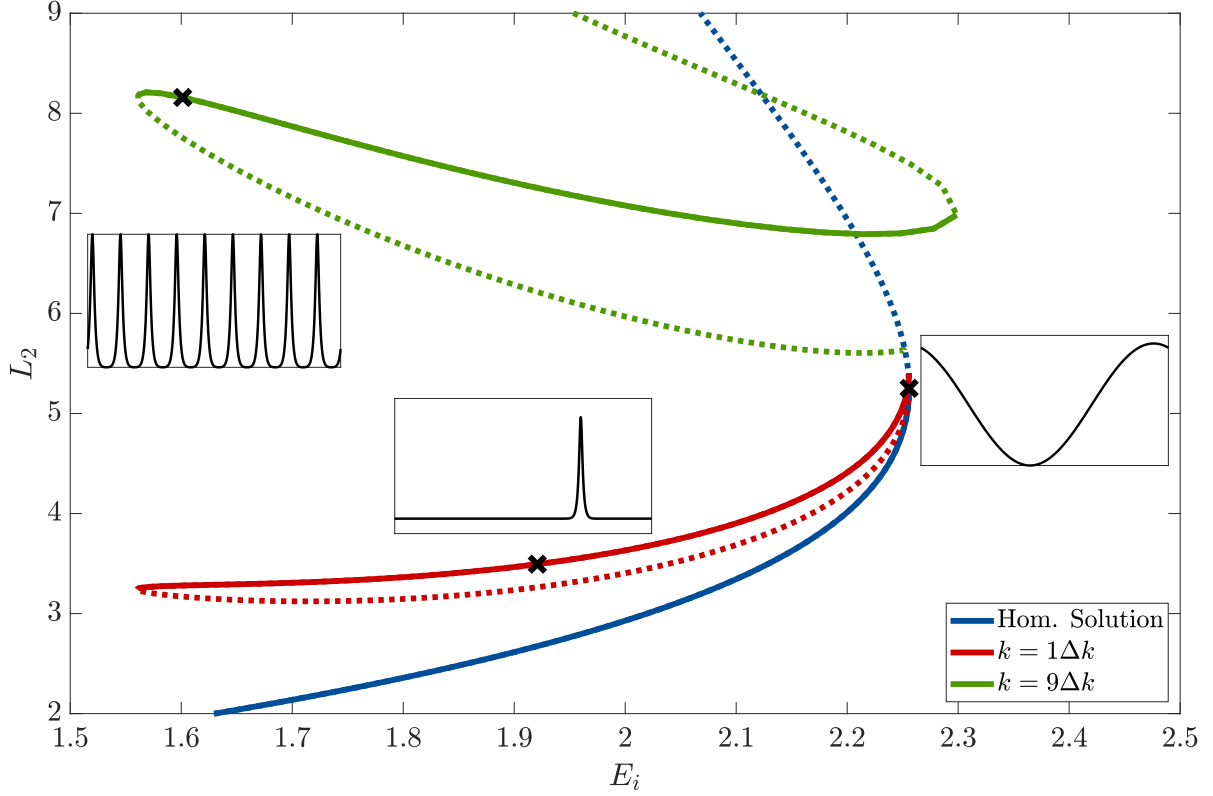
Figure 4.8: Bifurcation diagram showing the destabilization of the homogeneous solution (blue line) for $\theta = 3.0$. The curves are obtained by numerical continuation of Eq. (4.1) with E_i as the main continuation parameter and the L_2-norm as a solution measure. In this parameter regime, the lower branch of the homogeneous solution (see Fig. 4.2) is stable up to the fold associated with optical bistability. After the fold, periodic solutions with $k = n\Delta k$ branch off of the already unstable homogeneous solution in supercritical pitchfork bifurcations starting with $n = 1, 2, 3...$. The solution $k = \Delta k$ (red line) consisting of one peak develops into a sharp localized solution (see insets showing the solution profiles) and gains stability. This coarsening of the peaks also takes place for larger values of n with peaks assembling at a maximum possible distance, leading to periodic solutions of peaks, as depicted for $n = 9$ (green line). Parameters are $L = 100$ and $\Delta k = \frac{2\pi}{L} \approx 0.063$.

Frequency combs in general have found a variety of different useful applications in metrology, due to the possibility to precisely measure frequencies [UHH02, SLV07, UHH02, PBL$^+$14, HJL$^+$08]. Typically frequency combs are generated deploying mode-locked lasers. A more cost-efficient generation of KCs in much smaller microresonators can therefore be advantageous compared to the established generation via mode-locking. It is therefore of high interest to investigate the possibilities of KC generation in the LLE. In the following, we investigate the formation of LSs in the LLE, bearing in mind the possible application of temporal LSs to KC generation.

As described in chapter 1, LSs typically coexist with a stable homogeneous and a stable periodic solution. That is, the parameter region $\theta < \frac{41}{30}$ can be ruled out as a promising region to find LSs, since the periodic solution bifurcates from the homogeneous solution supercritically in this regime, i.e., the two solutions do not coexist stably. As can be seen in Fig. 4.4 and 4.5, a
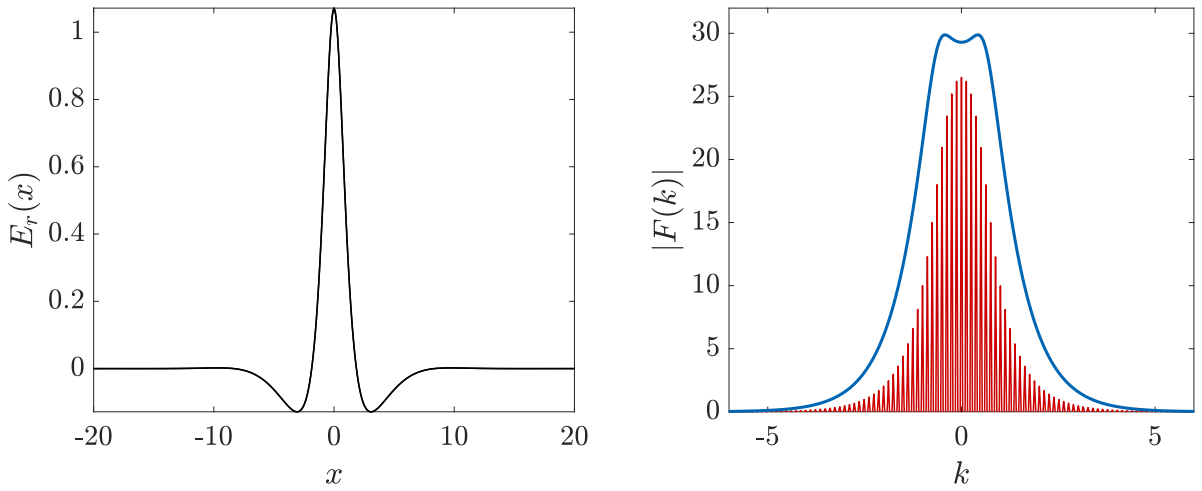

Figure 4.9: Left: Real part of the solution profile of a single LS for $\theta = 1.7$, $E_i = 1.2$. Right: Absolute value (blue) and real part (red) of the Fourier transform of the LS. The real part consists of a sequence of equidistant peaks (also called frequency comb). The imaginary part is not depicted for the sake of better visualization, however it exhibits the same comb-like structure. The figure was also published in [TFHP$^+$19].

stable periodic solution coexists with the stable homogeneous solution in the region, where the Turing bifurcation branches off subcritically ($\frac{41}{30} < \theta < 2$). In this parameter region, localized solutions do exist. Figure 4.10 shows two examples of LS in this region, one for lower θ with very pronounced oscillatory tails and one for larger θ where the oscillatory tails are less pronounced yet still present. The presence (or absence) of oscillatory tails is of great importance for the bifurcational structure of LS, since the form of the tails predicts the possibility of bound states between two or more LSs.

We now analyze the bifurcational structure of LSs in this regime by employing numerical continuation algorithms again using the Matlab package *pde2path*. As a measure we use the averaged L_1 norm $L_1 = \int d\xi |\text{Re}(E - \overline{E})|$. $\overline{E}$ denotes the mean value of the electrical field $E(\xi)$ averaged over the domain size, i.e., homogeneous solutions possess the norm $L_1 = 0$.

In Fig. 4.11, the emergence of a single LS (green line) bifurcating from the first periodic branch with an odd number of peaks (red line) is depicted. The fact that this solution branches
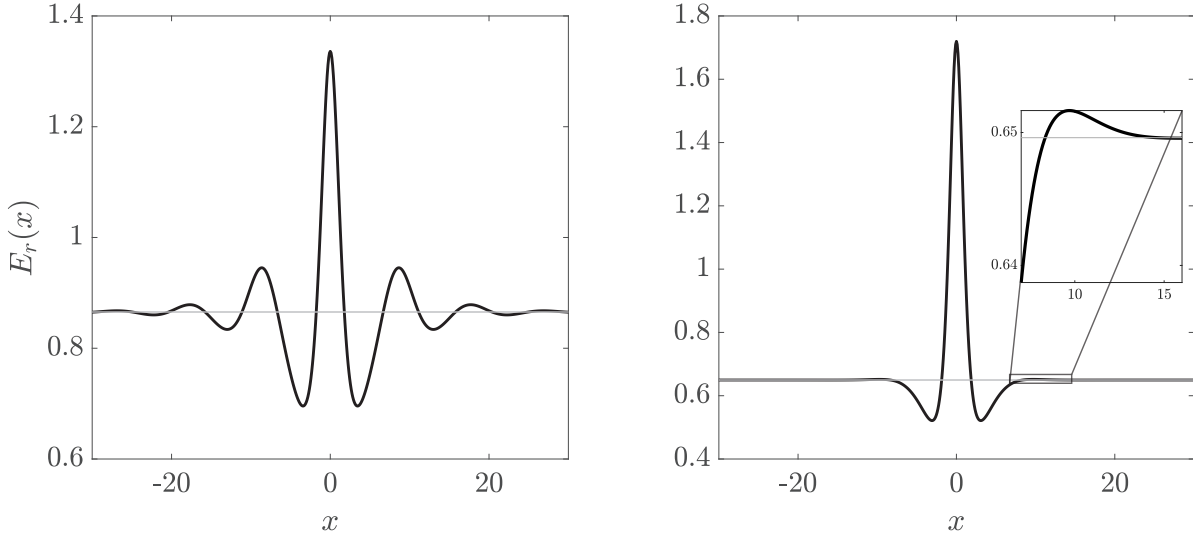
Figure 4.10: Real part of the solution profile of a single LS for $\theta = 1.5$, $E_i = 1.114$ (left) and $\theta = 1.7$, $E_i = 1.2$ (right). The amplitude of oscillatory tails decreases drastically with increasing θ. However, one side-maximum is still present in the case of $\theta = 1.7$ (see inset). The gray line marks the real part of the homogeneous solution and is depicted for a better visibility of the oscillatory tails.

off from the periodic branch close to the Turing point is due to a finite size effect [BBKM08]. On an infinite domain one would expect both the periodic branch and the LS branch to bifurcate at the same Turing point. The single LS then gains stability in a fold. The solution profile of the single LS is depicted on the bottom right of Fig. 4.11 as well as the solution profiles of all upper branches. The single LS then looses stability in another fold but gains two additional peaks, then stabilizes again as a three peak solution. This sequence of folds continues until the peaks fill the entire domain and the branch of LSs reconnects with the first stable periodic branch (in the case of Fig. 4.11 the same red branch it bifurcated from originally).

This sequence of consecutive folds is typically referred to as homoclinic snaking [Kno08]. It has been thoroughly studied in the LLE [GSF07, PRGM$^+$14a] as well as in other systems possessing LSs like the Swift-Hohenberg or conserved Swift-Hohenberg equation [BK07, Kno08, OGT18]. Besides the described branch consisting of an odd number of LSs, there exists also an even branch of LSs as depicted in Fig. 4.12 (gray line in Fig. 4.11). In this case, a solution consisting of two bound LSs (green line) bifurcates from the first periodic branch that becomes Turing unstable (in this case the orange eight-peak branch). In a sequence of folds the structure gains additional peaks as in the case of the odd branch until the entire domain is filled and the structure reconnects with the periodic ten-peak branch (red line). This ten-peak solution is the first periodic solution with an even number of peaks that gains stability. The eight-peak solution (orange) becomes Turing unstable before the ten-peak solution, however it does not reach stability. The fact that the even branch connects to a different periodic branch than the odd LSs branch can be attributed to a finite size effect [PRGGK18a].

The even and the odd branch of the homoclinic snaking are connected by so called „ladders"[PRGGK18a], i.e., unstable unsymmetrical solution branches connecting the two branches. However, since these branches are all unstable, they will not be in the focus of the following analysis.
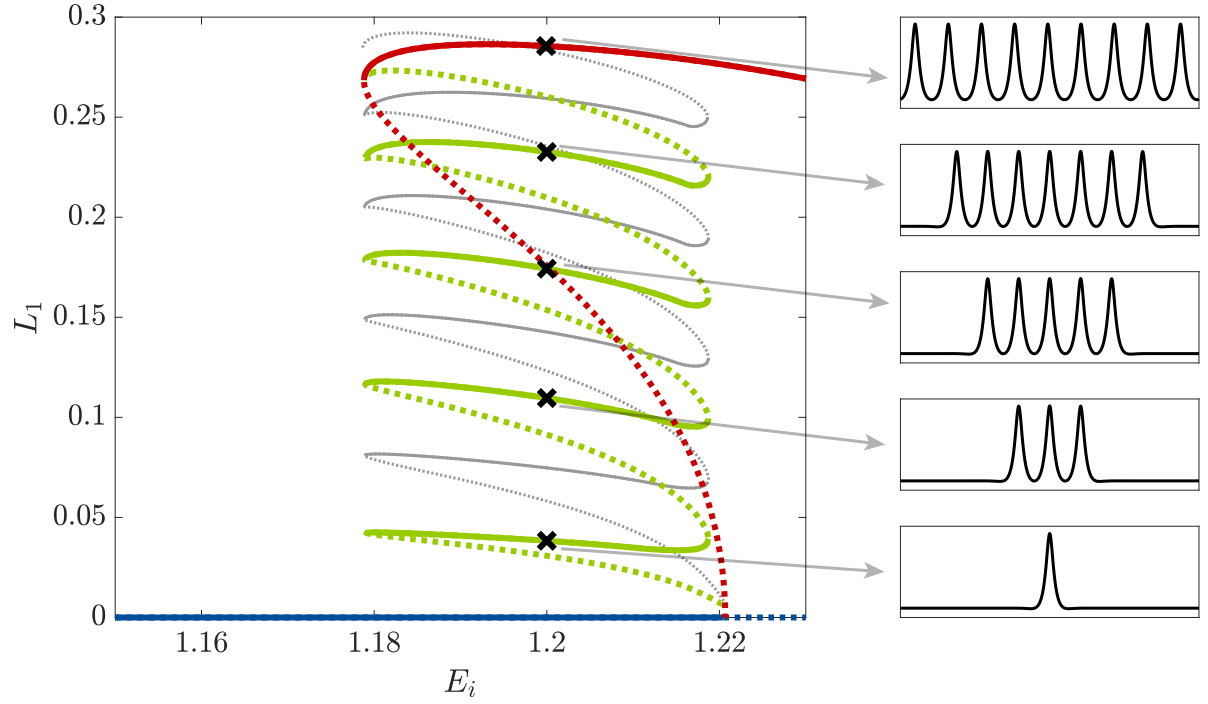
Figure 4.11: Left: Emergence of single LS and odd numbers of bound LSs in homoclinic
snaking for $\theta = 1.7$ with E_i as the continuation parameter and with the L_1 norm
as a measure. Shortly after the periodic nine-peak solution (red line) bifurcates
from the homogeneous solution (blue line) at the Turing point, a single LS
solution (green line) branches off of the periodic solution. In a sequence of
folds, the solution gains stability and then gains two extra peaks. This pattern
continues until the domain is filled with nine peaks and the branch of LSs
reconnects with the periodic branch. The thin gray lines in the background
depict the even branch of LSs which are thoroughly discussed in Fig. 4.12. Right:
Real part of the solution profiles of the LSs at the marked positions illustrating
the transition from a single LS to a domain-filling pattern by addition of peaks.
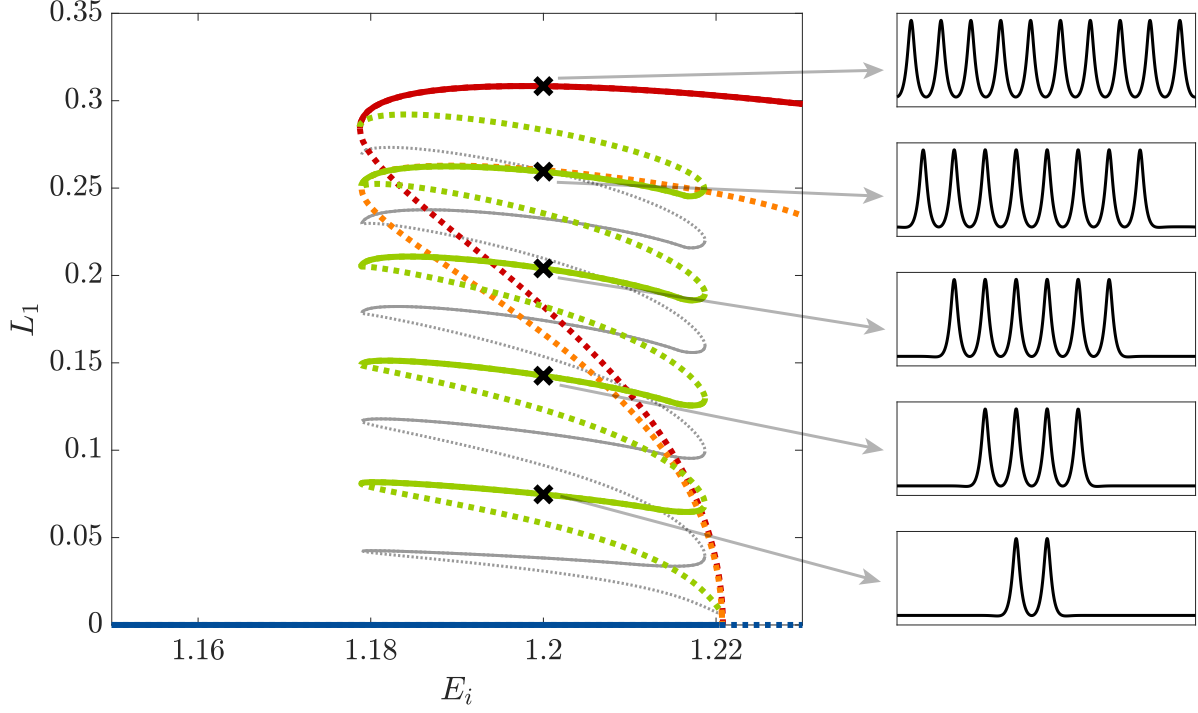
Figure 4.12: Left: Emergence of even numbers of bound LSs in homoclinic snaking for $\theta = 1.7$ with E_i as the continuation parameter and with the L_1 norm as a measure. A solution of two bound LS (green line) bifurcates from the eight-peak periodic solution (orange line) which is the first periodic solution with an even number of peaks to branch off of the homogeneous solution (blue line). In a sequence of folds, the solution gains stability and then gains two extra peaks. This pattern continues until the domain is filled with ten peaks and the branch of LSs reconnects with the periodic branch of ten peaks, which is the first periodic branch with an even number of peaks that gains stability. The thin gray lines in the background depict the odd branch of LSs which are thoroughly discussed in the context of Fig. 4.11. Right: Real part of the solution profiles of the LSs at the marked positions illustrating the transition from a single LS to a domain-filling pattern by addition of peaks.

With increasing detuning θ, the Turing bifurcation vanishes by colliding with the right fold of the cusp-like homogeneous branch at $\theta = 2.0$. Localized structures still exist and can be directly traced by direct continuation starting from a parameter regime $\theta < 2$ going into the regime of $\theta > 2$ [PRGGK18a], i.e., the stable single LS solution below and above $\theta = 2$ are connected. The same does not hold for bound states of two or more LS because the shape of the LSs changes qualitatively around $\theta \approx 2$. As can be seen in Fig. 4.13, the localized solution at the maximum possible injection E_i (i.e., at the fold of the single LS depicted in Fig. 4.11) looses its side maximum at $\theta = 2.08$. Therefore, LSs are not able to form stable bound states but repel each other above this value. The homoclinic snaking as described above thus breaks down [PRGGK18a].
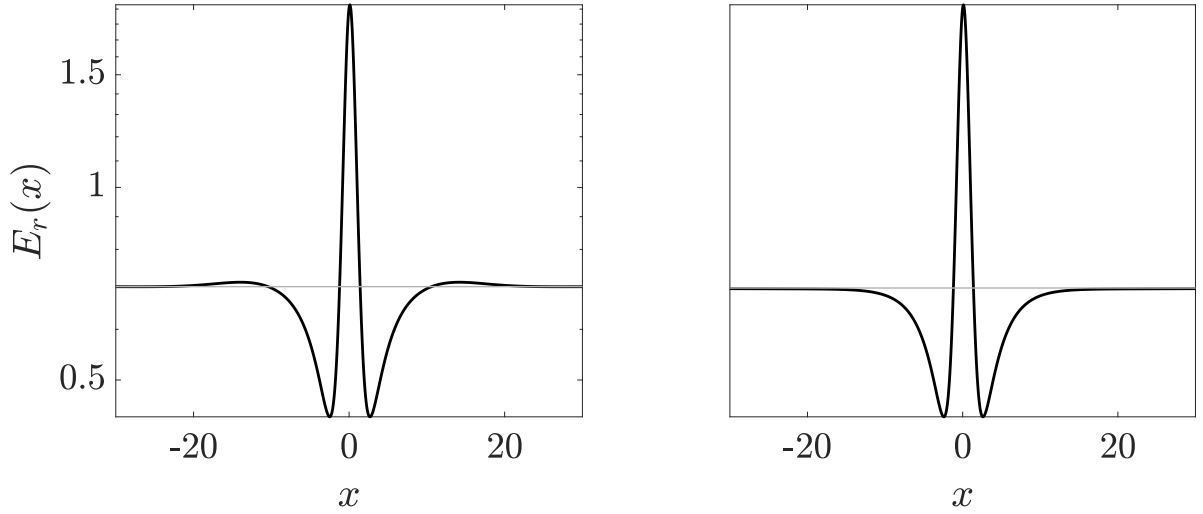

Figure 4.13: Real part of the solution profile of a single LS for $\theta = 2.0$ (left) and $\theta = 2.1$ (right) at the maximum possible value of E_i, i.e., at the right fold. The logarithmic scaling on the y-axis and the gray horizontal line marking the value of the homogeneous solution emphasize the transition from a solution with a side maximum (left) to a solution with only one side minimum (right). The figure was also published in [TFHP$^+$19].

In [PRGGK18a], this loss of tails was identified as a Belyakov-Devaney transition by analyzing the system of four first order ODEs describing the spatial dynamics of temporally stationary solutions. The linear stability analysis of the homogeneous solution in this framework shows a Belyakov-Devaney transition at $\theta = 2.0$ at the fold. That is, the system goes from having complex spatial eigenvalues $\lambda_{1,2,3,4} = \pm q_0 \pm ik_0$ to real eigenvalues $\lambda_{1,2} = \pm q_1$ and $\lambda_{3,4} = \pm q_2$. Loosing the imaginary part of the spatial eigenvalues is equivalent to a loss of oscillatory tails in the linearized limit. The fact that this transition takes place at $\theta = 2.0$, whereas numerically, reminiscences of the oscillatory tails can be found up to $\theta = 2.08$ is due to nonlinear effects that are not considered in the linearized framework of [PRGGK18a].

In contrast to the case of $\theta < 2$, the single LS does not bifurcate from the periodic branch close to the Turing bifurcation, the single LS branch for $\theta > 2$ is the first solution branch, bifurcating from the homogeneous solution. As can be seen in Fig. 4.8, the branch with the wave number $k = \Delta k$ starts with a sinusoidal solution that quickly develops into a sharp single peak, the LS.

In the same manner, the branch with $k = 2\Delta k$ develops to two peaks positioned at a distance of $L/2$. The same goes for higher values of k, where a number of peaks is positioned equidistantly on the domain, i.e., a differentiation between a periodic state and a state consisting of fewer equidistant LSs is not systematically possible. Bulks of LSs that are closer together can exist for small values of E_i below the Belyakov-Devaney transition, however the distance between the LSs diverges in the vicinity of the Belyakov-Devaney transition connecting these states to the branches of equidistant LSs [PRGGK18a]. A branch with the peak number n is also connected to the branch with the peak-number $2n$ by a ladder-like branch on which small peaks grow in between every pair of existing peaks. This structure is referred to as foliated snaking. A detailed discussion of this phenomenon is out of the scope of this chapter but can be found in [PRGGK18a].

Going to even larger values of the detuning $\theta > 3$, the LSs are destabilized in a Andronov-Hopf bifurcation leading to breathing LSs and through further instabilities to chaotic behavior [GSF07, PRGM$^+$14a]. Since this thesis focuses on the properties of stable LSs, a detailed analysis of these dynamics is not expedient at this point. However, it is necessary to determine, where this instability sets in, in order to obtain an overview over the parameter regime where LSs are stable. To that aim, we again deploy numerical continuation algorithms provided by *pde2path*. Instead of using only one continuation parameter while fixing all other parameters, we now use θ as the continuation parameter and E_i as a free parameter that is determined to fulfill an additional condition characterizing a fold or Andronov-Hopf bifurcation. In this manner it is possible to track the folds and the Andronov-Hopf bifurcation points that delimit the stability of LSs in parameter space. Results are depicted in Fig. 4.14, where the blue line depicts the left fold, delimiting the stability of the single LS solution (see Fig. 4.11) and the green line depicts the position of the right fold. The red line marks, where the first Andronov-Hopf bifurcation sets in. Therefore Fig. 4.14 comprises a full description of the parameter regime in which stable single LSs can be found (gray-shaded area).

4.2 The Lugiato-Lefever model with inhomogeneous Injection

The Lugiato-Lefever equation (LLE) in its original form (4.1) presented in the previous section exhibits localized solutions (LSs) in a broad parameter range. In the present section we expand the analysis to the case of inhomogeneous injection. In the classical LLE describing spatial pattern formation, the injected beam is assumed to be a plane wave, i.e., E_i is constant in the spatial coordinate ξ. Also in the temporal interpretation of the LLE, it is usually assumed that the amplitude of the injected beam is constant on both the time-scale of t and ξ.

The investigation of the effects of an inhomogeneous injection is important for two reasons: On the one hand, small spatial inhomogeneities are unavoidable in any experimental setup, yet they break the translational symmetry, which is typically assumed in theoretical models. This symmetry breaking effect can have a strong influence on the formation, position and dynamics of LSs and therefore needs to be investigated. On the other hand, it might proof beneficial to introduce small inhomogeneities deliberately in a controlled manner. Since especially the injected beam is comparatively easy to manipulate, this would provide a simple mechanism to alter properties of the system under consideration.

Although the LLE was intensively studied in the past decades, the effects of inhomogeneous injection have not been as extensively studied and have gotten into the focus of research in non-linear optics only recently [SJMO05, PRGM$^+$14b, OLH17, ORH$^+$19, TFHP$^+$19]. For example
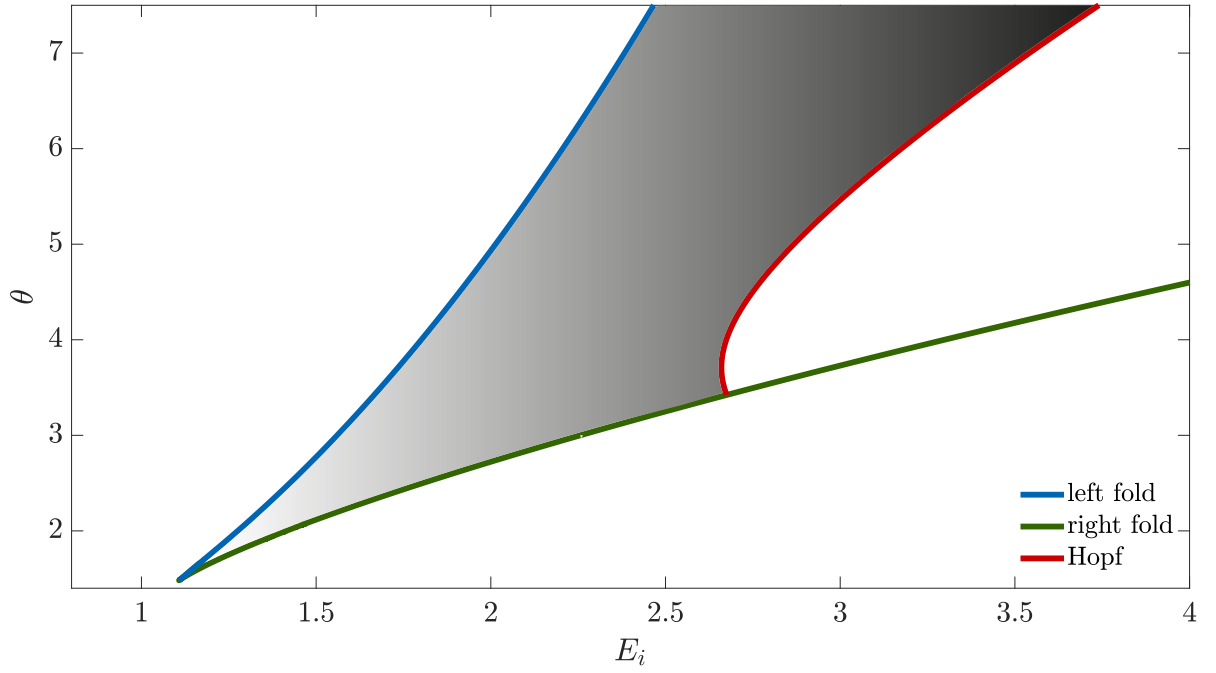
Figure 4.14: Full parameter regime in which single LSs of the LLE exist. The blue (green) line marks the position of the left (right) fold, delimiting the existence of a single LS obtained by numerical fold point continuation in *pde2path*. The red line marks the position of the Andronov-Hopf bifurcation obtained by numerical bifurcation point continuation. The gray-shaded area indicates the region in which single LSs are stable. A similar figure was also published in [TFHP$^+$19].

Hendry et al. [HCW$^+$18] have considered inhomogeneous injection in the LLE, replacing the constant injection by a Gaussian of comparable amplitude. Studying the formation of LSs in this setup they show that LSs do not necessarily stabilize at minima or maxima of the injection as was the case in chapter 3 but instead are drawn towards specific ideal values of the injection. This finding plays an import part in the understanding of the results discussed in section 4.2.2 Another example of the study of inhomogeneous injection can be found in Cole et al [CSE$^+$18], where the results suggest, that a phase-modulated injection can protect single LS generation by preventing the multistability between different numbers of LSs typically present in the LLE.

In this section we limit ourselves to the case of homogeneous injection with an additional inhomogeneous portion in the shape of a Gaussian. The LLE then reads:

$$\frac{\partial E(\xi, t)}{\partial t} = E_i + A \exp\left(-\frac{\xi^2}{B}\right) + \left[-(1 + i\theta) + i|E(\xi, t)|^2 + i\frac{\partial^2}{\partial \xi^2}\right] E(\xi, t). \qquad (4.5)$$

In contrast to Hendry et al [HCW$^+$18], who studied purely Gaussian injection, we mainly discuss the effects of small additional inhomogeneities, i.e., E_i is comparably large as in the homogeneous case, whereas the amplitude of the Gaussian typically is $A < E_i$. The width of the Gaussian is fixed to a moderate width of $B = 4.0$ comparable to the typical length-scale of the system. Altering this width within a reasonable regime does not affect the results presented here as drastically as altering A and therefore will not be discussed in this section. In the following, we are focusing on the effects of the introduced inhomogeneity on the properties of LSs in different parameter regimes, also briefly discussing the effects on homogeneous and periodic solutions.

In particular, we start with the analysis of the bifurcation structure of Eq. (4.5) in two different parameter regimes, namely the regime of homoclinic snaking in section 4.2.1 and the regime of foliated snaking in section 4.2.2. Here, we analyze the emergence of LSs with increasing E_i and discuss the effects of the inhomogeneity compared to the case of homogeneous injection. We show that the inhomogeneity can act either attracting or repelling on the LSs, leading to LSs that are pinned to the inhomogeneity on the center or on the side, respectively. Varying the amplitude A in parameter continuations we then discuss the transitions between the different LSs and identify the bifurcations responsible for these transitions.

We then apply the potential well model to the LLE, which was derived and discussed in the context of the Swift-Hohenberg equation (see chapter 3 and [TSTG17]) and analyze its benefits for the LLE. We close with a full exploration of parameter space, comparing the results in the case of inhomogeneous injection to those in the case of homogeneous injection already presented in Fig. 4.14 of the previous section.

4.2.1 Homoclinic snaking in the presence of inhomogeneities

In this section, we investigate the effects of small added inhomogeneities on the solution structure of the LLE in the regime of homoclinic snaking, i.e., in the regime of $\theta < 2$. One of the most obvious consequences of the introduction of an inhomogeneous term is that the perfectly homogeneous solution as described in Eq. (4.2-4.4) vanishes. However, especially in the case of small A we are interested in, one can still identify a solution that we denote as quasi-homogeneous due to its similarities to the homogeneous solution in the previous section. The quasi-homogeneous solution shows a slight bump or peak (depending on the sign of A) at the position of the inhomogeneity while consisting of the homogeneous solution elsewhere. An

example of the quasi-homogeneous solution for $A = 0.1$, $\theta = 1.7$, $E_i = 1.12$ can be found in the inset of Fig. 4.15 (gray line). The black line depicts a LS of Eq. (4.5) at the same position.

Apart from the obvious difference in amplitude, the quasi-homogeneous solution can be qualitatively distinguished from LSs by considering the different underlying mechanisms responsible for the peak formation. The shape and height of the peak (or bump) in the quasi-homogeneous solution is mainly determined by the locally increased (or decreased) injection. Spatial interactions due to the Laplacian or nonlinear effects hardly influence the peak formation. In other words, the value of the quasi-homogeneous solution at the peaks maximum approximately matches the value of the homogeneous solution with increased injection. On the contrary LSs form due to the complex interplay between dissipative, spatial and nonlinear effects described in chapter 1. Height, width and shape are determined in a complex process of self-organization and are not explicitly determined by external forcing.
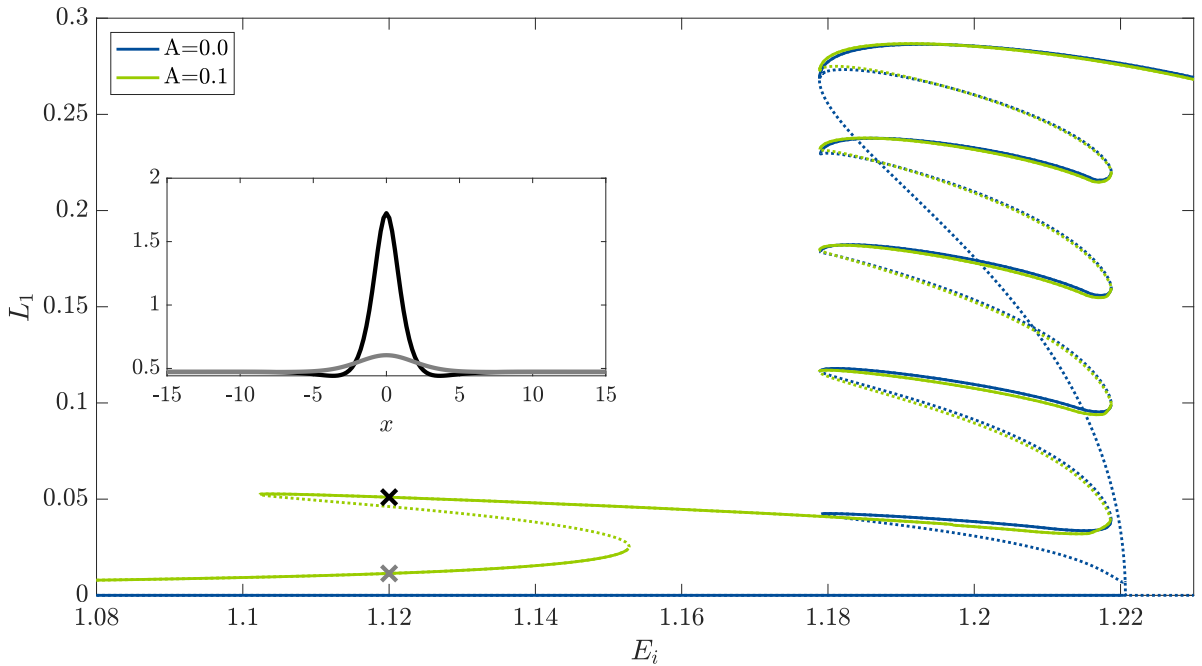

Figure 4.15: Homoclinic snaking as found in the LLE (4.5) in the presence of an attracting inhomogeneity for $A = 0.1$, $B = 4.0$, $\theta = 1.7$ (green line) and in the absence of the inhomogeneity (blue line) obtained by path continuation on a domain of $L = 100$. The inset depicts two solutions at the positions marked by the crosses. For $A = 0$, no perfectly homogeneous solution of Eq. (4.5) exists but a quasi-homogeneous solution (gray line, inset). This quasi-homogeneous solution is connected with the LS (black line, inset) via two folds. The region of existence (and stability) of the single LS is drastically increased by the inhomogeneity, whereas the higher branches of the snaking diagram remain almost unaltered. A similar figure was also published in [TFHP$^+$19].

Focusing now on the destabilization of the quasi-homogeneous solution one can note that the destabilization with respect to periodic perturbations as described in section 4.1.2 is unlikely to happen in the presence of an inhomogeneity, since the solution itself is inhomogeneous, defining a specific length-scale. Instead, the quasi-homogeneous solution looses stability in a

fold as depicted in Fig. 4.15. Following another fold, a stable LS positioned on the center of the inhomogeneity emerges.

Concerning the stability of the LS two important differences to the case of homogeneous injection have to be pointed out. First of all, the LS in the case of $A = 0.1$ is stable - not neutrally stable - with respect to perturbations in the form of an infinitesimal translation, i.e., the eigenvalue of the translational mode is negative. The breaking of the translational symmetry of the system by the inhomogeneity in the case of positive A leads to a pinning of the LS on the center of the inhomogeneity.

Secondly, the onset of the region of stability of the single LS is shifted drastically towards smaller values of E_i, as can be seen in Fig. 4.15. This shift is not surprising, since the overall injection $E_{\mathrm{inj.}}$ at the peak now consists of two contributions:

$$E_{\mathrm{inj.}}(x = 0) = E_i + A, \qquad (4.6)$$

i.e., a smaller amount of homogeneous injection E_i is needed for the creation of LSs. However more surprisingly, the next fold in the bifurcation diagram, delimiting the region of stability of a single LS is hardly affected at all by the additional inhomogeneous injection. In Fig. 4.15, the case of an attracting inhomogeneity ($A = 0.1$, green line) is depicted as well as the previously described case of homogeneous injection ($A = 0.0$, blue line), showing that the fold where a single LS looses stability is not drastically shifted. This difference provides valuable insights into the prerequisites necessary for the formation of LSs. Only the injection (or driving force in general) at the maximum of the LS needs to exceed a certain value to create a LS, however the amount of injection at the sides of the LS seems to determine the end of the region of stability.

Apart from this theoretical insights, this effect can be beneficial for the experimental realization of cavity solitons or Kerr frequency combs, since it shows that by deploying slightly inhomogeneous injection, one can drastically widen the region of stability of the desired structures. Furthermore, as Fig. 4.15 suggests, the upper branches of the snaking diagram are hardly affected by the inhomogeneity. At the end of the snaking branch, the LSs even connect to a solution that fills the entire domain with peaks, however this solution is not perfectly periodic and such a solution does not exist for all parameter values of θ and A. The fact that the upper branches of the homoclinic snaking do not change in the presence of the inhomogeneity leads to the second potentially useful result for experimental realizations: By using slightly inhomogeneous injection, the region where only a single LS is stable gets widened in contrast to the branches of several bound LSs yielding a parameter region where solely the single LS are stable. Avoiding the multistability associated with the homoclinic snaking might be a promising way to address single LS or Kerr combs more easily.

So far we restricted the analysis to the case of a small attracting inhomogeneity of $A = 0.1$. To investigate the effect of inhomogeneities more systematically, Fig. 4.16 depicts the branch of a single LS for different values of A (different shades of green), showing that the widening effect of the inhomogeneity can be drastically increased by simply choosing a larger inhomogeneity. The red line marks the result of a fold continuation, where both A as the main continuation parameter as well as E_i as an additional free parameter are determined to ascertain the position of the fold.

A more comprehensive visualization of the fold continuation can be found in Fig. 4.17, where the positions of the left and right fold are depicted in an A-E_i plane. As can be seen, the widening of the region of stability is consistent for small to moderate values of the inhomogeneity, as a notable shift of the right fold sets in only at $A \gtrsim 1.0$. The inset illustrates that, although
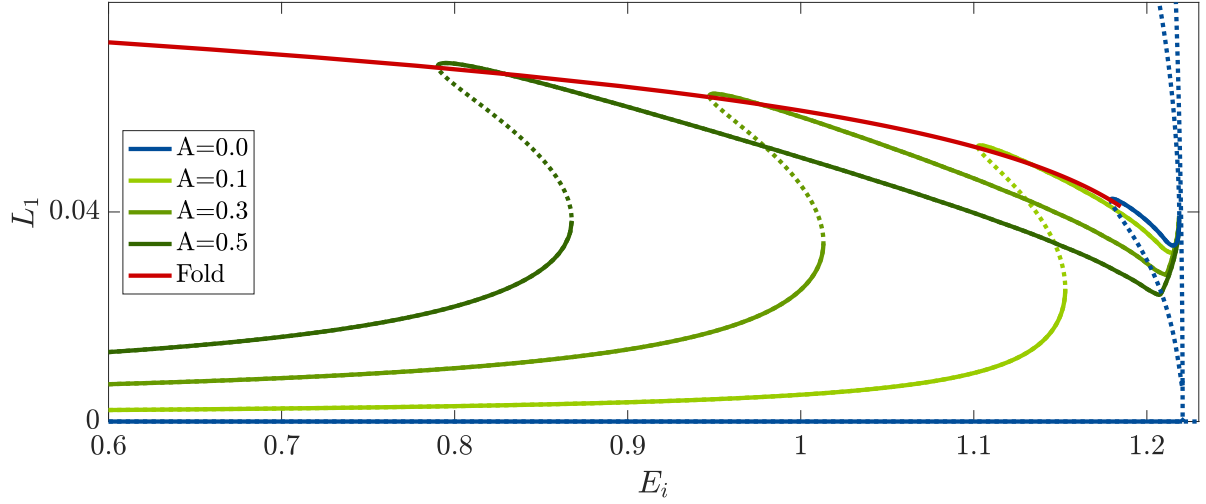
Figure 4.16: First LS branch of the homoclinic snaking diagram for different amplitudes of the inhomogeneity A (green lines), showing that the widening effect of the inhomogeneity increases drastically with growing amplitude. The red branch depicts a fold continuation marking the position of the left fold as a function of A. A more comprehensive depiction of the fold continuation can be found in Fig. 4.17. A similar figure was also published in [TFHP+19].
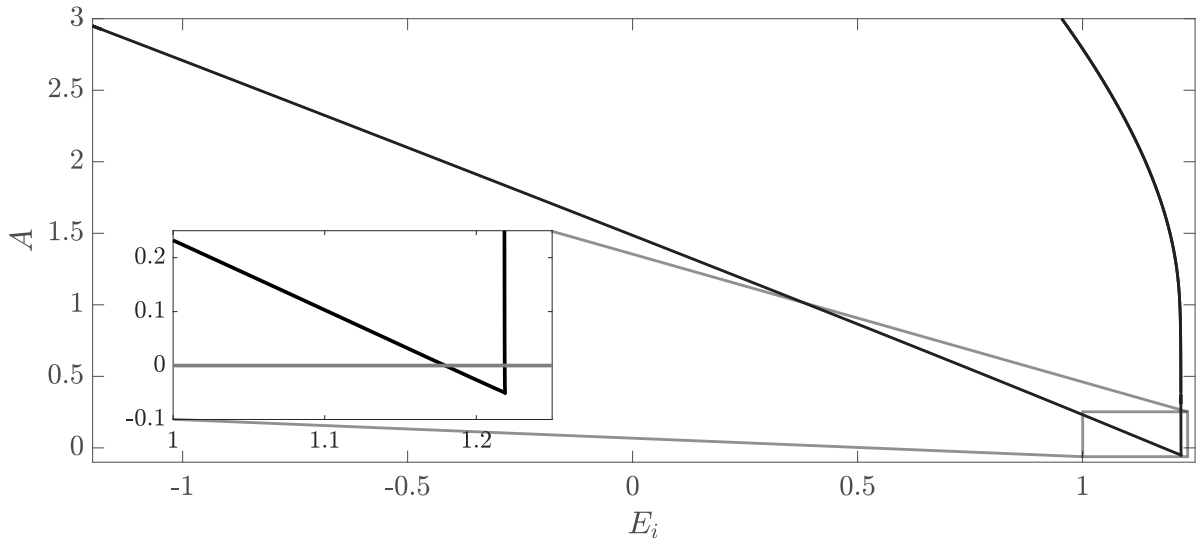

Figure 4.17: Results of a fold continuation depicting the position of the left and right fold delimiting the stability of single LSs as a function of A and E_i. In between the two lines, single LSs exist and are stable. The widening effect of an increasing amplitude of the inhomogeneity is again visible. The inset emphasizes that single LS pinned on the center also exist for negative A, although they are unstable (compare Fig. 4.19). For better visibility, the gray line in the inset marks $A = 0.0$. At a value of $A \approx -0.05$, the two folds collide, i.e., for lower values of A, no LSs pinned on the center of the inhomogeneity exist.

positive values of A act attracting on LS in this parameter regime, the LS pinned on the center of the inhomogeneity also persists for small negative values of the inhomogeneity before both folds collide at $A \approx -0.05$ and the LS vanishes for values of $A < -0.05$. However, as will be shown in the following, the solution pinned on the center of the inhomogeneity only exists as an unstable solution in this rather narrow regime of negative A.

This observation brings up the question, which kind of LSs, if any, exist for negative values of A. We therefore perform a similar analysis by means of path continuation as depicted in Fig. 4.15, starting now with the quasi-homogeneous solution for a small negative value of $A = -0.1$. The results can be found in Fig. 4.18, showing the bifurcation diagram in the center of the figure and the quasi-homogeneous solution on the bottom left. With increasing E_i, the quasi-homogeneous solution (lowest blue branch) becomes destabilized in a subcritical pitchfork bifurcation immediately followed by a fold. Following the blue branch, a pair of peaks forms at either side of the inhomogeneity. The solution profiles on the blue branch at the positions marked with a circle are depicted on the left side of Fig. 4.18, showing a close resemblance to the even branches of the homoclinic snaking without inhomogeneities in Fig. 4.12. In contrast to the case of homogeneous injection, the snaking diagram does not connect to a homogeneous solution but starts to wind down again, once the domain is filled with peaks.

It is also worthwhile to take a closer look at the subcritical pitchfork bifurcation close to the first fold in which an odd solution (green) branch bifurcates from the quasi-homogeneous solution. On this branch a single peak solution with one peak pinned on the side of the inhomogeneity is formed. This asymmetric branch resembles in its origin and in its solution profile the so-called ladders [BK06]. Ladders are asymmetric multi-peak solutions, which connect the even and the odd branches of a homoclinic snaking curve, they typically bifurcate close to the folds and are called ladders due to their small incline. Following the green branch, solution profiles at the positions marked with a cross are depicted on the right side of Fig. 4.18, showing that in this symmetry-broken version of a homoclinic-snaking diagram, peaks are not added in pairs to the solution but the solution gains additional peaks one by one. Since the depicted L_1-norm of an n-peak solution does not differ greatly for different peak positions, the green and the blue branch overlap when both branches show an even number of peaks. One can note that similar bifurcations to the one leading to the emergence of the green branch can be found close to every fold of the blue branch as is the case with so-called ladders [BK06]. The additional branches emerging from these bifurcations are not depicted in Fig. 4.18 for the sake of clarity but these branches would also exhibit solutions that show an unequal number of peaks on each side of the inhomogeneity. Therefore, not only the completely symmetric and the completely asymmetric case as depicted in Fig. 4.18 are possible, but every configuration of peaks on either side of the inhomogeneity.

Concerning the single LSs, which are the main subject of this thesis, we can now assess that in the parameter regime around $\theta = 1.7$, stable single LSs for both positive and negative values of A exist. In the case of positive A, the inhomogeneity acts attracting, i.e., LSs pinned on the center of the inhomogeneity are stable. In the case of negative A, the inhomogeneity acts repelling on the center of the LS and the LS pins with its side-minimum on the inhomogeneity which we refer to in the following as a LS pinned on the side of the inhomogeneity. We now investigate how both solution types change with varying A. Figure 4.19 shows the result of a numerical continuation for $\theta = 1.7$ and a fixed homogeneous injection of $E_i = 1.2$. There, the green line depicts the solutions pinned on the side, which are stable for negative A, while the blue line depicts the solution pinned on the center of the inhomogeneity, which is stable for positive A. Both solutions interchange their stability in a transcritical bifurcation at
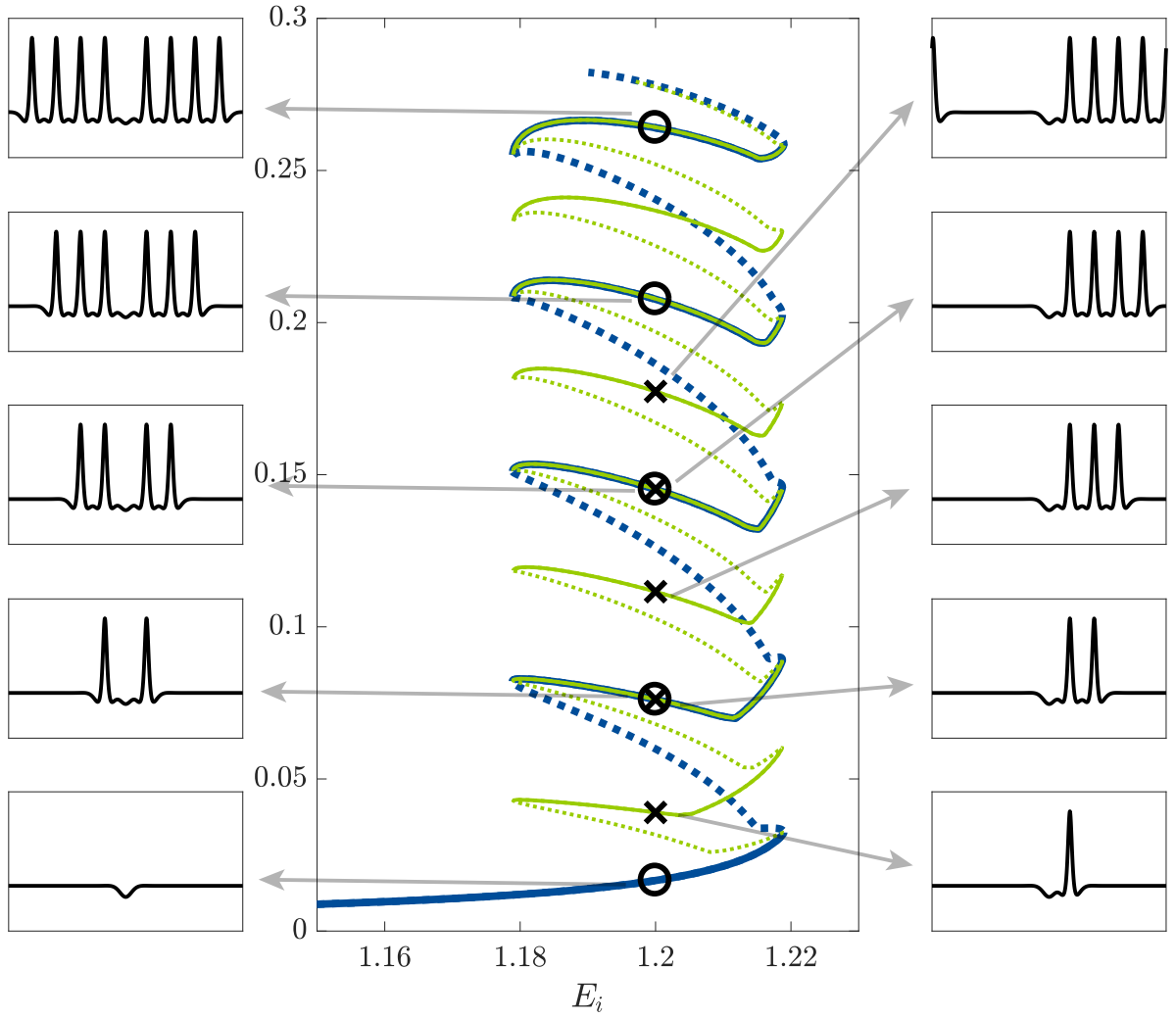
Figure 4.18: Bifurcation diagram showing homoclinic snaking in the presence of an inhomogeneity with a negative amplitude of $A = -0.1$. All other parameters as in Fig. 4.15. The quasi-homogeneous solution (lowest blue branch, solution profile depicted on the lower left) evolves into a solution with a peak on each side of the inhomogeneity. This branch (blue line) undergoes the classical homoclinic snaking pathway, with additional peaks growing on each side throughout the snaking. Solution profiles at the positions marked by circles are depicted in the left panels. Shortly before the first fold of the even branch, a single peak solution (solution profile on the lower right) bifurcates in a subcritical pitchfork bifurcation. This solution undergoes a symmetry broken snaking where with each second fold only one peak is added to the solution profile. Peaks are only added on the far side of the inhomogeneity. Solution profiles at the positions marked by the crosses are depicted in the right panels. Both the green and the blue branch overlap substantially, since, e.g., a two-peak solution possesses essentially the same L_1-norm, regardless of the position of the peaks. It should be noted that none of the branches connect to a periodic or a quasi-periodic solution branch. If one continues to follow the branch they wind down again towards lower peak solutions.
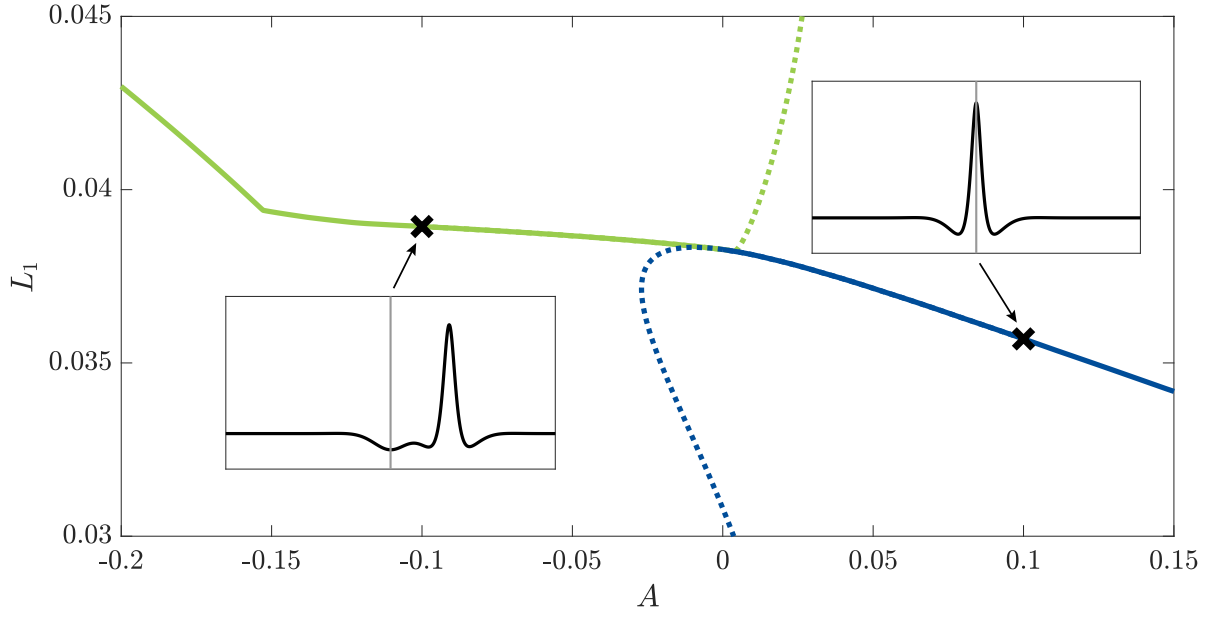
Figure 4.19: Continuation of Eq. (4.5) with A as the continuation parameter for $\theta = 1.7$, $E_i = 1.2$. As suggested by the previous results, the solution pinned on the center (blue line, right inset) is stable for positive A, while the solutions pinned on either side of the inhomogeneity (left inset, green line) are stable for negative A. Both solution types interchange stability in a transcritical bifurcation at $A = 0$. The centered solution exists (although unstable) in a narrow parameter regime of negative A before turning in a fold. The same goes for the solution pinned on the side for positive A. The figure was also published in [TFHP$^+$19].

$A = 0$. Note that, although both peaks are situated at different positions, the solutions are mathematically identical at the bifurcation point, since the vanishing of the inhomogeneity restores the translational symmetry of the system. As can be seen in Fig. 4.19, the solution pinned on the center exists for small negative values of A, which is in good agreement with the results presented in Fig. 4.17, where it was shown that the folds delimiting the stability of LS pinned on the center collide at a value of $A \approx -0.05$.

We have now thoroughly discussed the formation of LSs in the presence of small inhomogeneities in the homoclinic snaking regime. The results in this regime are rather promising since it was shown that one can create a comparatively broad region of monostability, where only a single LS exists by introducing small positive inhomogeneities. In general the effect of the inhomogeneity apart from the quantitative details is rather simple in this parameter regime: A local increment of the injected field leads to an attraction and stabilization of LSs, while locally decreasing the injection repels LSs. We will now turn towards larger values of the detuning, which have been widely discussed in the context of Kerr comb generation [PRGGK18a]. In this case we shall see, that the effects of inhomogeneities are far more complex.

4.2.2 The effect of inhomogeneities in the region of high detuning

We are now focusing on the region of higher detuning, where LSs in the case of homogeneous injection arise after bifurcating directly from the unstable homogeneous solution (see section 4.1.3). The homoclinic snaking breaks up in this parameter regime and is replaced by a so-called foliated snaking [PRGGK18a]. In the following we fix the detuning to $\theta = 3.0$ and analyze the emergence of single LS. As discussed previously, bound states of LSs do not exist in this region due to the lack of oscillatory tails. The behavior of equidistantly positioned LS will not be in the scope of this section. Since these structures hardly interact with each other, one can deduce their behavior in the presence of inhomogeneities from the study of a single LS, which we present in the following.

Again starting with a comparatively small inhomogeneity of $A = 0.1$, we first deploy a parameter continuation in E_i starting from the quasi-homogeneous solution. Figure 4.20 (top panels) shows that the emergence of single LSs from the quasi-homogeneous solution (blue line) resembles the case of lower detuning depicted in Fig. 4.15. In two consecutive folds, the solution goes from the quasi-homogeneous solution to a LS pinned on the center of the inhomogeneity (blue line). In contrast to the case of lower detuning, another bifurcation sets in at $E_i \approx 1.66$: In a supercritical pitchfork bifurcation, the LS pinned on the center of the inhomogeneity (blue line) looses stability and two stable solutions emerge (green line), which move away from the center with increasing E_i until they come to a halt at the side of the inhomogeneity. The bottom panel of Fig. 4.20 emphasizes this pitchfork bifurcation by using the center of mass position as a measure instead of the L_1-norm.

The aforementioned observation is rather surprising for two reasons: First of all, in contrast to the case of lower detuning or the Swift-Hohenberg case described in chapter 3, a given inhomogeneity of a fixed amplitude changes its impact on LSs from attracting to repelling, depending on other system parameters (E_i in this case). Secondly, shortly after the bifurcation the stable LSs are positioned very close to, but not directly on the center of the inhomogeneity. In section 4.2.1, the LSs were either positioned directly at the center, meaning they pinned to the inhomogeneity with its maximum, or pinned on the side, pinning to the inhomogeneity with its first minimum. In the present case, none of the above explanations applies shortly after the bifurcation point, the LSs seem to be positioned at an arbitrary position close to the
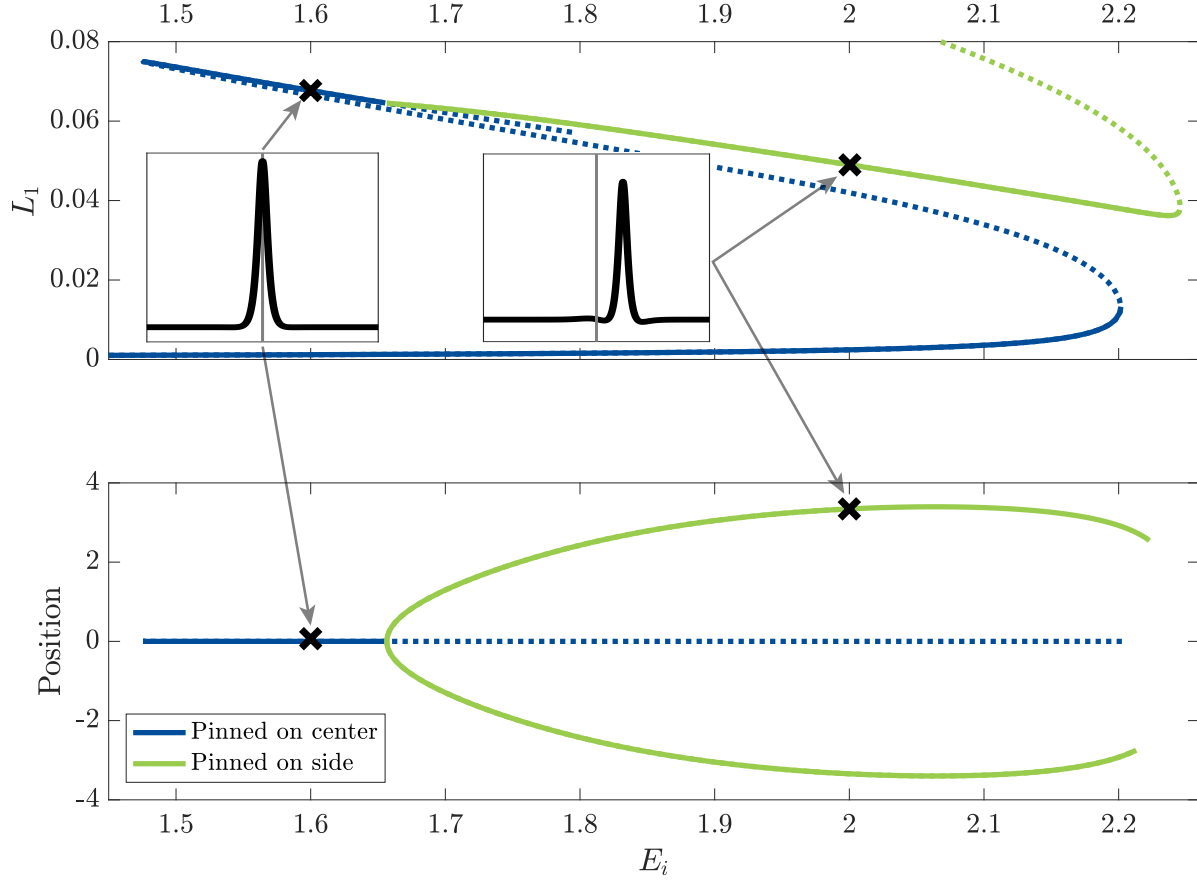
Figure 4.20: Emergence of a single LS in the non-snaking regime of $\theta = 3.0$ for an inhomogeneity with $A = 0.1$, $B = 4.0$. The continuation parameter is E_i. As a measure, we use the L_1-norm (top) and the position of the center of mass of the LS (bottom) respectively. As in Fig. 4.15, the stable LS pinned on the center arises from the quasi-homogeneous solution in a sequence of two folds (blue line). Unlike the case of lower θ, the solution pinned on the center (blue line, left inset) looses stability in a supercritical pitchfork bifurcation at $E_i \approx 1.66$ with respect to translational perturbations. Two new LS solutions positioned on either side of the inhomogeneity (green line, right inset) arise. The characteristic pitchfork shape of the bifurcation diagram is better visible in the lower representation, since the left and the right solution coincide when solely depicting the L_1-norm. The gray vertical line in the insets marks the center of the inhomogeneity in order to differentiate a solution pinned on the center from a solution pinned on the side. A similar figure was also published in [TFHP+19].

maximum of the inhomogeneity.

This striking behavior can be explained by taking into account the results of Hendry et al. [HCW+18]. Assuming a completely Gaussian injection in the LLE, they discovered that above a critical value of $\theta \approx 2.25$, LS are not drawn towards the maximum value of injection, but that in this regime certain ideal values $E_{\text{ideal}}(\theta)$ exist, which only depend on the detuning and strongly attract LSs.

The ideal value for the case of $\theta = 3.0$ is $E_{\text{ideal}} \approx 1.76$, which allows us to understand the behavior observed in Fig. 4.20: As long as $E_i + A < E_{\text{ideal}}$, even the injection at the peak of the Gaussian is smaller than the preferred value of the LSs. In this case, the LSs are attracted by the maximum possible injection leading to stable LS pinned on the center of the inhomogeneity. The position of the pitchfork bifurcation is defined by $E_i + A = E_{\text{ideal}}$, which is where the ideal value of injection is reached at the center of the inhomogeneity. Going slightly beyond the bifurcation point, to $E_i + A > E_{\text{ideal}}$, the injection at the center of the inhomogeneity slightly exceeds the ideal value E_{ideal}, however E_{ideal} can be found in the close vicinity of the center of the inhomogeneity, which is where the center of the LS is positioned, thus explaining the slight shift away from the center of the inhomogeneity. Going further away from the bifurcation point to a region where the homogeneous portion of the injection alone exceeds the ideal value ($E_i > E_{\text{ideal}}$), there is no point in the domain, where the ideal value of injection is present. In the case of Fig. 4.20, this results in the previously discussed situation, where the LS pins to the inhomogeneity with its first minimum, i.e., varying E_i in this parameter region does not results in a drastic change of position of the LS pinned on the side. The slight shift in position that can be seen in the bottom panel of Fig. 4.20 is due to a change in shape of the LS with increasing E_i.

Taking into consideration both single LSs pinned on the center as well as single LSs pinned on the side, the parameter regime where stable single LSs exist spans from the left fold inducing a stability of the centered solution to the right fold delimiting the stability of the solution pinned on the side. Figure 4.21 shows, how the left fold (blue line) and the right fold (green line) are positioned in an E_i-A parameter plane for $\theta = 3.0$. The orange line marks the position of the pitchfork bifurcation responsible for the change of stability from LSs pinned on the center in the blue area to LSs pinned on the side in the green area. It is worth noting that LSs pinned on the center exist as unstable solutions in most parts of the green area, whereas solutions pinned on the side do not exist in the blue area. In general, Fig. 4.21 shows that the widening effect of the inhomogeneity is not as strong compared to the case of lower detuning in Fig. 4.17, because in the present case both folds are strongly shifted by the inhomogeneity. However, a slight increment of the width is still notable.

As in section 4.2.1, we now turn towards a more detailed analysis of the transitions between the different stable LSs by employing parameter continuation in A. In contrast to the previously discussed case, one now has to differentiate two fundamentally different scenarios, because the homogeneous portion of the injection E_i can be either larger or smaller than the ideal value of injection E_{ideal}, which will fundamentally affect the bifurcational structure with varying A. We therefore investigate both cases separately. Figure 4.22 shows the bifurcation structure in A of single LSs for $\theta = 3.0$ and $E_i = 1.6$, i.e., $E_i < E_{\text{ideal}}$, whereas Fig. 4.23 shows the same diagram for an increased value of $E_i = 2.0 > E_{\text{ideal}}$.

Starting with the analysis of the case $E_i < E_{\text{ideal}}$ depicted in Fig 4.22, one can identify three qualitatively different regimes: In the case of $A < 0$, the situation is straightforward. The overall injection E_i already lies below the ideal value. Locally lowering the injection further by means of the inhomogeneity leads to a repulsion from this area of decreased injection. Since the
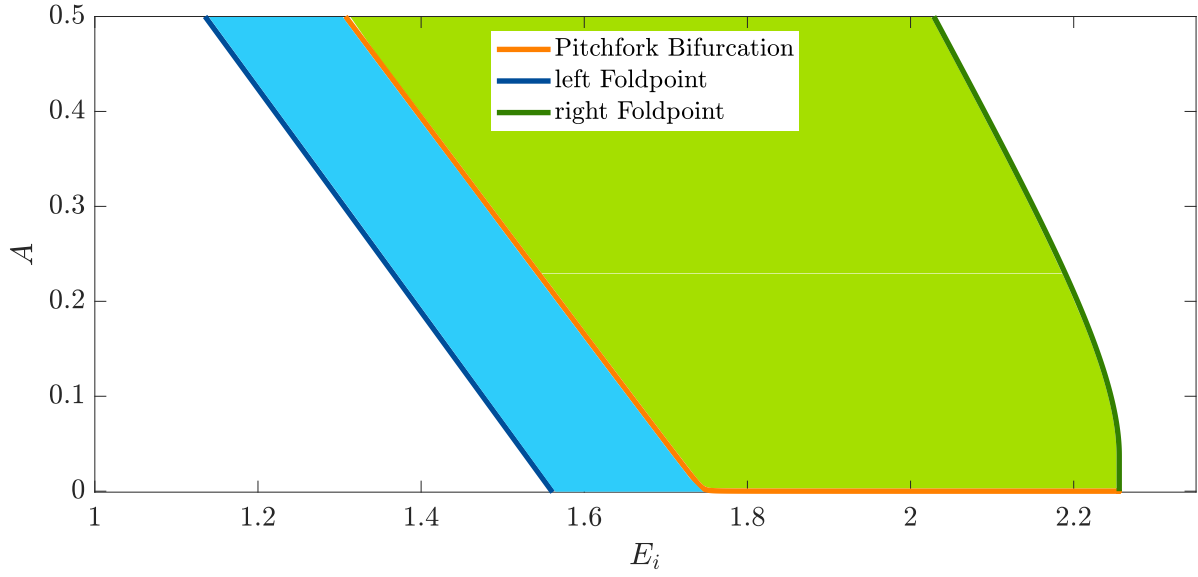
Figure 4.21: Fold and bifurcation continuation in the E_i-A plane for $\theta = 3.0$ marking the position of the left fold (blue line), the position of the right fold (green line) and the position of the pitchfork bifurcation (orange line) which gives rise to the solutions pinned on the side (cf. Fig. 4.20). The blue colored area marks the region of stability of centrally pinned LSs, whereas the green area marks the region of stability of LSs pinned on the side of the inhomogeneity. Note, that a solution pinned on the side does not exist in the blue area, although a centrally pinned solution exists throughout most of the green area, although as an unstable solution. A similar figure was also published in [TFHP$^+$19].
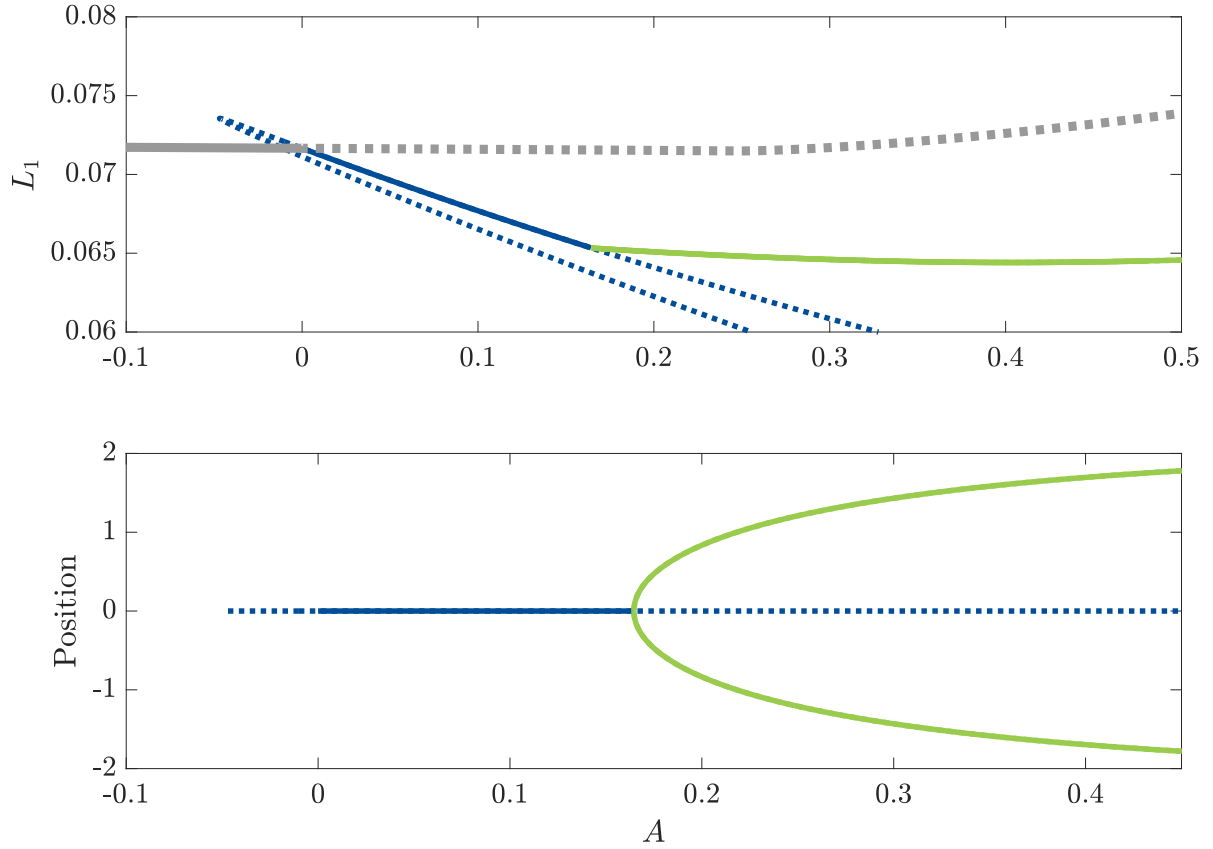
Figure 4.22: Bifurcation diagram for varying A and fixed $\theta = 3.0$. The homogeneous portion of the injection is $E_i = 1.6$, which is below the ideal value for LSs $E_{\text{ideal}} \approx 1.76$. In the upper (lower) representation the L_1-norm (position) is used as a measure. Two bifurcations can be identified, separating three qualitatively different parameter regimes: For $A < 0$, the inhomogeneity acts repulsive on LSs, hence a single LS positioned at the maximum distance of the inhomogeneity is stable (gray line). At $A = 0$ this solution interchanges stability with an LS pinned on the center of the inhomogeneity (blue line) in a transcritical bifurcation. I.e., the inhomogeneity now acts attracting. It should be noted that the stability change of the gray branch can not be detected with numerical continuation techniques since the influence of the inhomogeneity on this solution is extremely weak. However one can account for this stability change with analytical arguments. When the ideal value of injection is exceeded (in this case $E_i + A > 1.76$), the center of the inhomogeneity becomes again repulsive leading to the destabilization of the blue branch in a supercritical pitchfork bifurcation. The pitchfork bifurcation is best recognized in the lower representation, showing two stable solutions positioned at the side of the inhomogeneity which bifurcate from the solution pinned on the center. The figure was also published in [TFHP$^+$19].

LSs do not possess a side-minimum in this parameter regime, the inhomogeneity acts repelling in the whole domain leading to LSs which are pushed away to the borders of the domain. In the case of periodic boundaries considered here, this leads to stable LSs (gray line) which are positioned at the maximum possible distance from the inhomogeneity, i.e., at the domain borders.

At $A = 0$ the inhomogeneity goes from repelling to attracting. Although the ideal value of injection is still not reached anywhere in the system, LSs are drawn towards the maximum value of injection, which now is at the center of the inhomogeneity. This results in a transcritical bifurcation similar to the one depicted in Fig. 4.19, where the solution positioned at the side of the domain (gray line) interchanges stability with a solution pinned on the center of the inhomogeneity (blue line). The change in stability of the solution on the side of the domain (gray line) can actually not be detected numerically because the influence of the Gaussian inhomogeneity numerically vanishes at these distances. However, considering that the Gaussian decays monotonically one can argue that the force excerted on LSs has to go from monotonically repulsive to monotonically attractive when A changes its sign.

Further increasing E_i eventually leads to the point where $E_i + A = E_{ideal}$, i.e., where the injection at the center of the inhomogeneity matches the ideal value of injection. This is the point where, when varying E_i as a continuation parameter, a pitchfork bifurcation sets in (cf. Fig. 4.20). The same behavior can be observed when varying A around this bifurcation point. As soon as the injection at the center of the inhomogeneity slightly surpasses the ideal value, the LSs are pushed away from the center towards the ideal value which can be found close to the center. In Fig. 4.22, this results in a supercritical pitchfork bifurcation in which two new stable solutions positioned on the side of the inhomogeneity (green line) emerge, while the solution positioned on the center of the inhomogeneity (blue line) looses stability.

To summarize, in the case of $E_i < E_{ideal}$, three qualitatively different stable LSs can be found. That is, depending on A they can be positioned at the maximum distance of the inhomogeneity (gray line), at the center of the inhomogeneity (blue line) or on the side of the inhomogeneity (green line).

We now discuss the case of $E_i > E_{ideal}$ depicted in Fig. 4.23 in a similar way, this time starting with positive values of A. Since the homogeneous portion of the injection already surpasses the ideal value of injection, any local additional contribution of positive A will lead to the repulsion of LSs from the center of the inhomogeneity. In contrast to the similar case of negative A in Fig. 4.22, LSs possess a side minimum at this value of E_i, which results in the pinning of the LS on the side of the inhomogeneity (green line). At $A = 0$ a transcritical bifurcation can be found, where this solution pinned on the side interchanges stability with a solution pinned on the center (blue line). Again, the explanation for this change of stability is straightforward: As long as the overall injection is still above the ideal value everywhere in the domain, LSs are drawn towards the value of injection that comes closest to the ideal value (i.e., the smallest). For small negative A this value can be found at the center of the inhomogeneity.

The stability changes again, when A is lowered until $E_i + A = E_{ideal}$. Now, for the first time the ideal value of injection is present in the system. Lowering A further below this point will cause the LSs to be repelled from the center of the inhomogeneity, because now the ideal value of injection can be found close to the center, whereas the injection at the center is lower than the preferred value. This again results in a pitchfork bifurcation, where the solutions pinned on the side (green line) branch off, while the solution pinned on the center (blue line) looses stability. In contrast to Fig. 4.22, here only two qualitatively different solutions exist, since LSs can only be positioned at the center or on the side of the inhomogeneity. It is however
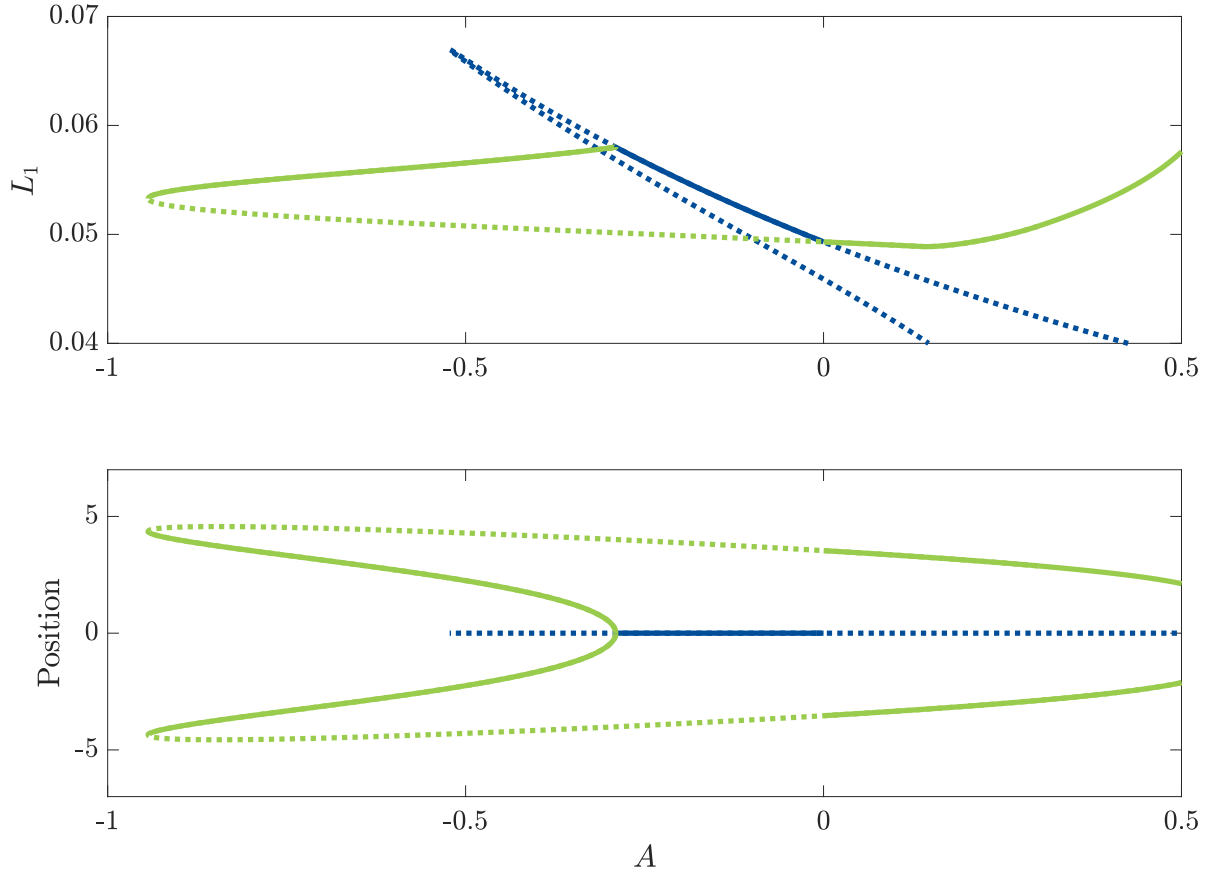
Figure 4.23: Bifurcation diagram for varying A and fixed $\theta = 3.0$. The homogeneous part of the injection is $E_i = 2.0$, which is above the ideal value for LSs $E_{\text{ideal}} \approx 1.76$. In the upper (lower) representation the L_1-norm (position) is used as a measure. As in Fig. 4.22, two bifurcations can be identified, separating three qualitatively different parameter regimes: For $A > 0$, the inhomogeneity acts repelling on LSs since the homogeneous part of the injection E_i is already larger than E_{ideal}. In contrast to Fig. 4.22, the LSs are not pushed towards the side of the domain but stabilize at the side of the inhomogeneity (green line). At $A = 0$, this solution interchanges stability with a centrally pinned solution (blue line). For small negative values of A, this solution is stable, i.e., LSs are drawn towards the minimal value of the overall injection. This behavior changes, when the overall injection $E_i + A$ at the center falls below the ideal value E_{ideal}: In this case the inhomogeneity again acts repelling, pushing LSs towards the ideal value of injection. This results in a stable solution pinned on the side emerging in a Pitchfork bifurcation (green line). The pitchfork behavior is best recognized in the lower representation, whereas the transcritical nature of the bifurcation at $A = 0$ is more obvious in the upper representation since the two branches interchanging stability do not intersect in the lower representation because they exist at different positions. They are however mathematically identical due to periodic boundary conditions and the restored translational symmetry at $A = 0$. The figure was also published in [TFHP+19].

worth noting that although the solutions pinned on the side are stable in the region of positive and large negative values of A, the two solution branches are connected by an unstable solution branch as can be seen in Fig. 4.23.

It was shown that, although the positioning of LSs in this parameter regime seems rather arbitrary and confusing at first glance, it can be explained very well by the ad-hoc assumption that certain ideal values of injection exist which act attracting on LSs. The assumption first made by Hendry et al. [HCW$^+$18] seems very well justified, since it was verified in direct numerical simulations in the original paper and also agrees very well with the presented results from numerical continuations. However, an analytical proof or a comprehensible explanation why LSs are drawn to these exact values is still needed.

4.2.3 The potential well model for the inhomogeneous Lugiato-Lefever equation

Since the impact of inhomogeneities in the injection on LSs is intriguing especially in the region of high detuning discussed in the previous section, it seems promising to apply the potential well approach derived in chapter 3 for the Swift-Hohenberg equation to the LLE. The derivation is completely analogous to the already discussed case and will therefore not be repeated here. The basic idea is that the change of shape of the LS when moving in the vicinity of the inhomogeneity can be neglected. Therefore, the dynamics of the LS can be reduced to an ODE describing the time evolution of the variable $R(t)$ which is the distance from the center of mass of the LS to the center of the inhomogeneity. Following the derivation presented in [TSTG17] (see also section 3.2.4) now neglecting the delayed term yields:

$$\dot{R} = -\frac{1}{\int \partial_\xi \mathbf{E}_{\mathrm{hls}}(\xi) \cdot \partial_\xi \mathbf{E}_{\mathrm{inhls}}(\xi) d\xi} \int \left\{ \mathrm{Re}[\partial_\xi E_{\mathrm{hls}}(\xi)] \, A e^{-(\xi+R)^2/B} \right\} d\xi =: F(R), \qquad (4.7)$$

where $\mathbf{E}_{\mathrm{hls}}(\xi)$ refers to the stationary LS in the homogeneous case ($A = 0$) written as a vector-function with the real and imaginary part as separate components, whereas $E_{\mathrm{hls}}(\xi)$ refers to the same solution not written in vector form but as a complex-valued function. Furthermore, $\mathbf{E}_{\mathrm{inhls}}$ is the stationary centered LS solution in the presence of the inhomogeneity (stable or unstable) also written in vector form. The right hand side of Eq. (4.7) can be interpreted as the force $F(R)$ excerted by the inhomogeneity on an overdamped particle at position R representing the LS. The corresponding potential $V(R)$ therefore is defined as:

$$-\partial_R V(R) = F(R), \qquad (4.8)$$

and can be calculated by numerically evaluating the integrals in Eq. (4.7). It has to be noted however, that the derivation looses its validity for large values of A since in this case the shape deformation due to the inhomogeneity can not be neglected anymore.

Two examples of the calculated potential $V(R)$ are depicted in Fig. 4.24, showing the potentials for the two solutions depicted in Fig. 4.20, i.e., for $\theta = 3.0$, $A = 0.1$ and $E_i = 1.6$ (left) and $E_i = 2.0$ (right), respectively. The transition from an attracting to a repulsive inhomogeneity, which has been discussed in the previous section can be reproduced by the potential well approach. Furthermore, the center of mass positions of the stable solutions (orange lines), which have been calculated numerically, coincide well with the minima of the potential. The potential well model therefore does not only qualitatively describe the transition from an attracting to a repelling inhomogeneity but can also be employed to quantitatively estimate the position of LSs in the vicinity of an inhomogeneity.
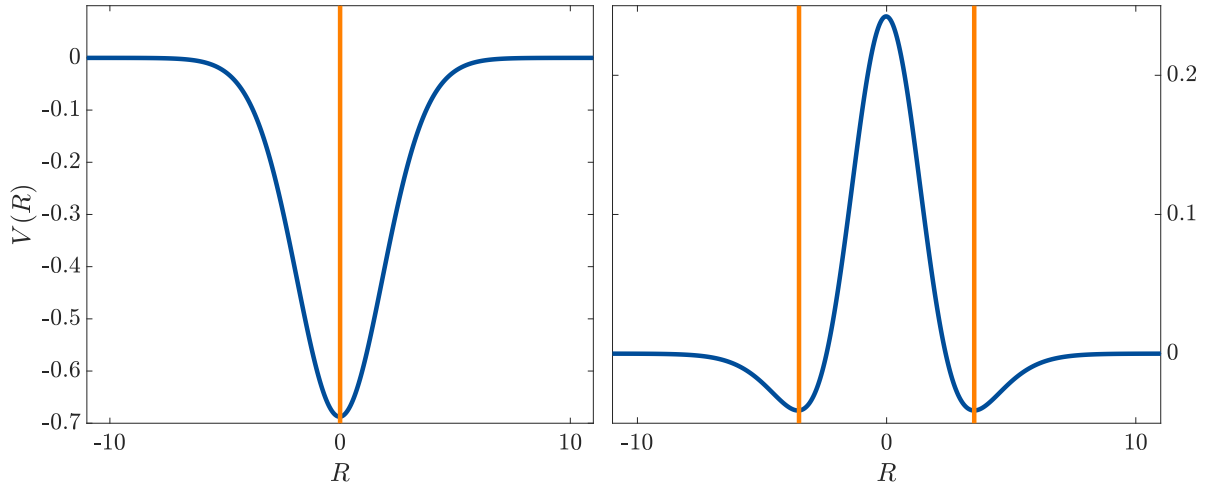
Figure 4.24: Potential $V(R)$ defined by Eqs. (4.7) and (4.8) induced by an inhomogeneity of $A = 0.1$, $B = 4.0$ for $\theta = 3.0$, $E_i = 1.6$ (left) and $E_i = 2.0$ (right). In agreement with the previous results, the inhomogeneity acts attracting in the case of the smaller injection on the left and repelling in the case of larger injection on the right. The orange lines mark the position of the center of mass obtained from numerical continuation showing a good agreement with the minima of the potential. The figure was also published in [TFHP+19].

The potential well model applied to the LLE given by Eq. (4.7) however has one limitation: The examples chosen in Fig. 4.24 both show cases, where the position of the LLE is determined by its shape, i.e., the LSs pin to the inhomogeneity either with their maximum in the attracting case, or with their first minimum in the repelling case. As described previously, in a small parameter regime in between, they are pinned by certain ideal values E_{ideal} of the injection, which can be between minima and maxima. The potential well model does not reflect this behavior and therefore is not suitable to shed light on it. It has to be noted though, that this parameter regime in the presence of small inhomogeneities is rather narrow, which is why the potential well model in general still can be applied successfully to the inhomogeneous LLE given by Eq. (4.5).

4.2.4 Exploration of parameter space

After thoroughly discussing the effects of small inhomogeneities for certain values of θ, we now would like to conclude with a full bifurcation analysis of the effects of a small inhomogeneity of $A = 0.1$ in the θ-E_i plane as we did in the case of homogeneous injection in Fig. 4.14.

In the left panel of Fig. 4.25, the results from Fig 4.14 are again depicted for the sake of comparison. In the right panel, the same analysis consisting of fold continuations and bifurcation point continuations of all relevant folds and bifurcations is carried out. In this case the lighter colored dashed lines represent the case of $A = 0.0$, whereas the solid darker lines show the results for $A = 0.1$. Although the lines marking the position of the right fold (green line) and the Andronov-Hopf bifurcation (red line) are hardly altered by the inhomogeneity, two major differences between the case of homogeneous and inhomogeneous injection can be noted: First of all, the pitchfork bifurcation (orange line) responsible for the transition from
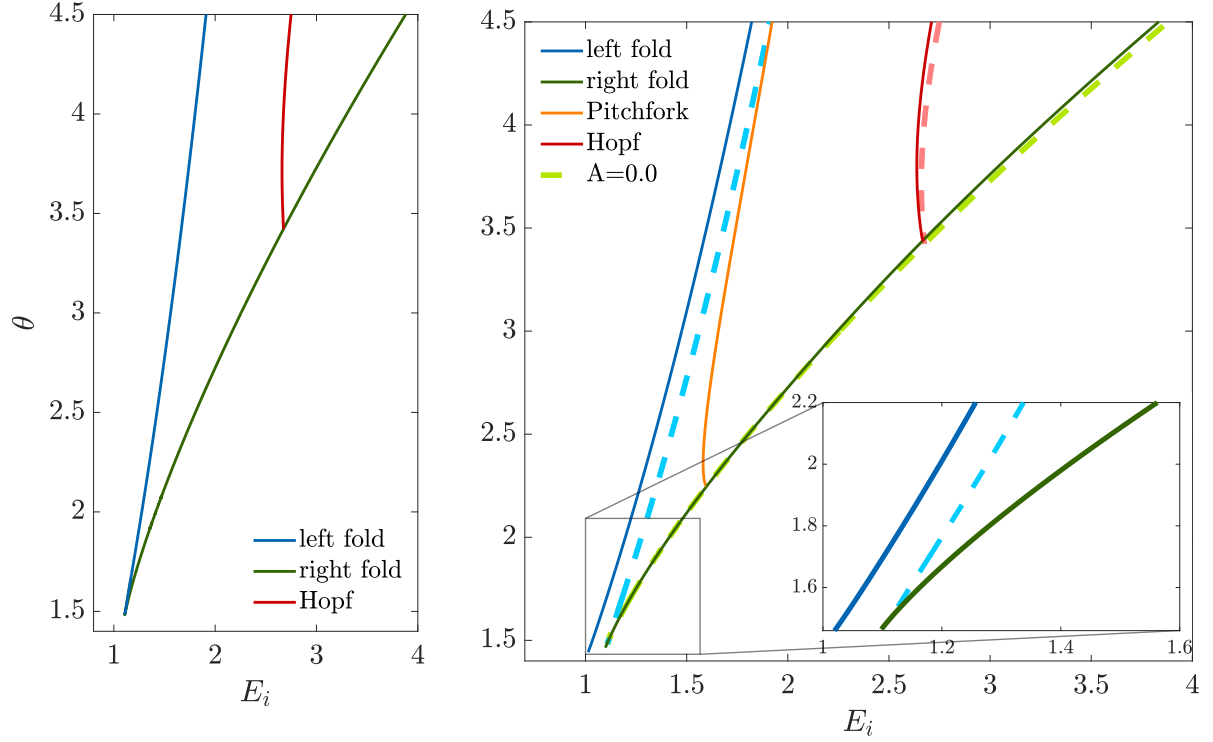
Figure 4.25: Left: Position of the folds and the Andronov-Hopf bifurcation without inhomogeneity (same as in Fig. 4.14) for comparison. Right: Position of the left (blue) and right fold (green) delimiting the existence of single LS. The orange line marks the position of the pitchfork bifurcation responsible for the transition from a centrally pinned LS to a LS pinned on the side of the inhomogeneity. The red line marks the onset of oscillations due to an Andronov-Hopf bifurcation. The lighter shaded dashed lines mark the positions without inhomogeneity for a better comparison. The inset illustrates that the changes due to the inhomogeneity are most drastic in the region of low detuning and mainly affect the position of the left fold. A similar figure was also published in [TFHP+19].

LSs pinned on the center to LSs pinned on the side does not have a counterpart in the case of homogeneous injection (A=0.0), it is solely a result of the inhomogeneity. Second of all, the left fold (blue line), marking the onset of stability of LSs is shifted to lower values of E_i, as has been discussed in section 4.2.1. The absolute shift is approximately constant for all values of θ, however relative to the overall width of the region of stability the shift has its strongest impact in the region of low detuning θ, as can be seen in the inset. The intentional implementation of small inhomogeneities therefore seems especially promising in experimental setups working in this parameter range, since it results in a drastic widening of the region of stability and, as discussed, creates a region of monostability where solely single LSs exist as stable solutions.

4.3 The inhomogeneous Lugiato-Lefever model with time-delayed feedback

In the following section, we introduce time-delayed feedback to the Lugiato- Lefever equation (LLE) to analyze the interplay between destabilizing time-delay and attracting inhomogeneities. Time-delayed feedback in the LLE has been discussed in [TP17, PPV$^+$16] and is typically implemented by introducing an external cavity to the system, where the round-trip time corresponds to the delay-time τ. Again, from a mathematical viewpoint it does not matter whether we consider the LLE in its spatial or in its temporal interpretation, since in principal, an external cavity could be introduced in both cases. However, one has to bear in mind, that the introduction of time-delay in the temporal interpretation would require a very large external cavity with a round-trip time on the time-scale of the slow variable t, while the shape of the solutions on the small time scale ξ has to remain unaltered. It is therefore easier to realize time-delay in the spatial interpretation of the LLE.

We first discuss the effects of time-delay on LSs in the classical LLE, showing how it affects the eigenvalues of stationary solutions and which dynamics can be induced. Furthermore we briefly discuss the stabilization of pulsating LSs by time-delayed feedback. In a second step, we analyze the competing effects of an attracting inhomogeneity and destabilizing time-delay discussing the main differences to the case of homogeneous injection. In the last paragraph, we introduce an inhomogeneous detuning parameter and briefly present similarities and differences to the setup with inhomogeneous injection. However this segment of the thesis constitutes only an introduction to the case of inhomogeneous detuning and therefore requires further investigation.

4.3.1 Delayed feedback in the classical Lugiato-Lefever equation

The LLE with additional time-delay in the form of Pyragas-control [Pyr92, TP17] reads:

$$\frac{\partial E(t,\xi)}{\partial t} = E_{\text{inj.}}(\xi) + \left[-(1+i\theta) + i|E(t,\xi)|^2 + i\frac{\partial^2}{\partial \xi^2} \right] E(t,\xi) + \alpha e^{i\phi} \left[E(t,\xi) - E(t-\tau,\xi) \right],$$

(4.9)

where the injected field $E_{\text{inj.}}(\xi)$ can be inhomogeneous (and thus depending on ξ), however in this paragraph we only discuss the classical case of homogeneous injection $E_{\text{inj.}} = E_i = \text{const.}$ in the presence of time-delayed feedback. The feedback parameters are the delay-time τ, the delay-strength α (sometimes referred to as delay-rate) and the phase-difference of the reinjected field ϕ. In the following we are restricting ourselves to the simplified case of $\phi = 0$, i.e., completely positive or negative interference depending on the sign of α.

As discussed in chapter 3 and in [GF13, Gur13, TSTG17], the Pyragas-control does not affect the stationary solutions of the system, since it vanishes, once a stationary solution is reached and maintained for a time τ. However, the time-delayed feedback can change the stability of the stationary solutions. It is therefore worthwhile to perform a linear stability analysis with and without time-delayed feedback to predict changes which are due to time-delay.

The linear stability analysis of a stationary LS without time-delay is performed by linearizing and spatially discretizing the system around the LS using finite differences. In one dimension the linear stability analysis without inhomogeneities or delay yields a neutrally stable eigenvalue $\mu = 0$ corresponding to an eigenfunction referred to as the Goldstone mode (cf. chapter 3) that, when added to the solution would induce an infinitesimal shift of the LS. The Goldstone mode is followed in the discrete part of the spectrum by two complex conjugated eigenvalues corresponding to modes that would induce a growth or a shrinkage of the LS (see inset of Fig. 4.29). Due to the complex nature of these eigenvalues, a destabilization would lead to pulsating oscillations in the size of the LS.

As discussed in chapter 3, the eigenvalues λ_m in the presence of time-delayed feedback can be calculated from the undelayed eigenvalue μ via:

$$\lambda_m = \mu + \alpha + \frac{1}{\tau} W_m \left[-\alpha\tau \cdot \mathrm{e}^{-\tau(\alpha+\eta)} \right], \qquad m \in \mathbb{Z}, \tag{4.10}$$

where W_m is the mth branch of the implicit Lambert W function, which is defined as the multi-valued inverse of a function $f(z) = z\mathrm{e}^z$. The Lambert W function is in general complex, which is why even for real-valued eigenvalues of the undelayed system μ, one can not rule out the possibility of complex eigenvalues in the delayed case.

In chapter 3 we thoroughly discussed the destabilization of neutral eigenvalues with corresponding translational eigenfunctions or Goldstone modes. Following [GF13, TVPT09], we showed that in the case of $\mu = 0$, the first delayed eigenvalue λ becomes unstable at $\alpha\tau = 1$ and is real-valued. The growth of the highest eigenvalue of the translational mode is depicted in the upper panel of Fig. 4.26 (green line) and shows a sharp kink at $\alpha\tau = 1$. As discussed in the Swift-Hohenberg case, this is the point where the two highest branches of the Lambert W function have the same value.

The real part of the highest delayed eigenvalue λ corresponding to the undelayed eigenvalue of the growth mode is also depicted in Fig. 4.26 for two different choices of the injection E_i (blue and red line), showing that, depending on the injection the growth mode can be destabilized either before or after the Goldstone mode, depending on the choice of parameters. In the case of lower injection $E_i = 2.0$, the Andronov-Hopf bifurcation that occurs when the eigenvalue of the growth mode becomes unstable sets in after the drift bifurcation associated with the destabilization of the Goldstone mode. In the case of higher injection $E_i = 2.6$, the Andronov-Hopf bifurcation sets in before the drift bifurcation, even though the eigenvalue of the growth mode possesses a smaller real part in the undelayed case depicted at $\alpha = 0$.

The bottom panel of Fig. 4.26 depicts zoomed in space-time plots of the dynamics induced by time-delayed feedback. On the left, only the Goldstone mode is unstable leading to a drift of the LS, a scenario which was already discussed in chapter 3. On the right, both the eigenvalues of the Goldstone mode and the growth mode are unstable leading to a drifting and pulsating LS. The case where only the eigenvalue of the growth mode becomes unstable would lead to a LS pulsating on the spot and is not depicted here.

The analysis of LSs in the classical LLE under the impact of time-delayed feedback so far hardly yields new results compared to the chapter on the Swift-Hohenberg equation. However,
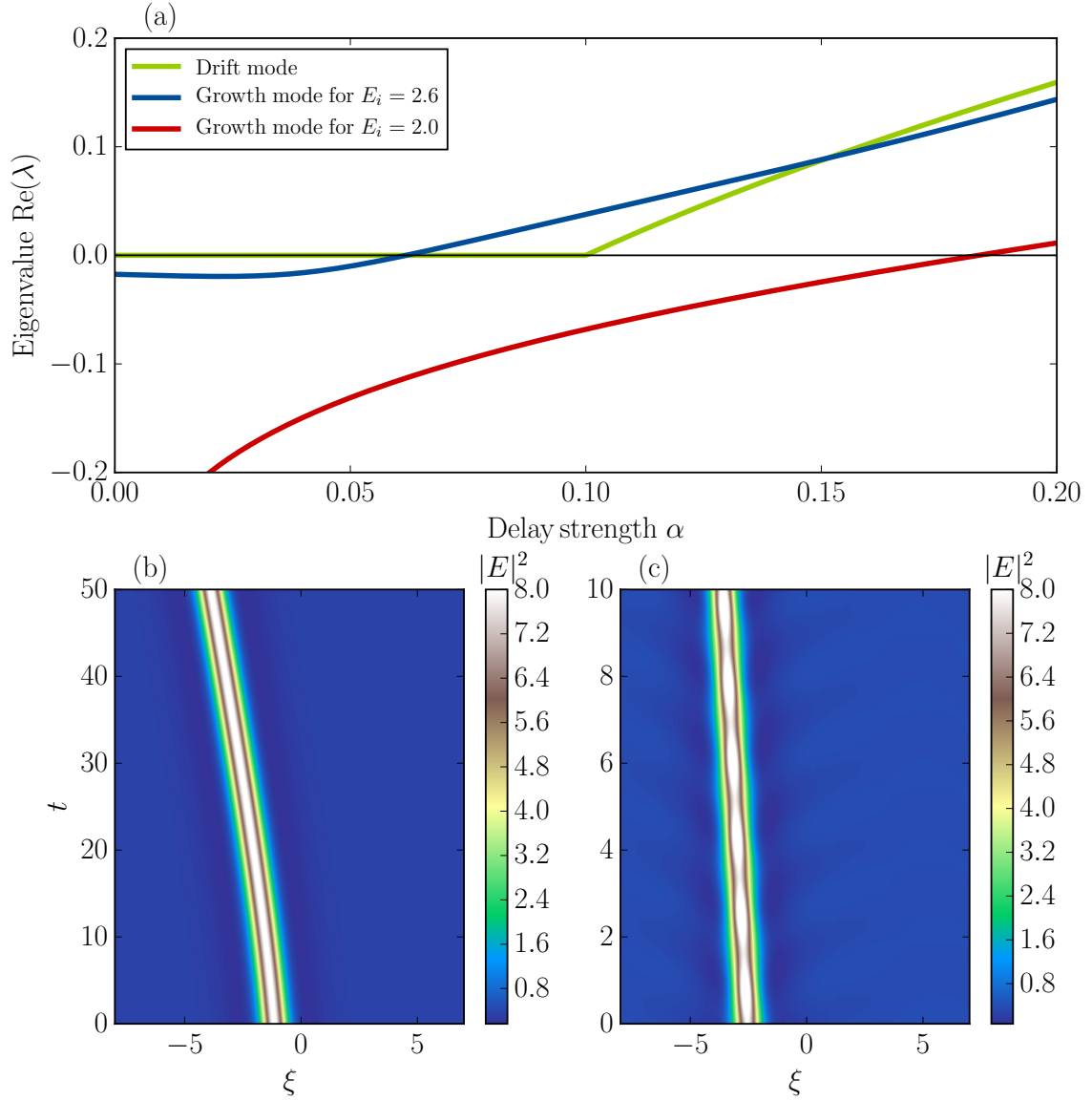
Figure 4.26: Dynamics of LSs in a homogeneous Kerr cavity induced by delayed feedback. (a): Real parts of the eigenvalues $\mathrm{Re}(\lambda)$ as a function of α. The green line corresponds to the eigenvalue of the neutral Goldstone mode leading to the drift bifurcation at $\eta\tau = 1$. The bifurcation point of the growth mode inducing the Andronov-Hopf bifurcation depends on the parameters E_i and θ. The blue and red curves indicate a case when the Andronov-Hopf bifurcation occurs before ($E_i = 2.6$) and after ($E_i = 2.0$) the drift bifurcation, respectively. (b),(c): Space-time plots showing the evolution of the intracavity intensity obtained by numerical integration of Eq. (4.9). (b) Drifting LS obtained for $E_i = 2.0$ and $\alpha = 0.13$; (c) Self-pulsating and drifting LS obtained for $E_i = 2.0$ and $\alpha = 0.19$. Other parameters are $\tau = 10$ and $\theta = 3.5$. All direct numerical time simulations in this section are obtained using a classical Runge-Kutta method for the time-stepping combined with a pseudo-spectral method with periodic boundary conditions to calculate spatial derivatives in Fourier space.
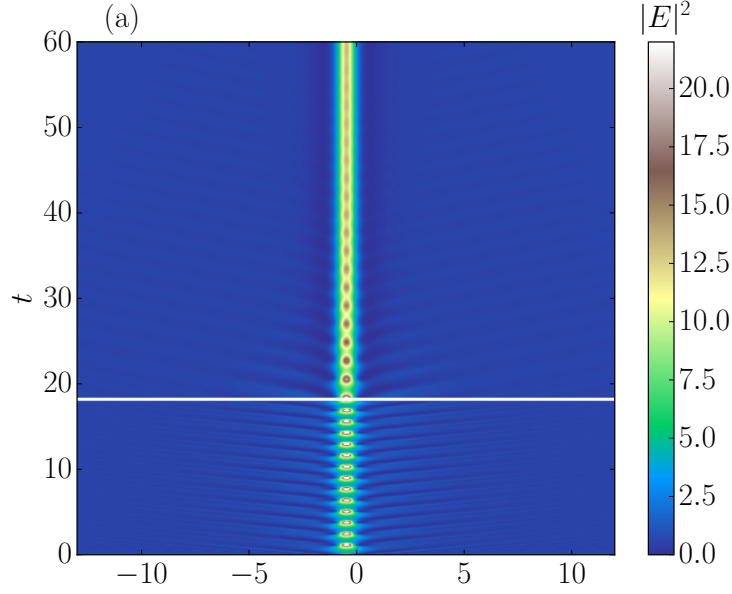
Figure 4.27: Stabilization of a LS by time-delayed feedback in direct numerical simulations represented in a space-time plot. The simulation starts without time-delay, then at the time marked by the white line, the feedback is switched on leading to an immediate stabilization of the LS. Parameters are $\theta = 5$, $E_i = 3.5$, $\alpha = -10$, $\tau = 0.1$.

one has to keep in mind, that the growth mode is also close to instability in the parameter regime we are considering. With increasing E_i, the growth mode becomes unstable even without time-delay leading to oscillations in size. This Andronov-Hopf bifurcation was briefly discussed in section 4.1 and in [PRGM⁺14a] and its position is depicted in Fig. 4.14 and Fig. 4.25 without and with inhomogeneities, respectively.

Going now to a parameter regime, where LS are already Hopf-unstable without feedback, i.e., $\theta = 5.0$, $E_i = 3.5$, one can deploy time-delayed feedback in a stabilizing manner, as was discussed, e.g., in [Gur13] in the context of a reaction diffusion system. In this scenario, one can stabilize an unstable solution by adding negatively interfering feedback (i.e., $\alpha < 0$). Figure 4.27 depicts an initially pulsating LS. At the time marked by the white line, time-delayed feedback is added, which leads to a fast stabilization of the LS.

To analyze the stabilizing potential of time-delayed feedback more systematically, than in the example given in Fig. 4.27, one only has to evaluate Eq. (4.10) for varying values of feedback strength α and delay-time τ. The results of this analysis are depicted in Fig. 4.28, in which the eigenvalues in the presence of time-delay $\lambda(\alpha, \tau)$ are color-coded in a binary system, i.e., black areas represent negative real-parts of the eigenvalue, while white depict areas with $\mathrm{Re}(\lambda(\alpha, \tau)) > 0$. The results show an intriguing pattern of tongue-like structures which was also observed in [Gur13] in the context of a reaction diffusion system. The dependency on the delay parameters is much more complex than in the case of destabilizing feedback, where one essentially could enforce a destabilization by choosing the delay parameters sufficiently large. In the present case, there exist certain values of the delay time, e.g., $\tau = 1.0$, where no stabilization can be achieved at all, no matter how one chooses the delay strength α. Both
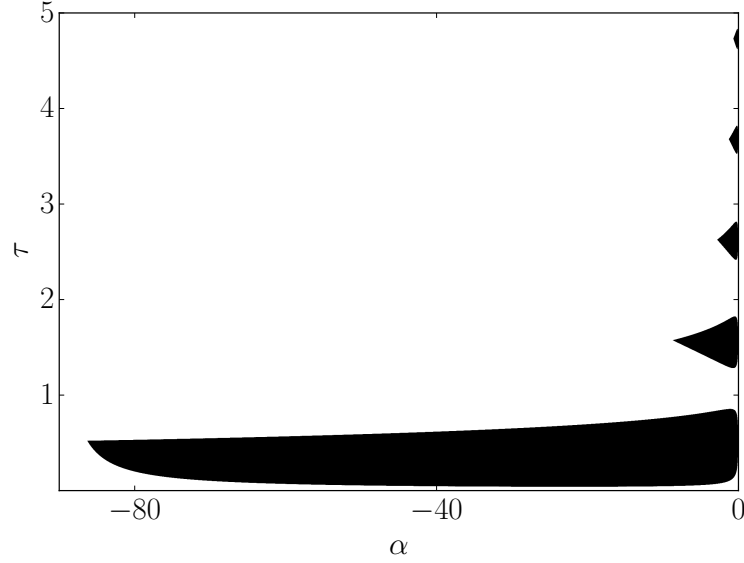
Figure 4.28: Parameter scan determining the regions in which a stabilization of an oscillating
LS $\theta = 5$, $E_i = 3.5$ occurs in an α-τ plane. The black areas mark a stabilization,
i.e., $\mathrm{Re}(\lambda) < 0$. whereas a stabilization can not be achieved in the white areas.
The regions of stabilization show a tongue-like shape and grow smaller with
increasing delay time τ. Furthermore it is worth noting that for certain fixed
values of τ a stabilization can not be achieved at all.

increasing and decreasing τ from this value can lead to a stabilization. Furthermore, one has
to note, that the regions of stabilization become smaller and smaller with increasing τ, i.e., for
large values of τ, one has to choose α very carefully to achieve a stabilization, if a suitable
value of α exists at all. Since small values of the delay time are in general harder to realize
experimentally, this limits the experimental realization of stabilizing time-delayed feedback
drastically.

We will therefore again focus on destabilizing time-delayed feedback and its interplay with
inhomogeneities, while leaving the remarks concerning the possibility of stabilizing feedback
as a side-note.

4.3.2 Interplay between delayed feedback and inhomogeneities

In this paragraph we analyze the interplay between weakly inhomogeneous injection and time-
delayed feedback. The injection $E_{\mathrm{inj.}}$ now reads

$$E_{\mathrm{inj.}} = E_i + A \, \exp\left(-\frac{\xi^2}{B}\right), \tag{4.11}$$

where again E_i is the homogeneous portion of the injected field, A is the amplitude of the
injected field and $\sqrt{B}$ is the width of the Gaussian beam which in the following is fixed as
$\sqrt{B} = 2.0$. We again consider the parameter regime of $\theta = 3.5$, where as discussed in section
4.2.2 both LSs pinned on the center and pinned on the side of the inhomogeneity exist for a

fixed value of A, depending on the value of E_i. First, we choose $E_i = 2.6$, which leads to LSs pinned on the center of the inhomogeneity as stable stationary solutions.

The pinning effect of the inhomogeneity becomes apparent when taking a closer look at the discrete eigenvalues of the LS without delay. In the inset of Fig. 4.29, the three eigenvalues which are closest to the imaginary axis are depicted with and without inhomogeneity. The gray crosses mark the positions without inhomogeneity, showing the previously discussed scenario where one eigenvalue $\mu = 0$ is neutrally stable corresponding to a Goldstone mode of translation, while two complex conjugate eigenvalues are stable $(\text{Re}(\mu < 0))$ and correspond to a growth or shrinkage inducing mode.
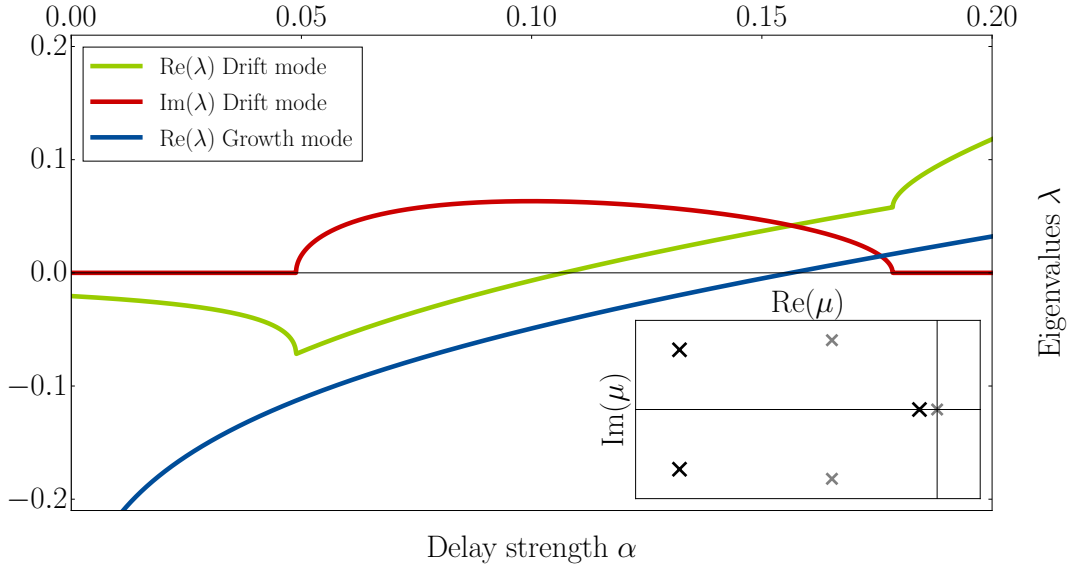

Figure 4.29: Large figure: Real (green) and imaginary (red) part of the eigenvalue of the drift inducing mode as well as the real part of the eigenvalue of the growth inducing mode (blue) for $A = -0.3$, $\theta = 3.5$, $E_i = 2.6$, $\tau = 10.0$ and different values of α. In contrast to the homogeneous case $A = 0$ described in Fig. 4.26, the eigenvalue λ of the drift inducing mode becomes complex around the onset of instability at $\alpha = 0.107$, suggesting an oscillatory behavior. The growth inducing mode becomes unstable in a second Andronov-Hopf bifurcation at larger values of α. Inset: First three eigenvalues μ without delay, with (black) and without (gray) an inhomogeneity of $A = -0.3$. The pinning effect of the inhomogeneity is clearly visible, lowering the real parts of the eigenvalues of both the drift inducing mode and the growth inducing mode.

Considering now an inhomogeneity of $A = -0.3$, the eigenvalues (black crosses in Fig. 4.29) are all shifted towards smaller real parts, i.e., they are stabilized by the inhomogeneity. In particular the eigenvalue of the translational mode, which can not be considered a Goldstone mode anymore due to $\mu \neq 0$ is stabilized, i.e., the system is not invariant to infinitesimal shifts of the LS. Instead such a shift will be damped, pulling the LS towards the center of the inhomogeneity again, which results in a pinning effect of the inhomogeneity.

The fact that the eigenvalue without delay of the translational mode is $\mu \neq 0$, has important consequences for the resulting eigenvalues λ with delay. As discussed in section 4.3.1, equation

(4.10) only yields real eigenvalues λ as highest eigenvalues in the special case where the original eigenvalue $\mu = 0$. Since this is not the case in the presence of the inhomogeneity, one now has to expect the eigenvalues of the translational mode to be complex. In fact, depicting the real (green) and imaginary part (red) part of the eigenvalue λ of the translational mode in Fig. 4.29 for fixed values of $A = -0.3$, $\theta = 3.5$, $E_i = 2.6$, $\tau = 10$ and varying values of the delay strength α shows, that the eigenvalue of the translational mode (or drift mode) undergoes a striking evolution. It is real-valued without delayed-feedback and for small values of α, then becomes complex valued before it becomes unstable at $\text{Re}(\lambda = 0)$. Due to the stabilizing effect of the inhomogeneity, the delay strength necessary for a destabilization is now $\alpha = 0.107$, i.e., $\alpha\tau > 1$, in contrast to the case of homogeneous injection, where it was $\alpha\tau = 1$. For even larger values of α, the eigenvalue becomes real-valued again, suggesting non-oscillatory dynamics. The eigenvalue of the growth mode (blue line) is complex-valued for every choice of delay parameters and becomes unstable after the drift mode for the given set of parameters.

Investigating the effect of time-delayed feedback on the pinned LS is rather straight-forward; we proceed in the same way as in chapter 3. Figure 4.30 shows the delay-induced dynamics of a LS for $\theta = 3.5$, $E_i = 2.6$, $\tau = 10.0$ in the presence of an inhomogeneity of $A = -0.3$ with increasing delay-strength α (from top to bottom). Choosing $\alpha = 0.13$ (Fig. 4.30 (a)), where the drift mode just became unstable leads to an approximately harmonic oscillation in the position of the LS. Further increasing the feedback-strength to $\alpha = 0.15$ (Fig. 4.30 (b)) leads to a growth of amplitude in the oscillations. Furthermore the oscillations become more anharmonic and the LS starts to visibly pulsate in size due to the growth mode which is close to instability. Finally, by increasing the feedback-strength to $\alpha = 0.16$ (Fig. 4.30 (c)), the amplitude of the oscillations grows large enough so that the LS breaks free from the inhomogeneity and starts to drift freely, while still pulsating in size. The value of feedback strength necessary for the depinning lies close to the value where the eigenvalue λ of the drift mode becomes once again real-valued in Fig. 4.29, however, the two values do not match perfectly. This is understandable since oscillations are still visible at the beginning of the simulation in (Fig. 4.30 (c)), the LS does not immediately leave the inhomogeneity. Moreover, nonlinear effects that come into play in the case of large-amplitude oscillations affect the dynamics of the oscillating LS. It would therefore be surprising if one could quantitatively predict the onset of depinning from a purely linear analysis of the stationary solution.

In contrast to chapter 3, we also analyze the destabilization of LSs pinned on the side of an inhomogeneity in the framework of the LLE, since as shown in section 4.2.2, a given inhomogeneity of fixed A can pin LSs on the center or on the side depending on the parameter E_i. As described previously, the pinning on the side can occur because the LS pins to the center of the inhomogeneity with its first minimum resulting in a pinning on the side, or it can pin on the side because the ideal value of injection E_{ideal} is realized at the side of the inhomogeneity. The first case is very well described by the potential well model (see Fig. 4.24), whereas the second case, which only occurs in a small parameter regime around the pitchfork bifurcation associated with the change from stable LSs on the center to stable LSs on the side of the inhomogeneity, cannot be described in terms of the potential well model.

We are therefore treating both cases separately. The latter case, where an LSs is pinned on the side at the ideal value of injection and subsequently is destabilized by time delayed feedback is depicted in Fig. 4.31 for $\theta = 3.5$, $E_i = 2.0$, $A = -0.3$, $\tau = 10$. Again, the delay-strength increases from top to bottom. Starting just above the instability threshold of the drift mode at $\alpha = 0.105$ (Fig. 4.31 (a)) , we see the typical oscillations induced by the unstable drift mode and the attracting inhomogeneity. However, the LS does not oscillate around the center of the
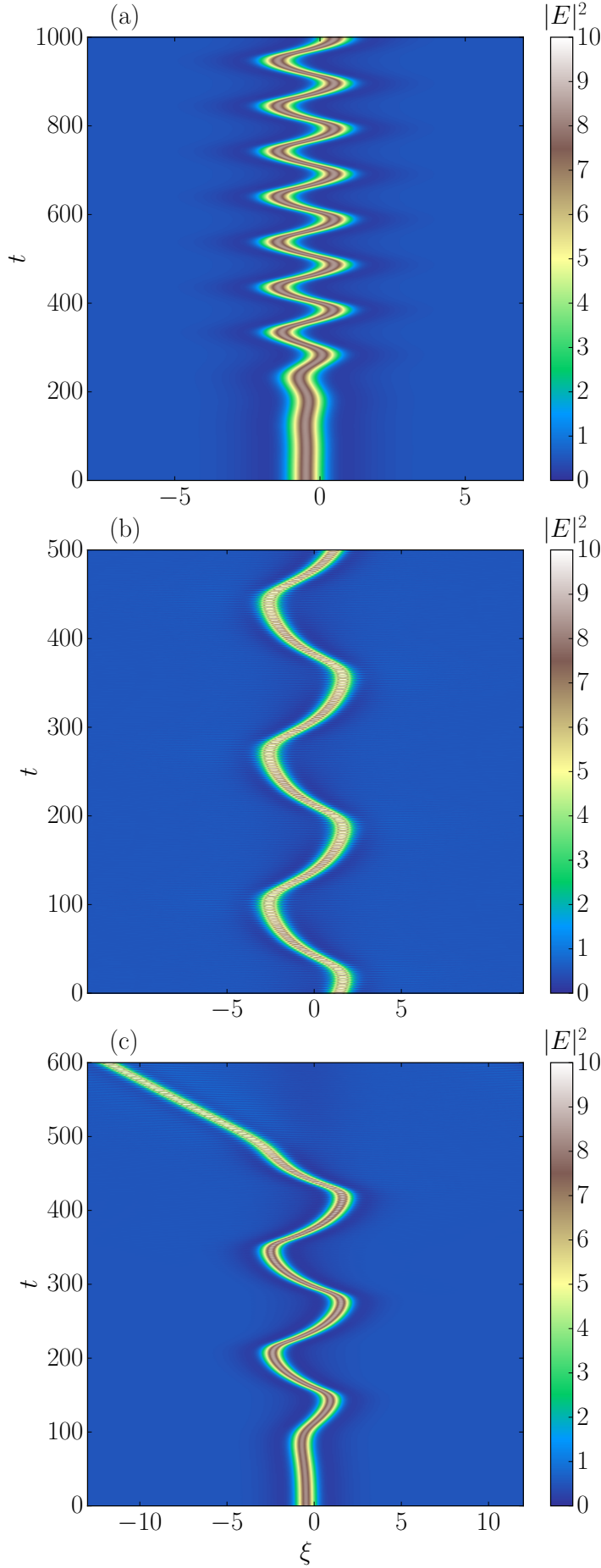
Figure 4.30: (a-c): Destabilization of an LS pinned on the center of the inhomogeneity for $E_i = 2.3$, $\theta = 3.5$, $A = -0.3$, $\tau = 10.0$ and increasing values of α:
(a) $\alpha = 0.13$: The destabilization of the drift inducing mode in an Andronov-Hopf bifurcation leads to an oscillatory motion of the LS.
(b) $\alpha = 0.15$: The unstable growth mode leads to an additional oscillation in size of the LS.
(c) $\alpha = 0.16$: The increased feedback strength leads to the depinning of the LS from the inhomogeneity. The space-time plots in the ξ-t plane show the intensity field obtained by direct numerical simulations of Eq. (4.9).
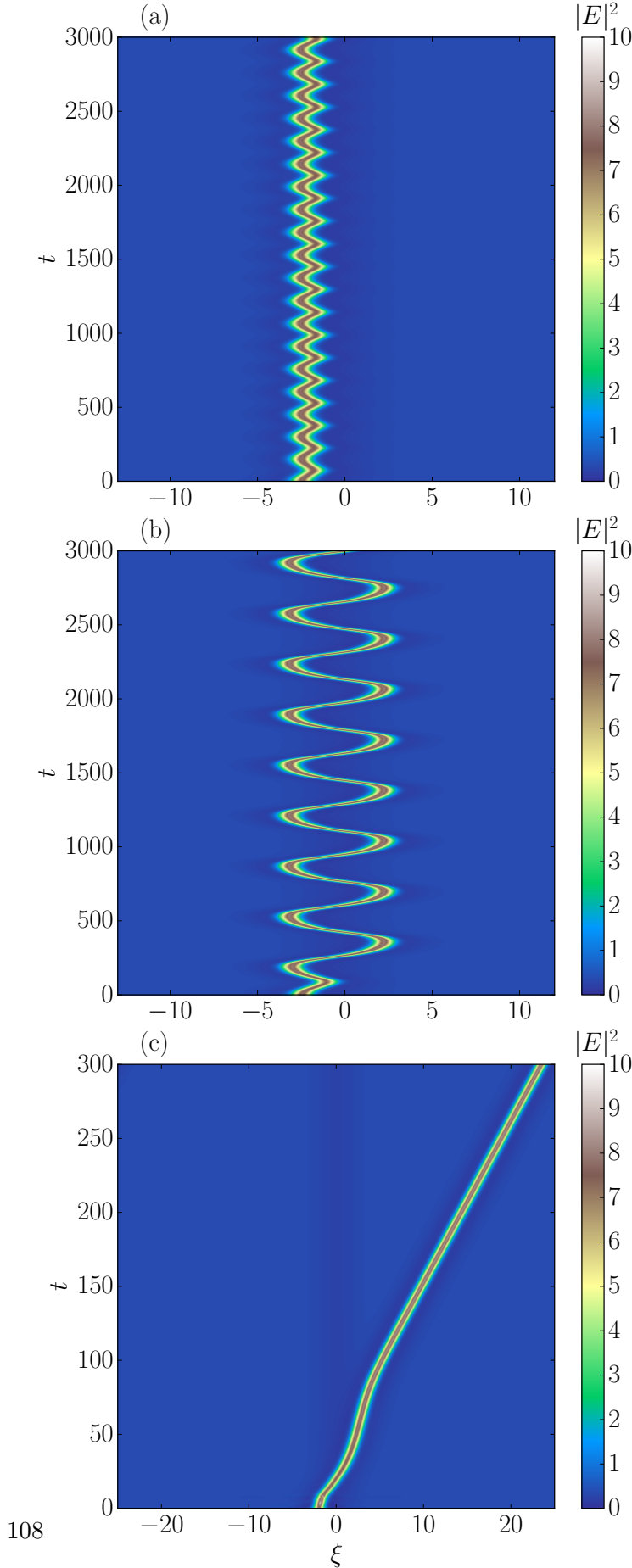
Figure 4.31: (a-c): Destabilization of a LS pinned on the side of the inhomogeneity for $E_i = 2.0$, $\theta = 3.5$, $A = -0.3$, $\tau = 10.0$ and increasing values of α:
(a) $\alpha = 0.105$: The destabilization of the drift inducing mode in an Andronov-Hopf bifurcation leads to an oscillatory motion of the LS around its previously stable position at the side of the inhomogeneity (see Fig. 4.24).
(b) $\alpha = 1.115$: The driving force induced by the delayed feedback is now strong enough to push the LS over the maximum of the inhomogeneity leading to bound oscillations around the whole inhomogeneity.
(c) $\alpha = 1.125$: The increased feedback strength leads to the depinning of the LS from the inhomogeneity.

inhomogeneity (at $\xi = 0$), but oscillates only around its previously stable position at the side of the inhomogeneity. Increasing the feedback to $\alpha = 0.115$ (Fig. 4.31 (b)), the LS now has enough energy to penetrate the center of the repelling inhomogeneity. However, the oscillations are still confined around the inhomogeneity. Finally, for even larger values of the delay-strength (e.g., $\alpha = 0.125$, Fig. 4.31 (c)) the structure depins completely from the inhomogeneity and starts to drift.

Focusing now on the parameter regime, where the LSs pin on the side of the inhomogeneity because their first minimum pins to the center of the inhomogeneity, it is convenient to examine the parameter regime already discussed in section 4.2.2. The LS we destabilize by time-delayed feedback is depicted in Fig. 4.20 in the right inset, the corresponding potential induced by the inhomogeneity is depicted in Fig. 4.24 on the right.

The destabilization of the LS for $\theta = 3.0$, $E_i = 2.0$, $A = 0.1$, $\tau = 10.0$ and increasing feedback strength α is depicted in Fig. 4.32. Slightly above the instability threshold of the drift mode (Fig. 4.32 (a)), the situation resembles the one depicted in the upper panel of Fig. 4.31, i.e., the LS oscillates at the side of the inhomogeneity within the local minimum of the potential from Fig. 4.24. The situation changes drastically compared to Fig. 4.31, when increasing the delay-strength. At $\alpha = 0.103$ (Fig. 4.32 (b)), the LS depins from the local minimum of the potential at the side of the inhomogeneity but still does not have enough energy to penetrate the center of the inhomogeneity. This leads to a drifting motion that, when being reintroduced due to periodic boundaries gets reflected by the center of the inhomogeneity. On the contrary in Fig. 4.31, the LS was able to penetrate the center of the inhomogeneity before it was able to depin, leading to an oscillation of larger amplitude. This again shows, that in the case displayed in Fig. 4.31, the repulsion from the center of the inhomogeneity is much weaker than in the present case shown in Fig. 4.32. This difference potentially yields an explanation, why the pinning of LSs on the side at the ideal value of injection can not be reproduced by the potential well model. The repelling force excerted by the center of the inhomogeneity is to weak to be reflected in the approximations of said model. Further increasing the delay strength finally leads to a drifting LS that also surpasses the center of the inhomogeneity (i.e., the maximum of the potential), when being reinjected due to periodic boundaries (Fig. 4.32).

The destabilization of LS in the LLE shows very similar results to the ones obtained for the Swift-Hohenberg equation in chapter 3. The similar results suggest that oscillations as a result of competing drift and pinning inhomogeneities are a rather generic phenomenon. This is also verified by other work, e.g., [PRGMC13, PRGM$^+$16], where the drift of the LSs was not induced by time-delayed feedback but by simply adding an explicit advection term to the Swift-Hohenberg equation. The quantitative description of inhomogeneities by a potential well acting on an overdamped particle also holds in the case of the LLE, which makes this approach a useful and promising semi-analytical tool for the description of inhomogeneities. However this model reaches its limits when treating inhomogeneities that do not occur in the pumping (mathematically speaking in the constant terms of the PDE under consideration), which we discuss in the next section.

4.3.3 Inhomogeneous detuning

In this last paragraph concerning the LLE we briefly discuss the inclusion of inhomogeneous detuning and its effects on LSs. This section should be understood as a short introduction to a promising field of research that needs further investigation. Small inhomogeneities in the detuning can occur involuntarily for different reasons. In the spatial interpretation of the LLE,
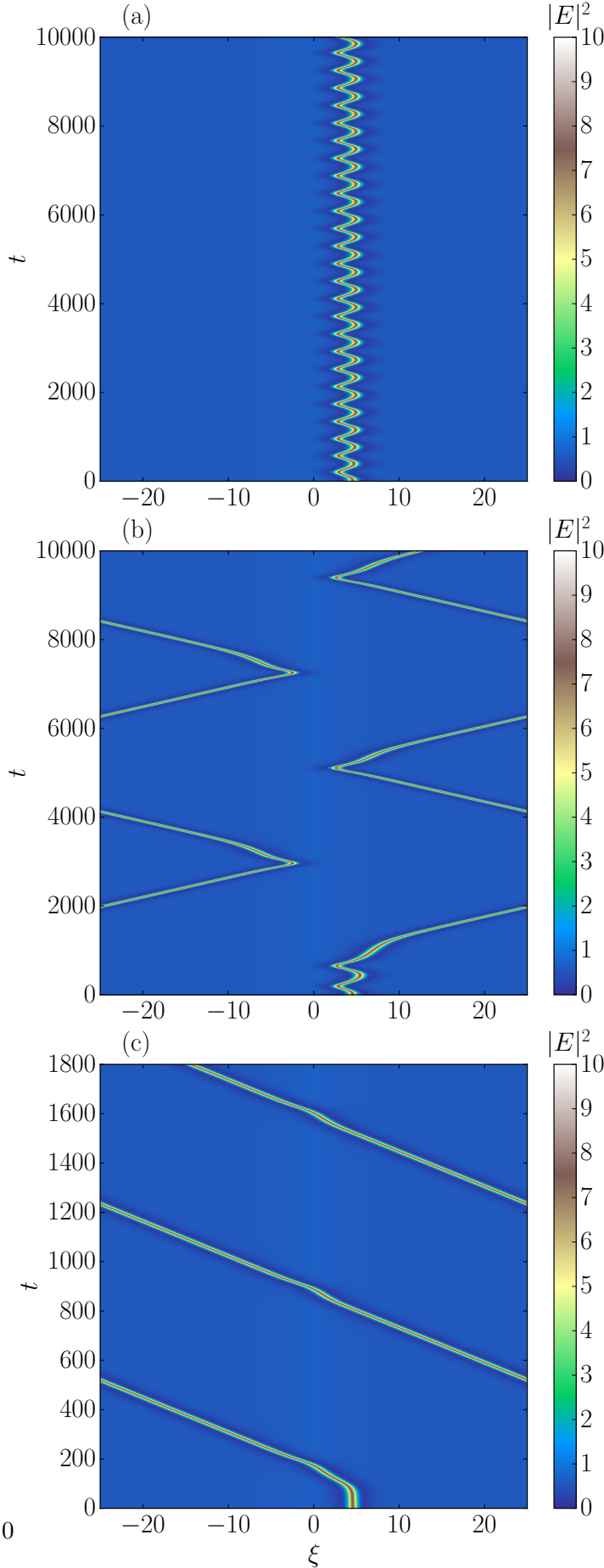
Figure 4.32: (a-c): Destabilization of a LS pinned on the side of the inhomogeneity for $E_i = 2.0$, $\theta = 3.0$, $A = 0.1$, $\tau = 10.0$ and increasing values of α:

(a) $\alpha = 0.102$: The destabilization of the drift inducing mode in an Andronov-Hopf bifurcation leads to an oscillatory motion of the LS only in the local minimum of the potential induced by the inhomogeneity (see Fig. 4.24).

(b) $\alpha = 0.103$: The driving force induced by the delayed feedback is now strong enough to depin the LS from the local minimum of the potential. The delayed-feedback however is not strong enough for the LS to penetrate the maximum of the potential at the center of the inhomogeneity. The repulsion by the center of the inhomogeneity leads to a reflected drift in the opposite direction, once the LS is reintroduced into the vicinity of the inhomogeneity, which is possible with periodic boundary conditions.

(c) $\alpha = 0.13$: The increased feedback strength leads to the depinning of the LS from the inhomogeneity. The delayed feedback is now strong enough for the LS to penetrate and surpass the maximum of the potential, when being reinjected into the domain due to periodic boundary conditions.

small inhomogeneities of the detuning can occur, when, e.g., the width of the cavity is not perfectly homogeneous. Small changes of the width of the cavity can be due to inaccuracies during production or if strain is excerted on the device under consideration in the experimental setup. Changes on the scale of nanometers in the width of the cavity would result in a change of the resonant frequency of the device and therefore in a small local change of detuning [BTB$^+$02, Ave18].

Inhomogeneous detuning in the temporal interpretation of the LLE is less likely to occur involuntarily, since, e.g., the frequency of the pumping source would have to vary on the fast time-scale of ξ without changing on the slower time-scale of t. However it could be implemented artificially if necessary.

In the following we consider Eq. (4.9) with homogeneous injection $E_{\text{inj.}} = E_i$ and an inhomogeneous detuning of the form:

$$\theta = \theta_0 + A_\theta \, \exp\left(-\frac{\xi^2}{B_\theta}\right), \tag{4.12}$$

In principle, this inhomogeneity can again either act attracting or repelling on LSs, depending on the sign of A_θ and on whether an increased detuning is favorable or unfavorable for LSs. The dynamics induced by delayed feedback of an LS that was originally pinned on the inhomogeneity can be seen in Fig. 4.33 in the upper panel. Here, the competing effects of delay and inhomogeneity once again lead to an oscillation, which however does not reach a constant amplitude but varies in amplitude. Eventually, as depicted in Fig. 4.33, the amplitude is large enough to escape the inhomogeneity. When being reintroduced into the vicinity of the inhomogeneity again due to periodic boundary conditions, the LS once again starts to oscillate around it. This phenomenon can not be reproduced by an inhomogeneity in the injection. In the case of inhomogeneous injection the LS either gains enough energy from sufficiently large delay parameters to leave the inhomogeneity but then surpasses it again and again if reinjected, or the LS does not gain enough energy which leads to a confined oscillation.

Intermittent behavior as depicted in Fig. 4.33 did not occur in the previous sections, which also becomes apparent when considering that the case of inhomogeneous injection can be very well approximated by considering a particle in a potential well, where the force excerted by the inhomogeneity only depends on the position of the LS relative to the inhomogeneity (see section 3.2.4 and 4.2.3). The force excerted by an inhomogeneity in the detuning depends much stronger on the exact shape of the LS, which becomes apparent, when considering that the detuning occurs in a term linear in the intracavity field E, whereas the injection is constant and therefore independent of E. The force excerted by an inhomogeneous detuning therefore more strongly reflects the shape changes during the oscillations, which causes the intermittent behavior depicted in Fig. 4.33. The application of a similar potential well approach as in section 4.2.3, which neglects shape deformations is therefore less promising to produce quantitatively accurate results.

Going one step further in the direct numerical simulations, one can now consider a larger domain with more than one inhomogeneity in the detuning. The bottom panel of Fig. 4.33 shows the dynamics of an LS induced by delayed feedback in the presence of seven equidistant inhomogeneities of the same amplitude and width. The LS exhibits an erratic motion, in which it oscillates around an inhomogeneity for a certain time, then breaks free and drifts until it gets trapped again in the vicinity of another inhomogeneity. Neither a preferred direction nor a fixed time of stay in the vicinity of an inhomogeneity can be identified. However, more and longer simulations are necessary to determine if this behavior is chaotic.
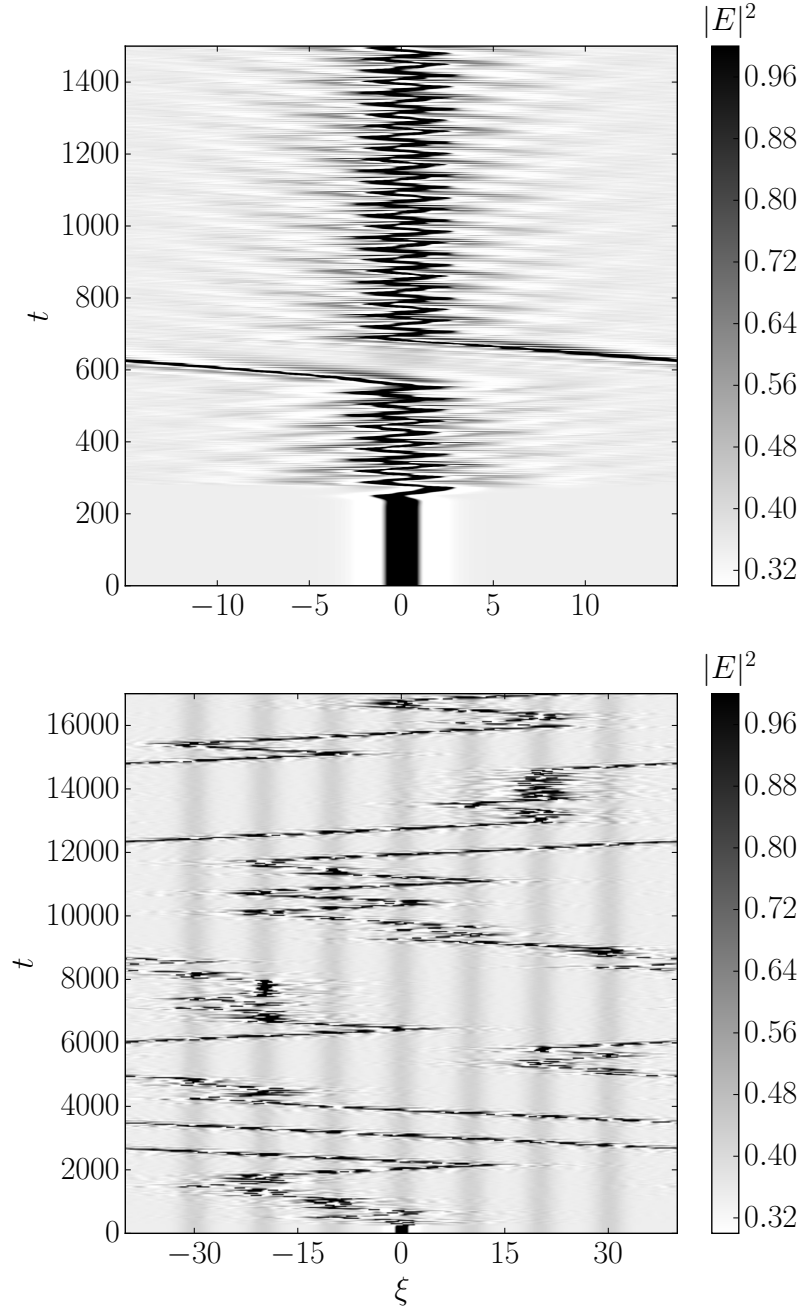
Figure 4.33: Top: Destabilization of a pinned LS by delayed feedback in the presence of an inhomogeneous detuning for $E_i = 2.0$, $\theta = 3.6$, $A_\theta = -0.3$, $B_\theta = 4.0$, $\alpha = 0.3$, $\tau = 10.0$ on a domain of $L = 30.0$. The competing effects of the destabilizing delayed feedback and the pinning inhomogeneity in the detuning lead to an oscillation, which in contrast to Fig. 4.30 and 4.31 does not have a constant amplitude, thus suggesting that the force excerted by the inhomogeneity varies. Eventually the LS breaks free from the inhomogeneity, reenters the system due to the periodic boundary conditions and then gets trapped in the inhomogeneity again.

Bottom: Dynamics of a single LS on a larger domain of $L = 80.0$ in the presence of seven equidistant inhomogeneities. The unpredictable sequence of oscillations intermitted by a drift leads to an erratic motion of the LS between the several inhomogeneities. The colormap was changed to a black and white map for a better visibility of the motion of the LS. All parameters are the same as in the top panel for $\alpha = 0.34$.

Although this section only briefly summarizes a few preliminary results on inhomogeneous detuning, we were able to identify one major difference in the delay-induced dynamics in the presence of inhomogeneous injection or inhomogeneous detuning. The fact that an inhomogeneity in the injection can be very well modeled by a potential that only depends on the position of the LS, whereas this simplified view fails in the case of inhomogeneous detuning makes the two cases distinguishable. This difference might be used to determine which kind of inhomogeneities one encounters in a given experimental setup and is therefore worth noting.

Summary and Outlook

In this thesis we studied the formation and the dynamics of localized structures (LSs) in dissipative systems with a particular focus on the effects of spatial or temporal inhomogeneities.

We started with an introduction of the concept of LSs pointing out similarities and differences to classical solitons which appear, e.g., as solutions of the nonlinear Schrödinger equation. In this part we mostly relied on previous work from Akhmediev et al. [AA08]. We then introduced the Brusselator model, which represents one of the first theoretical models for pattern formation in dissipative systems. Employing numerical path continuation techniques in two spatial dimensions we were able to construct the bifurcation diagram of LSs in this model. These results were already published in [KTT+18]. After a general discussion of the theory of LSs in dissipative systems and the brief detour into the field of pattern forming chemical systems, we focused on the formation of LSs in nonlinear optical systems. First, we gave a short historical overview of the theoretical and experimental investigation of spatial and temporal LSs in optical systems. Then, we provided experimental evidence of the formation of LSs in the transverse plane of a vertical cavity surface emitting laser (VCSEL).

The experimental investigation of the formation of LSs suggested, that there exist certain positions within the cavity which are especially favorable for the creation of LSs. These experimental results as well as the results reported from, e.g., [BTB+02] motivated the main focus of this thesis, i.e., the explicit consideration of spatial inhomogeneities in the theoretical modeling of pattern formation. To this aim, we presented the derivations of two paradigmatic and intensively studied homogeneous models in chapter 2 before implementing spatial inhomogeneities in the following chapters. We derived the Swift-Hohenberg equation (SHE), which in the context of nonlinear optics describes pattern formation in the transverse plane of a cavity at the onset of optical bistability. As a second system we introduced the Lugiato-Lefever equation (LLE). We provided two derivations, since the LLE can describe spatial pattern formation in the transverse plane of a cavity as well as longitudinal or temporal pattern formation in a ring cavity. Both the SHE and the LLE in their classical form are based on the idealized assumption of homogeneous injection. In the SHE and in the transversal LLE one presumes that the entire cavity is injected perfectly homogeneously by a plane wave. This assumption corresponds to a constant input beam without temporal modulations in the longitudinal interpretation of the LLE.

In the main two chapters 3 and 4 of this thesis we demonstrated that the inclusion of even small inhomogeneities in these paradigmatic models leads to a more realistic description of the pattern forming processes in the underlying system. Furthermore, the deliberate implementation of inhomogeneities can have desirable positive effects on, e.g., the stability properties of LSs.

We began our analysis of inhomogeneities in chapter 3 with the SHE. We briefly discussed the bifurcation structure of LSs in the homogeneous SHE and explained the emergence of elongated rodlike LSs. Continuing, we discussed the dynamics induced by time-delayed feedback which have been studied extensively in various models. The predominant dynamics in these scenarios is a drift of the LSs, which is, however, not observed in experimental realizations of

destabilizing time-delayed feedback in nonlinear optics [Ave17]. We argued that the predominance of delay-induced drift is not a result of specific properties of the SHE but occurs due to the translational symmetry of the considered system. The inclusion of spatial inhomogeneities resolves this discrepancy between theoretical and experimental results because it explicitly breaks the translational symmetry of the model.

Thus, we included a small inhomogeneity in the injection term of the SHE and demonstrated that the consideration of this effect leads to more realistic oscillatory dynamics of the LSs. Instead of drifting freely, the competing effects of an attracting inhomogeneity and the drift-inducing delayed feedback leads to oscillations around the inhomogeneity. Only for larger values of the feedback parameters (delay time or delay strength), the LS depins from the inhomogeneity and starts to drift freely. The transitions from a stable LS to an oscillating LS and from the oscillating to a drifting LS were then studied in the framework of two semi-analytical approaches. Following the first approach we were able to identify the bifurcation responsible for the onset of oscillations as a delay-induced Andronov-Hopf bifurcation. The second approach enabled us to describe the behavior of the LS in the vicinity of the inhomogeneity as an overdamped particle in a potential well. We provided an explicit expression for the potential induced by the inhomogeneity, which can be applied to other systems exhibiting LSs as well. Comparing the results from this potential well approach with results from the full model, we showed that the approach qualitatively captures both the onset of oscillations and the depinning process. Nevertheless, close to the depinning threshold, the quantitative accuracy of the approach decreases because we did not consider shape deformations of oscillating LSs, which become non-neglectable for large amplitude oscillations.

The proposed potential well approach represents a very effective method to reduce the numerically expensive investigation of the full delayed PDEs to a more intuitive and simpler model. It therefore is a promising tool for the investigation of inhomogeneities in PDE systems. Overall, we were able to corroborate the necessity of considering spatial inhomogeneities in this section based on the more realistic delay-induced dynamics. Most results concerning the inhomogeneous SHE were already published in [TSTG17].

In chapter 4, we focused on the LLE. We started with a discussion of the emergence of LSs and periodic solutions without inhomogeneities. To this end, we analyzed several qualitatively different parameter regimes. The formation of LSs has been discussed in depth in the region of low detuning $\theta < 2$, where we only reproduced and summarized previous results. The formation of LSs in the parameter regime $\theta > 2$ is more intricate, since no Turing instability of the stable homogeneous solution branch exists in this regime. However, we were able to explain the formation of LSs as solutions resulting of an instability of the maximum wave-length defined by the domain size. In this regime, several solutions consisting of equidistant peaks bifurcate from the unstable homogeneous branch. Hence, a clear differentiation between LSs formed of multiple peaks and periodic patterns is not possible.

We then introduced a small inhomogeneous injection term to the LLE and analyzed its effect. In the region of small detuning, an attracting inhomogeneity increases the region of stability of a single LS drastically, which can be beneficial for experimental implementation. Furthermore, a parameter region arises in the presence of an inhomogeneity, in which solely a single LS is stable, thus avoiding a potentially problematic multistability between periodic, homogeneous and bound state solutions, which we encountered in the case of homogeneous injection.

In parameter regions of large detuning $\theta > 2$, the influence of small inhomogeneities is more intricate than in the case of small detuning. In particular, we demonstrated that a given inhomogeneity can act either attracting or repelling depending on the overall injection, resulting

in LSs being either pinned on the center of the inhomogeneity, on the side of the inhomogeneity or being completely repelled by the inhomogeneity. We investigated these transitions employing numerical continuation techniques and identified the bifurcations responsible for each transition. Our results are in good agreement with results from Hendry et al [HCW+18], who showed in direct numerical simulations that LSs are drawn towards certain ideal values of injection. We were able to identify the pitchfork bifurcation taking place when this ideal value is reached at the center of the inhomogeneity. Additionally, the system exhibits a transcritical bifurcation when going from positive to negative amplitudes of the inhomogeneity (or vice versa).

After discussing this bifurcation structure in depth, we applied the potential well approach derived in chapter 3 and demonstrated that it is applicable to the LLE. We closed with a comparison of the overall parameter regime of the LLE without and with inhomogeneities. Most results from this section concerning the inhomogeneous LLE were already published in [TFHP+19]. In the last section of this chapter we discussed the destabilization of LSs by time-delayed feedback presenting similar results as observed in the case of the SHE. This similarity again underlines the argument made in chapter 3 stating that the induced dynamics merely rely on the symmetry properties of the system and the delayed feedback term. In a last section we briefly outlined further results considering a spatially inhomogeneous detuning. Spatial variations of the detuning parameter can occur due to small inaccuracies in the cavity width. Such a non-homogeneous detuning is actually the normal case in broad area VCSELs [BTB+02], where such inaccuracies are unavoidable. The consideration of inhomogeneous detuning results in more complex dynamics than in the case of inhomogeneous injection, since LSs can depin and repin to the inhomogeneity in a seemingly arbitrary sequence.

Both the SHE and the LLE are widely applicable to different pattern forming systems. The inclusion of spatial inhomogeneities leads to drastic changes in the solution structure and in the induced dynamics, even though we restricted ourselves to the case of small inhomogeneities. For this reason, we argue, that the inclusion of even small inhomogeneities is necessary because they change the symmetry properties of the considered system. As discussed, the broken translational symmetry effects, e.g., delay-induced dynamics. We therefore propose to continue the study of inhomogeneities to gain more realistic mathematical descriptions of pattern forming systems. Due to the wide applicability of, e.g., the SHE we believe that the study of inhomogeneities is promising not only in the case of optical systems. In the following we suggest further steps towards a better understanding of inhomogeneous effects in the field of nonlinear optics.

From a theoretical point of view one can alter the exact shape of the inhomogeneity to see whether or not this affects the stability of LSs. The potential well model presented in chapter 3 can serve as a powerful tool to gain insights concerning the effects of differently shaped inhomogeneities. Judging from the analytical expression for the induced potential it seems reasonable that the overall influence does not change qualitatively, as long as one considers an inhomogeneity with just one maximum (minimum). Considering, e.g., an inhomogeneity with oscillatory tails, one can expect further regions of attraction or repulsion judging from the convolution term in the potential.

Furthermore, for an exact quantitative comparison with experimental data, one should consider the inclusion of spatial inhomogeneities in theoretical models which describe the formation of LSs in VCSELs more precisely such as [BTB+02]. From a theoretical point of view, similar oscillations as described in this thesis can be expected in these models.

In conclusion, this thesis should be seen as a first motivation for the inclusion of inhomo-

geneities suggesting that the consideration of these effects potentially resolves the discrepancies between experimental and theoretical observations of delay-induced instabilities. To this end, we were able to show that the mechanism consisting of competing delay and an attracting inhomogeneity provides qualitatively more realistic results. However, experimental proof is still required to demonstrate that the described mechanism is responsible for the observed dynamics. Members of the K. Panajotov lab in Brussels therefore started an in-depth analysis of the experimentally observed oscillations. A quantitative comparison of these results with results from theoretical models can be based on, e.g., the parameter regimes in which oscillations occur or on the frequency of the oscillations. If such a quantitative comparison is successful, we are be able to verify that the mechanism presented in this thesis is in fact responsible for the occurring dynamics.

Regardless of the experimental verification of the proposed mechanisms leading to oscillations, we were able to demonstrate that even the inclusion of small amplitude inhomogeneities can change the behavior of a system dramatically. Nevertheless, spatial inhomogeneities are typically neglected in theoretical pattern formation in an effort to propose more elegant and simplistic mathematical models. As a consequence, we suggest to carefully question, whether spatially inhomogeneous effects are truly neglectable in a considered model, since inhomogeneities occur naturally in almost any experimental setup.

List of Publications

This list comprises the manuscripts published based on the work presented in this thesis:

[TSTG17] F. Tabbert, C. Schelte, M. Tlidi and S. V. Gurevich. Delay-induced depinning of localized structures in a spatially inhomogeneous Swift-Hohenberg model. *Phys. Rev. E*, 95:032213, 2017.

F.T. contributed all results presented in this publication except Fig. 5 which was produced by C.S. The manuscript was written entirely by F.T. with suggestions and improvements by M.T. and S.V.G. Results of this publication are presented in chapter 3, subsection 3.1.2 and section 3.2 of this thesis.

[KTT$^+$18] B. Kostet, M. Tlidi, F. Tabbert, T. Frohoff-Hülsmann, S. V. Gurevich, E. Averlant, R. Rojas, G. Sonnino and K. Panajotov. Stationary localized structures and the effect of the delayed feedback in the Brusselator model *Philos. Trans. Royal Soc. A*, 376(2135):20170385, 2018.

F.T. contributed the results depicted in Fig. 1 – Fig. 5 concerning the bifurcation structure of the localized structures in cooperation with T.F.H. The parts of the manuscript addressing these results were written by F.T. Results of this publication are presented in section 1.1.1 of this thesis.

[TFHP$^+$] F. Tabbert, T. Frohoff-Hülsmann, K. Panajotov, M. Tlidi and S. V. Gurevich. Stabilization of localized structures by inhomogeneous injection in Kerr resonators. arXiv:1901.02308. Submitted to *Phys. Rev. A* (Status: with reviewers).

F.T. contributed all results presented in this publication in cooperation with T.F.H. The manuscript was written entirely by F.T. with suggestions and improvements by all other authors. Results of this publication are presented in section 4.2 of this thesis.

Publications not included in this manuscript:

[STP$^+$17] T. Schemmelmann, F. Tabbert, A. Pimenov, A.G. Vladimirov, and S. V. Gurevich. Delayed feedback control of self-mobile cavity solitons in a wide-aperture laser with saturable absorber. *Chaos*, 27(11):114304, 2017.

Bibliography

[AA10]   H. Ayrton and W. E. Ayrton. The origin and growth of ripple-mark. *Proc. Royal Soc. Lond. A*, 84(571):285–310, 1910.

[AA08]   N. Akhmediev and A. Ankiewicz. *Dissipative Solitons: From optics to biology and medicine*. Springer, 2008.

[ABR99]   F. T. Arecchi, S. Boccaletti, and P. L. Ramazza. Pattern formation and competition in nonlinear optics. *Phys. Rep.*, 318(1–2):1 – 83, 1999.

[AFO09]   T. Ackemann, W. J. Firth, and G.-L. Oppo. Fundamentals and applications of spatial dissipative solitons in photonic devices. volume 57 of *Adv. Atom. Mol. Phys.*, pages 323 – 421. Academic Press, 2009.

[ATT⁺14]   E. Averlant, M. Tlidi, H. Thienpont, T. Ackemann, and K. Panajotov. Experimental observation of localized structures in medium size vcsels. *Opt. Express*, 22(1):762–772, Jan 2014.

[Ave17]   E. Averlant. *Localized structures in surface-emitting lasers: vectorial character and delay-induced motion*. PhD thesis, 2017.

[Ave18]   E. Averlant. Private discussions on experimental setups. 2018.

[BB99]   P. Ball and N. R. Borley. *The self-made tapestry: pattern formation in nature*, volume 198. Oxford University Press Oxford, 1999.

[BBKM08]   A. Bergeon, J. Burke, E. Knobloch, and I. Mercader. Eckhaus instability and homoclinic snaking. *Phys. Rev. E*, 78:046201, Oct 2008.

[BC15]   I. Bordeu and M. G. Clerc. Rodlike localized structure in isotropic pattern-forming systems. *Phys. Rev. E*, 92:042915, Oct 2015.

[BHE⁺08]   S. Barbay, X. Hachair, T. Elsass, I. Sagnes, and R. Kuszelewicz. Homoclinic snaking in a semiconductor-based optical system. *Phys. Rev. Lett.*, 101:253902, Dec 2008.

[BK06]   J. Burke and E. Knobloch. Localized states in the generalized Swift-Hohenberg equation. *Phys. Rev. E*, 73:056211, May 2006.

[BK07]   J. Burke and E. Knobloch. Homoclinic snaking: Structure and stability. *Chaos*, 17(3), 2007.

[BLP⁺97]   M. Brambilla, L. A. Lugiato, F. Prati, L. Spinelli, and W. J. Firth. Spatial soliton pixels in semiconductor devices. *Phys. Rev. Lett.*, 79:2042–2045, Sep 1997.

[BP95]   M. Bode and H. G. Purwins. Pattern formation in reaction-diffusion systems-dissipative solitons in physical systems. *Physica D*, 86(1-2):53–63, 1995.

[BTB+02]   S. Barland, J. R. Tredicce, M. Brambilla, L. A. Lugiato, S. Balle, M. Giudici, T. Maggipinto, L. Spinelli, G. Tissoni, T. Knoedl, et al. Cavity solitons as pixels in semiconductor microcavities. *Nature*, 419:699–702, 2002.

[BTV92]   V. Y. Bazhenov, V. B. Taranenko, and M. V. Vasnetsov. Transverse optical effects in bistable active cavity with nonlinear absorber on bacteriorhodopsin. In N. N. Rosanov, editor, *Transverse Patterns in Nonlinear Optics*. SPIE, dec 1992.

[CBG+17]   F. Castelli, M. Brambilla, A. Gatti, F. Prati, and L. A. Lugiato. The LLE, pattern formation and a novel coherent source. *Eur. Phys. J. D*, 71(4):84, Apr 2017.

[CGH+96]   R. M. Corless, G. H. Gonnet, D. E. G. Hare, D. J. Jeffrey, and D. E. Knuth. On the Lambert W function. *Adv. Comput. Math.*, 5:329–359, 1996.

[CH93]   M. C. Cross and P. C. Hohenberg. Pattern formation outside of equilibrium. *Rev. Mod. Phys.*, 65:851, 1993.

[CM13]   Y. K. Chembo and C. R. Menyuk. Spatiotemporal Lugiato-Lefever formalism for Kerr-comb generation in whispering-gallery-mode resonators. *Phys. Rev. A*, 87(5):053852, 2013.

[CRSE13]   S. Coen, H. G. Randle, T. Sylvestre, and M. Erkintalo. Modeling of octave-spanning Kerr frequency combs using a generalized mean-field Lugiato-Lefever model. *Opt. Lett.*, 38(1):37–39, Jan 2013.

[CSE+18]   D. C. Cole, J. R. Stone, M. Erkintalo, K. Y. Yang, X. Yi, K. J. Vahala, and S. B. Papp. Kerr-microresonator solitons from a chirped background. *Optica*, 5(10):1304–1310, Oct 2018.

[DSA+07]   P. Del'Haye, A. Schliesser, O. Arcizet, T. Wilken, R. Holzwarth, and T. J. Kippenberg. Optical frequency comb generation from a monolithic microresonator. *Nature*, 450(7173):1214–1217, dec 2007.

[Eck05]   R. Ecke. The turbulence problem. *Los Alamos Science*, 29:124–141, 2005.

[EGB+10]   T. Elsass, K. Gauthron, G. Beaudoin, I. Sagnes, R. Kuszelewicz, and S. Barbay. Fast manipulation of laser localized structures in a monolithic vertical cavity with saturable absorber. *Applied Physics B*, 98(2):327–331, Feb 2010.

[EGU+18]   S. Engelnkemper, S. V. Gurevich, H. Uecker, D. Wetzel, and U. Thiele. Computational modeling of bifurcations and instabilities in fluid mechanics, 2018.

[ELR02]   K. Engelborghs, T. Luzyanina, and D. Roose. Numerical bifurcation analysis of delay differential equations using DDE-BIFTOOL. *ACM Trans. Math. Softw.*, 28(1):1–21, 2002.

[ET17]   Sebastian Engelnkemper and Uwe Thiele. *Nichtlineare Analyse physikochemisch getriebener Entnetzung–Statik und Dynamik–*. PhD thesis, 2017.

[EWGT16]   S. Engelnkemper, M. Wilczek, S. V. Gurevich, and U. Thiele. Morphological transitions of sliding drops: Dynamics and bifurcations. *Phys. Rev. Fluids*, 1:073901, Nov 2016.

[FCS07]   W. J. Firth, L. Columbo, and A. J. Scroggie. Proposed resolution of theory-experiment discrepancy in homoclinic snaking. *Phys. Rev. Lett.*, 99:104503, Sep 2007.

[FML⁺11]   F. Ferdous, H. Miao, D. E. Leaird, K. Srinivasan, J. Wang, L. Chen, L T. Varghese, and A. M. Weiner. Spectral line-by-line pulse shaping of on-chip microresonator frequency combs. *Nat. Phott.*, 5(12):770, 2011.

[Fri93]   R. Friedrich. Higher instabilities in synergetic systems with continuous sysmmetries. *Z. Phys. B*, 90:373–376, 1993.

[GBCC14]   C. Godey, I. V. Balakireva, A. Coillet, and Y. K. Chembo. Stability analysis of the spatiotemporal Lugiato-Lefever model for Kerr optical frequency combs in the anomalous and normal dispersion regimes. *Phys. Rev. A*, 89:063814, Jun 2014.

[GF13]   S. V. Gurevich and R. Friedrich. Instabilities of localized structures in dissipative systems with delayed feedback. *Phys. Rev. Lett.*, 110:014101, 2013.

[GGKM67]   C. S. Gardner, J. M. Greene, M. D. Kruskal, and R. M. Miura. Method for solving the Korteweg-deVries equation. *Phys. Rev. Lett.*, 19:1095–1097, Nov 1967.

[GJ17]   S. V. Gurevich and J. Javaloyes. Spatial instabilities of light bullets in passively-mode-locked lasers. *Phys. Rev. A*, 96:023821, Aug 2017.

[Gom03]   D. Gomila. *Dynamics of spatial structures in nonlinear optics*. PhD thesis, 2003.

[GSF07]   D. Gomila, A. J. Scroggie, and W. J. Firth. Bifurcation structure of dissipative solitons. *Physica D*, 227(1):70 – 77, 2007.

[GSW62]   J. Goldstone, A. Salam, and S. Weinberg. Broken symmetries. *Phys. Rev.*, 127:965–970, Aug 1962.

[Gur13]   S. V. Gurevich. Dynamics of localized structures in reaction-diffusion systems induced by delayed feedback. *Phys. Rev. E*, 87:052922, 2013.

[Gur14]   S. V. Gurevich. Time-delayed feedback control of breathing localized structures in a three-component reaction–diffusion system. *Phil. Trans. R. Soc. A*, 376:20180113, 2014.

[Hak70]   H. Haken. Laser theory. In *Light and Matter*, pages 1–304. Springer, 1970.

[Hak83]   H. Haken. *Synergetics, An Introduction.* Springer, 1983.

[HBF⁺04]   X. Hachair, S. Barland, L. Furfaro, M. Giudici, S. Balle, J. R. Tredicce, M. Brambilla, T. Maggipinto, I. M. Perrini, G. Tissoni, and L. Lugiato. Cavity solitons in broad-area vertical-cavity surface-emitting lasers below threshold. *Phys. Rev. A*, 69:043817, Apr 2004.

[HCW⁺18]   I. Hendry, W. Chen, Y. Wang, B. Garbin, J. Javaloyes, G.-L. Oppo, S. Coen, S. G. Murdoch, and M. Erkintalo. Spontaneous symmetry breaking and trapping of temporal Kerr cavity solitons by pulsed or amplitude-modulated driving fields. *Phys. Rev. A*, 97:053834, May 2018.

[HDB96]   M'F. Hilali, G. Dewel, and P. Borckmans. Subharmonic and strong resonances through coupling with a zero mode. *Phys. Lett. A*, 217(4-5):263 – 268, 1996.

[HJL⁺08]   C. B. Huang, Z. Jiang, D. E. Leaird, J. Caraquitena, and A. M. Weiner. Spectral line-by-line shaping for optical and microwave arbitrary waveform generations. *Laser Photonics Rev.*, 2(4):227–248, aug 2008.

[HPC⁺06]   X. Hachair, F. Pedaci, E. Caboche, S. Barland, M. Giudici, J. R. Tredicce, F. Prati, G. Tissoni, R. Kheradmand, L. Lugiato, et al. Cavity solitons in a driven VCSEL above threshold. *IEEE J. Sel. Top. Quantum Electron*, 12(3):339–351, 2006.

[HTW92]   M. Haelterman, S. Trillo, and S. Wabnitz. Dissipative modulation instability in a nonlinear dispersive ring cavity. *Opt. Commun.*, 91(5):401 – 407, 1992.

[KA95]   S. Kondo and R. Asai. A reaction–diffusion wave on the skin of the marine angelfish pomacanthus. *Nature*, 376(6543):765, 1995.

[Kel79]   H. B. Keller. Constructive methods for bifurcation and nonlinear eigenvalue problems. In *Computing Methods in Applied Sciences and Engineering, 1977, I*, pages 241–251. Springer, 1979.

[KG16]   A. Kraft and S. V. Gurevich. Time-delayed feedback control of spatio-temporal self-organized patterns in dissipative systems. In E. Schöll, S. H. L. Klapp, and P. Hövel, editors, *Control of Self-Organizing Nonlinear Systems*, pages 413–430. Springer International Publishing, 2016.

[KGLG18]   T. J. Kippenberg, A. L. Gaeta, M. Lipson, and M. L. Gorodetsky. Dissipative Kerr solitons in optical microresonators. *Science*, 361(6402):eaan8083, 2018.

[KHD11]   T. J. Kippenberg, R. Holzwarth, and S. A. Diddams. Microresonator-based optical frequency combs. *Science*, 332(6029):555–559, 2011.

[Kno08]   E. Knobloch. Spatially localized structures in dissipative systems: open problems. *Nonlinearity*, 21(4):T45, 2008.

[KS09]   S. Kondo and H. Shirota. Theoretical analysis of mechanisms that generate the pigmentation pattern of animals. *Semin. Cell Dev. Biol.*, 20(1):82 – 89, 2009. A Special Edition on Biosensors and Development of Pigment Cells and Pigment Patterns.

[KT07]   G. Kozyreff and M. Tlidi. Nonvariational real Swift-Hohenberg equation for biological, chemical, and optical systems. *Chaos*, 17(3):037103, 2007.

[KTT$^+$18]   B. Kostet, M. Tlidi, F. Tabbert, T. Frohoff-Hülsmann, S. V. Gurevich, E. Averlant, R. Rojas, G. Sonnino, and K. Panajotov. Stationary localized structures and the effect of the delayed feedback in the Brusselator model. *Philos. Trans. Royal Soc. A*, 376(2135):20170385, 2018.

[LBCL09]   R. Lefever, N. Barbier, P. Couteron, and O. Lejeune. Deeply gapped vegetation patterns: on crown/root allometry, criticality and desertification. *J. Theor. Biol.*, 261:194–209, 2009.

[LK80]   R. Lang and K. Kobayashi. External optical feedback effects on semiconductor injection laser properties. *IEEE J. Quantum Electron.*, 16:347–355, 1980.

[LL87]   L. A. Lugiato and R. Lefever. Spatial dissipative structures in passive optical systems. *Phys. Rev. Lett.*, 58:2209–2211, May 1987.

[LO88]   L. A. Lugiato and C. Oldano. Stationary spatial patterns in passive optical systems: Two-level atoms. *Phys. Rev. A*, 37(10):3896–3908, may 1988.

[LPB15]   L. A. Lugiato, F. Prati, and M. Brambilla. *Nonlinear optical systems*. Cambridge University Press, 2015.

[LPGK18]   L. A. Lugiato, F. Prati, M. L. Gorodetsky, and T. J. Kippenberg. From the LLE to microresonator based soliton Kerr frequency combs. *Phil. Trans. R. Soc. A*, 2018.

[Man05]   P. Mandel. *Theoretical problems in cavity nonlinear optics*, volume 21. Cambridge University Press, 2005.

[MC00]   P. C. Matthews and S. M. Cox. Pattern formation with a conservation law. *Nonlinearity*, 13(4):1293, 2000.

[ML13]   A. M. Menzel and H. Löwen. Traveling and resting crystals in active systems. *Phys. Rev. Lett.*, 110:055702, 2013.

[MMF$^+$17] L. Manukyan, S. A. Montandon, A. Fofonjka, S. Smirnov, and M. C. Milinkovitch. A living mesoscopic cellular automaton made of skin scales. *Nature*, 544(7649):173, 2017.

[MPL97]   D. Michaelis, U. Peschel, and F. Lederer. Multistable localized structures and superlattices in semiconductor optical resonators. *Phys. Rev. A*, 56:R3366–R3369, Nov 1997.

[MSL$^+$11] A. B. Matsko, A. A. Savchenkov, W. Liang, V. S. Ilchenko, D. Seidel, and L. Maleki. Mode-locked kerr frequency combs. *Opt. Lett.*, 36(15):2845–2847, Aug 2011.

[MT04]   P. Mandel and M. Tlidi. Transverse dynamics in cavity nonlinear optics (2000–2003). *J. Opt.*, 6(9):R60, 2004.

[OGT18]   L. Ophaus, S. V. Gurevich, and U. Thiele.   Resting and traveling localized states in an active phase-field-crystal model. *Phys. Rev. E*, 98:022608, Aug 2018.

[OLH17]   E. Obrzud, S. Lecomte, and T. Herr.   Temporal solitons in microresonators driven by optical pulses. *Nat. Phot.*, 11(9):600, 2017.

[ORH+19]   E. Obrzud, M. Rainer, A. Harutyunyan, M. H. Anderson, J. Liu, M. Geiselmann, B. Chazelas, S. Kundermann, S. Lecomte, M. Cecconi, et al. A microphotonic astrocomb. *Nat. Phot.*, 13(1):31, 2019.

[OTC+14]   V. Odent, M. Tlidi, M. G. Clerc, P. Glorieux, and E. Louvergneaux. Experimental observation of front propagation in a negatively diffractive inhomogeneous Kerr cavity. *Phys. Rev. A*, 90:011806, Jul 2014.

[OTL11]   V. Odent, M. Taki, and E. Louvergneaux. Experimental evidence of dissipative spatial solitons in an optical passive Kerr cavity. *New J. Phys.*, 13(11):113026, nov 2011.

[PBL+14]   J. Pfeifle, V. Brasch, M. Lauermann, Y. Yu, D. Wegner, T. Herr, K. Hartinger, P. Schindler, J. Li, D. Hillerkuss, R. Schmogrow, C. Weimann, R. Holzwarth, W. Freude, J. Leuthold, T. J. Kippenberg, and C. Koos. Coherent terabit communications with microresonator Kerr frequency combs. *Nat. Phot.*, 8(5):375–380, apr 2014.

[PCT+07]   F. Prati, P. Caccia, G. Tissoni, L.A. Lugiato, K. Mahmoud Aghdami, and H. Tajalli. Effects of carrier radiative recombination on a VCSEL-based cavity soliton laser. *Applied Physics B*, 88(3):405–410, jun 2007.

[PL68]   I. Prigogine and R. Lefever.   Symmetry breaking instabilities in dissipative systems. ii. *J. Chem. Phys.*, 48(4):1695–1700, 1968.

[PL73]   I. Prigogine and R. Lefever.   Theory of dissipative structures.   In *Synergetics*, pages 124–135. Springer, 1973.

[PnPG01]   B. Peña and C. Pérez-García.   Stability of Turing patterns in the Brusselator model. *Phys. Rev. E*, 64:056213, Oct 2001.

[PPV+16]   K. Panajotov, D. Puzyrev, A. G. Vladimirov, S. V. Gurevich, and M. Tlidi. Impact of time-delayed feedback on spatiotemporal dynamics in the Lugiato-Lefever model. *Phys. Rev. A*, 93:043835, Apr 2016.

[PRGGK18a]   P. Parra-Rivas, D. Gomila, L. Gelens, and E. Knobloch. Bifurcation structure of localized states in the Lugiato-Lefever equation with anomalous dispersion. *Phys. Rev. E*, 97:042204, Apr 2018.

[PRGGK18b]   P. Parra-Rivas, D. Gomila, L. Gelens, and E. Knobloch. Bifurcation structure of periodic patterns in the lugiato-lefever equation with anomalous dispersion. *Phys. Rev. E*, 98:042212, Oct 2018.

[PRGM⁺14a] P. Parra-Rivas, D. Gomila, M. A. Matías, S. Coen, and L. Gelens. Dynamics of localized and patterned structures in the Lugiato-Lefever equation determine the stability and shape of optical frequency combs. *Phys. Rev. A*, 89:043813, Apr 2014.

[PRGM⁺14b] P. Parra-Rivas, D. Gomila, M. A. Matías, P. Colet, and L. Gelens. Effects of inhomogeneities and drift on the dynamics of temporal solitons in fiber cavities and microresonators. *Opt. Express*, 22(25):30943–30954, Dec 2014.

[PRGM⁺16] P. Parra-Rivas, D. Gomila, M. A. Matías, P. Colet, and L. Gelens. Competition between drift and spatial defects leads to oscillatory and excitable dynamics of dissipative solitons. *Phys. Rev. E*, 93:012211, Jan 2016.

[PRGMC13] P. Parra-Rivas, D. Gomila, M. A. Matias, and P. Colet. Dissipative soliton excitability induced by spatial inhomogeneities and drift. *Phys. Rev. Lett.*, 110:064103, 2013.

[Pri78] I. Prigogine. Time, structure, and fluctuations. *Science*, 201(4358):777–785, 1978.

[PT] K. Panajotov and M. Tlidi. Private communications.

[PT10] K. Panajotov and M. Tlidi. Spontaneous motion of cavity solitons in vertical-cavity lasers subject to optical injection and to delayed feedback. *Eur. Phys. J. D*, 59(1):67–72, Jul 2010.

[PT14] Krassimir Panajotov and Mustapha Tlidi. Chaotic behavior of cavity solitons induced by time delay feedback. *Opt. Lett.*, 39(16):4739–4742, 2014.

[PVG⁺13] A. Pimenov, A. G. Vladimirov, S. V. Gurevich, K. Panajotov, G. Huyet, and M. Tlidi. Delayed feedback control of self-mobile cavity solitons. *Phys. Rev. A*, 88:053830, Nov 2013.

[Pyr92] K. Pyragas. Continuous control of chaos by self-controlling feedback. *Phys. Lett. A*, 170:421–428, 1992.

[Roz75] N. N. Rozanov. Kinetics of a solid-state laser with an additional moving mirror. *Sov. J. Quantum Electron.*, 4(10):1191, 1975.

[SH77] J. Swift and P. C. Hohenberg. Hydrodynamic fluctuations at the convective instability. *Phys. Rev. A*, 15:319–328, 1977.

[SJG18] C. Schelte, J. Javaloyes, and S. V. Gurevich. Dynamics of temporally localized states in passively mode-locked semiconductor lasers. *Phys. Rev. A*, 97:053820, May 2018.

[SJMO05] A. J. Scroggie, J. Jeffers, G. McCartney, and G.-L. Oppo. Reversible soliton motion. *Phys. Rev. E*, 71:046602, Apr 2005.

[SLV07] A.D. Scott, H. Leo, and M. Vela. Molecular fingerprinting with the resolved modes of a femtosecond laser frequency comb. *Nature*, 445(7128):627, feb 2007.

[STB⁺98]   L. Spinelli, G. Tissoni, M. Brambilla, F. Prati, and L. A. Lugiato. Spatial solitons in semiconductor microcavities. *Phys. Rev. A*, 58:2542–2559, Sep 1998.

[STP⁺17]   T. Schemmelmann, F. Tabbert, A. Pimenov, A. G. Vladimirov, and S. V. Gurevich. Delayed feedback control of self-mobile cavity solitons in a wide-aperture laser with a saturable absorber. *Chaos*, 27(11):114304, 2017.

[Str01]   S. H. Strogatz. *Nonlinear dynamics and chaos: with applications to physics, biology and chemistry*. Perseus publishing, 2001.

[SZ72]   A. Shabat and V. Zakharov. Exact theory of two-dimensional self-focusing and one-dimensional self-modulation of waves in nonlinear media. *Soviet physics JETP*, 34(1):62, 1972.

[Tab14]   Felix Tabbert. Dynamik lokalisierter Strukturen mit Zeitverzögerung. Master's thesis, Westfälische Wilhelms-Universität Münster, 2014.

[TAFJ08]   Y. Tanguy, T. Ackemann, W. J. Firth, and R. Jäger. Realization of a semiconductor-based cavity soliton laser. *Phys. Rev. Lett.*, 100:013907, Jan 2008.

[TAR⁺13]   U. Thiele, A. J. Archer, M. J. Robbins, H. Gomez, and E. Knobloch. Localized states in the conserved Swift-Hohenberg equation with cubic nonlinearity. *Phys. Rev. E*, 87:042915, 2013.

[TAV⁺15]   M. Tlidi, E. Averlant, A. Vladimirov, A. Pimenov, S. V. Gurevich, and K. Panayotov. Localized structures in broad area VCSELs: experiments and delay-induced motion. In *Structural Nonlinear Dynamics and Diagnosis*, pages 417–437. Springer, 2015.

[TCP18]   M. Tlidi, M. G. Clerc, and K. Panajotov. Dissipative structures in matter out of equilibrium: from chemistry, photonics and biology, the legacy of Ilya Prigogine (part 1). *Phil. Trans. R. Soc. A*, 376:20140014, 2018.

[TFHP⁺19]   F. Tabbert, T. Frohoff-Hülsmann, K. Panajotov, M. Tlidi, and S. V. Gurevich. Stabilization of localized structures by inhomogeneous injection in Kerr resonators. *arXiv preprint arXiv:1901.02308.*, 2019.

[TGKW00]   V. B. Taranenko, I. Ganne, R. J. Kuszelewicz, and C. O. Weiss. Patterns and localized structures in bistable semiconductor resonators. *Physical Review A*, 61(6), may 2000.

[THM98]   M. Tlidi, M. Haelterman, and P. Mandel. Three-dimensional structures in diffractive and dispersive nonlinear ring cavities. *J. Opt. B*, 10(6):869–878, dec 1998.

[TLV08]   M. Tlidi, R. Lefever, and A. Vladimirov. On vegetation clustering, localized bare soil spots and fairy circles. In *Dissipative Solitons: From Optics to Biology and Medicine*, pages 1–22. Springer, 2008.

[TML94]   M. Tlidi, P. Mandel, and R. Lefever. Localized structures and localized patterns in optical bistability. *Phys. Rev. Lett.*, 73:640–643, 1994.

[TP17]   M. Tlidi and K. Panajotov. Two-dimensional dissipative rogue waves due to time-delayed feedback in cavity nonlinear optics. *Chaos*, 27(1):013119, 2017.

[TSP+14]   M. Tlidi, K. Staliunas, K. Panajotov, A.G. Vladimirov, and M.G. Clerc. Localized structures in dissipative media: from optics to plant ecology. *Phil. Trans. R. Soc. A*, 372(2027), 2014.

[TSS13]   M. Tlidi, A. Sonnino, and G. Sonnino. Delayed feedback induces motion of localized spots in reaction-diffusion systems. *Phys. Rev. E*, 87:042918, 2013.

[TSTG17]   F. Tabbert, C. Schelte, M. Tlidi, and S. V. Gurevich. Delay-induced depinning of localized structures in a spatially inhomogeneous swift-hohenberg model. *Phys. Rev. E*, 95:032213, Mar 2017.

[Tur90]   A Turing. The chemical basis of morphogenesis, Phil. Trans. Roy. Soc. B, 237 (1952), 37-72. *Reprinted in Bull. Math. Biol*, 52:153–197, 1990.

[TVPT09]   M. Tlidi, A. G. Vladimirov, D. Pieroux, and D. Turaev. Spontaneous motion of cavity solitons induced by a delayed feedback. *Phys. Rev. Lett.*, 103:103904, 2009.

[TVT+10]   M. Tlidi, A. G. Vladimirov, D. Turaev, G. Kozyreff, D. Pieroux, and T. Erneux. Spontaneous motion of localized structures and localized patterns induced by delayed feedback. *Eur. Phys. J. D*, 59:59–65, 2010.

[UHH02]   T. Udem, R. Holzwarth, and T. W. Hänsch. Optical frequency metrology. *Nature*, 416(6877):233–237, mar 2002.

[UWR14]   H. Uecker, D. Wetzel, and J. D. M. Rademacher. pde2path - a Matlab package for continuation and bifurcation in 2d elliptic systems. *Numerical Mathematics: Theory, Methods and Applications*, 7(1):58–106, 2014.

[vHMSZ01] J. von Hardenberg, E. Meron, M. Shachak, and Y. Zarmi. Diversity of vegetation patterns and desertification. *Phys. Rev. Lett.*, 87:198101, Oct 2001.

[VPG+14]   A. G. Vladimirov, A. Pimenov, S. V. Gurevich, K. Panajotov, E. Averlant, and M. Tlidi. Cavity solitons in vertical-cavity surface-emitting lasers. *Philos. Trans. Royal Soc. A*, 372(2027):20140013–20140013, sep 2014.

[vTL95]   G. H. M. van Tartwijk and D. Lenstra. Semiconductor lasers with optical injection and feedback. *J. Opt. B*, 7(2):87–143, apr 1995.

[Waz09]   A. M. Wazwaz. *Solitary Waves Theory*, pages 479–502. Springer Berlin Heidelberg, Berlin, Heidelberg, 2009.

[Wil16]   M. Wilczek. *Pattern Formation in Driven Thin Layers of Simple and Complex Liquids*. PhD thesis, Westfälische Wilhelms-Universität Münster, 2016.

[ZK65]   N. J. Zabusky and M. D. Kruskal. Interaction of solitons in a collisionless plasma and the recurrence of initial states. *Phys. Rev. Lett*, 15:240–243, 1965.

Lebenslauf

Name:	Felix Tabbert
Geburtsdatum:	02.07.1987
Geburtsort:	Frankfurt am Main
Staatsangehörigkeit:	deutsch
Familienstand:	ledig

Ausbildung

seit 04/2015	**Promotionsstudium** am Institut für Theoretische Physik der Westfälischen Wilhelms-Universität Münster mit Aufenthalten an der Université Libre de Bruxelles und der Vrije Universiteit Brussel, unter der Betreuung von PD Dr. Svetlana Gurevich, Prof. Dr. Cornelia Denz und Prof. Dr. Uwe Thiele
2012 – 2014	**Masterstudium im Fach Physik** an der Westfälischen Wilhelms-Universität Münster, Abschluss: M.Sc., Abschlussnote: 1,0 mit Auszeichnung
2010 – 2014	**Zweifachbachelorstudium Philosophie und Physik** an der Westfälischen Wilhelms-Universität Münster, Abschluss: B.A., Abschlussnote: 1,1
2010 – 2011	**Erasmusstudium** an der Universidad de Sevilla, Spanien
2008 – 2012	**Bachelorstudium im Fach Physik** an der Westfälischen Wilhelms-Universität Münster, Abschluss: B.Sc., Abschlussnote: 1,2
2007 – 2008	**Studium Generale** am Leibniz Kolleg, Tübingen
2007	**Allgemeine Hochschulreife** (Note 1,0) an der Elisabethenschule Frankfurt

Stipendien

04/2015 – 03/2019	Promotionsstipendum der Studienstiftung des deutschen Volkes
09/2017 und 10/2018	Forschungsstipendium des WWU-Programms International Promovieren für einen Aufenthalt and den Universitäten von Brüssel (ULB und VUB)
09/2010 – 07/2011	Auslandsstipendium (Studienstiftung des deutschen Volkes und Erasmus-Stipendium) für ein Auslandsjahr im Rahmen des Bachelorstudiums Physik an der Universidad de Sevilla, Spanien
12/2008 – 10/2014	Stipendium der Studienstiftung des deutschen Volkes

Berufstätigkeit

10/2014 – 03/2018	Wissenschaftliche Hilfskraft am Institut für Theoretische Physik der Westfälischen Wilhelms-Universität Münster
10/2013 – 09/2014	Studentische Hilfskraft am Fachbereich Physik der Westfälischen Wilhelms-Universität Münster
04/2012 – 09/2014	Studentische Hilfskraft am Institut für Theoretische Physik der Westfälischen Wilhelms-Universität Münster

Danksagung